Comparison of landslide tsunami models and exploration of fields of application

Alexandre Paris

Thèse présentée pour obtenir le grade de docteur

Université de Pau et des Pays de l'Adour

Laboratoires DASE/SLDG/LEGA (CEA) et SIAME (UPPA)
École Doctorale des Sciences Exactes et leurs Applications de l'Université de Pau et des Pays de l'Adour (ED 211)

Discipline : Géosciences

Comparison of landslide tsunami models and exploration of fields of application

Comparaison de modèles de tsunamis générés par glissements de terrain et exploration des champs d'application

Par : **Alexandre PARIS**

Sous la direction de Stéphane Abadie et Philippe Heinrich,

Membres du jury:

Rapportrice : Maria Ana Baptista - Professeure, Universidade de Lisboa

Rapporteur : Stephan Grilli - Professeur, University of Rhode Island

Examinatrice (Présidente) : Anne Le Friant - Directrice de recherche, IPGP

Examinatrice : Hélène Hébert - Ingénieure-chercheuse HDR, CEA/DAM

Examinateur : Yves Le Guer - Maître de conférence HDR, SIAME/UPPA

Thèse soutenue le : 13 septembre 2021

Preface - Avant-propos

The work presented in this thesis was carried out between September 2018 and June 2021. The reader will have remarked that this interval includes the now famous year 2020 which will have seen the birth of what no one would have imagined living in our contemporary societies, a pandemic. Thus, while my first year and the beginning of my second year took place in a carefree atmosphere, punctuated by conferences, meetings and collaborations, the rest of this thesis was an alternation of lockdowns and partial returns to the laboratory. Although I feel that I have been relatively spared from this strange situation, some of the trajectories envisaged at the beginning of the thesis could not be taken and the final result could have been different. Nevertheless, I am happy to present this work in which I have put everything I could despite the prevailing slump.

"You cannot win a game by giving up." – Xavier Tartakover

Le travail présenté dans cette thèse a été réalisé entre septembre 2018 et juin 2021. Il n'aura pas échappé à la lectrice ou au lecteur que cet intervalle comporte la désormais fameuse année 2020 qui aura vu naître ce que personne n'aurait imaginé vivre dans nos sociétés contemporaines, une pandémie. Ainsi, alors que ma première année et le début de ma deuxième année se sont déroulées dans l'insouciance, au rythme des congrès et des diverses rencontres et collaborations, le reste de cette thèse a été une alternance de confinements et de retours partiels au laboratoire. Bien que j'estime avoir été relativement épargné par cette étrange situation, certaines trajectoires envisagées au début de la thèse n'ont pas pu être empruntées et le résultat final aurait pu être différent. Néanmoins je suis heureux de présenter ce travail dans lequel j'ai mis tout ce que je pouvais malgré le marasme ambiant.

"On n'a jamais gagné une partie en abandonnant." – Xavier Tartakover

Remerciements

Je tiens tout d'abord à remercier Maria Ana Baptista et Stephan Grilli qui ont accepté de rapporter cette thèse. Merci également aux autres membres du jury, Anne Le Friant, Hélène Hébert et Yves Le Guer. Je suis heureux que mes travaux et ma présentation de soutenance vous aient plu.

Merci à Javier Lopez Lara et Raphaël Paris pour leurs remarques et conseils lors des deux comités de thèse.

Merci beaucoup à mon premier directeur de thèse, Stéphane Abadie. Tu as toujours été disponible et sans tes analyses pertinentes, cette thèse n'aurait pas pris la même direction.

Merci aussi à mon second directeur de thèse, Philippe Heinrich. Depuis que j'ai débuté mon stage au CEA tu as toujours été bienveillant et encourageant. Nos passionnantes discussions de café vont indubitablement me manquer. Désolé en revanche de n'être jamais venu sur le bateau.

Merci à mon chef de labo, Nicolas, qui m'a fait confiance durant ces trois ans. Merci également à toutes les personnes du laboratoire, du CENALT et du CSEM que je ne peux pas citer car trop nombreuses mais qui ont participé de près ou de loin à cette thèse en fournissant un environnement de travail agréable.

Cette thèse a été marquée par la crise sanitaire et les confinements successifs. Je tiens donc à remercier les con-finé • e • s du CEA qui se reconnaîtront, vous m'avez bien fait rire et les confinements sont passés plus vite. J'espère vous avoir diverti • e • s.

J'aimerais enfin remercier ma famille, en particulier mes parents qui m'ont accueilli pendant le deuxième confinement et qui ont englouti tous les gâteaux que je leur confectionnais.

Abstract - Résumé

After earthquakes, landslides are the second cause for tsunami generation. A proper understanding is required to prevent future disaster or to develop early warnings. This can be achieved through physical models in laboratory or numerical models. In the last category, several models exist and can provide very similar results for a case study. Among them, depth-averaged models using for example shallow water or Boussinesq equations, can be opposed to Navier-Stokes models. The main objective of this PhD thesis is to compare these two modeling strategies with two specific models, a depth-averaged model, AVALANCHE, and a Navier-Stokes model, OpenFOAM. First, two benchmarks (a subaerial and submerged one) are used to calibrate the models. This highlighted that both models could reproduce the experimental data and that several combinations of parameters led to similar results. Second, sensitivity studies are carried out to evaluate the influence of the initial landslide position and the slope angle and to observe the behavior of the different equations (shallow water, Boussinesq or Navier-Stokes) during the wave generation and propagation phases. Finally, both models are applied to two real cases, the June 17, 2017, Karrat Fjord, Greenland, landslide and tsunami, and the December 22, 2018, Anak Krakatau, Indonesia, collapse and tsunami, and are intercompared.

Les effondrements gravitaires sont la deuxième cause de génération de tsunamis après les séismes. Il est important de bien les comprendre afin de prévenir de futures catastrophes ou de développer les systèmes d'alerte. Pour cela, des modèles analogiques, en laboratoire, ou numériques sont utilisés. Dans la deuxième catégorie, de nombreux modèles existent et peuvent produire des résultats similaires pour un cas donné. Parmi eux, les modèles intégrés sur la profondeur qui utilisent par exemple les équations de type shallow water ou de Boussinesq, peuvent être opposés aux modèles Navier-Stokes. L'objectif de cette thèse est de comparer ces deux stratégies à l'aide de deux modèles spécifiques, un modèle intégré sur la hauteur, AVALANCHE, et un modèle Navier-Stokes, OpenFOAM. Tout d'abord, les deux modèles sont calibrés grâce à deux benchmarks, un glissement subaérien et un submergé. Cette étude a montré que les deux modèles pouvaient reproduire les données expérimentales et que plusieurs combinaisons de paramètres permettaient d'obtenir les mêmes résultats. Ensuite, des études de sensibilité sont réalisées afin d'évaluer l'influence de la position initiale du glissement et de la pente, et d'observer le comportement des différentes équations (shallow water, Boussinesq ou Navier-Stokes) pendant les phases de génération et de propagation de la vague. Enfin, l'application des deux modèles à deux cas réels, le glissement et le tsunami du 17 juin 2017 dans le Karrat Fjord au Groenland et le tsunami généré par l'effondrement du volcan Anak Krakatau le 22 décembre 2018, en Indonésie, permet de les comparer entre eux.

Contents

List of Figures

List of Tables

Introduction

Tsunamigenic landslides may be considered as an underestimated threat when it comes to natural hazards. Given the seismic origin of the two most famous tsunamis of the 21st century, Sumatra in 2004 and Tohoku in 2011, people generally think that tsunamis are only generated by earthquakes. A tsunami is a train of large-period waves generated by a sudden deformation of the water surface. The source of this deformation can be a displacement of the sea bottom, generated by an earthquake or a landslide (submarine or subaerial landslide falling into water), but also an atmospheric perturbation (it is then called a meteotsunami) or an asteroid fall. The two latter are not taken into account in this thesis, but the interested reader could refer to Vilibić and Šepić (2009); Vilibić et al. (2016) or Vilibić et al. (2021) concerning meteotsunamis and to Ward and Asphaug (2000); Robertson and Gisler (2019) or Violeau (2021) for asteroids. Earthquake-generated tsunamis (Hébert et al., 2020; Sugawara, 2021) will also not be studied in this thesis. About landslides, two categories can be distinguished: the submarine landslides and the partially submerged or located completely above the water surface, which we will refer to as subaerial landslides from now on. With the same volume, a subaerial landslide is generally more tsunamigenic than a submarine one, its velocity and its impact being higher due to a lesser friction of the air compared to that of the water. Both kinds can happen in marine or lake environments (Yavari-Ramshe and Ataie-Ashtiani, 2016).

After the deadly tsunami of 2004 in Sumatra, the tsunami research increased and the French authorities decided to create an alert center for the French coasts. The Tsunamis Alert Center (Centre d'Alerte aux Tsunamis, CENALT) was launched in 2012. Its role is to monitor the western Mediterranean coasts and the North-East Atlantic Ocean, to analyse any tsunamigenic seismic event in those areas and to provide an information bulletin to the authorities within 15 min after the earthquake. A database of tsunamigenic faults and the associated mechanisms was created and is used for each event to estimate the expected water heights at the French coastlines. This part of the work is fully mastered by operators working 24 hours a day, 7 days a week at the center. However, since their detection is acknowledgedly difficult, so far nothing is planned to take into account the landslide tsunamis.

On December 22, 2018, the coasts of the Sunda Strait, between the Java and Sumatra Islands in Indonesia, were struck by a devastating tsunami following the eruption of the Anak Krakatau volcano. A large part of the volcano collapsed into water, generating an 80 to 100 m high wave that propagated for several tens of minutes before hitting the coasts. Because no earthquake was detected, there was no warning. This event illustrates that

warning centers have to elaborate strategies against landslide tsunamis. This requires the development of fast, robust and reliable codes in order to either work in real-time response mode, or build databases such as the one already existing for faults and potential tsunamis.

Landslide tsunami models are mainly divided in two main categories: the depth-integrated and Navier-Stokes models. The latter is generally considered as more accurate, but the first one is faster and so could be better adapted for tsunami warning centers. For both categories, either the landslide is calculated apart and introduced in the tsunami model, or both the landslide and the tsunami are calculated in the same model.

The landslide can be considered as deformable or non deformable. In the first category, several rheological laws can be used to define the behavior of the landslide. For instance, the landslide can be considered as a Newtonian fluid, a Bingham fluid, a power-law fluid or it can follow a Coulomb law. For the tsunami part, the Navier-Stokes equations are solved in 3D models, whereas shallow water or Boussinesq equations are generally used in depth-integrated models.

All these rheological laws and tsunami equations lead to several models which $infine$ can produce very similar or different results, depending on the parameters used. The modeling of the 2018 Anak Krakatau event is a very good example of the diversity of landslide tsunami models. Grilli et al. (2019) used a 3D model (NHWAVE) for the landslide tsunami generation and a 2DH depth-integrated model (FUNWAVE-TVD) for the tsunami propagation; Paris et al. (2020) used a unique 2DH model (AVALANCHE) for the landslide simulation, the tsunami generation and propagation; Heidarzadeh et al. (2020) used a 2DH model (COMCOT) for the tsunami propagation with a simple initial elevation in order to introduce a generated water wave and Borrero et al. (2020) used a 2DH model (pCOULWAVE) with an initial tsunami waveform derived from an analytical solution.

All previously cited models reproduced most of the far-field tsunami observations, leading to several questions: is one model more accurate than the others, with respect to the generation and the propagation of the wave, the material (fine grains or large blocks) or the slope angle? Is a Navier-Stokes model always more accurate than a depth-integrated model? In the present thesis, a depth-integrated model, AVALANCHE, and a Navier-Stokes model, OpenFOAM are compared to one another to answer a few of the previous questions.

In Part I, Chapter 1 is dedicated to historical landslide tsunamis, Chapter 2 to recent landslide tsunami laboratory experiments, Chapter 3 to landslide tsunami modeling and Chapter 4 to a few scientific questions raised by the previous reviews.

In Part II, after a short introduction in Chapter 1 and a presentation of the numerical tools, AVALANCHE and OpenFOAM, used in this thesis in Chapter 2, Chapter 3 is dedicated to the calibration of both models with two benchmarks using a landslide made

of glass beads with an initial triangular shape (Viroulet et al., 2014; Grilli et al., 2017).

In Chapter 4, two studies are presented. In the first one, realized during the 2019 CEMRACS at Marseille, France, the collapse of a landslide with a parallelogram shape is simulated with OpenFOAM. The landslide solution obtained is then used as an input for two depth-integrated models, one using the shallow water equations, the other the Boussinesq equations. The objective is to evaluate the behavior of the two depth-integrated models both in the generation and propagation zones, considering the OpenFOAM results as a reference solution. In the second, sensitivity studies using a depth-integrated model and a Navier-Stokes model are conducted on the slope angle and on the initial position of the landslide regarding the water surface. The main objective is to compare both models, with slopes and submergence as parameters.

Finally, in Part III, the depth-averaged modeling of two real events, the June 17, 2017 Karrat Fjord, Greenland, landslide tsunami (Paris et al., 2019) and the December 22, 2018 Anak Krakatau, Indonesia collapse and tsunami (Paris et al., 2020) are presented in Chapter 2. Then, in Chapter 3, an application of a general setup for complex landslide tsunami modeling with OpenFOAM to these two events is proposed and the results are compared to the depth-averaged simulations.

Les glissements de terrain tsunamigènes sont une menace probablement sous-estimée en matière de risques naturels. Les deux tsunamis les plus célèbres du 21ème siècle, Sumatra en 2004 et Tohoku en 2011, étant d'origine sismique, il est généralement admis que les tsunamis sont uniquement générés par des tremblements de terre. Un tsunami est un train de vagues de grandes périodes généré par une déformation soudaine de la surface de l'eau. La source de cette déformation peut être un déplacement du fond marin, provoqué par un séisme ou un glissement de terrain (glissement sous-marin ou subaérien tombant dans l'eau), mais aussi une perturbation atmosphérique (on parle alors de météosunami) ou une chute d'astéroïde.

Ces deux derniers modes de génération ne sont pas pris en compte dans cette thèse, mais le lecteur intéressé pourra se référer à Vilibić and Šepić (2009); Vilibić et al. (2016) ou Vilibić et al. (2021) concernant les météosunamis et à Ward and Asphaug (2000); Robertson and Gisler (2019) ou Violeau (2021) pour les astéroïdes. Les tsunamis générés par les séismes (Hébert et al., 2020; Sugawara, 2021) ne seront pas non plus étudiés dans cette thèse. En ce qui concerne les glissements de terrain, on peut distinguer deux catégories : les glissements sous-marins et les glissements partiellement immergés ou situés au-dessus de la surface de l'eau, que nous appellerons à partir de maintenant glissements subaériens. À volume égal, un glissement de terrain subaérien est généralement plus tsunamigène qu'un glissement de terrain sous-marin, sa vitesse et son impact étant plus élevés en raison d'une friction de l'air plus faible que celle de l'eau. Les deux types de glissements peuvent se produire dans des environnements marins ou lacustres.

Après le tsunami meurtrier de 2004 à Sumatra, la recherche sur les tsunamis s'est accélérée et les autorités françaises ont décidé de créer un centre d'alerte pour les côtes françaises. Le CENtre d'ALerte aux Tsunamis (CENALT) a été lancé en 2012. Son rôle est de surveiller les côtes de la Méditerranée occidentale et de l'Atlantique Nord-Est, en analysant tout événement sismique tsunamigène dans ces zones et en fournissant un bulletin d'information aux autorités dans les 15 min suivant le séisme. Une base de données de failles tsunamigènes et des mécanismes associés a été créée et est utilisée pour chaque événement afin d'estimer les hauteurs d'eau attendues sur les côtes françaises. Cette partie du travail est entièrement gérée par les opérateurs qui travaillent 7 jours sur 7 et 24 heures sur 24 au centre. Cependant, leur détection étant reconnue comme difficile, rien n'est prévu à ce jour pour prendre en compte les tsunamis dus à des glissements de terrain.

Le 22 décembre 2018, les côtes du détroit de la Sonde, entre les îles de Java et de Sumatra en Indonésie, ont été frappées par un tsunami dévastateur suite à l'éruption du volcan Anak Krakatoa. Une grande partie du volcan s'est effondrée dans l'eau, générant une vague de 80 à 100 m de haut qui s'est propagée pendant plusieurs dizaines de minutes avant de frapper les côtes. Aucune alerte n'a été lancée car il n'y a pas eu de tremblement de terre détecté. Cet événement illustre la nécessité pour les centres

d'alerte d'élaborer des stratégies contre les tsunamis dus aux glissements de terrain. Cela passe par le développement de codes rapides, robustes et fiables afin de pouvoir soit travailler en mode réponse en temps réel, soit construire des bases de données comme celle qui existe déjà pour les failles et les tsunamis potentiels.

Les modèles numériques de tsunamis liés aux glissements de terrain se divisent principalement en deux catégories : les modèles intégrés sur la profondeur et les modèles de type Navier-Stokes. Ces derniers sont généralement considérés comme plus précis, mais les premiers sont plus rapides et pourraient donc être mieux adaptés aux centres d'alerte aux tsunamis. Pour les deux catégories, soit le glissement de terrain est calculé séparément et introduit dans un modèle de tsunami, soit le glissement de terrain et le tsunami sont calculés dans le même modèle.

Le glissement de terrain peut être considéré comme déformable ou non déformable. Dans la première catégorie, plusieurs lois rhéologiques peuvent être utilisées pour définir le comportement du glissement de terrain. Par exemple, le glissement de terrain peut être considéré comme un fluide newtonien, un fluide de Bingham, ou suivre une loi de Coulomb, ou encore une loi de puissance. Pour la partie tsunami, les équations de Navier-Stokes sont résolues dans les modèles 3D alors que les équations shallow water ou de Boussinesq sont généralement utilisées dans les modèles intégrés sur la profondeur.

Toutes ces lois de comportement et équations de tsunami conduisent à plusieurs modèles qui $infine$ peuvent produire des résultats très similaires ou différents selon les paramètres utilisés. La modélisation de l'événement Anak Krakatau de 2018 est un très bon exemple de la diversité de modèles. En effet, Grilli et al. (2019) ont utilisé un modèle 3D (NHWAVE) pour la génération du tsunami par le glissement de terrain et un modèle 2DH intégré sur la profondeur (FUNWAVE-TVD) pour la propagation du tsunami; Paris et al. (2020) ont utilisé un modèle 2DH unique (AVALANCHE) pour la simulation du glissement de terrain, la génération et la propagation du tsunami; Heidarzadeh et al. (2020) ont utilisé un modèle 2DH (COMCOT) pour la propagation du tsunami avec une simple élévation initiale afin d'introduire une vague et Borrero et al. (2020) ont utilisé un modèle 2DH (pCOULWAVE) avec une forme d'onde de tsunami initiale dérivée d'une solution analytique.

Tous ces modèles reproduisent la plupart des observations du tsunami en champ lointain, ce qui soulève plusieurs questions : un modèle est-il plus précis que les autres en ce qui concerne la génération et la propagation de la vague, le matériau (grains fins ou gros blocs) ou l'angle de la pente ? Un modèle Navier-Stokes est-il toujours plus précis qu'un modèle intégré sur la profondeur ? Dans cette thèse, un modèle intégré sur la profondeur, AVALANCHE, et un modèle Navier-Stokes, OpenFOAM, sont comparés l'un à l'autre pour répondre à quelques unes des questions précédentes.

Dans la Partie I, le Chapitre 1 est consacré aux tsunamis générés par des glissements de terrain historiques, le Chapitre 2 aux expériences en laboratoire récentes sur ce type

de tsunamis, le Chapitre 3 à la modélisation de ces tsunamis et le Chapitre 4 à quelques questions scientifiques soulevées par les précédentes revues.

Dans la Partie II, après une brève introduction au Chapitre 1 et une présentation des outils numériques, AVALANCHE et OpenFOAM, utilisés dans cette thèse au Chapitre 2, le Chapitre 3 est dédié à la calibration des deux modèles grâce aux expériences de Viroulet et al. (2014) et Grilli et al. (2017) qui utilisent un glissement triangulaire fait de billes de verre.

Le Chapitre 4 est consacré à deux études. Dans la première, réalisée lors du CEMRACS 2019 à Marseille, France, l'effondrement d'un glissement de terrain avec une forme de parallélogramme est simulé avec OpenFOAM. La solution de glissement obtenue est ensuite utilisée comme entrée pour deux modèles intégrés sur la profondeur, l'un utilisant les équations shallow water, l'autre les équations de Boussinesq. L'objectif est d'évaluer le comportement des deux modèles intégrés sur la profondeur dans les zones de génération et de propagation, en considérant les résultats d'OpenFOAM comme une solution de référence. Dans la deuxième étude, des analyses de sensibilité sont menées sur l'angle de la pente et sur la position initiale du glissement par rapport à la surface de l'eau. L'objectif principal est de comparer les deux modèles avec les pentes et la submersion comme paramètres.

Enfin, dans la Partie III, les modélisations par un modèle intégré sur la profondeur de deux événements réels, les événements du 17 juin 2017 dans le Karrat Fjord, au Groenland (Paris et al., 2019) et l'effondrement du volcan Anak Krakatoa et le tsunami généré le 22 décembre 2018, en Indonésie (Paris et al., 2020), sont présentées dans le Chapitre 2. Ensuite, dans le Chapitre 3, une méthode générale pour la modélisation de tsunamis complexes générés par glissement de terrain avec OpenFOAM est présentée et appliquée aux deux événements précédents. Les résultats sont comparés à ceux obtenus par le modèle intégré sur la profondeur.

Part I

State of the art

Chapter 1

Historical landslide tsunamis

In the past 150 years, around 40 significant landslide tsunamis have been observed. They are presented in the following sections, separated in two categories: the submarine and the subaerial ones. Some events are not listed below because they are relatively ancient but are nonetheless important, as for example the Storegga, Norway, slide (Bondevik, 2019) which is the biggest known submarine landslide tsunami and occurred around -8150 BP. With a volume of 2400-3200 km^3, the generated tsunami induced runups reached from 3 to 20 m on the coasts of Scotland, Norway, Shetland and Faroe Islands.

Another significant and non listed event is the tsunami generated by the 1883 Krakatoa, Indonesia, eruption. The collapse of the caldera produced a 40-50 m high wave and killed more than 30000 people in the Sunda Strait.

Other very large landslide tsunamis occurred in the past. For example, geological evidences of fourteen paleo-submarine landslides have been identified around Canary Islands (Masson et al., 2002).

In some cases that are not listed here, the tsunami can be generated by both an earthquake and a landslide (or several) it triggered. The 1908 Messina, Italy (80000 deaths) and 2018 Palu, Indonesia (2000 deaths) events belong to this category (Schambach et al., 2020, 2021).

For more details, recent reviews of historical landslide tsunamis can be found in Yavari-Ramshe and Ataie-Ashtiani (2016) and Tappin (2021).

1.1 Submarine events

Only 11 submarine landslide tsunamis are listed in Table 1. Among them, two events are more remarkable than the others.

The first one is the 1929 Grand Banks, Canada, landslide (Fine et al., 2005), which has the largest volume, 200 km^3. Triggered by a M=7.2 earthquake on November 18, it generated a wave that killed 28 people and reached a runup height of 13 m.

With a thirty to fifty times lower volume (4-6.4 km^3), the 1998 Papua New Guinea landslide (Synolakis et al., 2002; Heinrich et al., 2001; Tappin et al., 2008) is the second remarkable event of this list. On July 17, after a M=7.1 earthquake, a 10-15 m tsunami destroyed three villages in Papua New Guinea and killed over 2200 people, making it the most deadly submarine landslide tsunami. Bathymetric surveys highlighted the scar of a

Date	Location	Deaths	Type	V (million m³)	A	W	L	T	S (°)	H	R	References
1806	Goldau, CH	457	S_A	36	1100	300	1200	100	22.5	20		Thuro et al., 2010
1888	Brattora, NO		S_M	1.45	-80	600	320	8	6		6	L'Heureux et al., 2011 / Glimsdal et al., 2013
1908	Notre-Dame-de-la-Salette, CA	33	S_A	1.2		150	450	18			15	Locat et al., 2016
1929	Grand Banks, CA	28	S_M	200000	-2500			20		8	13	Fine et al., 2005
1930	Orkdalsfjorden, NO	1	S_A	18.5						15		L'Heureux et al., 2014
1934	Tafjord, NO	40	S_A	3	700	130	400	75		50	25	Harbitz, 2011
1936	Lovatnet, NO	74	S_A	1	800							Hansen et al. 2016 / Waldmann et al., 2021
1946	Mt Colonel Foster, CA		S_A	0.7	710					29	51	Evans, 1989
1950	Nidelva, NO		S_M	3	-10	600	150	20	6			Bornhold, 2011
1958	Lituya Bay, AK, US	5	S_A	30	600	730	900	45			520	Miller, 1960 / Mader, 2002
1963	Vajont, IT	2000	S_A	260	950	2000	1000	130				Ward & Day, 2011
1963	Corinth Gulf, GR		S_M	0.057	0	10	570	10		6		Papadopoulos et al., 2007
1965	Lago Cabrera, CL	27	S_A	9	1500		700	150	45	25	60	Watt et al., 2009
1975	Kitimat, CA		S_M	27	0	1000	2000	13.5	14	8.2		Skvortsov & Bornhold, 2007
1979	Lembata Island, ID	540	S_A	50	200	300	3000	50	20		50	Lassa, 2009 / Yudhicara et al., 2015
1979	Bindalsfjorden, NO		S_A	0.005	110						2	Maramai et al., 2003
1979	Nice, FR	11	S_A	10	0	700	900	15	10	3		Assier-Rzadkiewicz et al., 2000
1987	La Grande River, CA		S_A	3.5	15		550		35			Lefebvre et al., 1991
1988	La Fossa, IT		S_A	0.2	200	250	270	3		2		Tinti et al., 1999
1990	Nidelva, NO		S_M	5	-15	750	600	10	12			L'Heureux et al., 2010
1994	Skagway, AK, US	1	S_M	0.8	0	330	160	15	30	10		Kulikov et al., 1996 / Rabinovich et al., 1999
1998	PNG	2200	S_M	4000	-1000	4000	4500	400	15		15	Heinrich et al., 2000 / Synolakis et al., 2002 / Tappin et al., 2008
1999	Fatu Hiva, PF		S_A	2.4		300	300	27		5		Hébert et al., 2002
2000	Paatuut, GL		S_A	90	1200	350	1300	200	26		50	Pedersen et al., 2002
2002	Stromboli, IT		S_M	20								Tinti et al., 2006
			S_A	5	550	500					10	
2003	Qianjiangping, CN	24	S_A	24	315	1000	1200	20	32		30	Wang et al., 2004
2006	Nicolet, CA		S_A+S_M	0.013	10	80	40	4	16			Franz et al., 2015
2007	Mentirosa Island, CL		S_A	7						10		Naranjo et al., 2009
2007	Punta Cola, CL		S_A	12		760	1000	530			150	Redfield et al., 2011
2007	Chehalis lake, CA		S_A	3	800	210	400	40			38	Wang et al., 2015
2008	Gongjiafang, CN		S_A	0.38	120	60	400	17	50		13	Xiao et al., 2015
2014	Statland, NO		S_M	0.4	380	100	200	20		4	10	Glimsdal et al., 2016
2014	Lac-des-Seize-Îles, CA		S_A	0.0305		55	94	5.9			1.8	Leblanc et al., 2016
2014	Tangjiaxi, CN	12	S_A	0.16	160	40	250	15	40		22.7	Huang et al., 2017
2014	Askja, IS		S_A	20	350	550	800	45			71	Gylfadóttir et al., 2017
2015	Taan Fjord, AK, US		S_A	180	850	700	1450	75	25		193	Haeussler et al., 2018 / Higman et al., 2018
2017	Nuugaatsiaq, GL	4	S_A	50	1000	1000	500	240				Paris et al., 2019
2018	Anak Krakatoa, ID	430	S_A+S_M	150	300	2000	1500				30	Grilli et al., 2019 / Paris et al., 2020 / Heidarzadeh et al., 2020

Table 1: Non-exhaustive list of historical landslides tsunamis since the 19th century. Type of landslide is either subaerial (S_A) or submarine (S_M). For each event and as far as possible, the following characteristics are collected: the volume (V), the altitude (A), the width (W), the length (L), the thickness (T), the slope (S), the generated wave height (H) and the runup (R). All lengths are given in meters.

4.2 km wide, 4.5 km long and 600-750 m thick submarine landslide. It is also the deepest submarine landslide (1000 m) and the event which produced the largest runup (15 m).

However, none of the two previous events generated the highest water wave, which was hypothetically produced by the 1994 Skagway landslide (Kulikov et al., 1996; Rabinovich et al., 1999) in Alaska, US, with a water wave height of 10 m. A piece of 800000 m^3 of an under construction harbor collapsed on the evening of the 3rd of November, killing one person.

With its numerous fjords, Norway is a place prone to landslide tsunamis, among them Brattora in 1888 (L'Heureux et al., 2011; Glimsdal et al., 2013), two similar landslides in Nidelva in 1950 (Bornhold, 2011) and 1990 (L'Heureux et al., 2010), and Statland in 2014 (Glimsdal et al., 2016). Luckily, the casualties of these events were only material damage.

The 1963 Corinth Gulf, Greece (Papadopoulos et al., 2007), and 1975 Kitimat, Canada (Skvortsov and Bornhold, 2007), events are two examples of submarine landslides that occurred close to the shoreline in shallow water. The proximity of the coasts makes them potentially more dangerous than in deep seas but in these two cases, most of the tsunami energy propagated offshore in perpendicular direction to the coastline.

1.2 Subaerial events

With a volume of 260 million m^3, the disaster of the 1963 Vajont dam in Italy (Ward and Day, 2011) is likely the subaerial landslide with the biggest volume. By collapsing into the reservoir, it generated a wave that overstepped the dam, killing about 2000 people in the valley. This makes it the deadliest known event too.

The wave generated by a subaerial landslide can be impressively high, such as the hypothetical 50 m wave of the 1934 Tafjord, Norway event (Harbitz and Glimsdal, 2011) or the 80-100 m wave generated by the collapse of the Anak Krakatau, Indonesia, in 2018 (Grilli et al., 2019; Heidarzadeh et al., 2020; Paris et al., 2020). These two events produced runups around 20-30 m, which is small compared to the 1958 Lituya Bay, Alaska, US, landslide tsunami (Miller, 1960; Mader and Gittings, 2002). In this area, on July 8, 1958, the collapse of a 30 million m^3 volume triggered by a M=7.5 earthquake generated a wave that reached a runup height of 524 m on the opposite bank.

Subaerial landslides can be located close to the water surface but also far from it, such as the 1965 Lago Cabrera, Chile, debris flow (Watt et al., 2009) that travelled from its initial altitude of 2000 m to the Lago Cabrera at 500 m, which represents a fall of 1500 m.

Subaerial landslides in lakes are very common worldwide (1906 Goldau, Switzerland (Thuro and Hatem, 2010); 1946 Mt Colonel Foster, Canada (Evans, 1989); 1965 Lago Cabrera, Chile (Watt et al., 2009); 2007 Chehalis Lake, Canada (Wang et al., 2015); 2014 Lac-des-Seize-Îles, Canada (Leblanc et al., 2016); 2014 Askja, Iceland Gylfadóttir et al.

(2017)).

In northern regions, subaerial landslides are numerous in fjords: in Norway (1930 Orkdalsfjorden (L'Heureux et al., 2014); 1934 Tafjord (Harbitz and Glimsdal, 2011); 1936 Lovatnet (Hansen et al., 2016; Waldmann et al., 2021); 1979 Bindalsfjorden (Maramai et al., 2003)), in Alaska, US (1958 Lituya Bay (Miller, 1960; Mader and Gittings, 2002); 2015 Taan Fjord (Haeussler et al., 2018; Higman et al., 2018))) and in Greenland (2000 Paatuut (Pedersen et al., 2002); 2017 Nuugaatsiaq (Paris et al., 2019)).

Volcanoes are also affected by subaerial landslides (Sosio et al., 2012). In 1979, a landslide triggered by the geothermal system of the Lembata Island, Indonesia, (Lassa, 2009; Yudhicara et al., 2015) generated a tsunami that reached an elevation of 50 m and killed more than 500 people. Unrest phases of volcanoes are favorable to subaerial landslides on their slopes, as at La Fossa, Italy, in 1988 (Tinti et al., 1999) or in Stromboli, Italy in 2002 (Tinti et al., 2006). The last event of this kind is the December 22, 2018 Anak Krakatau eruption and the landslide tsunami generated (Grilli et al., 2019; Heidarzadeh et al., 2020; Paris et al., 2020).

Subaerial landslides can be found on river banks, like in Canada with the Notre-Dame-de-la-Salette collapse in the Lièvre River in 1908 (Locat et al., 2016), the 1987 La Grande River slide (Lefebvre et al., 1991) or the Nicolet slide in the Nicolet Sud-Ouest River in 2006 (Franz et al., 2015). In these cases, the volume and so the damage kept limited.

Several events were recorded on rivers and associated with the fill of a dam reservoir, such as the 1963 Vajont, Italy, landslide (Ward and Day, 2011) or the 2014 Tangjiaxi, China, granular flow (Huang et al., 2017). During the latter event, the generated wave reached an elevation of 22.7 m and 12 people lost their lives. Still in China, the periods of fill of the Three Gorge Reservoir weaken the Yangtze River banks and numerous landslides have been observed, such as the 2003 Qianjiangping landslide after the first impoundment (Wang et al., 2004) or the 2008 Gongjiafang landslide (Xiao et al., 2015).

Some other events are remarkable, like the 1979 Nice collapse and tsunami, which remains to date the only case in Metropolitan France (Assier-Rzadkiewicz et al., 2000). It is also one of the few events caused by human activities. On October 16, 1979, during the expansion works at the harbor of Nice, France, at least 10 million m^3 collapsed, causing a wave which flooded the Baie des Anges with runup heights of 3 m in some places.

1.3 Conclusions

This previous historical research shows that the identified tsunamigenic landslides are mostly subaerial. It also illustrates the diversity of landslide tsunamis, of their location, width, thickness, altitude, above or under water.

Volumes of subaerial landslides are on average lower than submerged landslides. In Table 1, the average volume of subaerial landslides is 35 million m^3 whereas for the

submarine ones it is 18500 million m^3 if the Grand Banks and PNG landslides are taken into account, only 400 million m^3 without Grand Banks, and only 6.5 million m^3 without these both large events. Although the data are incomplete for a lot of events, the wave generated is about 18 m for subaerial landslides, against about 7.5 m for submarine ones (Grand Banks included), which confirms that subaerial landslides may be generally the most dangerous, as shown by the 2200 deaths of the Papua New Guinea event.

In general, altitude refers to the difference between the slide and the water surface, but in the literature, the "altitude" can be the altitude of the top of the slide, the center, or the bottom of the slip. The average of difference between the landslide and the water surface is about 560 m. Concerning the size, on average the subaerial landslides are 575 m wide, 845 m long and 90 m thick. Note that the thickness value is difficult to obtain. For some authors it is the average thickness of the landslide, for others the maximum thickness, for others it is calculated directly from volume, width and length. With these average values of width, length and thickness, a volume of about 45 million m^3 is obtained. Finally, little information is available about the slope, but the average value is about 25°. Note that these averaged values are not statistically significant due to the small size of the sample and missing events.

Chapter 2

Laboratory experiments

Laboratory experiments are divided in two categories: 2D experiments in channels and 3D experiments in basins. In both cases, depending on the materials, the landslide can be considered as rigid or as deformable. Rigid landslides can represent the behavior of cohesive landslides, while deformable landslides can represent debris flows or granular flows. Laboratory experiments are performed since the 1970s (Noda, 1970; Kamphuis and Bowering, 1970) but the state of the art in this chapter focuses on the experiments realized since the early 2000s. A review of previous laboratory experiments can be found in Ataie-Ashitiani and Najafi-Jilani (2008).

2.1 Rigid landslide

In a 104 m long, 3.7 m wide and 4.6 m deep basin of the Oregon State University, USA, Liu et al. (2005) proposed experiments using a wedge and a hemisphere, both rigid, on a slope of 26.6°. Wheels under the two aluminium blocks allowed the slides to move down the slope. The authors varied the slide position, subaerial or submerged, and the slides mass. Their objective was to validate their numerical model to study the generated water waves and runup/rundown.

Walder et al. (2003) wanted to study the prediction of wave features in the near-field. They conducted two sets of experiments with solid blocks, with or without initial velocity. They found an empirical formula giving the amplitude of the generated wave in function of dimensionless landslide time travel and volume.

In the LIAM laboratory of the DISAT department at l'Aquila University, Italy, Panizzo (2004) conducted 2D experiments of a solid block falling vertically into water, and 3D experiments of a rectangular box sliding in a ramp. They obtained a formula giving the maximum generated wave height in function of dimensionless parameters of the landslide, in particular the non dimensional time of underwater landslide motion (Panizzo et al., 2005).

Enet and Grilli (2007) also used an aluminium hemisphere in a 15 m long, 3.7 m wide basin with a 15° slope in the Ocean Engineering Department at the University of Rhode Island, USA. A system of guiding rail allowed the slide to move with a small friction. They studied the effect of submergence and tried to find how the runup was affected. They also validate previous empirical formulas.

Using blocks made of steel plates and sliding on a slope between 15 and 60° in a 2.5 m wide, 1.8 m deep and 25 m long channel at the Sharif University of Technology, Iran, Ataie-Ashitiani and Najafi-Jilani (2008) established that the important parameters during the wave generation were the slope angle, the initial landslide position, its thickness and its kinematics.

Sue et al. (2011) conducted experiments with an aluminium hemisphere and a slope angle of 15°, but in 2D in a 14.667 m long, 0.250 m wide and 0.505 m deep wave tank of the Department of Civil Engineering of the University of Canterbury, New-Zealand. A silicone grease helped to reduce the friction on the slope. They showed that the amplitude of the generated waves was more influenced by the landslide acceleration than the initial submergence. They also linked the runup with the landslide deceleration at the toe of the slope.

To model a threatening subaerial landslide in the Three Gorges Reservoir, China, Bolin et al. (2014) conducted experiments in a 24.5 m long, 5.5 m wide and 1.2 m deep wave tank of the Wuhan Centre of China Geological Survey, China. They used concrete blocks with different volumes, shapes, on slope angles from 35 to 60°, and varied the still water depth. They obtained a formula giving the amplitude of the generated wave as a function of the still water depth, the slope angle, and the landslide characteristics (width, thickness, length and initial position).

In order to study the influence of a 3D geometry, Heller and Spinneken (2015) used a 21 m long, 0.6 m wide flume and a 20 m long, 7.4 m wide basin of the Hydrodynamics Laboratory of the Department of Civil and Environmental Engineering at Imperial College London, UK. They used a slope angle of 45° on which was installed a subaerial block of PVC with a sharp end to facilitate the penetration into water. They varied the mass, density and length of the block, keeping the same thickness and width and they compared their results with previous empirical formulas. They found that the wave dispersion was larger in 3D experiments than in 2D and the waves generated in 3D were less non-linear.

2.2 Deformable landslide

Fritz (2002) used 4 mm granular material made of polypropylene and barium sulfate, sliding on a 45° slope in a 11 m long, 0.5 m wide and 1 m high wave channel of the Laboratory of Hydraulics, Hydrology and Glaciology (VAW) of the Swiss Federal Institute of Technology (ETH). The landslide Froude number and its relative volume and thickness were identified as predominant parameters for the characteristics of the generated wave. The equations obtained matched the observations of the 1958 Lituya Bay, Akaska, event. The same set-up was used by Heller et al. (2008) to study scale effects in subaerial landslide tsunamis and Heller and Spinneken (2013) to improve empirical predictive equations.

A 1.2 m long and 0.25 m wide flume above a 0.8 m long, 0.3 m high and 0.6 m wide

wave tank were used by Mazzanti and Vittorio de Blasio (2011) to study the behavior of granular non-cohesive landslides during the impact with the water surface. The slope varied from 10 to 90° and the size of grains ranged from 0.5 to 80 mm, along with variations of material and density. They found in particular that in the case of flat grain material, some blocks bounced against the water surface, while with finer grain, the entire landslide entered into water.

Mohammed and Fritz (2012) studied tsunamis generated by 3D deformable granular landslides in a 48.8 m long and 26.5 m wide basin of the Network for Earthquake Engineering Simulation at Oregon State University in Corvallis, USA. The slope angle was 27.1° and different water depths were tested. They used landslides made of river gravel with grain size ranging from 6.35 to 19.05 mm. They studied the wave profiles, amplitudes, celerity, periods, lengths and nonlinearity and the energy conversion and they used multivariable regression analysis to obtain numerous empirical formulas. The same basin was used later by McFall and Fritz (2016) when they conducted very similar experiments but with a conical island as the starting point of the landslide.

Bregoli et al. (2013) also conducted experiments to study granular material falling in a 4.10 m long and 2.45 m wide basin in the laboratory of Hydraulic Engineering of the Technical University of Catalonia, Spain. The landslide was contained in a box on wheels in a 6.20 m long channel on a slope angle of 27.5° and entered into water with a deep from 0.2 to 0.6 m. They highlighted the importance of the height of the landslide in the generation of impulsed waves.

In addition to their solid landslide experiments cited above, Bolin et al. (2014) also conducted granular landslide experiments to study the Gongjiafang event that happened in 2008 in China. They used the same configuration as that for their solid experiments, using here granular material with size ranging from a few millimeters to 10 cm. They found empirical relations to evaluate the wave amplitude that would be generated in the case of similar events.

In France, at the Ecole Centrale Marseille, Viroulet et al. (2016) studied the collapse of a triangular subaerial landslide made of 1.5, 4 or 10 mm glass beads, on a 45° slope, in a 2.2 m long, 0.4 m high and 0.2 m wide wave tank. They found power law relationships between the maximum generated amplitude and the landslide mass and used their experiments to validate their numerical model.

In the frame of the US National Tsunami Hazard Mitigation Program, Grilli et al. (2017) validated their numerical model NHWAVE with experiments performed at the Ecole Centrale Marseille, France, too. The tank they used was 6.27 m long and 0.25 m wide with a slope of 35°, and the submerged landslide was made of glass beads of 4 or 10 mm.

Ceramic beads of 3 mm diameter were chosen by Mulligan and Take (2017) to conduct experiments with triangular shape landslides on a 6.7 m long and 30° slope, above a 33 m

long wave flume at the Queen's Coastal Engineering Laboratory of the Queen's University, Canada. They validated previous empirical formulas and they evaluated the momentum transfer from landslides to water waves.

To develop empirical prediction equations of wave amplitudes, Evers et al. (2019) used a box of granular material made of barium sulfate and polypropylene collapsing on a slope from 30 to 90° into a 8 m long, 4.5 m wide and 0.75 m high wave basin of the Laboratory of Hydraulics, Hydrology and Glaciology of Zurich, Switzerland. They used the still water depth and landslide and impact characteristics as governing parameters of their empirical equations.

More simply, water was used by Bullard et al. (2019) to simulate deformable subaerial landslides, on a 6.73 m long and 30° slope. They studied in particular the shape and the vertical asymmetry of the generated waves and they managed to elaborate empirical formulas to evaluate this asymmetry.

Finally, very interesting granular experiments were conducted in the FAST laboratory at Orsay, France, by Robbe-Saule (2019). A very simple formula to calculate the height of the generated wave by the collapse of a granular column was derived from these experiments. This formula seems to predict the good heights for real events.

2.3 Summary

Laboratory experiments are very useful to study all the steps of landslide tsunamis: generation, propagation and impact on the coast. They can be carried out to reproduce real cases in order to understand the past events or used as benchmarks to validate numerical models. Finally they can serve as a basis to develop empirical formulas in order to find relationships between different parameters.

Landslide tsunamis are complex as they involve numerous parameters. This complexity leads to a wide range of laboratory experiments in the literature. Most of them consist of varying the parameters, among them the slope angle (from 10 to 90°), the initial position of the slide (subaerial or submerged), the nature of the slide (rigid or deformable), the material (water, sand, glass beads, ...), the depth of water or the shape of the slide.

Chapter 3

Landslide tsunami models

Numerical models are widely used to study landslide tsunamis. These models can be calibrated and validated using analytical solutions or by simulating laboratory benchmarks or real past events. Less restrictive than laboratory experiments, numerical models allow to simulate a landslide tsunami in a few minutes or hours. The reproducibility of simulations allows for example to easily study the influence of a parameter. Numerical models can also be used to evaluate the threat of potential landslides and establish maps of hazards or risks. However, due to the relatively small size of landslides compared to their zone of influence, fine resolutions are needed, at least in the landslide area. Moreover, some rheology parameters can be complex to obtain.

The following sections will try to describe the variety of numerical models, through the diverse rheology or strategy used. Note that recent and complete review of landslide tsunami models can be found in Yavari-Ramshe and Ataie-Ashtiani (2016).

Section 3.1 is dedicated to the one-way or full-coupling strategies, Section 3.2 to the kind of models, namely depth-integrated or Navier-Stokes, and Section 3.3 presents the different rheologies available to model the landslide.

3.1 One-way or full-coupling

The landslide tsunami modeling involves two physical phenomena and can be divided in two categories: a one-way coupling or a full-coupling. In the full-coupling category both the landslide and the tsunami interact with one another and, in particular, the landslide movement is affected by water (Jiang and LeBlond, 1992). In the one-way coupling case, the landslide is calculated regardless of the surface pressure gradients and the generated bottom deformation is reported on the water surface.

Full coupling

In the case of full coupling, vertical velocities and hydrodynamic forces interact with the landslide during its propagation (when in contact with water). In contrast with the following formulas with no interaction between water and landslide, here the solution of the chosen equations will reflect the bottom deformation to the sea surface more accurately. The full-coupling strategy can be used in both Navier-Stokes or depth-averaged models

(Jiang and LeBlond, 1992). The latter reference concluded that this strategy was useful for mudslide with low density in shallow water.

One-way coupling

In the case where the water does not interact with the landslide, the generation of the waves is induced by a bottom deformation. This deformation can be the result of a previous simulation, laboratory experiments, or be calculated at the same time as the tsunami.

The sea-bottom deformation due to the landslide has to be transmitted to the water surface. This can be achieved by applying an identical deformation to the surface or by applying a filter in order to spread out the water deformation at the surface, for instance following Kelfoun et al. (2010):

$$\Delta d_w = a \times \frac{V}{b^2} \times e^{-\ln(\pi)\times\frac{b}{h}} \tag{3.1}$$

where V is the volume displaced vertically at the bottom, a is a parameter that allows mass conservation in order that $\int_{x=-\infty}^{\infty}\int_{y=-\infty}^{\infty}\Delta d_w dxdy = V$, and $b = \sqrt{x^2+y^2+h^2}$ is the distance between a given point (x, y, h) of the water surface and the point at the bottom $(x = 0, y = 0, z = 0)$ where volume change occurs. This formula of the sudden elevation of the water is exact for a horizontal plane at the bottom and is assumed to be a good approximation in steep slopes environments.

Glimsdal et al. (2013) also detailed how to obtain the initial surface elevation $\eta(x, y, 0)$ following an earthquake, and this procedure could be applied to landslides:

$$\eta(x,y,0) = h^{-2}\int_{-\infty}^{\infty}\int_{-\infty}^{\infty} D(x',y')\left(\frac{1}{\pi}\sum_{n=0}^{\infty}\frac{(-1)^n(2n+1)}{\left\{(2n+1)^2+\left(\frac{|\mathbf{r}-\mathbf{r}'|}{h}\right)^2\right\}^{\frac{3}{2}}}\right)dx'dy' \tag{3.2}$$

where h is the constant depth, $D(x, y)$ is the final uplift distribution with x and y the horizontal coordinates and $\mathbf{r}$ is the position vector.

3.2 Depth-integrated or Navier-Stokes models

For both landslide and tsunami, the simulation can be carried out by solving the full Navier-Stokes equations or depth-integrated approximations.

3.2.1 Depth-integrated models

Different type of models have been adopted by the scientific community to simulate landslide tsunamis. Among them, the most used ones are likely the depth-integrated type. In these models, the computational domain is represented by a 2D grid including

the bathymetry and topography, in a (x, y) coordinate system. The domain is composed of grid cells to which is associated a value of each physical quantity (velocity, water height, ...) that corresponds to the average value of the vertical column.

The depth-integrated models have generally the advantage of being fast and easy to use. Several of them have been successfully used for landslide tsunami modeling in the past few years, among them, the models of Jiang and LeBlond (1992, 1994) or Omira et al. (2016), VolcFlow (Kelfoun et al., 2010), HySEA (Macías et al., 2015) and BingClaw (Kim et al., 2019).

Non-Linear Shallow Water Equations

Depth-integrated models are often based on the shallow water equations. Assuming that the wavelength is much larger than the water depth, the previous Navier-Stokes equations can be depth-averaged, leading to the standard shallow water equations:

$$\frac{\partial u}{\partial t} + u\frac{\partial u}{\partial x} + v\frac{\partial u}{\partial y} + g\frac{\partial \eta}{\partial x} - fv = 0 \tag{3.3}$$

$$\frac{\partial v}{\partial t} + u\frac{\partial v}{\partial x} + v\frac{\partial v}{\partial y} + g\frac{\partial \eta}{\partial x} + fu = 0 \tag{3.4}$$

$$\frac{\partial \eta}{\partial t} + \frac{\partial}{\partial x}[(\eta + d)u] + \frac{\partial}{\partial y}[(\eta + d)v] = 0 \tag{3.5}$$

where $\mathbf{u} = (u, v)$ is the velocity, η the surface elevation, d the still water depth and f the Coriolis parameter, which can be neglected. Friction parameters can also be added, as in Part II, Chapter 2, Section 2.2.2.

Boussinesq equations

In 1872, Boussinesq introduced a set of equations close to the shallow water equations, but including additional terms to take into account the linear frequency dispersion. These equations are valid for weakly non-linear and fairly long-waves and are written in Chapter 2, Section 2.2.2. In this model, the wave celerity becomes:

$$c = \sqrt{gh(1 - \frac{1}{3}k^2d^2)} \tag{3.6}$$

Among the numerous models based on the Boussinesq equations, GloBouss is applied to landslide tsunamis in Norvegian studies (Pedersen and Løvholt, 2008; Løvholt et al., 2008, 2010; Harbitz et al., 2014). Solving fully non-linear Boussinesq equations, FUNWAVE-TVD (Wei et al., 1995) is widely used to model tsunamis (Grilli et al., 2013; Abadie et al., 2020).

Note that depth-integrated equations similar to the shallow water equations for

tsunami can be used for the landslide, such as the ones described in Part II, Chapter 2, Section 2.2.1. These equations are generally based on the models of Savage and Hutter (1989) or Jiang and LeBlond (1992).

3.2.2 Navier-Stokes models

With the reputation of being more accurate because more complete, the Navier-Stokes models are more and more used, especially with the reduction of the CPU cost. The computational domain is divided in points or meshes represented by (x, y, z) coordinates, from the sea-bottom to the water surface and beyond. This can lead to large file sizes and so to long computational times.

Over the past two decades, several Navier-Stokes models have been developed, among them, THETIS (Abadie et al., 2008), FLUENT (Biscarini, 2010), Fluidity (Davies et al., 2011), TSUNAMI3D (Horrillo et al., 2013), Splash3D (Wu et al., 2020) and OpenFOAM (Lee et al., 2016; Si et al., 2018; Romano et al., 2020; Lee and Huang, 2021).

Recently, (Abadie et al., 2020) used THETIS to simulate the generation of a tsunami generated by the collapse of La Palma, using the VOF (Volume Of Fluid) method (Hirt and Nichols, 1981) to track the fluid-fluid interfaces, Grilli et al. (2019, 2021) applied NHWAVE to simulate the 2018 Anak Krakatau collapse and tsunami and some authors (Si et al., 2018; Yu and Lee, 2019; Rauter et al., 2021) used the model OpenFOAM to simulate landslide tsunamis, the two first references simulating the slide as a two-phase flow.

The Navier-Stokes equations are based on the conservation of mass and momentum and read:

$$\frac{\partial}{\partial t}(\rho \mathbf{u}) + \nabla \cdot (\rho \mathbf{u} \otimes \mathbf{u}) = -\nabla p + \nabla \cdot \tau + \rho \mathbf{g} \tag{3.7}$$

where ρ is the density, $\mathbf{u}$ is the flow velocity, p is the pressure, τ is the stress tensor and g the gravity acceleration.

Considering an incompressible fluid, they can be written as follows:

$$\frac{\partial \mathbf{u}}{\partial t} + (\mathbf{u} \cdot \nabla)\mathbf{u} - \nu \nabla^2 \mathbf{u} = -\frac{\nabla p}{\rho} + \mathbf{g} \tag{3.8}$$

$$\nabla \mathbf{u} = 0 \tag{3.9}$$

where ν is the kinematic viscosity.

A turbulence model can be added, as described in Part II, Chapter 2, Section 2.3 for OpenFOAM.

A third class of models, called 3D non-hydrostatic models, has been developed. These models (for instance NHWAVE (Ma et al., 2013; Zhang et al., 2021a,b)) solve the 3D

Navier-Stokes equations, based on a 2D horizontal mesh at the bottom and adding layers in the vertical direction. One of the advantages is the ability to follow the irregularities of the bathymetry.

3.3 Landslide modeling

Whatever the coupling strategy or the kind of model, the rheology of the landslide can be more or less complex.

Rigid

The most basic landslide model is the rigid block (Fuhrman and Madsen, 2009; Ataie-Ashtiani and Yavari-Ramshe, 2011; Bosa and Petti, 2011; Dutykh and Kalisch, 2013).

If the landslide trajectory is known, for example in the case of the numerical reproduction of laboratory experiments, it can be implemented as a bathymetry variation in a tsunami code (Audusse et al., 2021) or as a moving mesh (Romano et al., 2020). In both methods, the landslide is not calculated.

Harbitz and Glimsdal (2011) used an energy-line approach and a trajectory based on experiments to simulate the 1934 Tafjord, Norway, event. Based on observations and adjusting parameters in the simulation, Gylfadóttir et al. (2017) modeled the 2014 Lake Askja rockslide using a solid slide. Chen et al. (2020) used a motion solver that calculates the total force vector, taking into account the pressure, viscosity, drag and gravity forces.

Another approach is to penalize the landslide using a very high viscosity, as developed by Abadie et al. (2010) and Clous (2018).

Newtonian

Another approach for landslide modeling is to consider the landslide as a Newtonian viscous fluid (Abadie et al., 2012; Horrillo et al., 2013; Rauter et al., 2021). The key parameter for this rheology is the viscosity and a large range of values is used in the literature (e.g. around 10^4 (Abadie et al., 2020), 10^{-1} (Grilli et al., 2019), 10^{-2} (Abadie et al., 2010), 10^{-3} (Viroulet et al., 2016; Clous and Abadie, 2019), 10^{-4} (Clous and Abadie, 2019), 10^{-5} (Horrillo et al., 2013) or 10^{-6} (Grilli et al., 2017) for the kinematic viscosity ($m^2.s$)).

Non Newtonian

A rheology involving a non-Newtonian fluid can be used, such as the Bingham rheology (De Blasio et al., 2004; Skvortsov and Bornhold, 2007; Serrano-Pacheco et al., 2009; Glimsdal et al., 2016; Salmanidou et al., 2018). In this approach, the landslide is considered

as a rigid body if the shear stress remains under a critical value. Once this value is exceeded, the landslide behaves like a viscous fluid.

Granular

According to Yavari-Ramshe and Ataie-Ashtiani (2016), a granular rheology following Coulomb (or Voellmy) law represented more than 50% of the existing landslide models. These rheology laws require parameters such as the friction angle or the internal friction angle (Mangeney et al., 2000; Kelfoun et al., 2010). Values of these parameters can be found through sensitivity studies and range from low values for volcanic material, below 5° (Kelfoun et al., 2010; Giachetti et al., 2012), to higher values for debris avalanches, around 20-25° (Mangeney et al., 2000; Heller and Hager, 2010; Pudasaini and Miller, 2012).

Summary of rheology laws

By varying the parameters of the shear stress formulation, many different rheology laws can be used (Table 2). According to Yavari-Ramshe and Ataie-Ashtiani (2016), granular rheology laws (Coulomb or Voellmy for instance) are the most common ones. The Newtonian rheology involves only one parameter (see Table 2) and then is one of the easiest to use and can be a good approximation for debris, clay or mud flows.

$\tau = \tau_c + a'\dot{\gamma}^n + b'(u)$				
Rheology	τ_c	a'	n	$b'(u)$
Newtonian	0	μ_d	1	0
Bingham	constant	μ_B	1	0
Coulomb	$\sigma' \tan\delta$	0	0	0
Voellmy	$\sigma' \tan\phi$	0	0	$(u/c_z)^2$
Herschel-Bulkley	constant	k_{HB}	$\leq$1	0
Dilatant	0	k_D	>1	0
Bagnold's grain inertia	0	k_D	2	0
Bagnold's macroviscous	0	k_D	1	0
$\mu(I)$	0	$\mu_{eff}P$	0	0

Table 2: Some well-known landslide rheological relations found in literature. τ Shear stress, τ_c critical shear stress, $\dot{\gamma}$ shear rate, σ' normal stress, u flow velocity, δ basal friction angle, ϕ internal friction angle, μ_d dynamic viscosity, μ_B Bingham fluid viscosity, k_{HB} Herschel-Bulkley consistency index, c_z Chezy coefficient, k_D dilatant consistency index, μ_{eff} effective friction coefficient of $\mu(I)$, P pressure, I inertial number $F(\dot{\gamma}, P)$. Table and legend from Yavari-Ramshe and Ataie-Ashtiani (2016).

Chapter 4

Conclusion and scientific questions

There is a wide choice of models to simulate landslide tsunamis, each with their strengths and weaknesses, but is there one model more accurate than another? What is the contribution of the resolution of the flow in the water column? Is one model more pertinent for the generation or for a particular landslide geometry?

Comparison between depth-integrated and Navier-Stokes models have been carried out for seismic tsunamis propagation (Sogut and Yalçiner, 2019), tsunami inundation (Qin et al., 2018; Horrillo et al., 2015; Sogut and Yalçiner, 2019) and generated coastal currents (Lynett et al., 2017; Sogut and Yalçiner, 2019). In Kim et al. (2020), the authors question the applicability of depth-integrated models to landslide tsunamis, suggesting that Navier-Stokes models taking into account the vertical acceleration should produce more accurate results. However, an extensive comparison between depth-averaged and Navier-Stokes models for landslide tsunamis generation is not available.

The main objective of the present thesis is to identify the application fields of depth-averaged models (represented below by AVALANCHE) by comparing the results of simulations over a large range of parameters with those obtained with a multiphase Navier-Stokes model (here OpenFOAM). Both models will be intercompared through benchmarks, sensitivity studies and real cases. To that purpose, the models are benchmarked over experimental measurements, sensitivity studies are carried out and finally real studies are conducted.

Part II

Comparison of depth-averaged and Navier-Stokes models

Chapter 1

Introduction

This part is dedicated to the comparison of depth-averaged and Navier-Stokes models. Chapter 2 is devoted to the description of numerical models used for this study. Chapter 3 presents the validation of a depth-averaged model and a Navier-Stokes model against experimental subaerial and submerged benchmarks. In Chapter 4, Section 4.1 presents a study realized during a summer school (CEMRACS 2019, Marseille, France) and published in Audusse et al. (2021). The objective is to compare shallow water and Boussinesq models to a Navier-Stokes model considered as a reference. Section 4.2 is dedicated to a sensitivity study on the slope angle and the initial position of the landslide. This section and Chapter 3 were published in Paris et al. (2021).

Chapter 2

Numerical models used in Part II and III

2.1 Hydra

Hydra is a depth-averaged model (Section 4.1) that solves the shallow water equations written in a conservative form as follows:

$$\frac{\partial h}{\partial t} + \frac{\partial (hu)}{\partial x} = 0 \tag{2.1}$$

$$\frac{\partial (hu)}{\partial t} + \frac{\partial}{\partial x}(hu^2 + \frac{g}{2}h^2) = gh\frac{\partial d}{\partial x} \tag{2.2}$$

where h is the water depth, u the main horizontal velocity and d the bottom elevation.

The gradient of d is treated as a source term by using a hydrostatic reconstruction (Bouchut, 2004). The numerical resolution is performed through a finite volume Godunov-type solver with MUSCL second order reconstruction and a second order Runge-Kutta time scheme (Audusse et al., 2004).

2.2 AVALANCHE

AVALANCHE is the code developed by CEA for the landslides simulations and the generated tsunamis propagation. It is a 2D depth-integrated model, written in Fortran 90/95, parallelised via the MPI library and that solves the shallow water equations or the Boussinesq equations. The landslide is modeled as a granular flow, falling under gravity and following a Coulomb friction law or a viscous law. The code can use a system of nested grids with a coarse grid over deep water regions and fine grids over coastal regions to model local effects of bathymetry. It has been successfully employed to simulate subaerial or submarine landslides (Heinrich and Piatanesi, 2000; Hébert et al., 2002; Le Friant et al., 2003; Rodriguez et al., 2013; Poupardin et al., 2017; Paris et al., 2019).

2.2.1 Landslide model

Regarding the landslide part, AVALANCHE solves the following equations of momentum and mass conservation from the one-phase grain-flow model of Savage and Hutter (1989), in a x', y' coordinate system parallel to the slope:

$$\frac{\partial h_s}{\partial t} + \frac{\partial}{\partial x'}(h_s u_s) + \frac{\partial}{\partial y'}(h_s v_s) = 0; \tag{2.3}$$

$$\frac{\partial}{\partial t}(h_s u_s) + \frac{\partial}{\partial x'}(h_s u_s^2) + \frac{\partial}{\partial y'}(h_s u_s v_s) = -\frac{1}{2}\kappa\frac{\partial}{\partial x'}(g h_s^2 \cos\theta) + \kappa g h_s \sin\theta_x + F_{x'}; \tag{2.4}$$

$$\frac{\partial}{\partial t}(h_s v_s) + \frac{\partial}{\partial x'}(h_s v_s u_s) + \frac{\partial}{\partial y'}(h_s v_s^2) = -\frac{1}{2}\kappa\frac{\partial}{\partial y'}(g h_s^2 \cos\theta) + \kappa g h_s \sin\theta_y + F_{y'} \tag{2.5}$$

where h_s is the slide's thickness in a direction perpendicular to the slope, $\mathbf{u} = (u_s, v_s)$ the depth-averaged velocity vector parallel to the bed, $\kappa = 1 - \rho_w/\rho_s$ where ρ_w and ρ_s are the water and rock densities with a ratio $\rho_s/\rho_w = 1.5$ (for the subaerial part of the slide, κ is identically equal to 1), $\theta(x, y)$ the local steepest slope angle, θ_x and θ_y the slope angles along the x and y axes respectively, and $\mathbf{F} = -\kappa g h \cos(\theta)\tan(\phi)\mathbf{u}/\|\mathbf{u}\|$ the friction forces, where ϕ is the friction angle.

The landslide can be modeled as a granular flow without cohesion or as viscous fluid. Its thickness is considered to be very small compared to its spatial extension, which allows to satisfy the shallow water approximation and ignore the precise behavior inside the landslide.

2.2.2 Tsunami model

The tsunami propagation can be simulated by solving either the shallow water equations (2.6), (2.7), (2.8) or the Boussinesq equations of Løvholt et al. (2008) (2.9), (2.10), (2.11). A switch between the two sets of equations allows to use the shallow water equations for a few instants during the water wave generation in the near-field and the Boussinesq model for the far-field propagation.

The shallow water equations solved by AVALANCHE are written as:

$$\frac{\partial \eta}{\partial t} + \frac{\partial (hu)}{\partial x} + \frac{\partial (hv)}{\partial y} = -\frac{\partial d}{\partial t}; \tag{2.6}$$

$$\frac{\partial u}{\partial t} + u\frac{\partial u}{\partial x} + v\frac{\partial u}{\partial y} = -g\frac{\partial \eta}{\partial x} + F_x; \tag{2.7}$$

$$\frac{\partial v}{\partial t} + u\frac{\partial v}{\partial x} + v\frac{\partial v}{\partial y} = -g\frac{\partial \eta}{\partial y} + F_y \tag{2.8}$$

where η is the surface elevation, $h{=}\eta{+}d$ the water column height, d is the depth, u and v the depth-averaged velocities along the x and y axes respectively and F_x and F_y the friction and Coriolis forces, which are assumed to be negligible in our modeling.

Following Løvholt et al. (2008), the Boussinesq equations read:

$$\frac{\partial \eta}{\partial t} + \frac{\partial (hu)}{\partial x} + \frac{\partial (hv)}{\partial y} = -\frac{\partial d}{\partial t}; \tag{2.9}$$

$$\begin{aligned}\frac{\partial u}{\partial t} + u\frac{\partial u}{\partial x} + v\frac{\partial u}{\partial y} = -g\frac{\partial \eta}{\partial x} + \frac{d^3}{3}\left[\frac{\partial^2 u_t}{\partial x^2} + \frac{\partial^2 v_t}{\partial x \partial y}\right] \\ + \frac{d}{2}\left[u_t\frac{\partial^2 d}{\partial x^2} + u_t\frac{\partial^2 d}{\partial x \partial y}\right] + d\frac{\partial d}{\partial x}\frac{\partial u_t}{\partial x} + \frac{d}{2}\left[\frac{\partial d}{\partial x}\frac{\partial v_t}{\partial y} + \frac{\partial d}{\partial y}\frac{\partial v_t}{\partial x}\right] + F_x;\end{aligned} \tag{2.10}$$

$$\begin{aligned}\frac{\partial v}{\partial t} + u\frac{\partial v}{\partial x} + v\frac{\partial v}{\partial y} = -g\frac{\partial \eta}{\partial y} + \frac{d^3}{3}\left[\frac{\partial^2 v_t}{\partial y^2} + \frac{\partial^2 u_t}{\partial x \partial y}\right] \\ + \frac{d}{2}\left[v_t\frac{\partial^2 d}{\partial y^2} + v_t\frac{\partial^2 d}{\partial x \partial y}\right] + d\frac{\partial d}{\partial y}\frac{\partial v_t}{\partial y} + \frac{d}{2}\left[\frac{\partial d}{\partial x}\frac{\partial u_t}{\partial y} + \frac{\partial d}{\partial y}\frac{\partial u_t}{\partial x}\right] + F_y\end{aligned} \tag{2.11}$$

where u_t and v_t the time-derivatives of u and v.

The sea-bottom deformation due to the landslide, $\partial d/\partial t$ in Equation (2.9), is computed as a forcing term:

$$\frac{\partial d}{\partial t} = \frac{1}{\cos\theta}\frac{\partial h_s}{\partial t} \tag{2.12}$$

2.2.3 Numerical resolution

To solve the shallow water equations taking into account the bathymetric deformation due to the landslide, AVALANCHE uses a Godunov type numerical scheme (Toro, 2009). In this scheme, the equations are written in a conservative form. The resolution starts with a Lagrangian phase followed by a projection phase in which the conservative variables are projected on the fixed origin mesh. To evaluate the new water surface, the first step consists in moving the right and left mesh boundaries considering the calculated velocities at the interfaces. The new water surface is then inferred at the center of the mesh by conservation of the mass in the Lagrangian phase.

The Boussinesq equations are solved by a time iterative method of Crank-Nicolson, with a fix point method at each iteration. The convergence test is realised on the continuity equation in order to rigorously preserve the water volume. The continuity equation discretization explicitly calculates the water surface elevation considering the

previously calculated η, u and v during the precedent iteration. The two movement equations discretization is inspired from Pedersen and Løvholt (2008) and uses a splitting method separating the x and y directions. These equations are solved by an ADI (Alternating Direction Implicit) scheme in which the terms in one direction are handled implicitly while they are handled explicitly in the other direction. In this way, the equations system is transformed in tridiagonal inverse matrices by a LU method (Quarteroni et al., 2006).

2.3 OpenFOAM

OpenFOAM (Open-source Field Operation And Manipulation) is an open source CFD software developed by OpenCFD Ltd since 2004. It allows to simulate any multiphase flow, solving the 3D Navier-Stokes equations. It is written in C++ and uses a system of modules that the user can assemble to build his own case and in which all the files can be modified. OpenFOAM is able to deal with incompressible/compressible turbulence, thermophysical, multiphase or wave modeling. It handles the mesh generation, the model simulation and the output readings thanks to it third-party libraries such as ParaFOAM with ParaView.

Among others, it was used by Qin et al. (2018b) to study the inundation and impact of a tsunami on a coastal city or by Honarmand et al. (2020) to propagate the initial elevation generated by the Makran earthquake in 1945. Romano et al. (2020) also developed an approach to simulate tsunamis generated by a solid landslide using the Overset mesh technique. Considering a deformable landslide, Rauter et al. (2021) reproduced the experiments of Bullard et al. (2019) using the solver multiphaseInterFoam with two viscous fluids. Closer to the present work since it concerns the same benchmarks, Si et al. (2018), Yu and Lee (2019) and Lee and Huang (2021) used models based on OpenFOAM to simulate the subaerial experiments of Viroulet et al. (2016) and submerged experiments of Grilli et al. (2017), respectively. The first authors introduced a granular temperature in the granular phase, while the second ones used a Navier-slip boundary condition adapted for granular flows.

We use the Navier-Stokes equations to simulate three fluids (air, water and sediment). The continuity equation reads:

$$\nabla \cdot \mathbf{u} = 0 \tag{2.13}$$

where $\mathbf{u}$ is the velocity, and the momentum equation reads:

$$\frac{\partial \rho \mathbf{u}}{\partial t} + \nabla \cdot (\rho \mathbf{u}\mathbf{u}) = -\nabla p + \nabla \cdot (2\mu \mathbf{D}) + \rho \mathbf{g} \tag{2.14}$$

where $\mathbf{D}$ is the strain rate tensor, $\mathbf{g}$ the gravitational acceleration, $p(\mathbf{x}, t)$ the pressure field and ρ, μ and μ_t are the local fluid density, molecular dynamic viscosity and eddy

viscosity, respectively and are defined as follows:

$$\rho = \sum_i \alpha_i(\mathbf{x}, t)\rho_i \tag{2.15}$$

$$\mu = \sum_i \alpha_i(\mathbf{x}, t)\mu_i \tag{2.16}$$

$$\mu_t = \rho C_\mu \frac{k^2}{\epsilon} \tag{2.17}$$

where ϵ is the turbulent kinetic energy dissipation rate and k is the turbulent kinetic energy. They are implemented as follows:

$$\frac{\partial}{\partial t}(\alpha\rho\epsilon) + \nabla\cdot(\alpha\rho\mathbf{u}\epsilon) - \nabla^2(\alpha\rho D_\epsilon\epsilon) = C_1\alpha\rho G\frac{\epsilon}{k} - \left(\left(\frac{2}{3}C_1 - C_{3,RDT}\right)\alpha\rho\nabla\cdot\mathbf{u}\epsilon\right) - \left(C_2\alpha\rho\frac{\epsilon}{k}\epsilon\right) + S_\epsilon + S_{fvOptions} \tag{2.18}$$

$$\frac{\partial}{\partial t}(\alpha\rho k) + \nabla\cdot(\alpha\rho\mathbf{u}k) - \nabla^2(\alpha\rho D_k k) = \alpha\rho G - \left(\frac{2}{3}\alpha\rho\nabla\cdot\mathbf{u}k\right) - \left(\alpha\rho\frac{\epsilon}{k}k\right) + S_k + S_{fvOptions} \tag{2.19}$$

where G is the turbulent kinetic energy production rate due to the anisotropic part of the Reynolds-stress tensor ($\mathrm{m}^2\ \mathrm{s}^{-3}$), D_ϵ is the effective diffusivity for ϵ, C_1 (s) and C_2 are two model coefficients, $C_{3,RDT}$ is the rapid-distortion theory compression term coefficient, S_ϵ is the internal source term for ϵ, $S_{fvOptions}$ are source terms introduced by fvOptions dictionary for ϵ, S_k is the internal source term for k and $S_{fvOptions}$ are source terms introduced by fvOptions dictionary for k.

In Equations 2.15, 2.16, 2.18 and 2.19, phase indicator α_i is defined as follows:

$$\alpha_i(x,t) = \begin{cases} 1 & \text{if phase i is present at x,t} \\ 0 & \text{else} \end{cases} \tag{2.20}$$

and is calculated in a volumetric phase fraction equation:

$$\frac{\partial\alpha_i}{\partial t} + \nabla\cdot(\alpha_i\mathbf{u}) + \sum_j \nabla\cdot(\alpha_i\alpha_j\mathbf{u}_{r,ij}) = 0 \tag{2.21}$$

where $\mathbf{u}_{r,ij}$ is the relative velocity between phases.

The following default values were used:

$$C_\mu = 0.09; C_1 = 1.44; C_2 = 1.92; C_{3,RDT} = 0$$

Here, the multiphaseInterFoam solver is used with three viscous fluids, the air, the water and the landslide, and the PIMPLE algorithm which combines PISO (Pressure Implicit with Splitting of Operator) and SIMPLE (Semi-Implicit Method for Pressure-Linked Equations). Cartesian grids are generated by blockMesh and refined by snappyHexMesh using triangular elements in the area along the slope. The landslide is modeled as a Newtonian non-miscible fluid. Python scripts are used to postprocess the results (local free surface time series, cross-sectional views of the landslide).

In Chapter 3 and Chapter 4, Section 4.2 , the solver is used in laminar mode ($\mu_t = 0$ in Equation 2.14) in order to compare the depth-averaged and the Navier-Stokes models in the simplest possible way. Further, in Chapter 4, Section 4.3, the influence of the turbulence is studied, considering a $k - \epsilon$ model.

Chapter 3

Tests based on laboratory experiments

3.1 Cases description

3.1.1 Subaerial benchmark

These subaerial experiments conducted by Viroulet et al. (2014) consist in a wave tank of 2.2 m length, 0.4 m height and 0.2 m width, in which a granular slide composed of glass beads collapses on a slope of 45° (Figure 1). The beads used have a density of 2000 kg.m^{-3} and a diameter of 1.5 mm. Considering the air between the beads, the slide has a equivalent density of 1500 kg.m^{-3}. The subaerial slide has an isosceles right-angled triangular shape with 0.11 m sides. A polyvinyl plate retains the slide and is lifted to initialize the experiment. A high speed camera records the evolution of the collapse (Figure 1) while the evolution of the generated surface elevation is recorded by four resistive gauges located at 0.45, 0.75, 1.05 and 1.35 m from the plate.

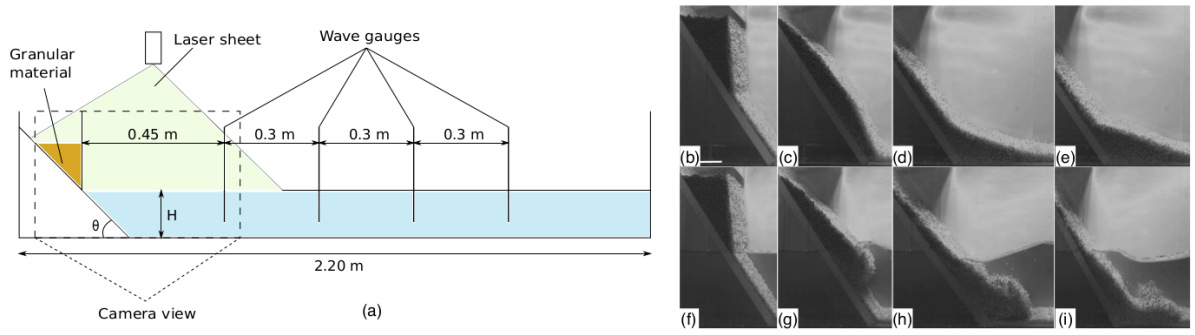

Figure 1: Schematic view of the subaerial experimental setup. The shape of the granular flow and the generation of the waves are recorded by the high speed camera. The evolution of the amplitude is measured with four contact-type wave gauges. Successive instants of the collapse of the granular material ($m = 2$ kg) (b-e) in the dry case, and (f-i) in presence of water. The pictures are taken every 0.2 seconds and the scale bar is 5 cm. Figure and caption from Viroulet et al. (2014).

3.1.2 Submerged benchmark

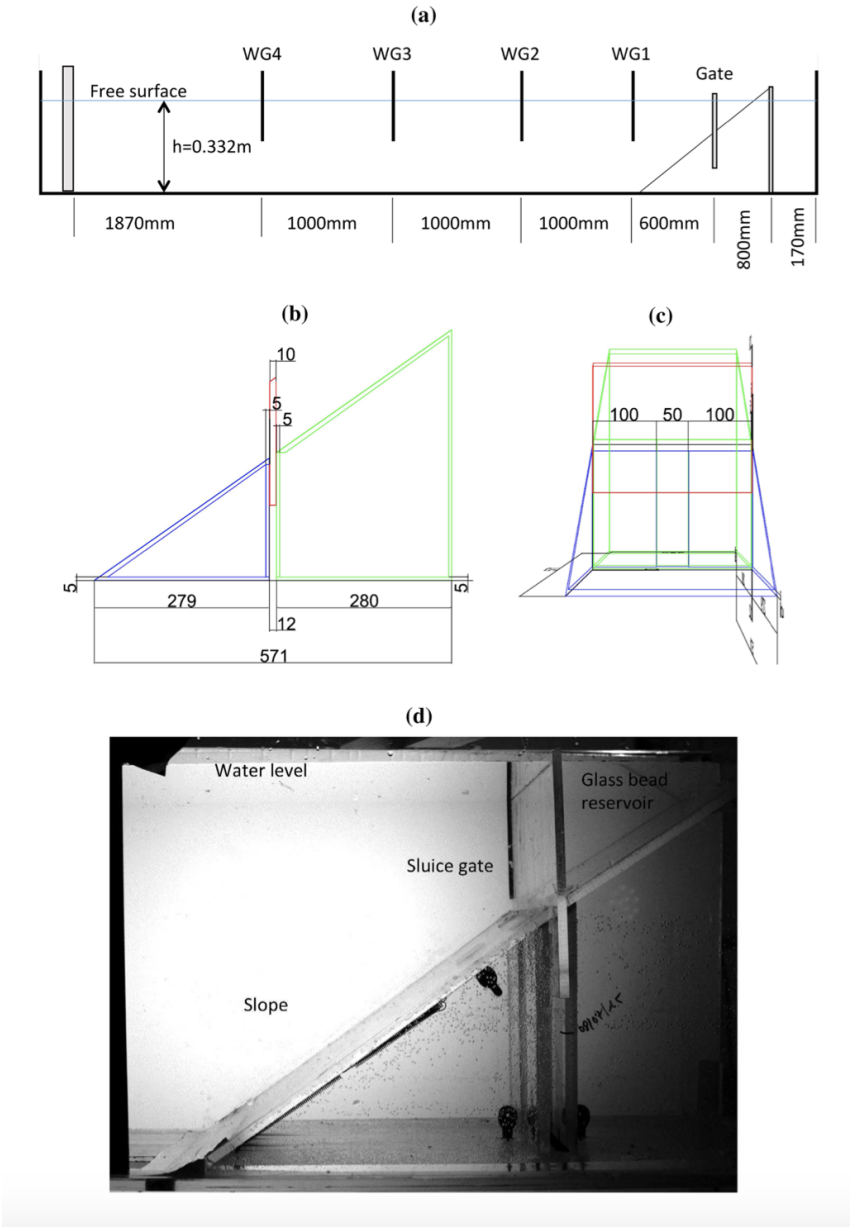

Figure 2: Setup for laboratory experiments of tsunami generation by underwater slides made of glass beads performed in the Ecole Centrale de Marseille (IRPHE) precision tank of (useful) length l=6.27 m, width w=0.25 m, and water depth h=0.330 m. Upon release, beads are moving down a θ=35 degree slope. **a** Longitudinal cross section with marked location of sluice gate and 4 wave gages (WG1, WG2, WG3, WG4). **b**, **c** Zoom-in on side and cross-sectional views of slope and sluice gate (dimensions marked in mm). **d** Picture of experimental setup around slope and sluice gate. Figure and caption from Grilli et al. (2017).

The landslide in this submerged experiment from Grilli et al. (2017) is composed of 0.004 m diameter glass beads, contained in a 0.12 m long, 0.085 m high right-angled triangle by a sluice gate. The density of the beads is 2500 kg.m^{-3} leading to an equivalent density

of 1951 kg.m^{-3}. The collapse occurs on a 35° slope into 0.33 m of water, in a 6.27 m long and 0.25 m wide tank (Figure 2). In a similar way to the subaerial experiment, a high speed camera (1000 fps) records the landslide evolution, while gauges located at 0.6, 1.6, 2.6 and 3.6 m from the gate record the water surface elevation.

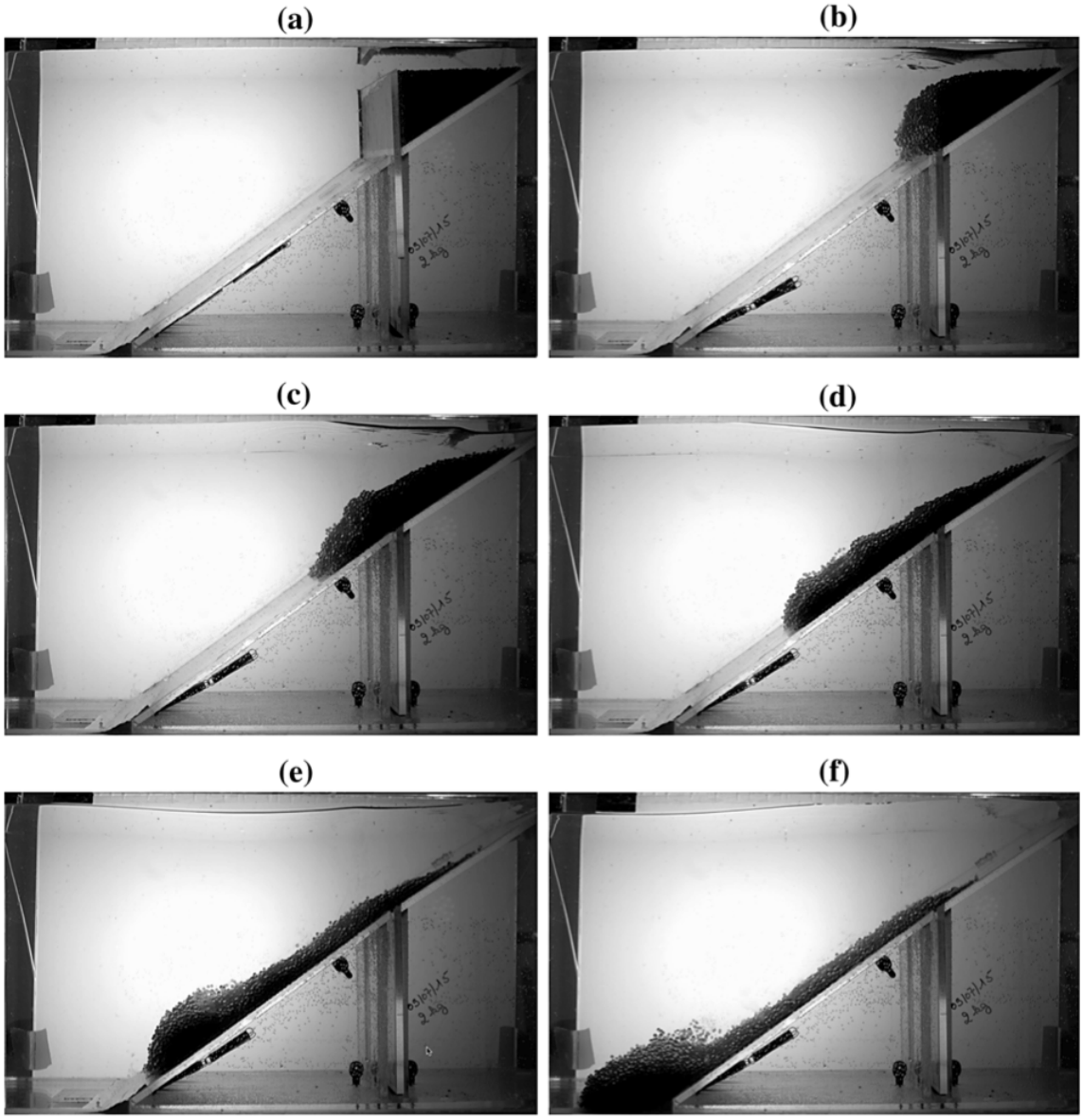

Figure 3: Snapshots of laboratory experiments of tsunami generation by underwater slides made of glass beads (Fig. 2), for h=0.330 m, d_b=4 mm, W_b=2 kg and no glued beads on the slope, at times t=**a** -0.125, **b** 0.02, **c** 0.17, **d** 0.32, **e** 0.47, and **f** 0.62 s. Glass beads are initially stored within a triangular reservoir, with the sluice gate up; once the gate has withdrawn into its cavity (t= 0), the deforming slide moves down the 35° slope causing the free surface deformation. Figure and caption from Grilli et al. (2017).

3.2 Mesh, parameters and analysis

The two previous benchmarks are simulated by AVALANCHE and OpenFOAM, which will be referenced as the depth-averaged model and the Navier-Stokes model from now on.

3.2.1 Mesh

To simulate the experiments with the depth-averaged model, 1D cartesian grids with a resolution of 0.001 m in the x-direction are built, with only one cell in the y-direction. Convergence studies for the subaerial benchmark did not show any significant differences between this resolution and a two times finer one (Figure 4).

To simulate the experiments with the Navier-Stokes model, 2D cartesian grids with a resolution of 0.005 m in the x and z directions, with only one cell in the y-direction, are used. The resolution is five times coarser than that of the depth-averaged model due to high computational cost. Convergence studies for the subaerial benchmark did not show any significant differences between this resolution and a two times finer one (Figure 5).

3.2.2 Parameters

Subaerial benchmark

In both models, the density chosen for the simulations is the equivalent density of the experiment, 1500 kg.m^{-3}.

In the depth-averaged model, the landslide is considered as a viscous fluid with a viscosity μ in the range [0.01; 40] Pa.s. Both shallow water and Boussinesq equations are solved, the latter taking over as soon as the generated water wave is separated from the slide.

In the Navier-Stokes model, the slide is also considered as Newtonian fluid with a viscosity μ in the range [0.01; 50] Pa.s. Sensitivity study is also conducted on the lowerWall (slope and bottom) boundary condition (*i.e.* noSlip and partialSlip). The latter is defined through a coefficient α between 0 and 1. If u_0 is the tangential velocity along the wall and u_1 the tangential velocity of the adjacent cell, α is defined as follows: $u_0 = (1-\alpha)u_1$, α being defined as $\alpha = d/(d+2\lambda)$ where λ is the slip length and d the cell size. With these definitions, a noSlip boundary condition corresponds to a α value of 1. In the following, a 0.1 partialSlip condition will refer to a partialSlip condition with α=0.1.

Submerged benchmark

Two density values are chosen for the simulation in both models: the density of the glass beads, 2500 kg.m^{-3}, and the equivalent density considering the water between the beads,

1951 kg.m^{-3}.

The parameters and the sensitivity studies are the same as the subaerial benchmark ones. Only the range of viscosity values changes: [0.01; 12] Pa.s in both models.

3.2.3 Analysis

The comparison of the free surface signals obtained from the simulations (f_1) and the experiments (f_2) is carried out based on the Q parameter, built on Sobolev norms (Perlin and Bustamante, 2016):

$$Q(f_1, f_2) = \frac{\left(\int |F_1(\omega) - F_2(\omega)|^2 d\omega\right)^{1/2}}{\left(\int |F_1(\omega)|^2 d\omega\right)^{1/2} + \left(\int |F_2(\omega)|^2 d\omega\right)^{1/2}} \tag{3.1}$$

where f_1, f_2 are the two temporal signals and $F_1(\omega)$, $F_2(\omega)$ the associated Fourier transforms.

This parameter Q gives a measure of the phase shift of the two signals. For identical time series, Q=0, whereas Q=1 for two ideal (sinusoidal) signals separated by a half-period (e.g. $sin(x)$ and $sin(x + \pi)$).

As regards the landslide evolution, comparisons between simulations and experiments are made in a qualitative way simply by overlapping simulated and observed snapshots of slice views of the landslide at different instants.

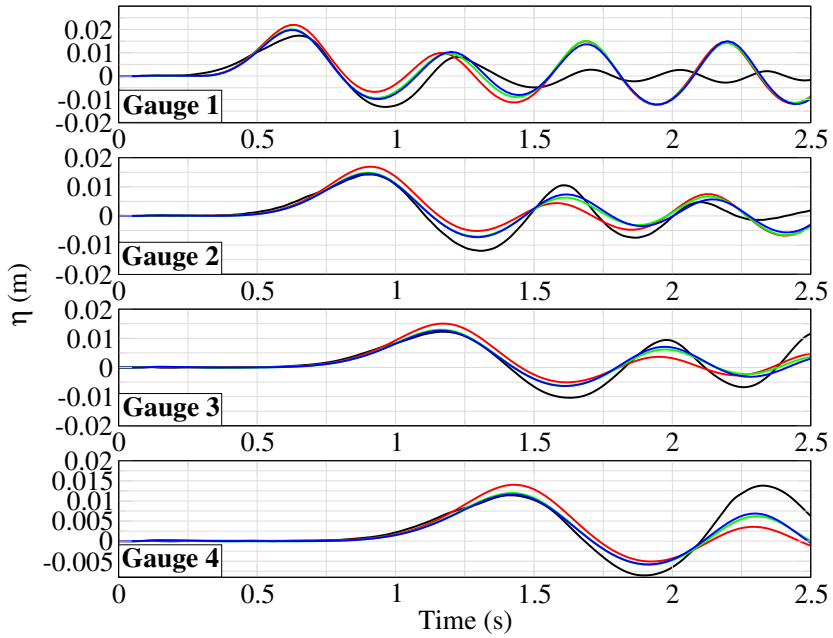

Figure 4: Subaerial benchmark: comparison between the experiment (black) and results computed with the depth-averaged model using resolutions of 0.002 m (red), 0.001 m (green) and 0.0005 m (blue).

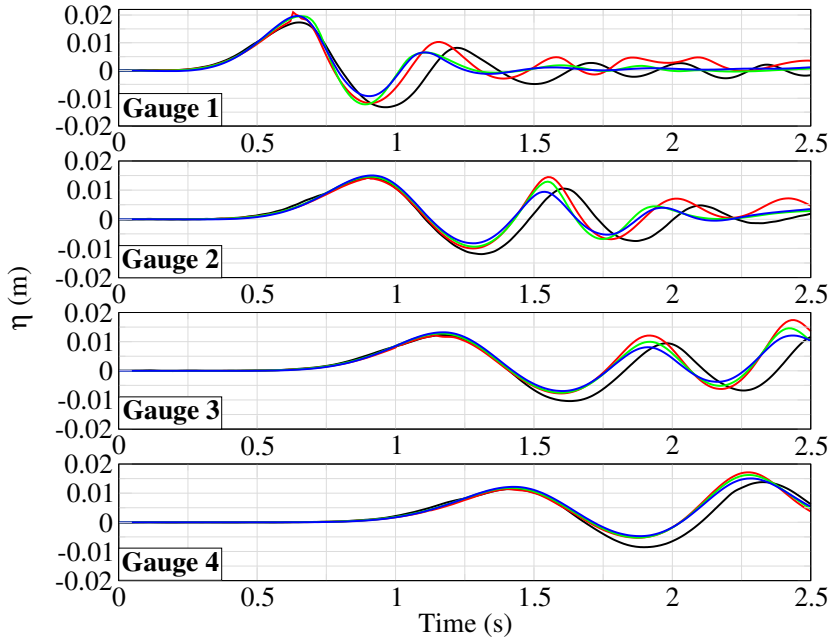

Figure 5: Subaerial benchmark: comparison between the experiment (black) and results computed with the Navier-Stokes model using resolutions of 0.01 m (red), 0.005 m (green) and 0.0025 m (blue).

3.3 Simulations results

3.3.1 Subaerial benchmark

Depth-averaged model

Water waves

Figure 6 shows that the best average Q-value for the four gauges is obtained with a viscosity μ of 12.8 Pa.s. This value corresponds to the $\mu(I)$-rheology viscosity calculated by Clous and Abadie (2019) following Ionescu et al. (2015). In a general way, in the "far-field" (Gauge 4), Q-values are lower than those in the "near-field" (Gauge 1), showing that the depth-averaged model is more accurate in the far-field.

For viscosity values between 6 and 15 Pa.s, results are similar with low Q-values. This is illustrated by the analysis of the free surface elevation time series at the four gauges (Figure 7) which shows similar results, close to the experimental water waves whatever the viscosity taken in this range. Nevertheless, we note that if the characteristics of the leading wave (period and height) are reproduced accurately, the fit is lower for the following water waves.

Landslide

Considering the landslide itself, the simulation with a viscosity value μ of 12.8 Pa.s gives satisfactory results, as shown in Figure 8. Due to the landslide model hypothesis, the experimental front shape is not properly reproduced but the quantity of material entering into water at different times is very similar in the simulation and in the experiment. Moreover, as shown by Clous and Abadie (2019), most of the energy transfer between the landslide and the wave occurs within the first instants (before t=0.3s) in this case, so it is not essential to reproduce perfectly the landslide behavior afterward to properly simulate the water waves generated.

For lower and higher values of viscosity, Q-values increase, probably due to incorrect landslide velocities, as supported by Figure 9, which illustrates the variety of the average slide velocity observed in the simulations.

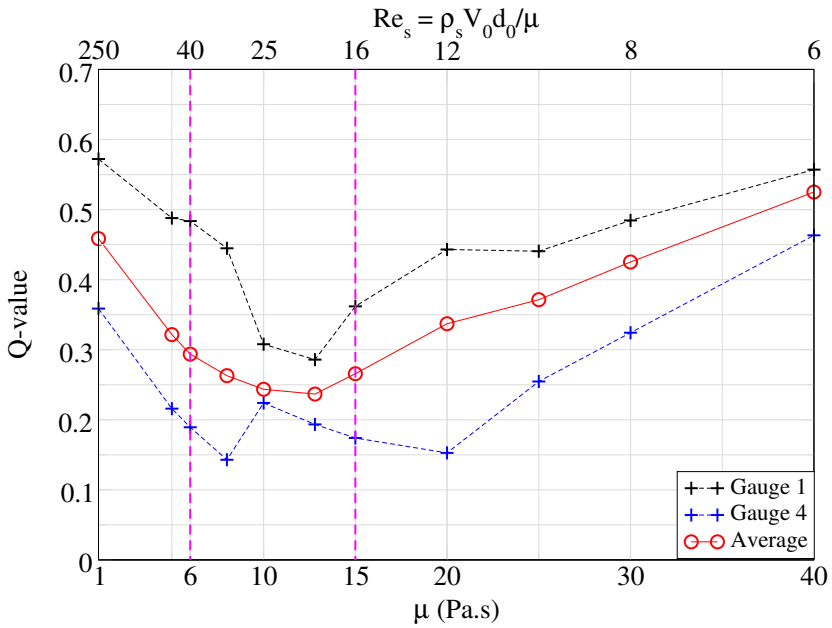

Figure 6: Subaerial benchmark: Q-values calculated for surface elevation time series from the depth-averaged model as functions of the viscosity μ (Pa.s) at Gauges 1 (black) and 4 (blue). Red curve represents the average Q-value for the four gauges. Pink lines define a zone where results are considered satisfactory in average.

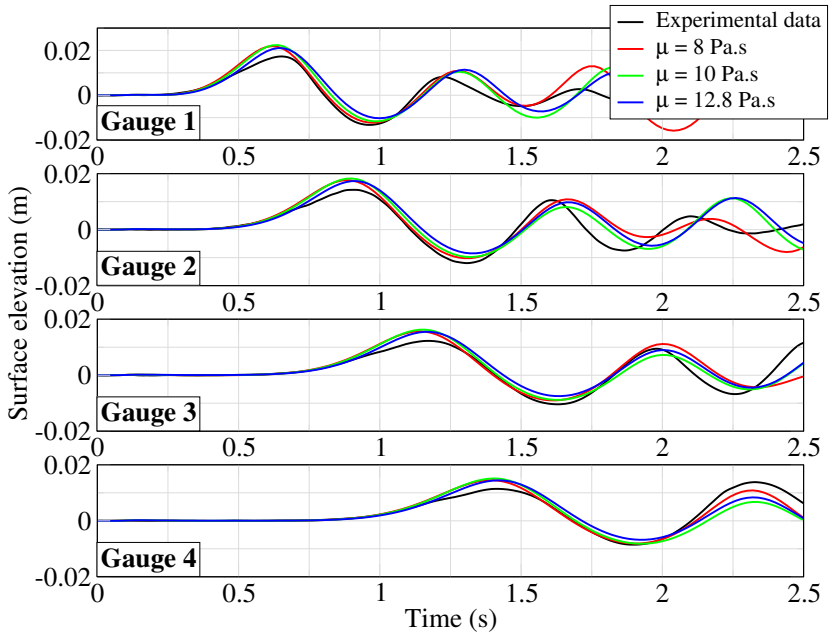

Figure 7: Subaerial benchmark: comparison of surface elevation time series between the experiments (black) and the depth-averaged model simulations using slide viscosity μ of 8 Pa.s (red), 10 Pa.s (green) and 12.8 Pa.s (blue).

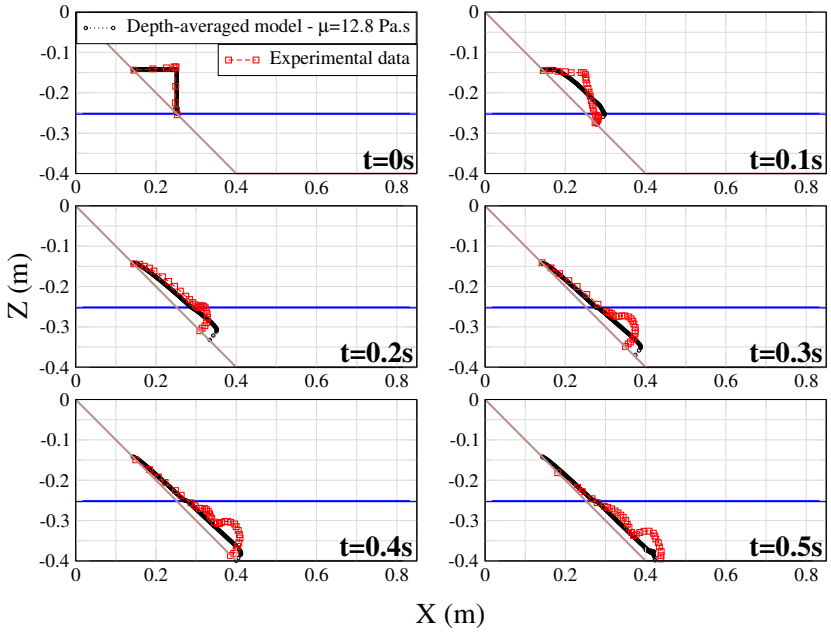

Figure 8: Subaerial benchmark: comparison of slide contours between experiments (red squares) and the depth-averaged model simulation with μ=12.8 Pa.s (black circles). From left to right and up to down, contours are represented every 0.1 s from t=0 to t=0.5 s. The blue line represents the initial water surface. The brown line represents the slope.

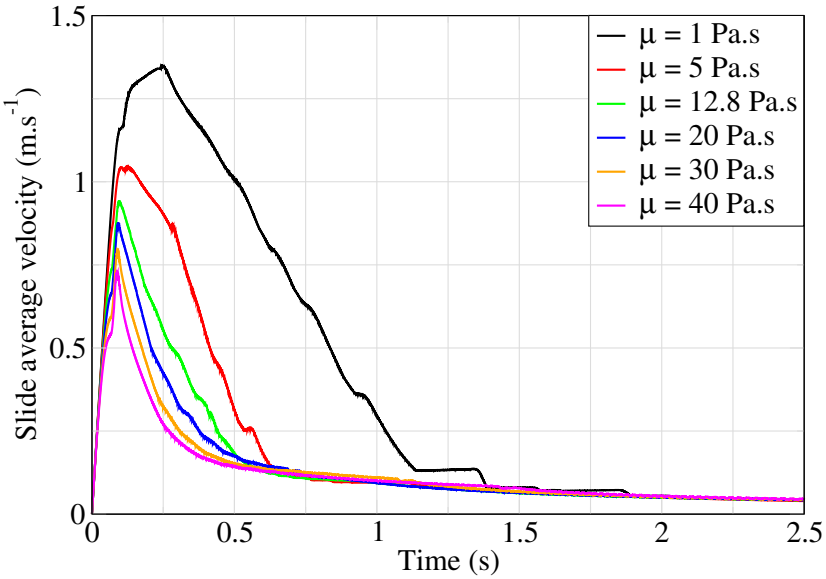

Figure 9: Subaerial benchmark: evolution of the average landslide velocity during the depth-averaged model simulation as a function of the viscosity (μ ranging from 1 to 40 Pa.s).

Navier-Stokes model

Water waves

Figure 10A highlights the existence of a plateau between viscosity values of 12.8 and 30 Pa.s (pink lines) where Q-values are satisfactory. Note that similar values are obtained for the three tested boundary conditions in this viscosity range.

Before the plateau, the noSlip condition gives better results (lower Q-values) whereas best values are obtained after the plateau for the 0.1 partialSlip condition. This stresses the importance of the slide average velocity at the beginning of the process which is controlled both by viscosity and bottom boundary condition.

Figure 11 shows indeed that different combinations of viscosity values and boundary conditions give similar results regarding the leading wave.

Figure 10B shows that, as for the depth-averaged model, Q-values in the far-field (Gauge 4) are lower than those computed in the near-field (Gauge 1).

Landslide

Using a viscosity of 12.8 Pa.s, the simulated slide kinematics is correct up to t=0.2s (Figure 12). Beyond this time, the landslide is too slow independently of the bottom boundary condition. This behavior differs from the one obtained with the depth-averaged model (Figure 8). To reproduce the experimental landslide behavior with the Navier-Stokes model, at least the overall trajectory of the gravity center, a viscosity value μ of 1 Pa.s with a 0.1 partialSlip boundary condition (Figure 13) has to be used, but in this case the landslide front is too large, producing incorrect waves (more than two times larger that the experimental data).

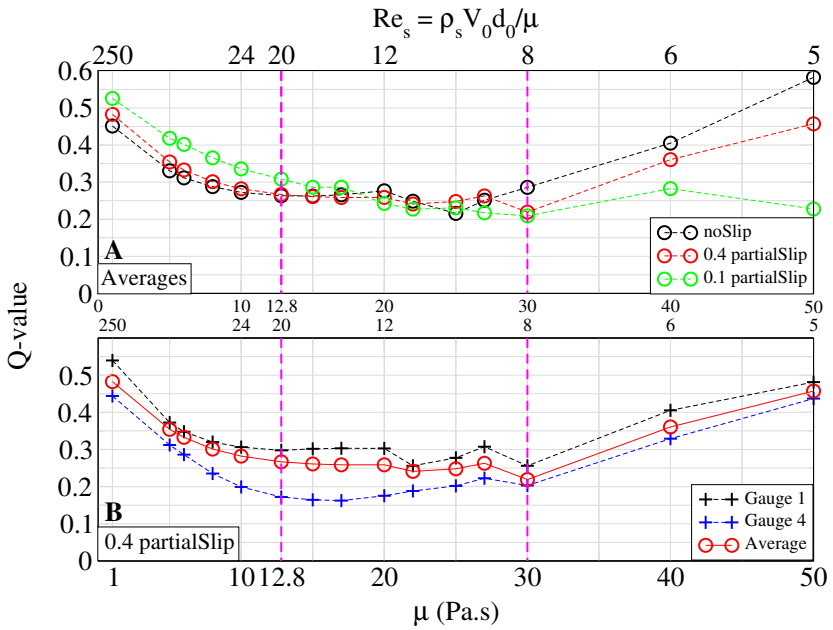

Figure 10: Subaerial benchmark: Q-values calculated for surface elevation time series from the Navier-Stokes model as functions of the viscosity μ (Pa.s). **A**. Average Q-values for the four gauges calculated using the three slip boundary conditions (noSlip (black), 0.4 partialSlip (red) and 0.1 partialSlip (green)). **B**. Q-values calculated for Gauges 1 (black) and 4 (blue) and average Q-values for the four gauges (red) using the 0.4 partialSlip condition.

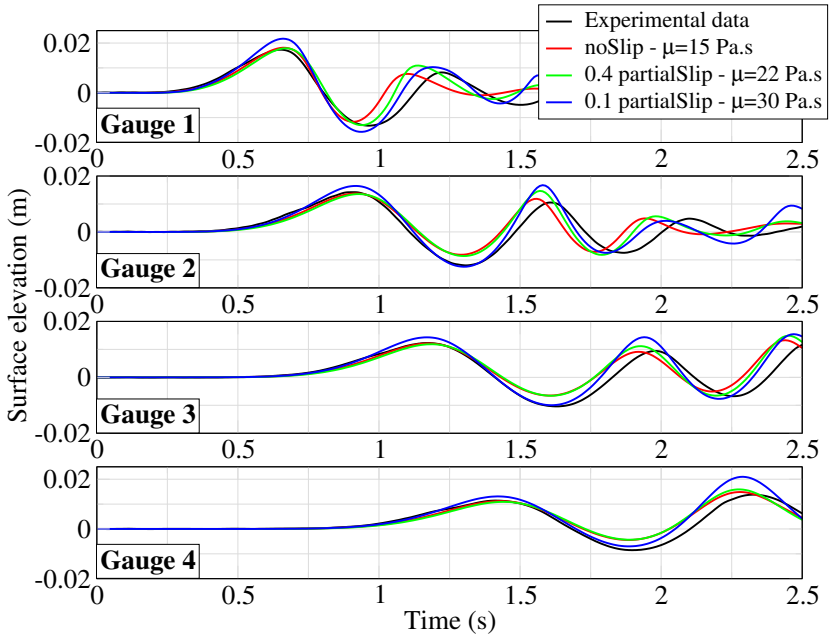

Figure 11: Subaerial benchmark: comparison of surface elevation time series (m) between the experiments (black) and the Navier-Stokes model simulations using viscosity μ of 15 Pa.s with a noSlip boundary condition (red), 22 Pa.s with a 0.4 partialSlip condition (green) and 30 Pa.s with a 0.1 partialSlip condition (blue).

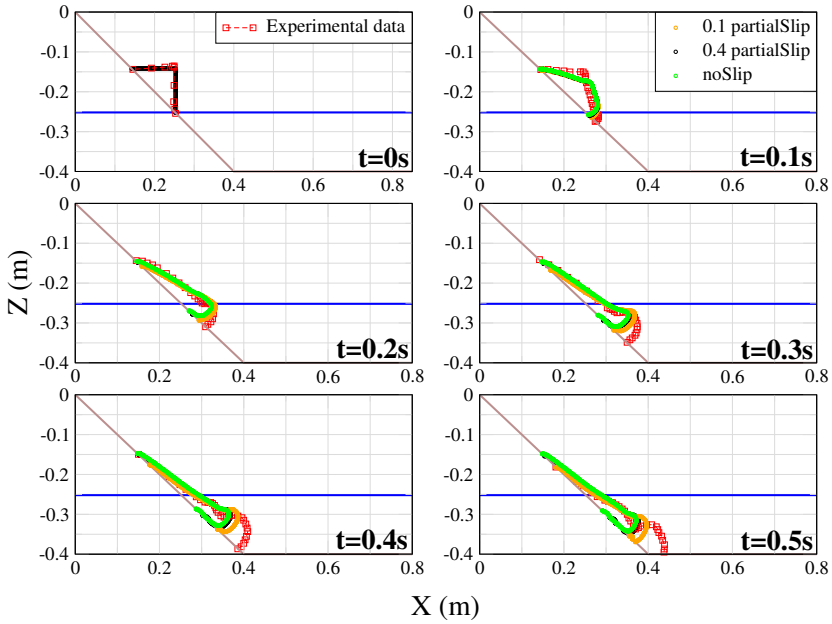

Figure 12: Subaerial benchmark: comparison of slide contours between experiments (red squares) and the Navier-Stokes model simulations with μ=12.8 Pa.s and noSlip (green), 0.4 partialSlip (black) or 0.1 partialSlip (orange) slip conditions. From left to right and up to down, contours are represented every 0.1 s from t=0 to t=0.5s. The blue line represents the initial water surface. The brown line represents the slope.

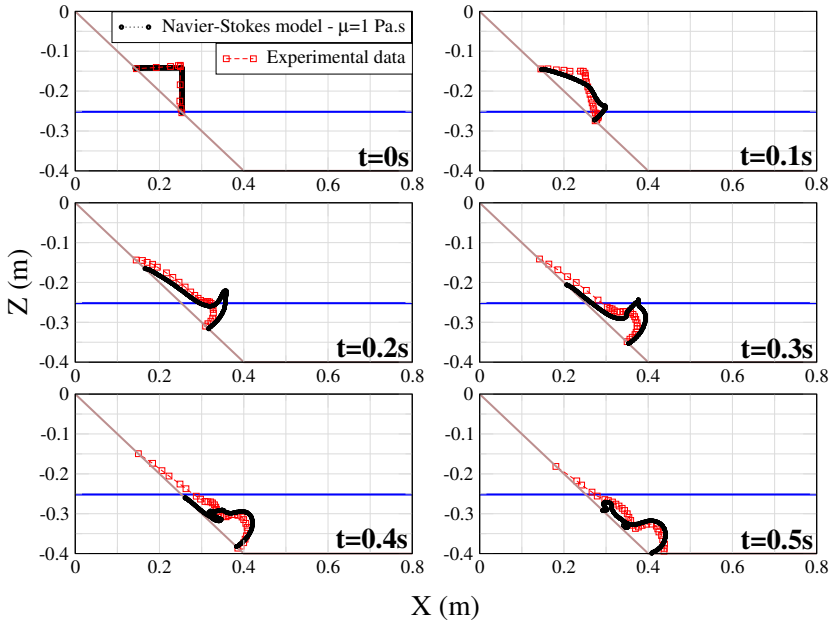

Figure 13: Subaerial benchmark: comparison of slide contours between experiments (red squares) and the Navier-Stokes model simulations with μ=1 Pa.s and 0.1 partialSlip (black) slip condition. From left to right and up to down, contours are represented every 0.1 s from t=0 to t=0.5s. The blue line represents the initial water surface. The brown line represents the slope.

3.3.2 Submerged benchmark

Depth-averaged model

Water waves

In the submerged landslide case, the same shape for the Q-values curve as that of the subaerial benchmark is observed, a trough and a plateau of optimal viscosity. The best performances are obtained with viscosity values between 0.1 and 1 Pa.s (Figure 14). Overall, considering the four gauges, a viscosity of 1 Pa.s gives the best results.

Surface elevations are globally well reproduced using a viscosity value μ between 0.1 and 1 Pa.s (Figure 15). This is especially true for the first wave, the next waves being slightly too high compared to the experiments, especially at Gauge 1 (top panel in Figure 15).

Landslide

With μ=1 Pa.s (Figure 16), the simulated landslide matches the experimental data up to t=0.17s (middle left panel, Figure 16) and deviates afterward due to larger velocities. With μ=3 Pa.s, the landslide behavior is better reproduced (Figure 17), the simulation being close to the experimental data up to t=0.47s (bottom left panel).

Figure 18 shows the simulated landslides at times when they touch the bottom and start to slow down in cases with μ=0.01, 0.1, 0.5 and 1 Pa.s (peaks of corresponding lines in Figure 18) whereas for μ=5 or 10 Pa.s, the landslide starts to slow down before reaching the bottom which likely affects waves generation.

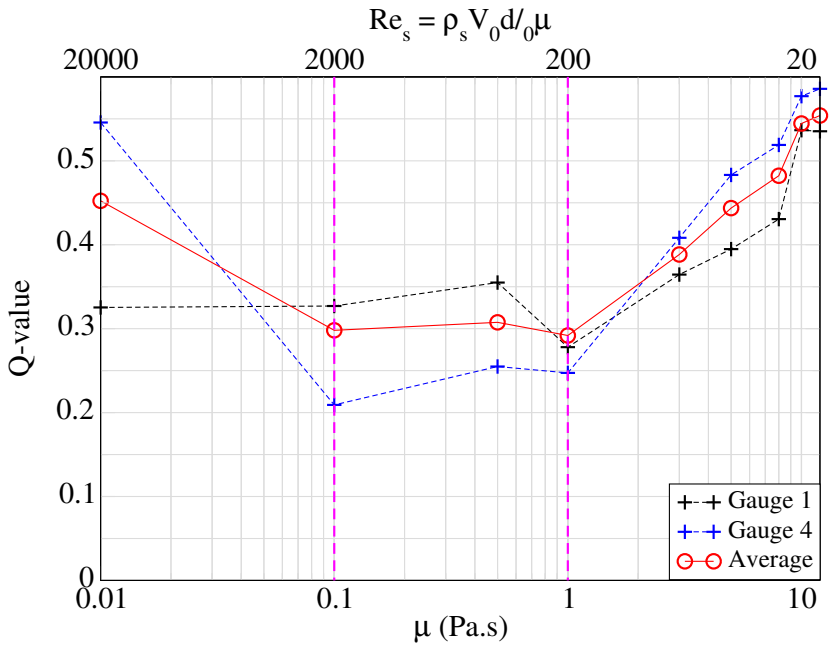

Figure 14: Submerged benchmark: Q-values calculated for surface elevation time series from the depth-averaged model as functions of the viscosity μ at Gauges 1 (black) and 4 (blue). Red curve represents the average Q-value for the four gauges. Pink lines define a zone where results are considered satisfactory in average. X-axis is logarithmic.

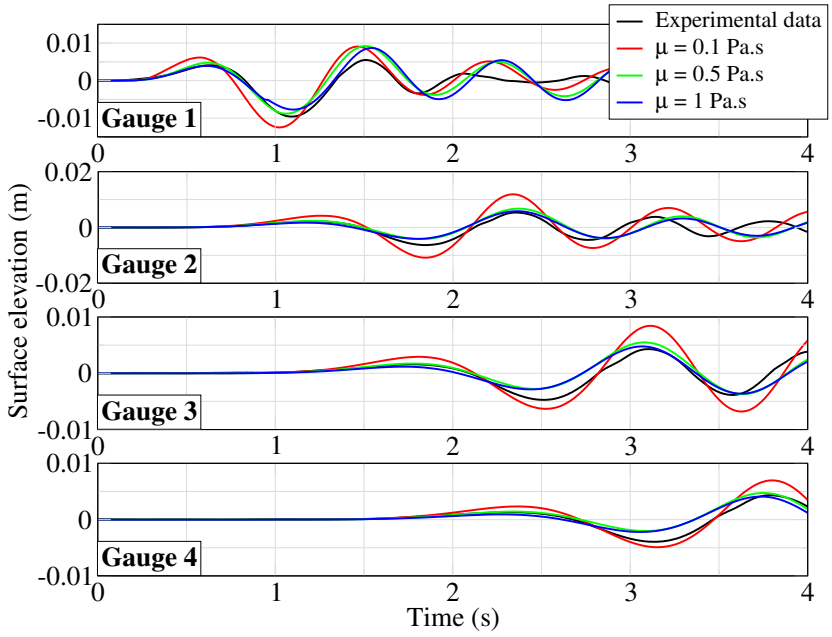

Figure 15: Submerged benchmark: comparison of surface elevation time series (m) between the experiments (black) and the depth-averaged model simulations using a viscosity μ of 0.1 Pa.s (red), 0.5 Pa.s (green) and 1 Pa.s (blue).

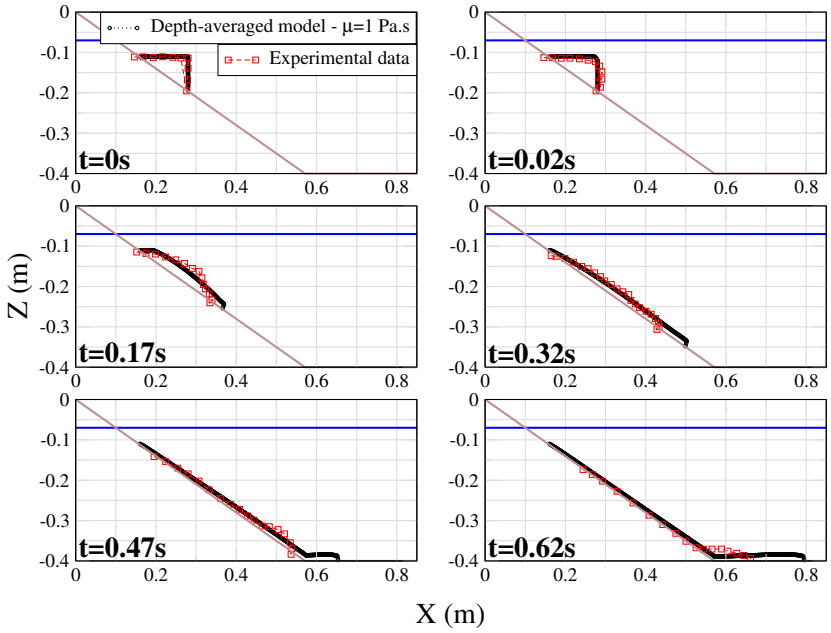

Figure 16: Submerged benchmark: comparison of slide contours between experiments (red squares) and the depth-averaged simulation with μ=1 Pa.s (black circles). From left to right and up to down, contours are represented at t=0, 0.02, 0.17, 0.32, 0.47 and 0.62 s. The blue line represents the initial water surface. The brown line represents the slope.

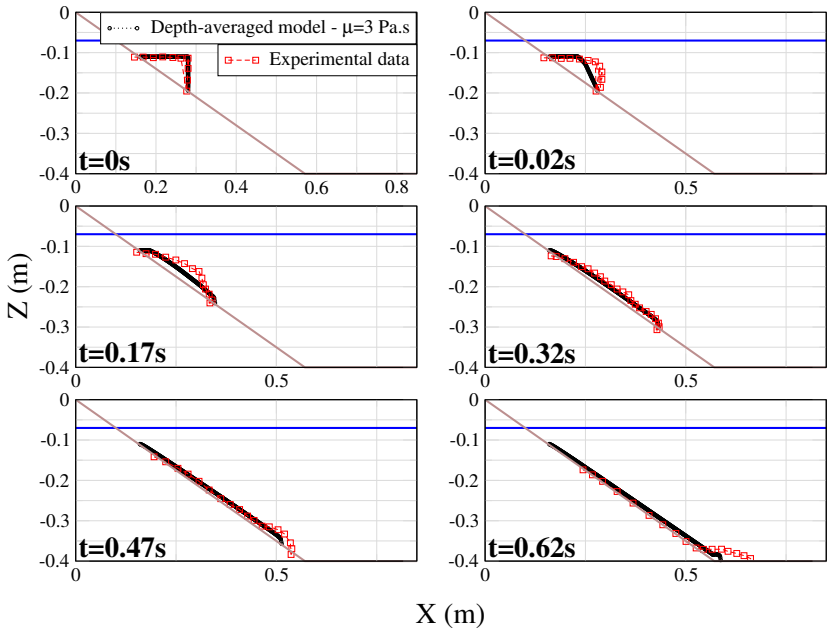

Figure 17: Same as Figure 16 for μ=3 Pa.s.

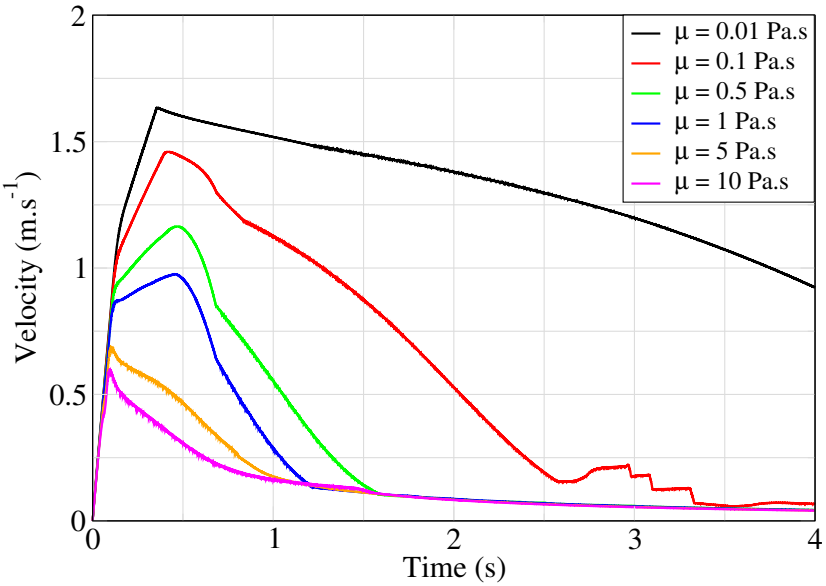

Figure 18: Submerged benchmark: evolution of the average landslide velocity during the depth-averaged simulation as a function of the viscosity μ ranging from 0.01 to 12 Pa.s.

Navier-Stokes model

Water waves

Figure 19A shows again that optimal results are similarly obtained for the noSlip and 0.4 partialSlip conditions using viscosity values between 1 and 5 Pa.s. With the 0.1 partialSlip condition, best Q-values are obtained for higher viscosity values. Considering the 0.4 partialSlip condition (Figure 19B), the best results are obtained with a viscosity value of 3 Pa.s. Moreover, as previously seen, waves are better reproduced in the far-field than the near-field.

Figure 20 presents the comparison between the Navier-Stokes model simulations and the experimental data for the three best combinations of parameters (*i.e.*, viscosity value and bottom boundary condition). Surprisingly, the behavior of the model is very similar at the four gauges whatever the combination. At Gauge 1 (top panel), the peak of the first wave is well reproduced whereas the following waves are attenuated. The latter are better reproduced on the three other gauges. Hence, to generate the same wave, a full slip condition (0.1 partialSlip) requires a higher viscosity value (μ=8 Pa.s) than a medium slip condition (0.4 partialSlip, μ=3 Pa.s) or a noSlip condition (μ=5 Pa.s).

Landslide

Although simulations with the following combination (0.4 partialSlip and μ=3 Pa.s) give good results regarding the waves, they do not reproduce the landslide correctly (Figure 21). A lower viscosity value (μ=0.1 Pa.s) is actually needed to better reproduce the landslide motion at the first instants (*i.e.*, until t=0.17 s in Figure 22). Beyond t=0.17 s, even a quasi full slip condition (*i.e.*, 0.1 partialSlip, in orange) is not sufficient to reach the position of the experiment slide front. The difference along the slope between the observed and the simulated locations of the landslide front increases progressively and reaches 7.2 cm at t=0.32 s and about 17 cm at t=0.62 s (Figure 22). The difference observed could be explained by the absence of water incorporation within the landslide.

Additionally, whatever the viscosity value and regardless of the boundary condition at the bed, a 5-10 cm high flow front forms slowing down the whole landslide.

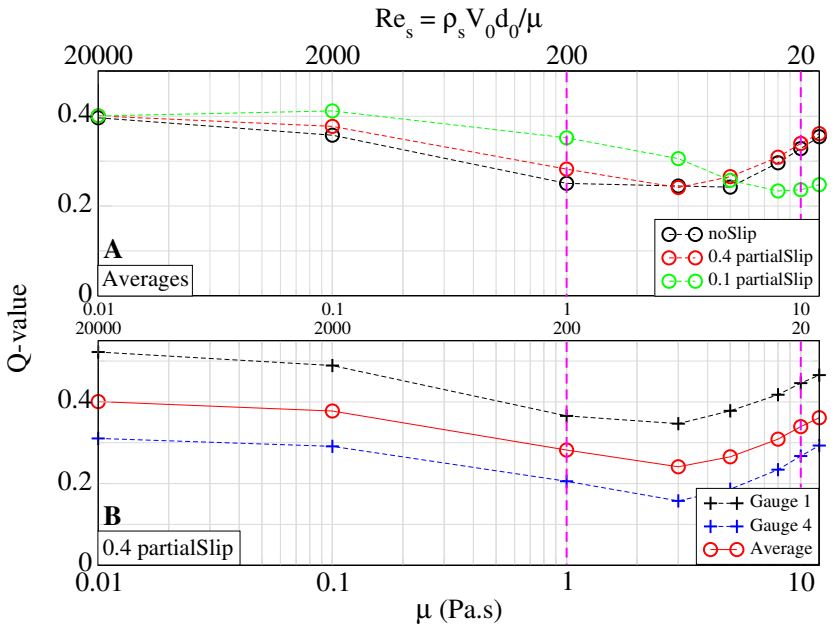

Figure 19: Submerged benchmark: Q-values calculated for surface elevation time series from the Navier-Stokes model as functions of the viscosity μ. **A**. Average Q-values for the four gauges calculated using the three slip boundary conditions (noSlip (black), 0.4 partialSlip (red) and 0.1 partialSlip (green)). **B**. Q-values calculated for Gauges 1 (black) and 4 (blue) and average Q-values for the four gauges (red) using the 0.4 partialSlip condition. X-axis is logarithmic.

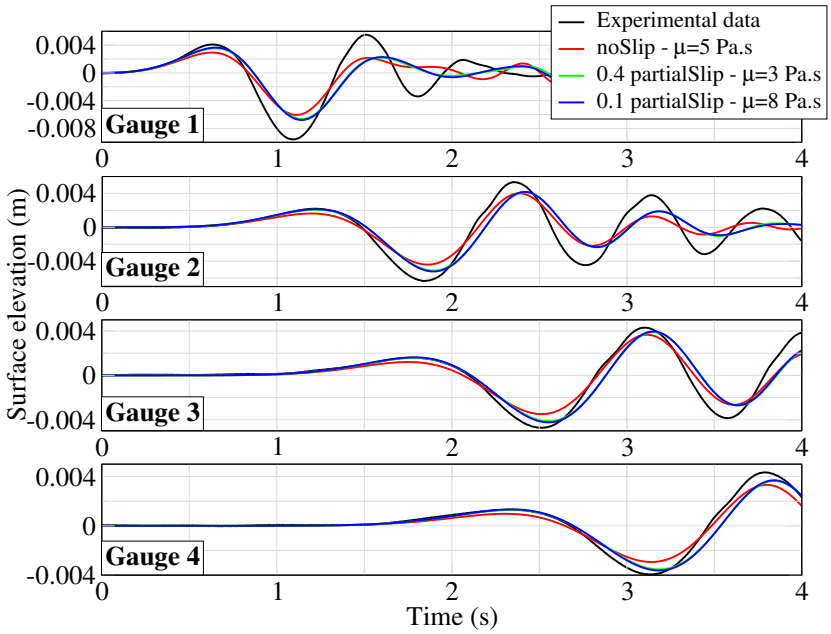

Figure 20: Submerged benchmark: comparison of surface elevation time series (m) between the experiments (black) and the Navier-Stokes model simulations using viscosity μ of 5 Pa.s with a noSlip boundary condition (red), 3 Pa.s with a 0.4 partialSlip condition (green) and 8 Pa.s with a 0.1 partialSlip condition (blue).

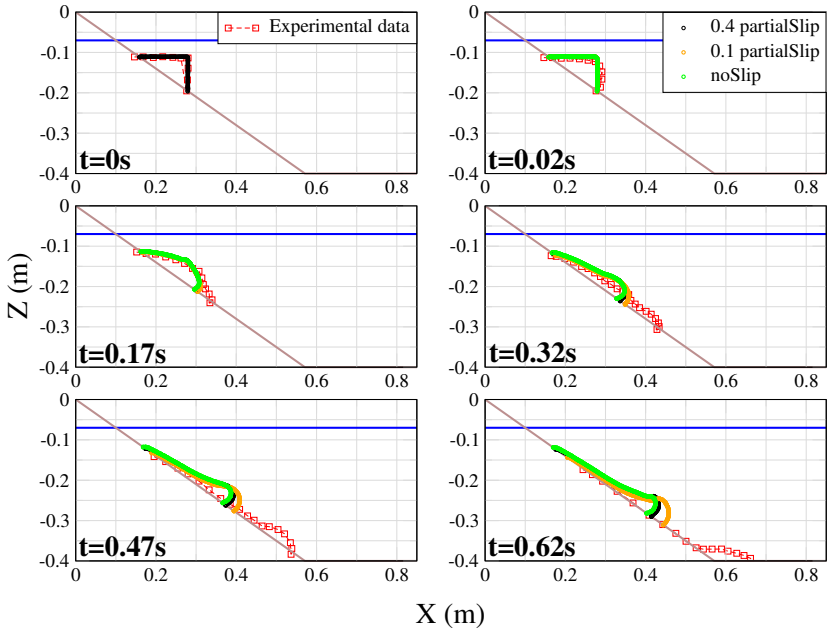

Figure 21: Submerged benchmark: comparison of slide contours between experiments (red squares) and the Navier-Stokes model simulations with μ=3 Pa.s and noSlip (green), 0.1 partialSlip (orange) or 0.4 partialSlip (black) slip conditions. From left to right and up to down, contours are represented at t=0, 0.02, 0.17, 0.32, 0.47 and 0.62 s. The blue line represents the initial water surface. The brown line represents the slope.

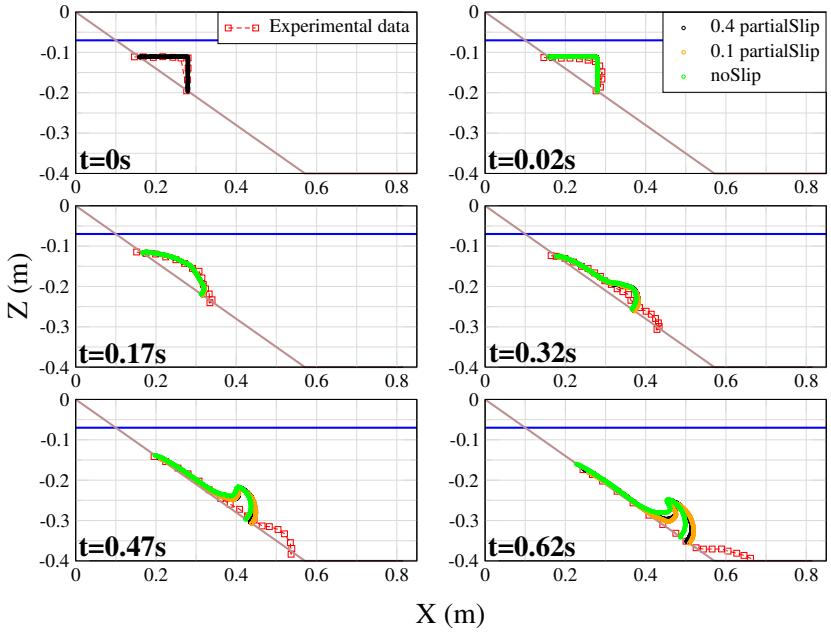

Figure 22: Same as Figure 21 with $\mu = 0.1$ Pa.s.

3.4 Discussion

Both the depth-averaged and the Navier-Stokes models can reproduce the benchmarks waves using their own sets of parameters with approximately the same accuracy. The viscosity is generally lower in the depth-averaged model than in the Navier-Stokes model, as summarized in Table 3. However, both models share viscosity values in their intervals of validity: between 12 and 15 Pa.s for the subaerial benchmark (higher than Viroulet et al. (2016), 5 Pa.s, but similar to Clous and Abadie (2019), 10 Pa.s) and around 1 Pa.s for the submerged benchmark (higher than Grilli et al. (2017), 0.01 Pa.s, but similar to Clous and Abadie (2019), 1 Pa.s). This difference between both models is likely due both to the nature of the equations formulations in the depth-averaged model and to the boundary condition that leads to higher viscosity values in the Navier-Stokes model.

Relative low influence of the slide viscosity on the waves

Similar water surface elevations are calculated for a range of viscosity values (Sections 3.3.1 and 3.3.2 and Table 3). The relative low sensitivity to viscosity value is illustrated by the plateau of lower Q-value depictable in Figures 6, 10, 14 and 19. We note that the waves in the far-field are even less sensitive to the viscosity.

Poor landslide reproduction especially for the Navier-Stokes model

The optimal parameters to get the correct generated first wave generally do not allow to reproduce the exact measured landslide behavior for both benchmarks and with both models. Hence, as already mentioned by Grilli et al. (2017), the accurate modeling of water waves does not depend on details of the landslide deformation. Moreover, although the equations governing the landslide motion in the depth-averaged model do not make possible to reproduce the bulbous shape of the landslide front, the model allows to obtain correct landslide velocity and quantity of materials entering water for the subaerial benchmark (Figure 8). As regards the submerged benchmark, the landslide simulated by the depth-averaged model is a bit faster than the experimental one (Figure 16). By contrast, the Navier-Stokes model produces a bulbous front that progressively develops while traveling down the slope. This bulbous front is due to a vortex generated at the water/slide interface. In this case, the simulated slide is much slower than in the experiment.

	Subaerial	Submerged
Depth-averaged	6-15 [16-40]	0.1-1 [200-2000]
Navier-Stokes	12.8-30 [8-20]	1-10 [20-200]

Table 3: Summary table of viscosity μ and Reynolds number Re_s values (in [ ]) that give the best results relatively to the two benchmarks studied.

Calibration of the viscosity value

In every practical case, the major issue is to determine the viscosity value. For the subaerial case, the approximation of Ionescu et al. (2015) seems to be valid and both models reproduce the experimental results. For the submerged benchmark, the viscosity values considering in this study are around 10 times lower than those for the subaerial benchmark. A simple extrapolation of these results to other cases is however dangerous. Indeed, this approach requires intrinsic landslide parameters (μ(I) parameters, grain density and grain diameter) to which access is conditioned to a field survey. Moreover, the grain size in the submerged benchmark is about four times greater than the one in the subaerial benchmark, so there is more water between the grains in the submerged case. Because of this water, the landslide becomes more fluid and a lower viscosity is required.

Study limitations

The reproduction of the benchmarks could be improved by using more sophisticated landslide rheology (e.g. a granular rheology instead of a viscous fluid) or boundary conditions but beyond the idea of a perfect reproduction, we were looking for fast solutions in order to use both models in tsunami early warning systems. We note that numerous sets of parameters can lead to very similar water waves and landslide behaviors.

Chapter 4

Intercomparison of depth-averaged and Navier-Stokes models in different situations

In this chapter, Navier-Stokes, shallow water and Boussinesq equations are compared to each other through two main cases. In Section 4.1, an arbitrary slide case is used to define which set of equations is best for generation or propagation of water waves. The landslide is simulated in the Navier-Stokes model and the results are introduced in the depth-averaged models as a time varying bathymetry. In this way, the landslide behavior is identical for all models and only the tsunami equations are evaluated. In Section 4.2, the influence of the slope and the slide submergence are studied with a case based on the subaerial experiment of the previous chapter.

4.1 Which model strategy for the generation and propagation zones?

The aim of this study is to compare three sets of equations, Navier-Stokes, shallow water and Boussinesq, through the comparison of three models, OpenFOAM, Hydra and AVALANCHE, respectively.

The case consists in a subaerial parallelogram starting at the bottom and which dimensions (H, L) vary, sliding on a slope of 45° and entering into 0.15 m of water (Figure 23). 27 combinations are tested with the height $H \in \{0.10, ..., 0.50\}$ m and the width $L \in \{0.10, ..., 0.50\}$ m increasing 0.05 m by 0.05 m in both dimensions. Synthetic gauges are located at every 0.2 m, from $x = 1$ m to $x = 3$ m.

The first landslide simulation is realized with OpenFOAM and the landslide behavior results are integrated to the two depth-averaged models as a bottom deformation. This procedure guarantees that the landslide is identical for the three models and the comparison is realized only on the water waves generation and propagation which is the aim of this section.

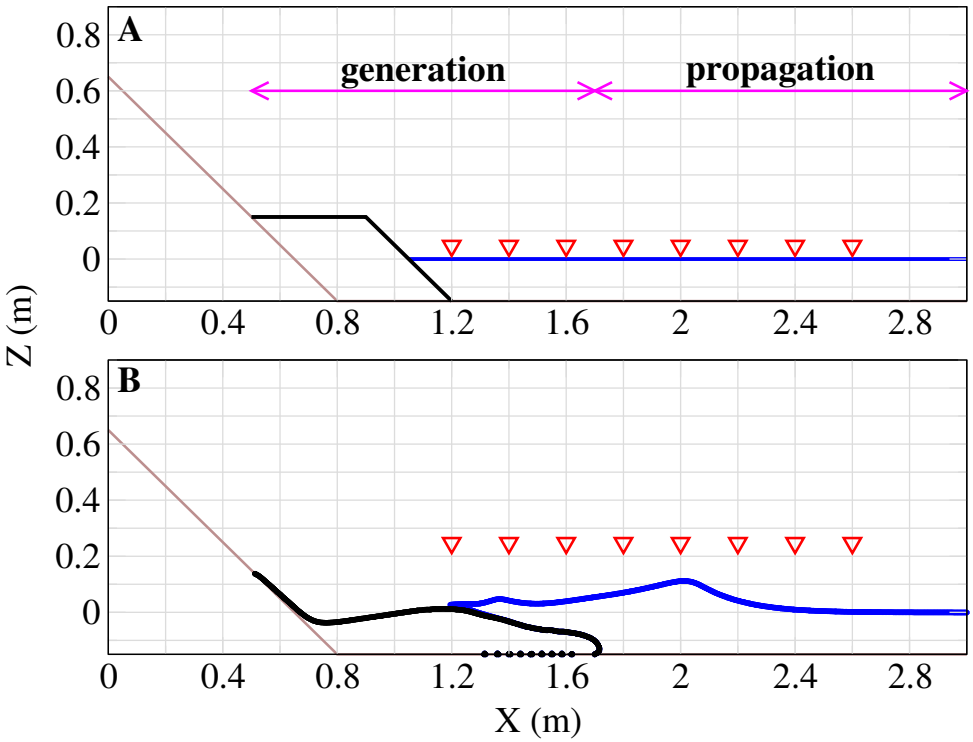

Figure 23: Initial (A) and intermediate (B) states of the test case. The landslide is in black, slope in brown and water in blue. Synthetic gauges are indicated by red triangles.

4.1.1 Comparison in the generation zone

The limit of the generation zone is defined as the final position reached by the landslide (Figure 23A). Figure 24 represents the time series of the water surface elevation for the four test cases at a gauge located at the border of their wave generation zone, *i.e.* $(H, L) = (0.25\text{ m}, 0.20\text{ m})$ case $x = 1.2$ m, $(H, L) = (0.30\text{ m}, 0.40\text{ m})$ case $x = 1.4$ m, $(H, L) = (0.20\text{ m}, 0.60\text{ m})$ case $x = 1.6$ m and $(H, L) = (0.45\text{ m}, 0.40\text{ m})$ $x = 1.8$ m. These cases correspond to a small and a large volume compared to the water mass, and two intermediate similar volumes but with different geometries. In the same graphs we plot the landslide thickness (red dashed line) when the landslide reaches the position of the probe.

We first observe that both shallow water and Boussinesq models, for which the dynamic of the landslide was imposed as a time varying bathymetry, are very sensitive to the variation of the bathymetry. Indeed, when the landslide reaches the gauge location (beginning of the red dashed line in each graph in Figure 24), peaks are observed for the shallow water and Boussinesq simulations. Studies in the literature that impose the landslide displacement using the same kind of simplified model (for example Zech et al. (2009); Fernández-Nieto et al. (2017)) do not present such kind of peaks, however the dynamic of the landslide is significantly different.

We also observe that for all the cases, the shallow water model is closer to the Navier-Stokes model than the Boussinesq model in the wave generation zone. An explanation may

be that the Boussinesq model is weakly nonlinear, so the water elevation in the dispersive part of the model (right-hand side of the momentum equation) is replaced by the mean depth d. However in the derivation of the model, the mean depth should not change in time, or at least much slower than the free surface, which is not the case here. In addition, the advection term of the Boussinesq model (left-hand side of the momentum equation) is written in the non-conservative form. It is well known that this form is not suitable for discontinuous solutions, at least in the case of the shallow water model, because it leads to wrong weak solutions. It is generally not a problem for the Boussinesq model, which does not develop discontinuous solutions. However, in our test cases, because of the discontinuous bottom, discontinuous solutions appear.

4.1.2 Comparison in the propagation zone

Here we focus on the wave propagation zone (Figure 23A) for the same test cases as in Section 4.1.1. The time series of the water surface elevation at the gauges $x = 2.0$ m, $x = 2.2$ m, $x = 2.4$ m and $x = 2.6$ m for cases $(H, L) = (0.25\text{ m}, 0.20\text{ m})$, $(H, L) = (0.30\text{ m}, 0.40\text{ m})$, $(H, L) = (0.20\text{ m}, 0.60\text{ m})$ and $(H, L) = (0.45\text{ m}, 0.40\text{ m})$, respectively, are represented in Figure 25.

In the propagation zone, shallow water results are not always the closest to the Navier-Stokes ones. Moreover results differ strongly from one test case to another.

In the simulations realized in this work, the Navier-Stokes results are better reproduced in the propagation zone by the Boussinesq model for small landslides and by the shallow water for large landslides. This can be explained by the fact that the Boussinesq model takes into account the dispersive effects. Anyway this observation suggests that the quality of the approximations given by the simplified models is related to the volume of the landslide. However, as shown by Figure 26, the results of $(H, L) = (0.25\text{ m}, 0.45\text{ m})$ and $(H, L) = (0.45\text{ m}, 0.25\text{ m})$ cases are also different in spite of the same volume of the landslide. For parameters $(H, L) = (0.25\text{ m}, 0.45\text{ m})$, shallow water results are close to the Navier-Stokes results in the wave generation zone but the Boussinesq model gives better results in the propagation zone. For parameters $(H, L) = (0.45\text{ m}, 0.25\text{ m})$, the shallow water model gives better results in both zones. In Section 4.1.3, a better criterion than the volume is discussed. The objective of this criterion is to define the validity of the two depth-averaged models with respect to the Navier-Stokes model.

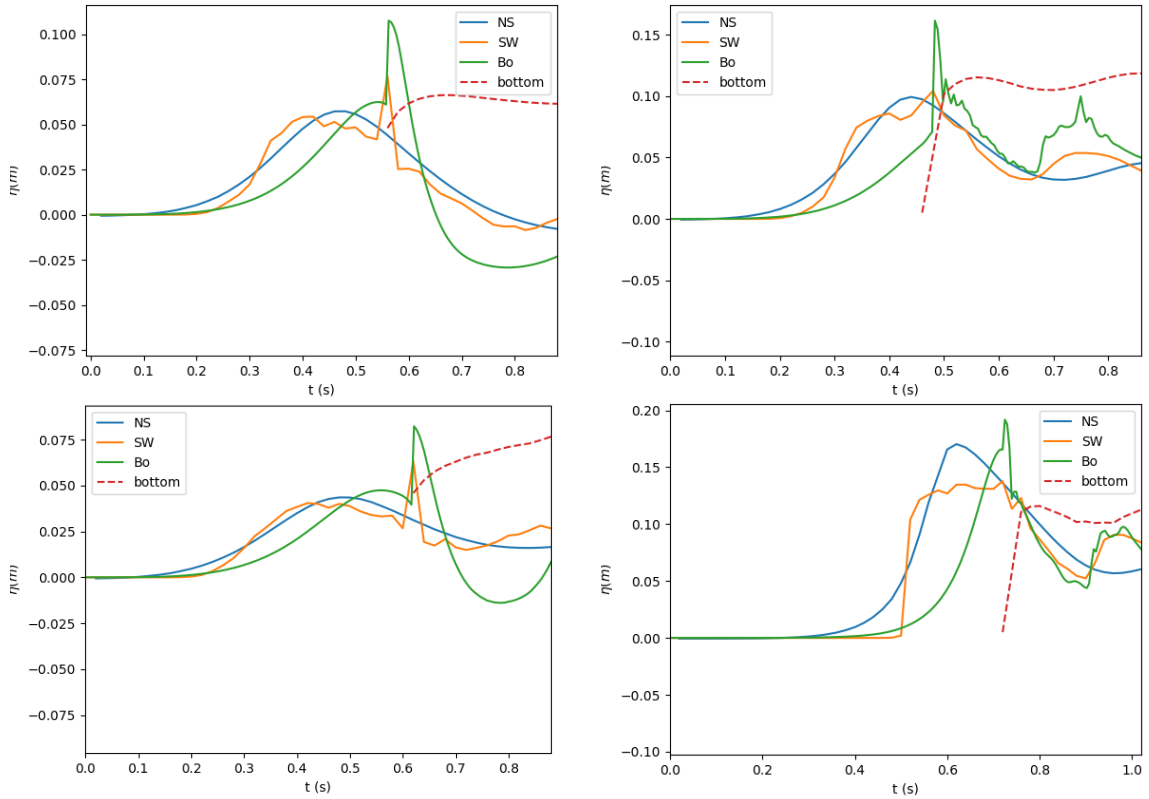

Figure 24: Comparison between the results of the three models for four selected test cases, in the wave generation zone. The top left corresponds to the $(H, L) = (0.25\text{ m}, 0.20\text{ m})$ case at the probe $x = 1.2$ m. The top right corresponds to the $(H, L) = (0.30\text{ m}, 0.40\text{ m})$ case at the probe $x = 1.4$ m. The bottom left corresponds to the $(H, L) = (0.20\text{ m}, 0.60\text{ m})$ case at the probe $x = 1.6$ m. The bottom right corresponds to the $(H, L) = (0.45\text{ m}, 0.40\text{ m})$ case at the probe $x = 1.8$ m. Blue, orange and green lines represent respectively the Navier-Stokes, the shallow water and the Boussinesq simulations. Red dashed line represents the evolution of the bottom.

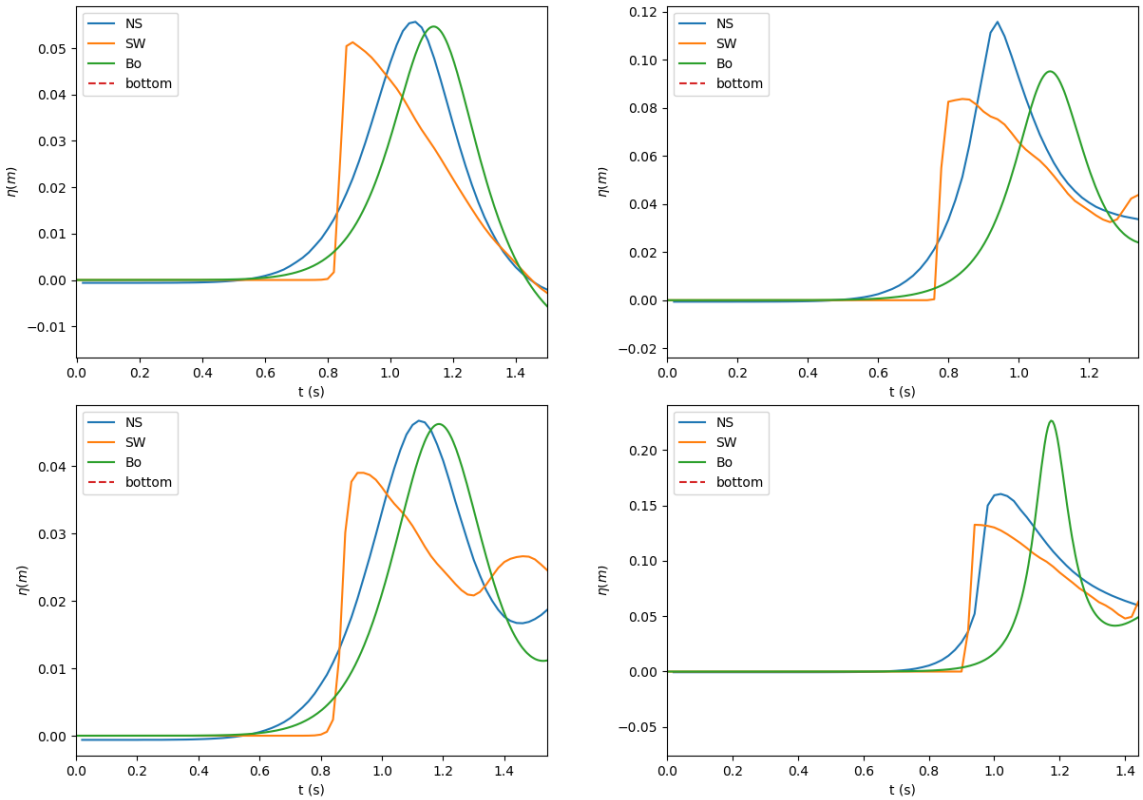

Figure 25: Comparison between the results of the three models for four selected test cases, in the wave propagation zone. The top left corresponds to the $(H, L) = (0.25\text{ m}, 0.20\text{ m})$ case at the probe $x = 2.0$ m. The top right corresponds to the $(H, L) = (0.30\text{ m}, 0.40\text{ m})$ case at the probe $x = 2.2$ m. The bottom left corresponds to the $(H, L) = (0.20\text{ m}, 0.60\text{ m})$ case at the probe $x = 2.4$ m. The bottom right corresponds to the $(H, L) = (0.45\text{ m}, 0.40\text{ m})$ case at the probe $x = 2.6$ m. Blue, orange and green lines represent respectively the Navier-Stokes, the shallow water and the Boussinesq simulations.

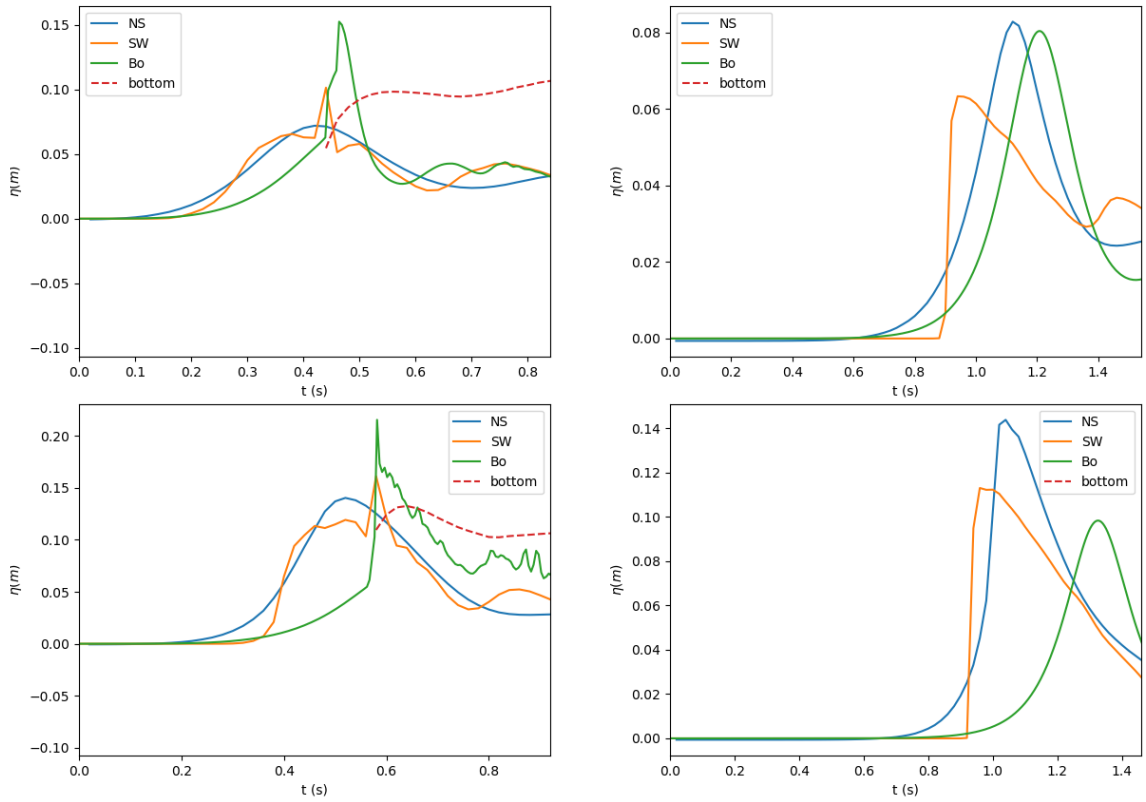

Figure 26: Comparison between the results of the three models with the same landslide size. The top line corresponds to the parameters $(H, L) = (0.25\text{ m}, 0.45\text{ m})$ while the bottom line corresponds to the parameters $(H, L) = (0.45\text{ m}, 0.25\text{ m})$. The left column corresponds to a probe at $x = 1.4$ m (wave generation zone) while the right column corresponds to a probe at $x = 2.4$ m (wave propagation zone).

4.1.3 Discussion

Quantities of interest and correlations between the models

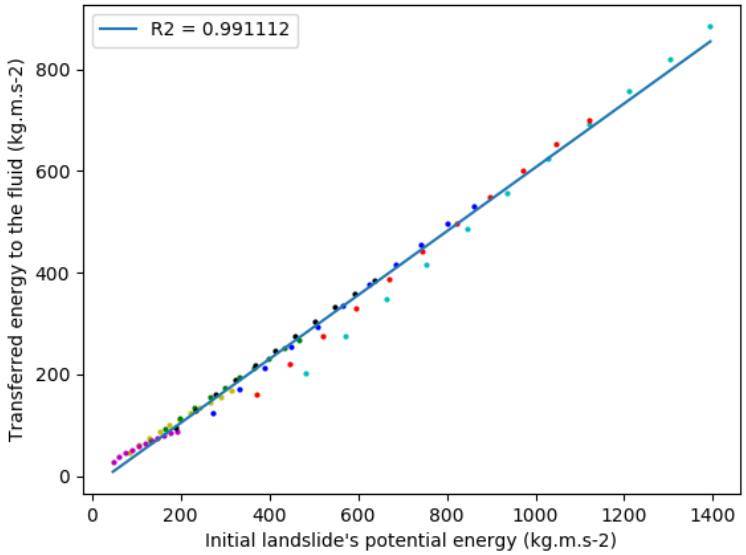

Figure 27: Correlation between the initial energy in the landslide and the energy transferred to the water mass. Each point corresponds to a parameter couple (H, L) while the same color corresponds to the same H.

Since the flow is initially at rest, the initial energy of the landslide can be computed from its initial configuration, *i.e.* $P^0 = P(t = 0)$ where P is the potential energy given by

$$P(t) = \frac{g}{2} \int_x (\beta(t, x) - B(x))^2 dx \tag{4.1}$$

where $\beta(t, x)$ is the top interface of the landslide.

This integral is computed numerically from the output of OpenFOAM. Instead of the energy transferred, we can easily compute the final potential energy, *i.e.* $P(t = 2)$. At time $t = 2$ s the landslide is at rest so all its energy is potential energy. The energy obtained by subtracting the two potential energies is the total energy lost by the landslide during its motion and it is supposed to be the energy transferred to water, neglecting the landslide viscosity.

In the last part, we concluded that the volume of the landslide is not a key parameter to evaluate the validity of the depth-averaged models. Instead, we can suppose that there exists a more direct link with the energy transferred from landslide to water. However, in practice it is not easy to measure *apriori* the energy transferred. Figure 27 first shows that, as expected, the energy transferred from landslide to water is strongly related to the initial energy of the landslide. More precisely, results show that for all the performed simulations, between 50% and 60% of the initial energy was transferred to water.

Correlations between the volume, the energy transferred from landslide to water and the generated wave amplitude were investigated at the gauge located at the beginning of

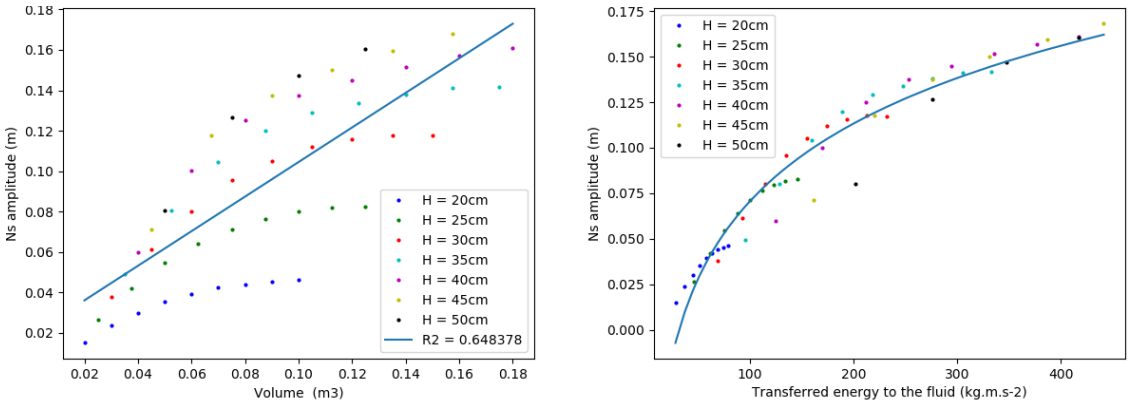

Figure 28: Correlation between the amplitude of the wave and respectively the volume of the landslide (left) and the energy transferred to water (right) for the Navier-Stokes model (Ns).

the wave propagation zone, *i.e.* $x = 2.0$ m. As the extent of the wave generation zone is not the same for all the tests, the ones corresponding to the biggest volumes were not considered when computing the correlation curves presented here, since the wave amplitude may still be affected by the landslide at the selected gauge. Therefore, among the 77 test cases performed, 61 were retained for the correlations.

In Figure 28, the graph on the left shows that the volume alone is not relevant to characterize the generated wave amplitude which is more dependent on the landslide height and length. The graph to the right illustrates that between the amplitude and the energy transferred to water the correlation is more evident and almost all the simulations can be fitted by a logarithm law.

Time delays and difference of amplitudes between the Navier-Stokes solution and both depth-averaged models are then calculated. Figure 29 shows that the first waves generated by the shallow water model are always late compared to the Navier-Stokes results, while the first waves generated by the Boussinesq model are ahead. Moreover, an increase of the energy transferred by landslide to water, which means an increase of the initial landslide potential energy, results in a decrease of the time delay for the shallow water model and an increase for the Boussinesq model.

The results in terms of difference of amplitude are less obvious. For the shallow water model, a logarithm deviation seems to appear. However, the deviation of the Boussinesq model is a succession of logarithms which seems to indicate that some information is still missing to characterize the flow.

Analysis of a mixed shallow water/Boussinesq model

Obviously one solution to approach the Navier-Stokes results with a depth-averaged model would be to use a fully nonlinear weakly dispersive model, such as the so called Serre/Green-Naghdi model (Lannes, 2013). Even with a very robust, entropy-satisfying

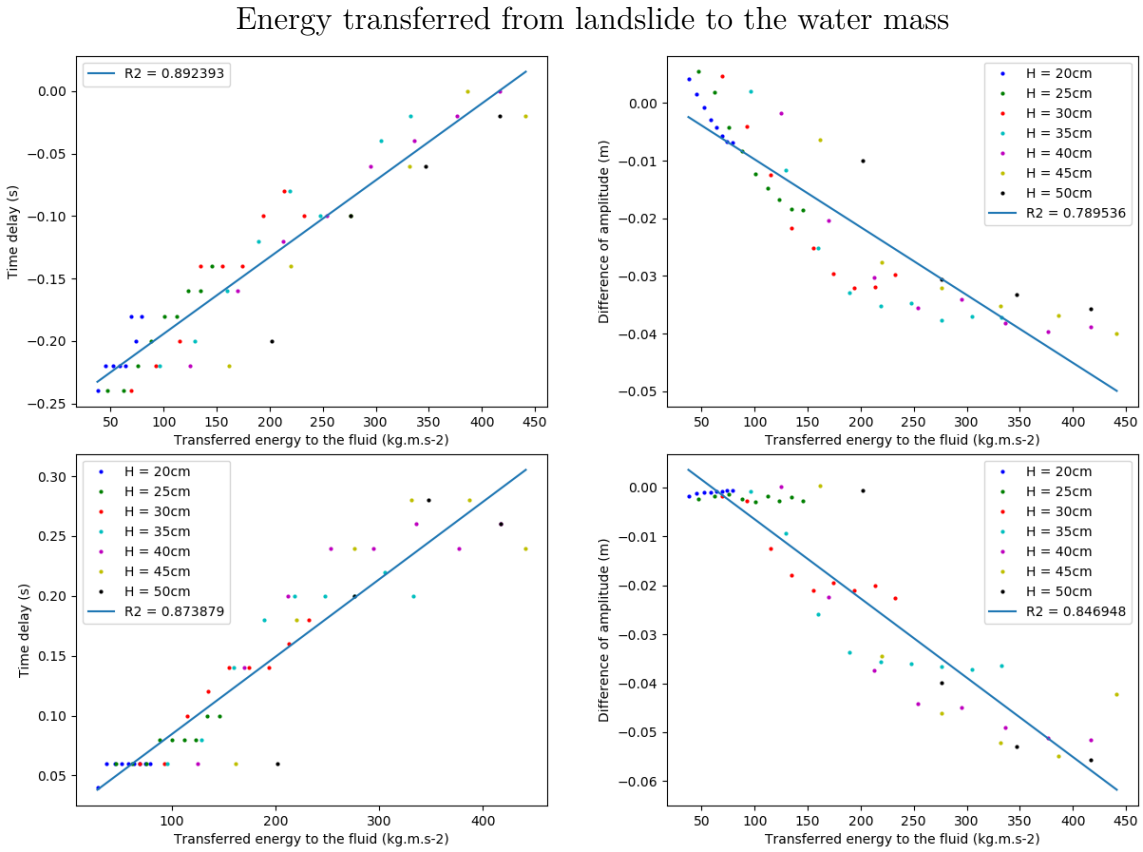

Figure 29: Deviation of the first wave with respect to the Navier-Stokes solution at $x = 2.0$ m in terms of time delay (left column) and in terms of amplitude (right column) for the shallow water model (top line) and the Boussinesq model (bottom line). Blue lines are linear regressions.

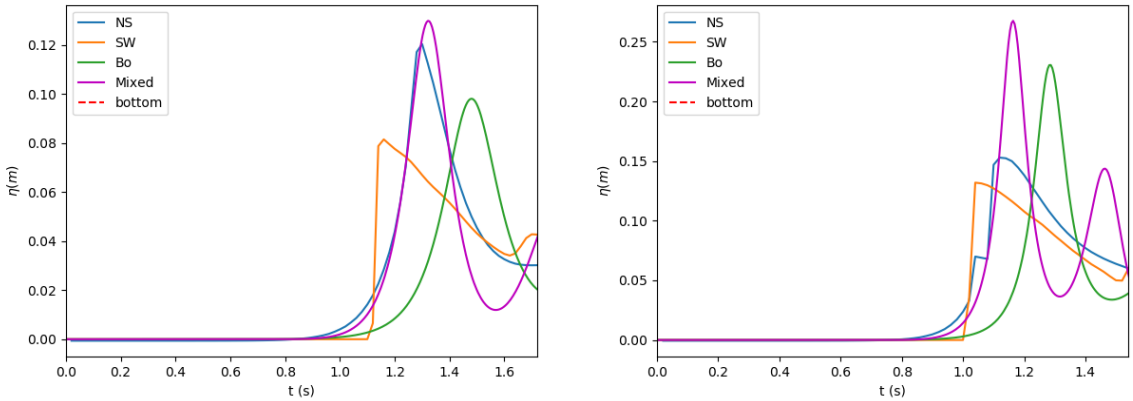

Figure 30: Comparison between the three previous models and the proposed mixed shallow water/Boussinesq model, for cases $(H, L) = (0.3\text{ m}, 0.4\text{ m})$ (left) and $(H, L) = (0.45\text{ m}, 0.4\text{ m})$ (right) at $x = 2.8$ m.

method (Parisot, 2019) we were not able to run the test cases.

We propose here another strategy using a combination of the two previous depth-averaged models. Since the shallow water model gives a better description of the wave generation process, we propose to use it in the beginning of the simulation (generation), before switching to the Boussinesq model in the propagation zone.

The question of the switch time between models remains. The determination of this parameter could be based on the motion of the bottom. However, in this preliminary study we simply adjust it to reproduce as well as possible the reference Navier-Stokes solution. After a visual inspection of the simulations we decided to choose the approximate instant $t_{\text{switch}} \simeq 0.75$ s.

In Figure 30, we add the mixed model, *i.e.* the model where the numerical simulation switches from the shallow water model to the Boussinesq model, to the three models already presented at the probe $x = 2.8$ m (far in the wave propagation zone). Note that the switch time is not adapted to each simulation.

For both cases, the mixed model leads to a very good agreement with the Navier-Stokes solution in term of time arrival of the first wave. However, the amplitude of the wave with the mixed model is significantly higher compared to the Navier-Stokes solution when the transferred energy is large (right-hand graph in Figure 30). As far as we understand, this difference is due to the breaking of the wave in the Navier-Stokes solution, which is not taken into account in the mixed model.

4.2 Which model for given slope and submergence?

4.2.1 Definition of the sensitivity study

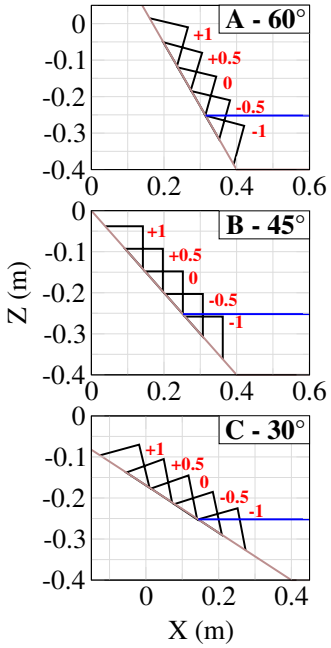

Figure 31: Initial slides positions (in black) for slopes (in brown) of 60° (A), 45° (B) and 30° (C) and different relative submergences (S_{-1}, $S_{-0.5}$, S_0, $S_{+0.5}$ and S_{+1}, in red). The blue line is the initial water surface.

The simulation of the two benchmarks of Chapter 3 and the comparison with the data allowed to select a set of optimal parameters for each code (viscosity, type of equations for the depth-averaged model, slip condition for the Navier-Stokes model). These parameters are now used in a sensitivity study consisting in varying the slope and the submergence considered in the first benchmark (Figure 31), keeping the same shape, volume, gauges locations and water depth (*i.e.*, a triangle, 0.00605*1 m^3, x=0.702, 1.002, 1.302, 1.602 and 0.15 m, respectively).

In the sensitivity study, simulations are performed with slope angles ranging from 20 to 60° with 5° step. Considering the reference point for the submergence as the foot of the landslide, we tested five values of relative submergences S from -1 to +1, a submergence S_{+1} being a raise of one landslide length along the slope (Figure 31). The initial geometry of the subaerial benchmark does not allow to simulate a submergence deeper than -1 without changing the water depth.

We chose to keep the same volume for all the simulations. Therefore, the portion of slide under water is not identical for submerged cases and different slopes. Consequently, comparing a same submergence for different slope angles will be delicate and we can only study the influence of the submergence for a given slope.

The analysis of the results of the sensitivity studies is performed using the following dimensionless variables:

- The dimensionless wave height H/h where H is the wave height and h the water depth (over the flat bottom part).
- The dimensionless velocity V_s/V_0 where V_s is the landslide velocity and $V_0 = \sqrt{2gd_0}$ a characteristic velocity with d_0 the landslide thickness at t=0 s. V_0 approximates the initial fluid velocity appearing in the bottom part of the slide (here considering no energy loss).

The landslide viscosity μ is linked to the Reynolds number through the following relationship:

$$Re_s = \frac{\rho_s V_0 d_0}{\mu} \tag{4.2}$$

where ρ_s is the landslide density.

4.2.2 Results

This section presents a sensitivity analysis aiming at better understanding the influence of the slope angle and the landslide submergence, on the first generated wave height. The main objective is to define the sets of parameters for which both models give similar results and the ones leading to differences. Results are presented in dimensionless variables (see Section 4.2.1 which introduces the landslide Reynolds number Re_s).

The viscosity in each model has been chosen so that the first water wave is similar in both models and close to the two previous experimental data. This is achieved with: a $Re_s \sim 20$ (μ=12.8 Pa.s) (and a 0.4 partialSlip condition for the Navier-Stokes model). We also decided to include a second Reynolds number closer to the one used in our submerged benchmark simulations: $Re_s \sim 250$ (μ=1 Pa.s).

With the depth-averaged model, the following results are obtained (Figure 32):

- For both Reynolds values, the higher the slope angle, the larger the first generated wave, following quasi linear relationships.
- For any slope angles and for both Reynolds, when the landslide starts near or just above the water surface (submergences $S_{-0.5}$ and S_0) the generated wave is larger than with the other submergences tested. Submergences $S_{-0.5}$ and S_0 give very similar results, except from 50° for $Re_s \sim 250$.
- With the large slide Reynolds number Re_s (250), the water waves generated are about two times higher than those obtained with a lower Re_s (Figure 32).

The following main results are obtained with the Navier-Stokes model (Figure 33):

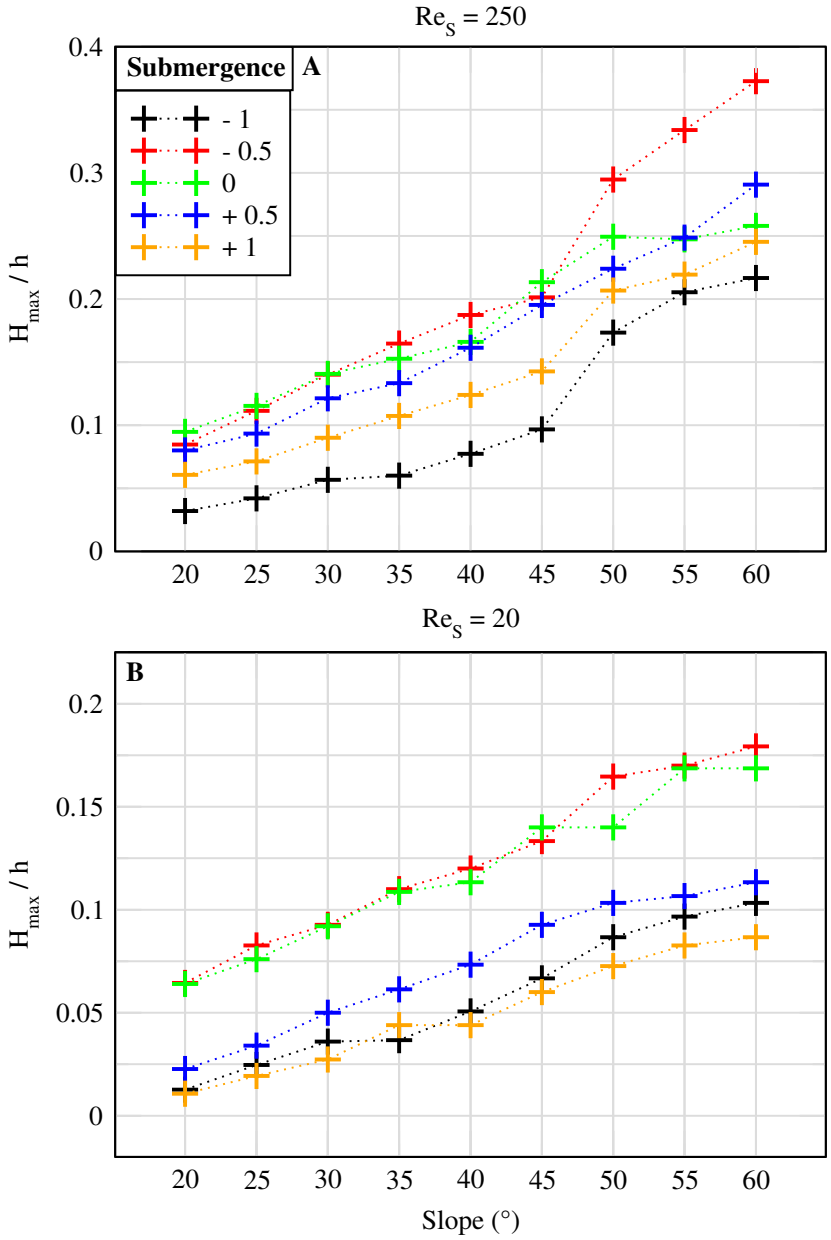

Figure 32: Amplitude of the first wave (m), measured at Gauge 1, as a function of the slope angle (in degree) for the depth-averaged model, five submergences (S_{-1} in black, $S_{-0.5}$ in red, S_0 in green, $S_{+0.5}$ in blue and S_{+1} in orange) and two slide Reynolds numbers Re_s: 250 (A) and 20 (B).

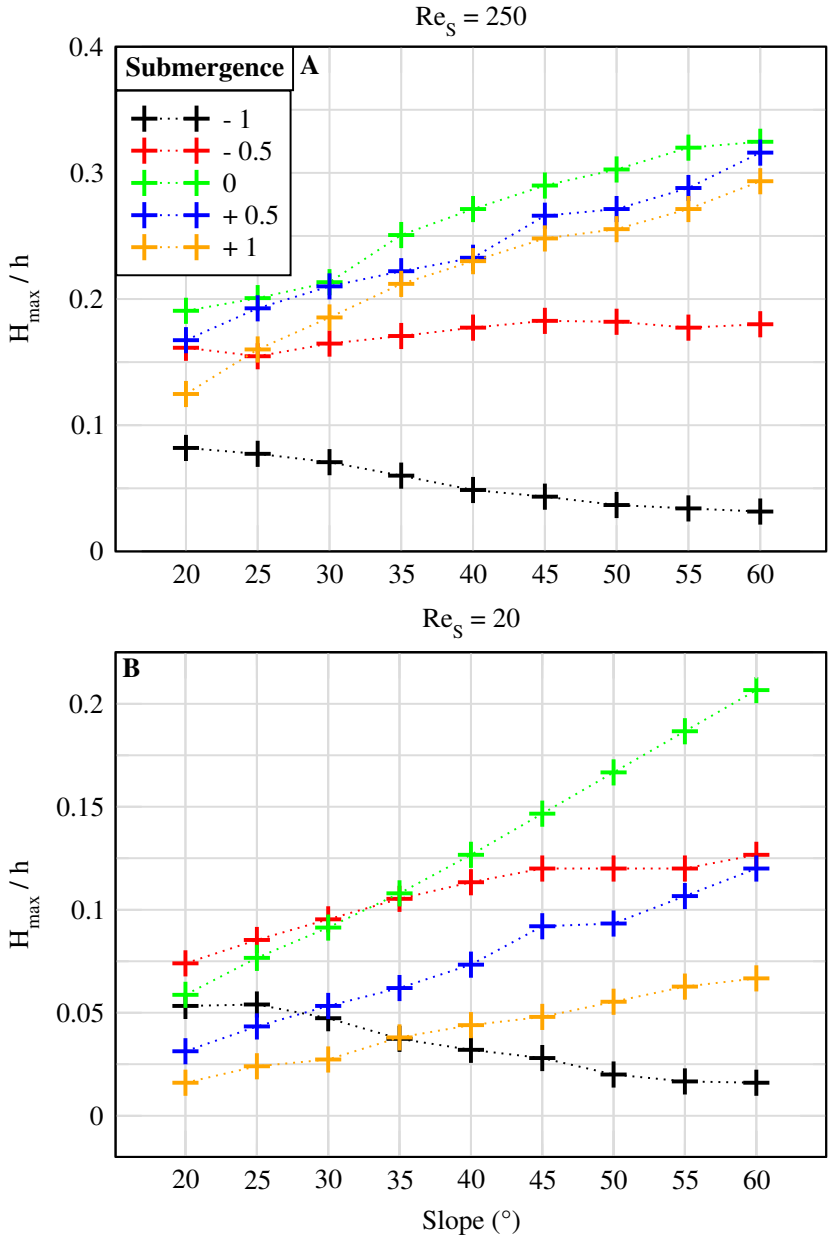

Figure 33: Amplitude of the first wave (m), measured at Gauge 1, as a function of the slope angle (in degree) for the Navier-Stokes model, five submergences (-S_{-1} in black, $S_{-0.5}$ in red, S_0 in green, $S_{+0.5}$ in blue and S_{+1} in orange) and two slide Reynolds numbers Re_s: 250 (A) and 20 (B).

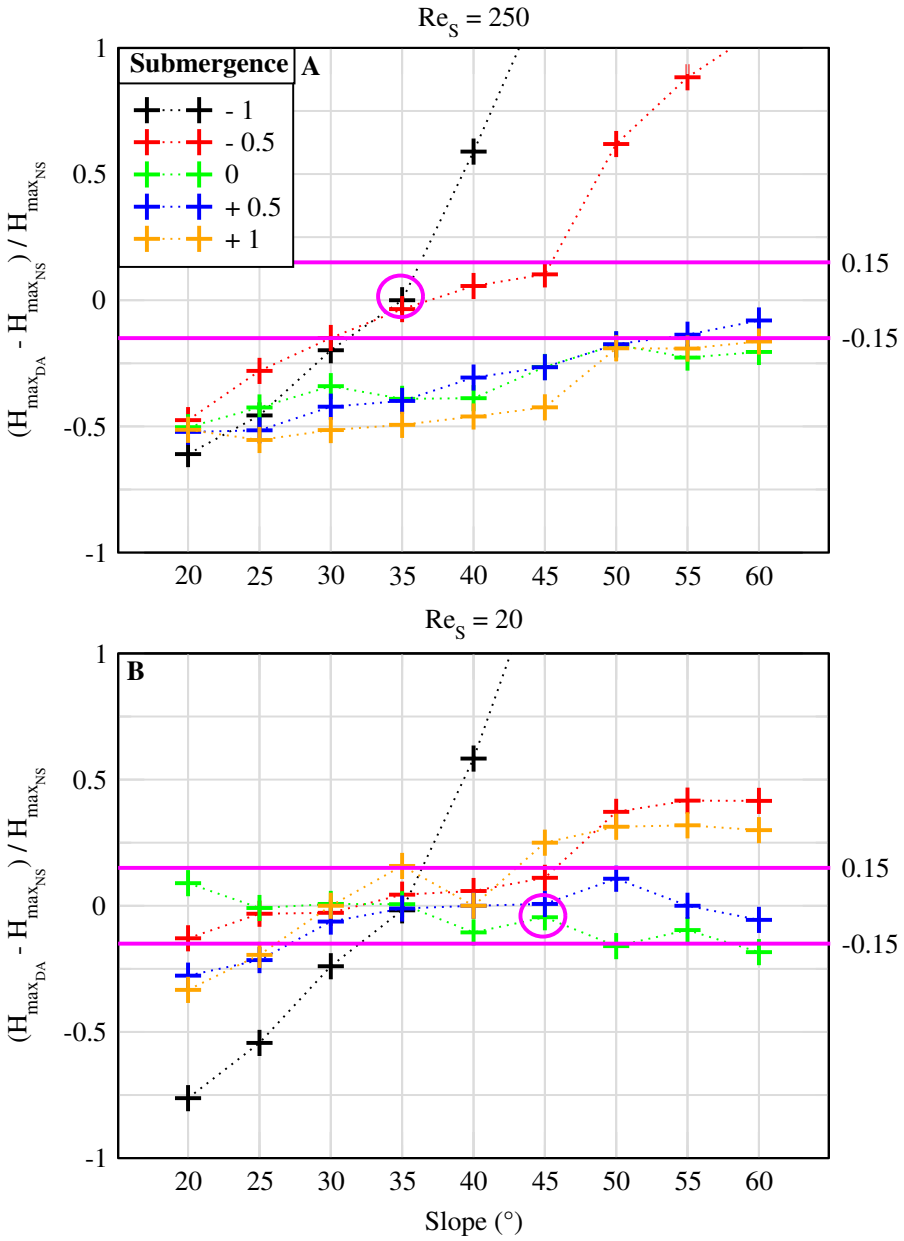

Figure 34: Computed difference for the amplitude of the first wave between the depth-averaged (DA) model and the Navier-Stokes (NS) model (reference) as a function of the slope angle (°) for Reynolds numbers of 250 (μ=1 Pa.s, A) and 20 (μ=12.8 Pa.s, B) and for submergences $S_{-0.5}$ (red), S_0 (green), $S_{+0.5}$ (blue) and S_{+1} (orange). Horizontal pink lines mark an interval of $\pm$ 15% within which results with both models are considered similar. Pink circles correspond to the cases the closest to the benchmarks simulated in Sections 3.3.2 (A) and 3.3.1 (B).

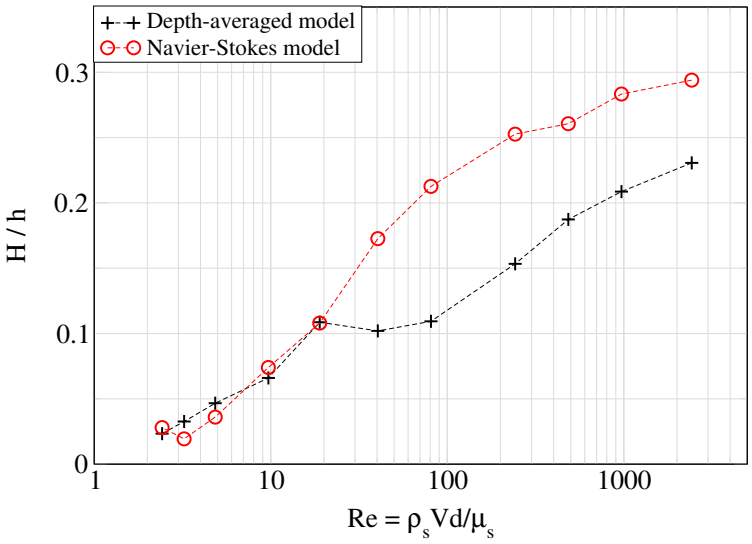

Figure 35: Dimensionless maximal water wave height computed by the depth-averaged model (black) and the Navier-Stokes model (red) as a function of the slide Reynolds number. The submergence is S_0 and the slope 35°.

- As for the depth-averaged model, the wave height increases quasi linearly with the bed slope, except for the submergence S_{-1} for which the relationship is reversed, and the submergence $S_{-0.5}$, for which the maximal wave height reaches an asymptotic value for slopes larger than 45° (Figure 33).

- We see again that with an initial landslide position crossing the water surface or just above, higher generated water waves are generated compared to more distant initial positions.

- Overall, as for the depth-averaged model, the wave height is two times larger with $Re_s \sim 250$ (Figure 32) than with a lower Re_s.

Differences of water heights between the two models are presented in Figure 34. In this figure, the two following statements can be made:

- With the higher Re_s, the models give different results, whatever the slope angles or the submergence. Overall, the wave heights obtained with the depth-averaged model are smaller than those obtained with the Navier-Stokes model, except for negative initial submergences and large slope angles. As expected, results are similar for the combination corresponding to the submerged benchmark (Section 3.3.2) represented by the pink circle in Figure 34(A).

- With the lower Re_s, the agreement is much better except for the negative submergence as previously and large slopes (above 45°) for which the depth-averaged model gives higher waves.

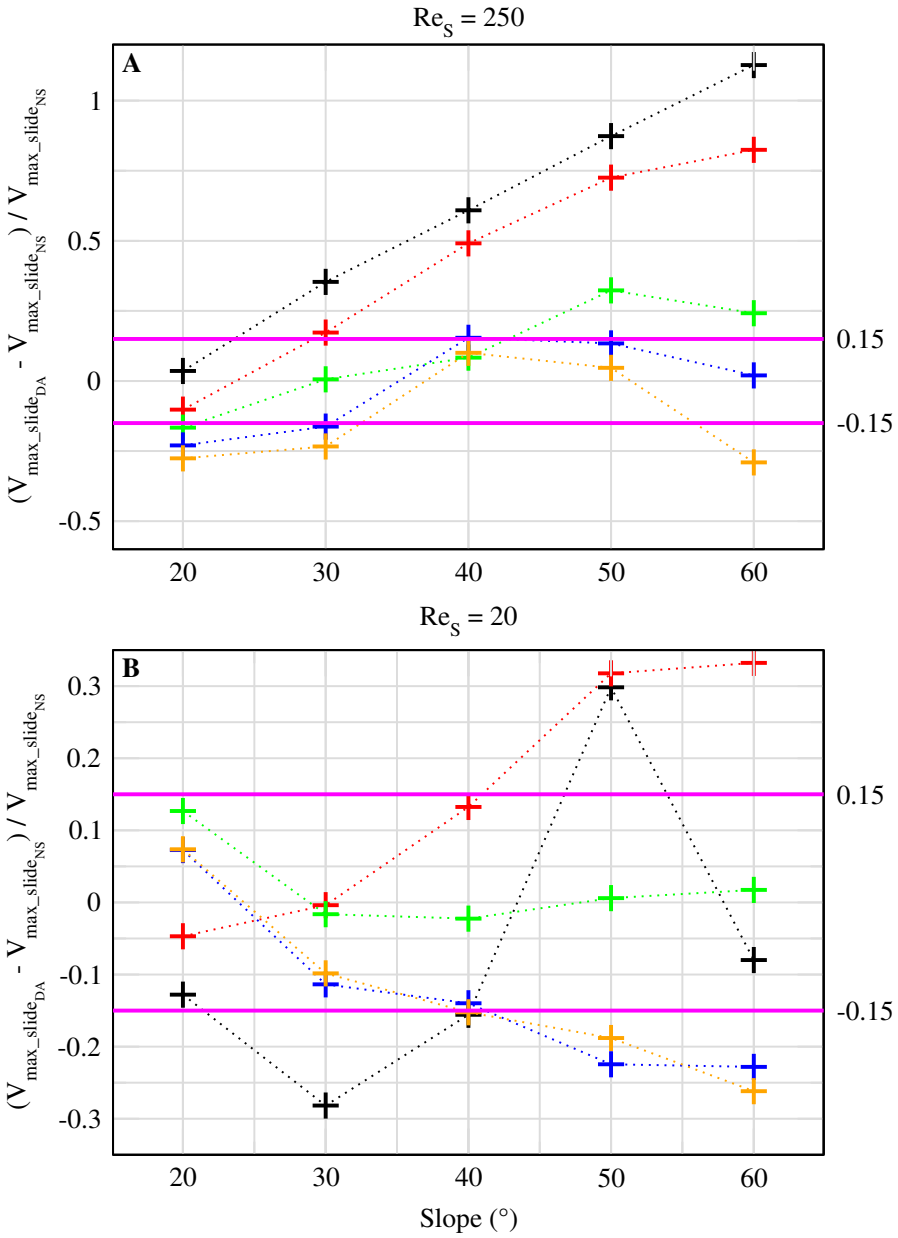

Figure 36: Landslide velocity ($m.s^{-1}$) as a function of the slope angle (in degree) for the depth-averaged model (A) and the Navier-Stokes model (B), five submergences (S_{-1} in black, $S_{-0.5}$ in red, S_0 in green, $S_{+0.5}$ in blue and S_{+1} in orange) and two Reynolds numbers Re_s: 20 (plus) and 250 (circles).

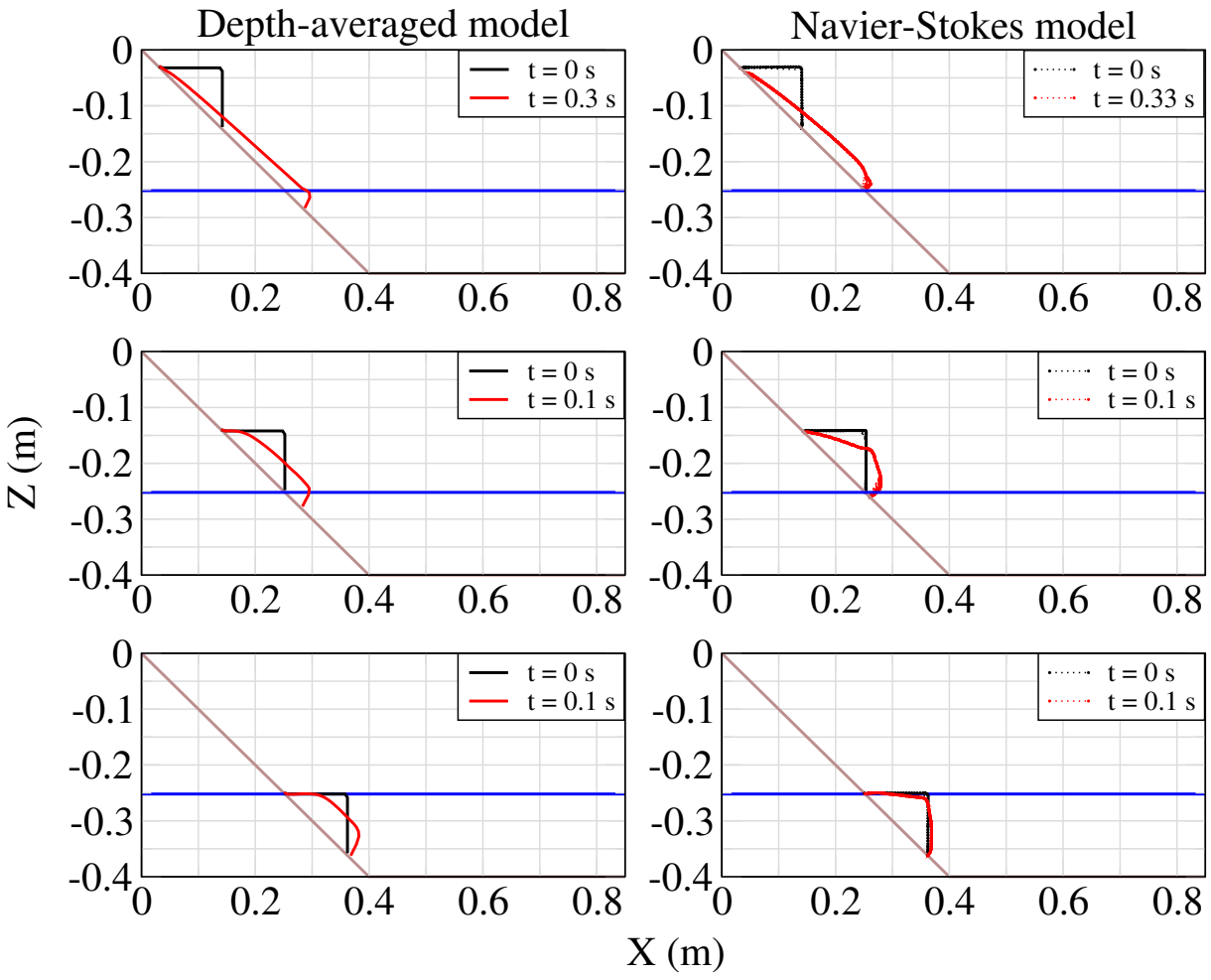

Figure 37: Snapshots of initial (in black) and entering or just entered into the water (in red) landslides for a slope angle of 45° and three submergences, S_{+1} (top panels), S_0 (middle panels) and S_{-1} (bottom panels), for the depth-averaged model (left panels) and the Navier-Stokes model (right panels) and $Re_s \sim 20$. The blue line represents the initial water surface. The brown line represents the slope.

Figure 35 shows the sensitivity of both models to the Reynolds number for a given submergence and slope. Below $Re_s \sim 20$, both models tend to give similar results, whereas above this value, the depth-averaged model produces smaller water waves. Nevertheless, the difference between the two models does not increase with the Reynolds but rather reaches a constant value.

4.2.3 Discussion

Overall results

Energy transfers

For both models, the generated waves are higher if the initial landslide position is close to the surface and this may be explained by the combination of the slide front height and the landslide velocity. As shown in Figure 36, the deeper the landslide, the smaller the velocity, so the largest velocities are always calculated for subaerial cases. However, for both models, the most suberial cases result in thinner landslide fronts at the free surface since these landslides stretch rapidly along the slope (see Figure 37 for an illustration with a slope angle of 45° and three submergences, S_{+1}, S_0 and S_{-1}) and the duration close to the free surface is also shorter. In consequences, the energy transfer is reduced for these landslides.

Slope effect

The landslide velocity in the depth-averaged model increases with the slope angle for both Reynolds, which leads to higher water waves for large slope angles (Figure 36A). The behavior is more complex in the case of the Navier-Stokes model (Figure 36B).

Slide Reynolds

Results in Figure 32 and 33 show that wave heights strongly depend on the Reynolds number. For a given submergence and a given slope angle, wave heights are about two times larger with $Re_s \sim 250$ compared to $Re_s \sim 20$. In the case of the depth-averaged model, landslide velocities are about two times larger for $Re_s \sim 250$ (Figure 36A) which results in larger wave heights. In the case of the Navier-Stokes model, the variation of slide velocities with the slope is more complex (Figure 36B) and the slide shape plays a stronger role in energy transfers.

Models concordance

Importance of the first instants

For a given slope angle, both models produce similar waves with $Re_s \sim 20$ if the landslide initial position is close to the surface or just above (submergences S_0 and $S_{+0.5}$). In these cases, there is no clear difference of landslide behavior in the first instants (see for example the results of the subaerial benchmark in Section 3.3.1), and the energy transfers

should be similar. It is also the case for submergences S_{+1} and $S_{-0.5}$ if the slope angle stays below 45°.

Differences between models

For both Re_s, if the landslide velocities are similar (e.g. subaerial cases for $Re_s \sim 250$ in Figure 36A), the waves are larger with the Navier-Stokes model because the depth-averaged model landslide is thinner inherently. Moreover, for small slope angles, the landslide in the depth-averaged model is more likely to spread on both sides of its initial position.

For cases where landslide velocities are larger with the depth-averaged model (e.g. submerged cases for slope angles above 40-45° in Figure 36), the waves are larger too. In these cases, the landslide in the Navier-Stokes model is slowed down by the bulbous shape of the landslide front.

Finally, for large slope angles, the depth-averaged model produces higher waves for the highest submergence, although the average landslide velocity is lower than the one calculated by the Navier-Stokes model (Figure 36). Further analysis of the Navier-Stokes simulations shows that this averaged velocity is not representative of the velocity of the landslide front. In these cases, the front is slowed down by the bottom friction which results in lower water wave heights.

Study limitations

We did not address the influence of the shape of the initial landslide in this study. The triangular shape of the landslide is favorable to the generation of large water waves. However, the slide in the first instants violates the shallow water hypothesis. Further studies with different shapes (such as a more stretched rectangle or an ellipsoid) would be required to reinforce our conclusions.

As seen previously, the initial landslides for the submergence S_{-1} were not fully submerged for small slope angles. Due to the benchmarks geometry, we could not define deeper submergences but it would be definitely interesting to study.

4.3 On the turbulence modeling

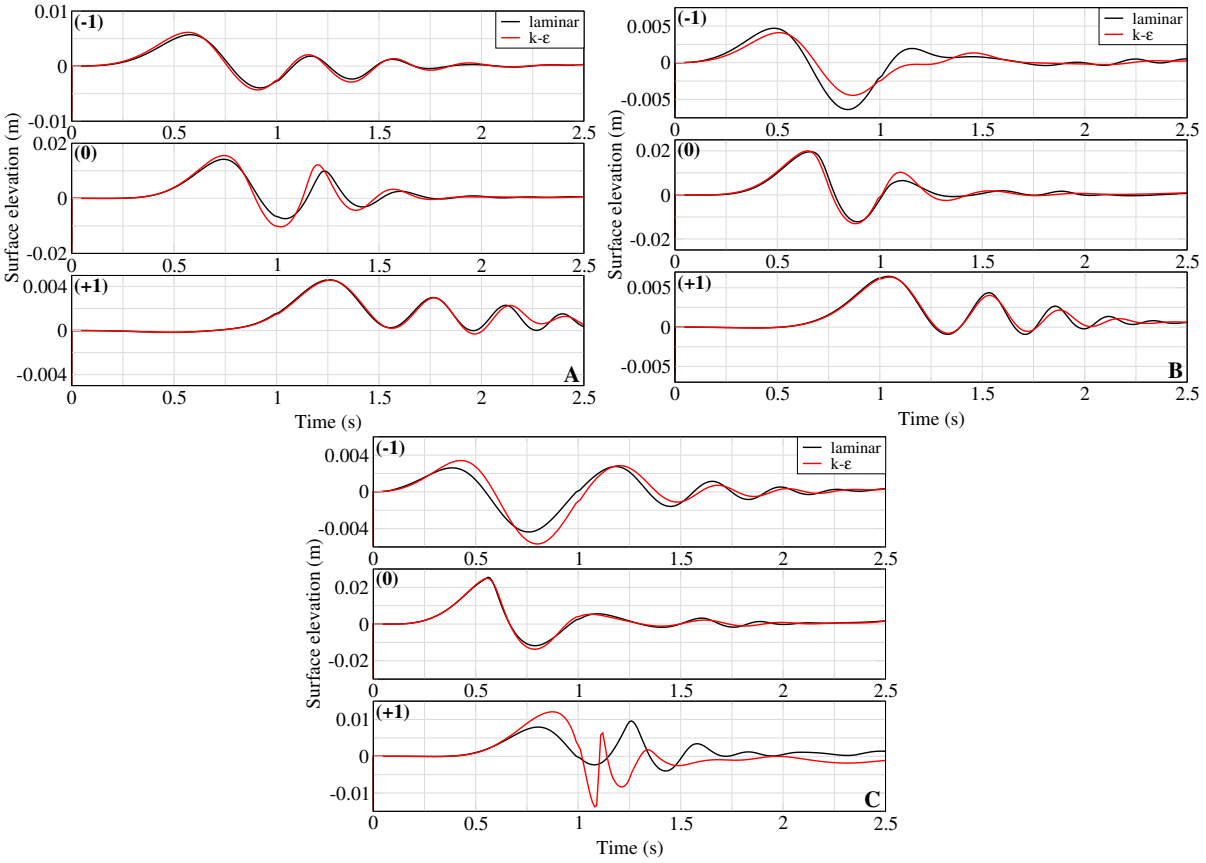

Figure 38: Comparison of surface elevation time series (m) between laminar (black) and $k-\epsilon$ (red) simulations with the Navier-Stokes model using $Re_s \sim 20$ with a noSlip boundary condition for submergences S_{-1} (top panels), S_0 (middle panels) and S_{+1} (bottom panels) and for slope angles of 35° (A), 45° (B) and 60° (C).

In the previous section, we focused mainly on the vertical structure of the flow, questioning the interest and effects of resolving this structure (*i.e.*, in the Navier-Stokes model) in this specific problem. Now, we propose to show the influence of the turbulence modeling basically by turning on and off a $k-\epsilon$ model (same as Rauter et al. (2021)) in the Navier-Stokes simulations. As shown in the previous part, the molecular viscosities required in the slide for the simulations to compare favorably with granular experiments are quite high and the slide Reynols numbers correspondingly low. Therefore, the turbulence should be quite limited in the slide but may play a role in water and at the interface between the slide and water. Nine cases have been simulated with the Navier-Stokes model in both laminar and turbulent modes to investigate the influence of $k-\epsilon$ involving the slope angles of 35, 45 and 60°, three submergences (S_{-1}, S_0 and S_{+1}) with $Re_s \sim 20$ (in laminar cases).

Results of simulated waves in laminar and turbulent modes are shown on Figure 38. Turbulence is shown to play a complex role in some cases enhancing the wave field in others reducing it. A careful investigation of the fields evolution during the simulations

allows interesting observations.

First, the slide dynamics with and without turbulence modeling is very similar. Most of the time, the additional viscosity within the slide due to turbulence induces a very slight delay and momentum decrease when slide is transferring energy to the free surface. In some cases, this difference does not change the wave field. This happens when there is only a delay of the process but not a change in the direction slide is pushing water (Figure 38A for S_{+1}).

In others, the difference in the wave amplitude is very large as in Figure 38C for S_{+1}. In this case, the turbulent slide shows an increase of about 10% of its front thickness due to the slightly different interaction with water at the penetration instant compared to the laminar case. This difference induces a larger horizontal momentum transfer to water and subsequently larger waves.

The contrary can occur as in the submarine case shown in Figure 38B for S_{-1}. In this case, the wave is generated immediately and the initial shape has a critical effect. In this particular situation, the laminar case induces more horizontal momentum transfer that the turbulent case.

We also note that when the slide dynamics and especially the ratio between horizontal and vertical momentum transfer is comparable, even though turbulence is present in water with an additional viscosity of about 100 times the molecular value, this does not change significantly the wave field.

Chapter 5

Intermediate conclusion

This part was devoted to the intercomparison of depth-averaged and Navier-Stokes models.

In Chapter 3, a subaerial and a submerged benchmarks are used to validate viscous depth-averaged and Navier-Stokes models. Both can reproduce waves generated by granular slides by calibrating the viscosity but generally the slide dynamics is not properly calculated, especially for the Navier-Stokes model. Far enough from the generation area, the wave field is less sensitive to the viscosity value. The optimal viscosity range is lower in the depth-averaged model, but there is an overlap between the two models ranges which allows to use the same value with comparable results.

In Chapter 4 Section 4.1, a shallow water and a Boussinesq model were compared to each other with respect to a Navier-Stokes reference solution. In this work, Boussinesq model appears not able to represent the wave generated in the wave generation zone. For large landslides, the shallow water model is efficient in both the generation and the propagation zone. A strategy based on a switch from the shallow water model just after wave generation to the Boussinesq model for the propagation seems relevant to improve the simulations accuracy. In addition, the landslide is better characterized by the energy transferred to water than its volume.

In Chapter 4 Section 4.2, a depth-averaged model is compared to a Navier-Stokes model, using numerical simulations of a triangular landslide collapsing into water. With this triangle initial slide shape, the largest waves are generally generated when the initial slide is close to the free surface. For higher or lower submergences, the waves are smaller. In the depth-averaged model, waves increase continuously with the slope and the slide Reynolds number. The Navier-Stokes model behavior is more complex. The concordance of the two models is strongly dependent on the initial submergence and the slide Reynolds number. When the latter is around 20 (*i.e.* relatively high viscosity influence on the slide dynamics), both models behave similarly in terms of waves generated for initial slides crossing or above the free surface. When the slide Reynolds increases, the difference between the two models is much more pronounced.

All the Navier-Stokes simulations of this part were conducted in laminar mode. A sensitivity study using a $k - \epsilon$ model showed that the role of turbulence is complex sometimes leading to similar waves, sometimes not, depending on the submergence and the slope.

Part III

Comparison of depth-averaged and Navier-Stokes models in real situations studies

Chapter 1

Introduction

The previous part showed that it was possible to model landslide tsunamis with OpenFOAM and that the results obtained could be very different or close to the ones generated by depth-averaged simulations.

These results were obtained at small scale. In the present part, both models are used to simulate two real events which implies a significant change of scale. The objective is to compare the models on a larger scale and to complexify previous OpenFOAM setup, by taking into account complex geometries (*i.e.* of the bathymetry and the landslide).

Chapter 2 presents the numerical modeling of the two chosen events, Karrat Fjord 2017 (Section 2.1) and Anak Krakatau 2018 (Section 2.2), using AVALANCHE and a Coulomb friction law for the landslide.

Chapter 3 presents a general setup to model complex landslide tsunamis with OpenFOAM (Section 3.1), some tests on the mesh (Section 3.2) and an application of the OpenFOAM method to the two previous real events (Sections 3.3 and 3.4).

Chapter 2

Modeling of real events with the depth-averaged model

In this chapter, we simulated two real recent events denoted as Karrat Fjord, Greenland, 2017 and Anak Krakatau, Indonesia, 2018, with the model AVALANCHE. Both studies in this chapter were the subject of two published papers presented hereafter. In Chapter 3, the results obtained in these studies are compared to Navier-Stokes simulations carried out with OpenFOAM.

The first paper (Section 2.1) is dedicated to the simulation of the 2017 Karrat Fjord, Greenland, landslide and tsunami, carried out with AVALANCHE and using a rheology based on a Coulomb friction law with a basal friction coefficient ϕ=50°. The landslide volume is about 50 million m^3 (almost all the volume enters into water). The landslide scarp was well defined and the thickness well reconstructed thanks to satellite images. However, if the damage at Nuugaatsiaq, 30 km away from the landslide, were significant and well documented, no tide gauges recorded the tsunami, which makes the validation of the model difficult. The transformation of seismic records into equivalent water wave elevation time series gives an idea of the water amplitude that stroke Nuugaatsiaq, around 1 m, 30 km away from the landslide. This study was initiated just before the beginning of this thesis, in the frame of the LRC Yves Rocard (Laboratoire de Recherche Conventionné CEA-ENS) and the results were published in Paris et al. (2019).

The second paper (Section 2.2) is devoted to the December 22, 2018, collapse of the Anak Krakatau, Indonesia. This event generated a tsunami that devastated the coasts of the Sunda Strait, between the islands of Java and Sumatra, killing more than 430 people. The collapse was partly subaerial and submarine. If the landslide reconstruction was possible for the aerial part, uncertainties remain concerning the submarine portion that collapsed. Assuming a constant collapse slope of 8°, a volume of 150 million m^3 has been defined. Using a basal friction coefficient ϕ=2°, results of tsunami generation and propagation with AVALANCHE were in general agreement with the numerous data from the field surveys, except in the Panjang Bay, north from the volcano. This event happened at the beginning of this thesis and the study was published in Paris et al. (2020).

2.1 Numerical modeling of the June 17, 2017 landslide and tsunami events in Karrat Fjord, West Greenland

Pure Appl. Geophys.

https://doi.org/10.1007/s00024-019-02123-5

Pure and Applied Geophysics

Numerical Modeling of the June 17, 2017 Landslide and Tsunami Events in Karrat Fjord, West Greenland

Alexandre Paris,[1,3] Emile A. Okal,[2] Cyrielle Guérin,[3] Philippe Heinrich,[3] François Schindelé,[3] and Hélène Hébert[3]

Abstract—On June 17 2017, the western coast of Greenland was the site of a tsunami which flooded several villages, killing 4 people and destroying 11 houses in the village of Nuugaatsiaq. This tsunami was triggered by a subaerial landslide which occurred in a fjord 32 km ENE of Nuugaatsiaq. This paper presents the numerical modeling of this landslide of $\sim$ 50 million m^3 and of the tsunami propagation from its source to Nuugaatsiaq. The landslide is considered as a granular flow under gravity forces and the water waves generated are related to the displacement of the sea bottom. The results obtained are similar in amplitude to our inferences from videos, *i.e.*, three water waves between 1 and 1.5 m arriving at Nuugaatsiaq with a period of roughly 3 min, and are also in general agreement with the amplitude (1 m) resulting from deconvolution of oscillations recorded on a horizontal seismogram operating at Nuugaatsiaq (NUUG). According to the field survey performed by Fritz et al. (EGU General Assembly Conference Abstracts, Vol. 20 of EGU General Assembly Conference Abstracts, p 18345, 2018a) on July 2017, a second mass next to the landslide is threatening Karrat Fjord. A sensitivity study is realized on its volume, with 2, 7, 14 and 38 million m^3 reaching the sea. The shape of the water waves is found to be independent of volume, and linearity is observed between the volume and the water wave heights. Finally, the orientation of the slide does not seem to influence either the period or the shape of the generated water waves.

Key words: Tsunami, landslide, Greenland, simulation.

1. Introduction

Tsunamis generated by landslides, either subaerial or submarine, can be as dangerous for coastal populations as earthquake-generated tsunamis (Thomson et al. 2001; Synolakis et al. 2002). Because landslides are often (but not always) triggered by major earthquakes, and because, especially in the marine environment, they can remain conspicuously hidden to direct observation, it can occasionally be difficult to determine the exact generation process of major tsunamis (Geist 2000; Okal and Synolakis 2001; Synolakis et al. 2002). On the other hand, the different physical nature of the source has allowed the definition of robust discriminants (Okal and Synolakis 2003). A review of problems associated with a simulation of landslide tsunamis can be found for example in Fine et al. (2003).

Subaerial landslides, which initiate above sea level and penetrate the water column, pose additional challenges. Their aerial components lend themselves to direct observation, which can provide important constraints on the initial dynamics of the sliding process. However, their evolution into the water column, and in particular the degree of cohesion of the material, is often poorly documented. The landmark subaerial slide remains to this day the Lituya Bay event of 10 July 1958, which was triggered by a major strike-slip earthquake on the Fairweather fault in the panhandle of Alaska (Miller 1960) and resulted in a record-breaking 525-m run-up on the opposite side of Gilbert Inlet, a geometry repeated on a smaller scale during the 2007 Aysén earthquake in Southern Chile (Sepúlveda and Serey 2009). By contrast, "orphan" subaerial landslides have taken place in the absence of any detectable seismic trigger, a typical example being the 1999 event at Fatu Hiva, Marquesas (Okal et al. 2002; Hébert et al. 2002). The 2015 Taan Fjord landslide at Icy Bay, Alaska featured a geometry of sliding strikingly similar to that of the 1958 Lituya

[1] Laboratoire de Géologie, Ecole Normale Supérieure, CNRS UMR8538, PSL Research University, Paris, France. E-mail: alexandre.antoine.paris@gmail.com

[2] Department of Earth and Planetary Sciences, Northwestern University, Evanston, IL, USA.

[3] CEA, DAM, DIF, 91297 Arpajon Cedex, France.

Published online: 11 February 2019

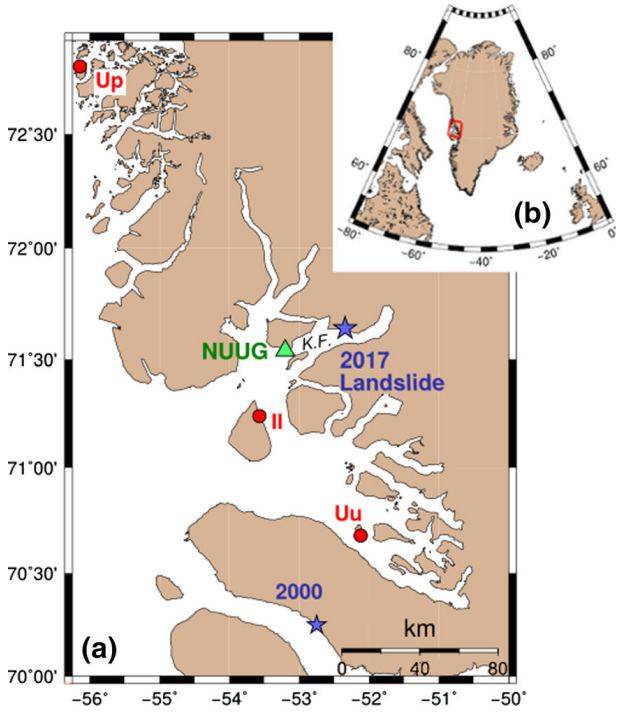

Figure 1
a Close-up Mercator projection of the western coast of Greenland, showing location of the 2017 landslide (star) in Karrat Fjord (K.F.), and of the village of Nuugaatsiaq (triangle). The red dots identify other locations where the tsunami was observed (*Il* Illorsuit, *Up* Upernavik, *Uu* Uummannaq). The location of the 2000 slide is also shown. **b** Map of Greenland showing boundaries of the close-up map (**a**) in thick red

Bay event, albeit on a smaller scale reaching "only" 193 m of run-up, and with no detectable seismic trigger (Higman et al. 2018). Subaerial landslides have been studied in the laboratory and successfully modeled analytically, notably by Fritz (2002), Weiss et al. (2009) and Viroulet et al. (2013).

This paper deals with a subaerial landslide that occurred on June 17, 2017, on the Northern slope of the Karrat Fjord along the western coast of Greenland (see Fig. 1 for context and location). It was followed by a tsunami which was observed in several villages up to a distance of 160 km. In Nuugaatsiaq (pop. ∼ 80), 11 houses were damaged or washed away, 4 persons were reported killed or missing, and 9 injured (Clinton et al. 2017). Several videos,[1] posted on the Internet after the event, document water flooding houses in Nuugaatsiaq. Thanks to the ruler tool and the location of houses at different times before and after the event on GoogleEarth, the maximum inundation length is estimated at 150 m and maximum run-up heights at about 10 m in Nuugaatsiaq.

The 2017 landslide was identified the next day by an aerial survey of the Arktisk Kommando of the Danish Defence,[2] about 32 km ENE of Nuugaatsiaq, upstream Karrat Fjord. The failed mass consists of a portion of bluff about 1000 m wide and 500 m tall (see red ellipse on Fig. 2); its scar is well identified on photographs from the aerial survey, and from before-and-after satellite imagery. We note (see blue ellipse on Fig. 2) that a second mass seems about to fail, immediately to the West of the 2017 slide.

As discussed below, three previous landslide-generated tsunamis had been documented in Greenland in 1954, 2000 and 2012, with the 2000 event similar in nature to the 2017 one, making this kind of event a recurring hazard in the region.

The 2017 landslide in Karrat Fjord was detected as a seismic event worldwide (up to distances of 95°); however, the NEIC of the USGS did not locate the event, but simply used the location reported from satellite imagery (71.640°N; 52.344°W), for which they obtained an origin time of 23:39:12 GMT. The event was given magnitudes M_L = 3.3, m_b = 3.6 and M_s = 4.0 by the International Data Center of the CTBTO, and M_s = 4.2 by the NEIC. The growth of magnitude with period is typical of a non dislocative event, whose source is expected to have a longer duration than a genuine seismic source of comparable size, and as a result to be deficient in high frequencies (Okal 2003).

In addition to teleseismic recordings, the 2017 Karrat Fjord event was observed in Nuugaatsiaq (NUUG) on a 3-component Streckeisen STS-2 seismometer operated by the Danish Geological Survey. As will be detailed in Sect. 3.3, a remarkable aspect of the resulting waveforms is that they include a quantifiable recording of the tsunami, a priceless occurrence in the absence of a tidal gauge station.

[1] To see the videos, click on the links below:
https://www.youtube.com/watch?v=jBmkT5y52ng
https://www.youtube.com/watch?v=LzSUDBbSsPI
https://www.youtube.com/watch?v=amWshLXe74s
https://www.youtube.com/watch?v=tWvYFMo2LsQ.

[2] Photos of the aerial survey are visible here: https://goo.gl/XRJomU.

Figure 2
Aerial photograph of the 2017 slide (red ellipse) and the western potential landslide (blue ellipse)

The purpose of this paper is to provide a numerical modeling of the landslide and of the tsunami, as well as a quantitative interpretation of the seismic record at NUUG. We model both the Karrat slide and its tsunami using the numerical code Avalanche (Heinrich et al. 2001a), developed at the Commissariat à l'énergie atomique et aux énergies alternatives, and widely applied in previous landslide studies, both submarine (Rodriguez et al. 2013; Poupardin et al. 2017) and subaerial (Heinrich et al. 2001b). Assuming the collapse of a 53 million m^3 landslide, we simulate water waves of 1–1.5 m amplitude, at 8 m water depth, reaching the village after 8 min.

In addition, we simulate the potential failure of the "second", precarious mass identified to the West of the 2017 slide (see blue ellipse on Fig. 2), using several volume scenarios, the purpose being to try to identify the potential threat for the village of Nuugaatsiaq.

2. *Previous Similar Events*

Three other tsunamis are documented for Greenland in the NOAA/PMEL database in 1954, 2000 and 2012. However, the 1954 event is a rogue wave whose origin is undetermined (ICAO 1955), and that in 2012 is due to calving of a fjord glacier into the ocean (NOAA 2018). By contrast, the November 21, 2000 tsunami, investigated in detail by Pedersen et al. (2002) and Dahl-Jensen et al. (2004), is directly comparable to the 2017 event. It consisted of a large volume of 90 million m^3 of rock, sliding at Paatut, only 155 km South of Karrat Fjord, between altitudes of 1400 and 1000 m, of which 30 million m^3 sunk into the ocean. The resulting tsunami reached a height of 50 m at the source, and inundated 250 m for a run-up of 28 m at the village of Qullissat which, fortunately, had been abandoned 28 years earlier. Dahl-Jensen et al. (2004) also document another tsunamigenic landslide at Qullissat in 1952, which killed 1 person.

Landslides having generated tsunamis of comparable characteristics have been described worldwide and can be triggered by several mechanisms. Paramount among them are local earthquakes, in a context reminiscent of the record 1958 event at Lituya Bay (Miller 1960): for example, the 2007 landslides in Aysen, Southern Chile (Naranjo et al. 2009), totalling $\sim$ 20 million m^3 in volume, generated a tsunami which ran up $\sim$ 30 m at the source and 14 m on the

opposite side of the fjord, following a strike-slip earthquake of magnitude $m_b = 6.1$, only 30 km away. Volcanic eruptions can result in the build-up of unstable or precarious structures, failing through large scale submarine or aerial landslides, as happened on December 30, 2002, at Stromboli, Italy, with two slides separated by 7 min, one submarine (20 million m^3), the other aerial with a volume of 4–9 million m^3 (Tinti et al. 2006). The aerial one was more similar to the 2017 Karrat case, as it had an altitude of 550 m, and generated waves 12 m high at a village located 2 km away.

In many cases, the triggering mechanism is of such small magnitude as to remain unnoticed. That would be the case, for example, of the 1999 Fatu Hiva landslide in the Marquesas Islands (4 million m^3 of brecciated volcanic material), which flooded the nearby village of Omoa (Hébert et al. 2002; Okal et al. 2002), or of the large, tragic landslides in Norwegian fjords described by Hermanns et al. (2006) at Tafjord (1934) and Loen (1905 and 1936), the latter involving the closed Lovatnet lake. The Tafjord failure (1.5 million m^3) took place $\sim$ 800 m above sea level and produced a tsunami which ran up 62 m and killed 41 people; the 1905 Loen failure was smaller (0.4 million m^3) but its tsunami ran up 41 m, and killed 61 people, while the 1936 slide involved 1 million m^3, a 74-m runup and 73 fatalities. The 2007 landslide into Chehalis Lake, B.C. involved 3 million m^3 of rock and produced a run-up of 38 m on the opposite side of the lake (Wang et al. 2015), fortunately without loss of life. A particularly tragic case of a landslide-generated tsunami in a closed lake occurred in 1963 in the Vajont reservoir in Northern Italy, where a 200-m tall splash overtopped the dam and wiped out the village of Longarone in its lee, killing upwards of 1900 people (Ward and Day 2011). A possible, if not probable, repeat of this situation at Sarez Lake, Tajikistan could reach even more catastrophic dimensions, as it would probably destroy the precarious natural dam holding the lake, itself the result of the blockage of the valley by a much larger, 2.4-km^3 landslide during the earthquake of 18 February 1911 (Schuster and Alford 2004; Ambraseys and Bilham 2012).

With the exception of the latter, the selection of events listed above are generally comparable to the 2017 Karrat Fjord landslide. In the context of global warming, and of the melting of ice caps, it is expected that the weakening of permafrost will lead to an increase in catastrophic landslides in that part of the world (Haeberli and Gruber 2009; Huggel et al. 2012).

3. Observations of the 17 June 2017 Event

3.1. Numerical Reconstruction of the Landslide

In order to perform a numerical modeling of the landslide, two digital surface models (DSM) of the area were compiled before and after the event. The "before" DSM was realized from Spot6 stereoscopic images, acquired on July 22, 2013 at 1.5-m spatial resolution. The "after" DSM was obtained from Pleiades tri-stereoscopic images, acquired right after the event, on July 08, 2017, at 0.7-m spatial resolution, with estimated 1 m in vertical precision (Guérin et al. 2014).

The DSMs are calculated through an automatic pipeline which performs the data co-registration and the DSM generation, as described in Guérin et al. (2014). The data co-registration is realized as a preprocessing step in order to ensure that the image (and hence the DSM) are finely registered between them. This operation consists in a bundle-block adjustment of all the available data which can be performed without any Ground Control Points (GCP), as none are available over the area of interest. The complete methodology is presented in Guérin (2017) and is based on a tie-points detection according to a pairwise image correlation followed by an iterative refinement of the image acquisition models provided as Rational Polynomial Coefficients. Tie-points detection remains a sensitive part of the method, especially when dealing with areas featuring steep slopes. In order to get accurate tie-points, the detection is then performed on the images after their orthorectification with the most accurate digital terrain model (DTM) available (Guérin 2017).

Once the registration is performed, the DSMs are generated at each date according to the methodology described in Guérin et al. (2014) and based on so-called ground space image matching, performed with

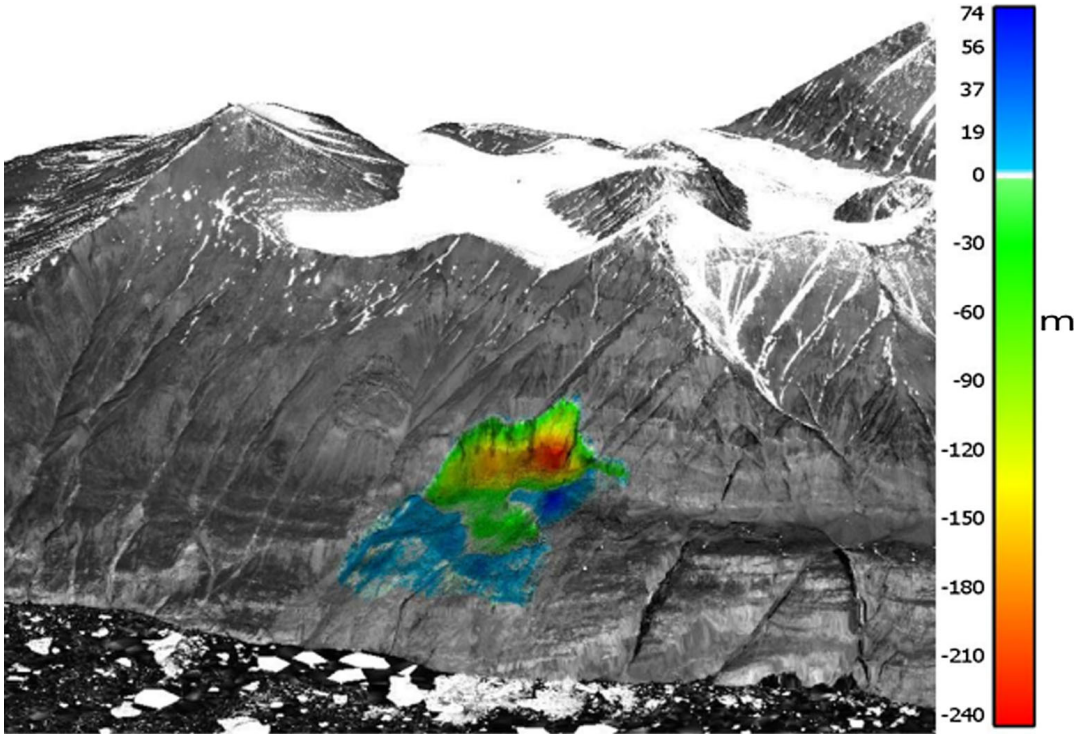

Figure 3
Difference between the "before" and "after" digital surface models (DSM), superimposed on the "after" DSM, computed from the pleiades tri-stereoscopic images from 2017. The variations of the difference elevation values (in m) are represented with the color bar

the open source software MICMAC, developed by the French National Geographic Institute (IGN) (Pierrot-Deseilligny and Paparoditis 2006). This methodology allows the calculation of an elevation value for each point on a grid defined on the ground space with both planimetric and altimetric steps. In practice, for each ground point of the grid, the image coordinates are obtained according to refined acquisition models of the images that link the ground position of the point and its coordinates on the images. A correlation score is then computed between pixel windows selected over each image and at each altitude of the grid. The final altitude value is chosen considering the correlation score and a regularization term (Guérin et al. 2014). Figure 4 represents the DSM obtained from the pleiades tri-stereoscopic images acquired after the event. For this study, both DSM were generated with a 2 m planimetric step and 1 m altimetric step.

Finally, one computes the difference between the DSMs, at the same resolution and hence perfectly comparable. Figure 3 represents the resulting differential DSM over the collapsed area, superimposed on the "after event" DSM. We use it to infer that the collapsed area reached a height of 240 m and a total volume of 48 million m^3. However, part of this volume did not spill into the ocean, as confirmed by the presence of important subaerial debris on the mountain side (Fig. 2); we estimate a volume of 45 million m^3 for the effective spill into the ocean. The inferred width of the slide is 1000 m, and its length 500 m (Fig. 4).

These numbers are in general agreement with Gauthier et al. (2018), who describe the Karrat landslide as a rock avalanche of 58 million m^3, of which only 45 million m^3 reached the water, the slide being initially 950 m wide and 800 m long, at altitudes between 800 and 1200 m. The origin of the 10% discrepancy in volume may be rooted in the decimation of the high-resolution satellite images (sampled at 1.5 and 0.7 m) when building the simulation grid (sampled at 25 m).

In a recent contribution, Chao et al. (2018) have used regional recordings of the Karrat Fjord event across Greenland to invert the source characteristics, using Ekström and Stark's (2013) methodology. They

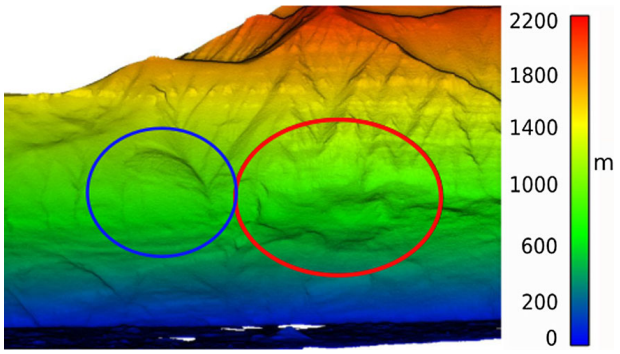

Figure 4
Digital surface model computed from the pleiades tri-stereoscopic images from 2017 with a 2 m planimetric step and a 1 m altimetric step. The color bar corresponds to the elevation values (in m). The red ellipse identifies the collapsed area; the blue ellipse identifies the potential West slide

obtain a significantly larger volume penetrating the sea of about 75 million m^3.

3.2. Damage

The tsunami reached and flooded the two main villages in the area, first Nuugaatsiaq, 32 km WSW of the landslide, and later Illorsuit, an additional 35 km to the SSW. At Nuugaatsiaq, 4 people were killed and 11 houses were completely washed away by the water waves. Figure 5 shows examples of damage by the tsunami at Nuugaatsiaq. Much smaller impact and flood were observed at Illorsuit.

GoogleEarth images taken before and after the event clearly show holes where houses once stood (Fig. 6), which document scouring of their foundations, possibly during an ebbing phase. Several photos and videos taken during the event are available and allow a further evaluation of the damage caused by the tsunami. On some videos,[3] recording starts before any visually detectable wave arrival, which suggests a first wave with either a negative amplitude (leading depression, withdrawal), or a positive one of very small amplitude.

One of the videos[4] shows the water waves stopping before the cemetery at Nuugaatsiaq. As an effect of perspective, the exact line of inundation is difficult to evaluate. According to GoogleEarth, the distance between the coast and the cemetery is about 200 m, so we can conclude that the inundation distance was about 150 m at this location, with an estimated run-up of about 10 m.

3.3. Analysis of the Seismic Signal

Figure 7 shows a record of the event at the seismic station NUUG (71.538°N, 53.200°W), located at Nuugaatsiaq, 32 km from the landslide, and part of the Danish Seismological Network. Note that the horizontal components were, at the time, rotated 79° clockwise from their standard orientation (Clinton, pers. comm., 2018). In addition to classical P and S phases (interpreted here as crustal P_g and S_g), a long-period oscillation with a period of about 3 min is present starting at 23:47 GMT, *i.e.*, 8 min after the body waves. This waveform is much too late to be interpreted as a traditional surface wave from the same source as the body waves (as it would have reached NUUG in at most 15 s); we also note that it is not observed at others stations in Greenland and across Baffin Bay in Canada. Accordingly, we tentatively interpret it as a seismic record of the tsunami.

We note the remarkable similarity between the waveforms obtained at NUUG and those recorded at Panarea Island during the tsunamigenic landslides of 30 December 2002 at Stromboli Volcano, Italy (La Rocca et al. 2004). In particular, a spectrogram analysis of the S11°E seismogram (Fig. 8) shows that the long-period oscillation is peaked between 6 and 8 mHz, within the range of frequencies (6–15 mHz) quoted by La Rocca et al. (2004).

However, we observe on Figs. 7 and 9 that the principal component of ground motion is horizontal and polarized in the direction $N20°W$ which is close to 90° away from the azimuth from NUUG to the source ($\beta = 69°$), as was the case at Panerea. Rather, the observed polarization of the signals at NUUG is essentially across the width of the narrow Karrat channel offshore of Nuugaatsiaq (Fig. 9), and as such reminiscent of the geometry of seiching reported in the Panama Canal by McNamara et al. (2011), where the seismic signals recorded by a local seismometer were polarized perpendicular to the axis of the canal. This observation indicates that part of the wave

[3] This video for example: https://www.youtube.com/watch?v=amWshLXe74s.
[4] Around 0:46 on this video: https://www.youtube.com/watch?v=jBmkT5y52ng.

Figure 5
a, **b** Examples of damage from 2017 at Nuugaatsiaq. **c** Screenshot from a YouTube video (https://www.youtube.com/watch?v=jBmkT5y52ng) showing the tsunami flooding Nuugaatsiaq. The blue house is being washed away. Rocks in the foreground delimit the cemetery of Nuugaatsiaq. The running man (yellow arrow) escaped safely

activity in the channel, as recorded on the NUUG seismometer, may involve seiching of the channel.

In the absence of a tidal gauge at Nuugaatsiaq, we next attempt to quantify the seismic record in order to obtain an estimate of the amplitude of the tsunami in Karrat Fjord. For this purpose, we recall that seismic recording of tsunamis was documented in the far field by Yuan et al. (2005) and Hanson and Bowman (2005) at stations located on islands in the Indian Ocean during the 2004 Sumatra tsunami. Using Ward's (1980) representation of tsunamis as a special branch of the Earth's normal modes, Okal (2007) later showed that such recordings could be successfully interpreted and quantified by assuming that the horizontal seismometer is simply deployed on the ocean floor in the absence of the island, and responds to the combination $u_x^{app\cdot}$ of the horizontal displacement of the solid Earth, of the tilt induced on the ocean floor by the passage of the tsunami wave, and of a change of gravitational potential accompanying the tsunami, as detailed by Gilbert (1980), who had been motivated by the need to apply small corrections (of at most 10%) to the precise quantification of the conventional spheroidal modes of the Earth. By contrast, Okal (2007) showed that these "corrections" could reach several orders of magnitudes in the case of tsunami modes, and defined a "Gilbert Response Function", $GRF(\omega)$, that could be used in the frequency domain to restore the spectral amplitude of the vertical sea-surface motion of the tsunami, $\eta(\omega)$, from that of the apparent ground motion recorded by the instrument, $u_x^{app\cdot}(\omega)$:

$$\eta(\omega) = \frac{u_x^{app\cdot}(\omega)}{GRF(\omega)} \tag{1}$$

with $GRF(\omega)$ readily computed from the various components of the tsunami eigenfunction at the ocean floor:

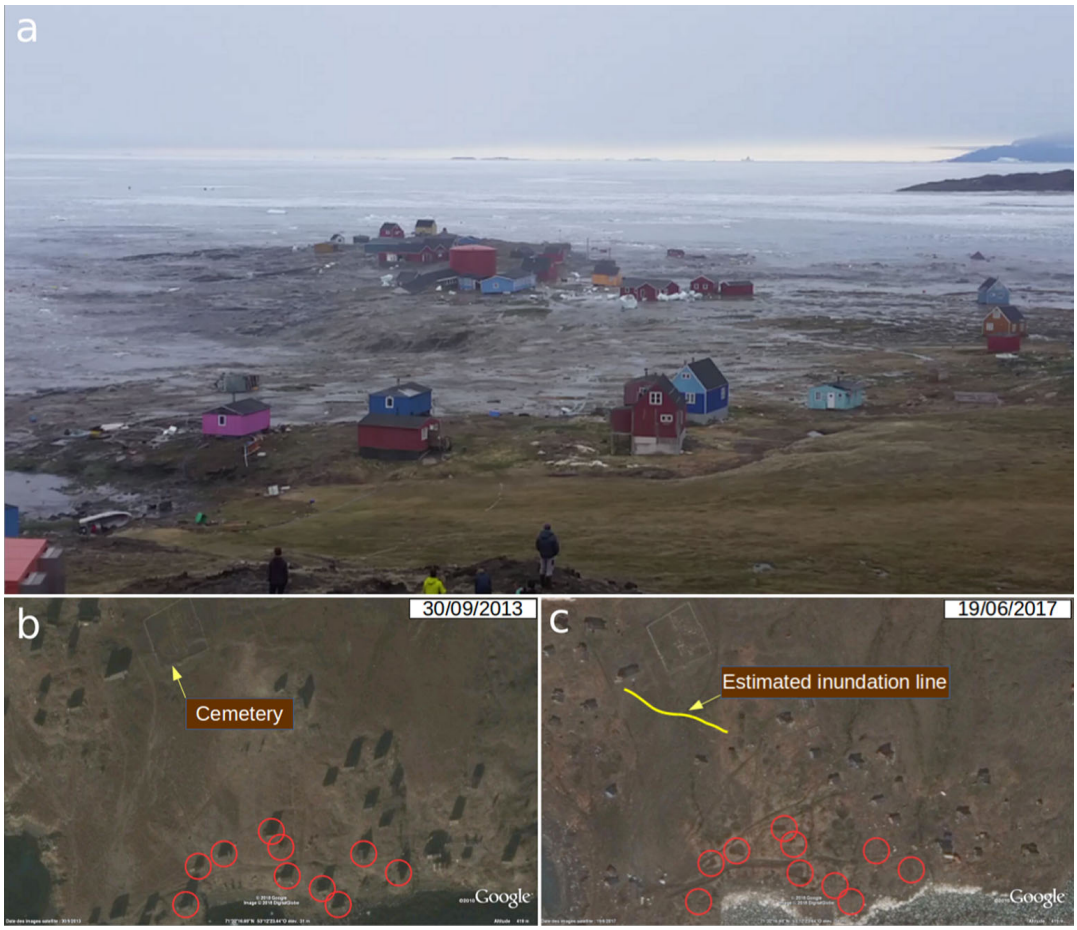

Figure 6
a Looking south, view of Nuugaatsiaq in the aftermath of the tsunami, identifying the inundated zone. Photo from: https://goo.gl/2CYybt. **b**, **c** GoogleEarth images before (30/09/2013) and after (19/06/2017) the event. The yellow line represents the estimated inundation line of the tsunami. Red circles surround the houses washed away by the water waves

$$GRF(\omega) = ly_3 - \frac{l}{r\omega^2}(gy_1 - y_5) \qquad (2)$$

in the notation of Saito (1967) and with all details given in Okal (2007).

Despite the extreme simplifying assumptions of this model (ignoring the island or receiving shore), Okal (2007) showed in particular that a deconvolution of a seismic recording using (1) compared favorably with time series obtained on the high seas by DART buoys, and could actually be used quantitatively to estimate an acceptable value of the seismic moment of the parent earthquake.

In the present case, and notwithstanding the added complexity of the probable seiching in Karrat Channel, we adapt the formalism to the case of propagation in very shallow waters, ranging from a probable 400 m in the fjord to $\sim$ 100 m in the channel facing the village of Nuugaatsiaq. In this context, a remarkable aspect of the function $GRF(\omega)$ is that it is essentially independent of water depth H. This property had been verified numerically in the range $H = 4$–5 km and a simple justification provided, in the Appendix to Okal (2007). On Fig. 10 we extend this investigation by computing systematically values of $GRF(\omega)$ for ocean models with depths varying between 100 m and 4 km; we verify that this function varies only minimally with H, and can be approximated by regressing it logarithmically as

$$\log_{10} GRF(\omega) = -2\log_{10} f - 1.317 \qquad (3)$$

where f is the frequency in mHz and the slope has been forced to the exact value -2, on the basis of the approximation suggested in Equation (A.3) of Okal (2007); we further verify that the constant (-1.317)

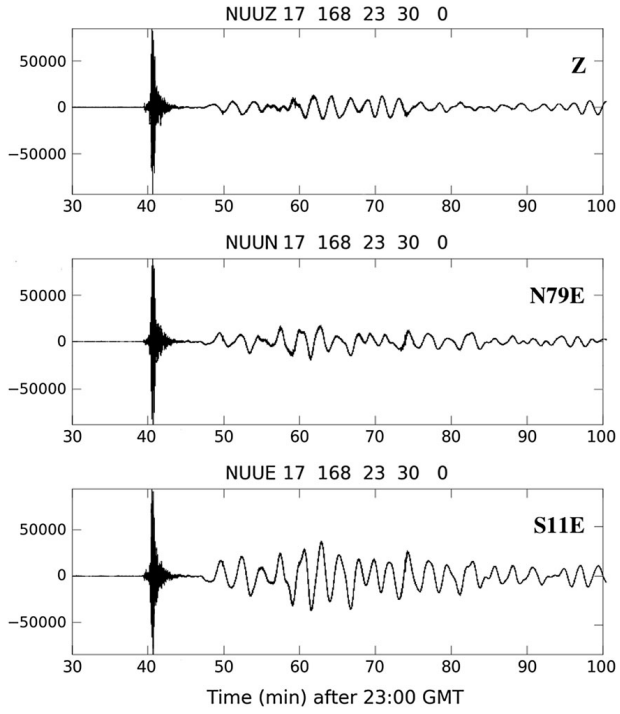

Figure 7
Three-component record of the 2017 Karrat landslide and tsunami at Nuugaatsiaq (NUUG), 32 km away. These are raw seismograms, expressed in digital units, and uncorrected for instrument response (common to the three components). Note that the horizontal components were misoriented, and therefore recorded motion along the N79°E and S11°E directions, respectively (Clinton, pers. comm., 2018). The tsunami is recorded as the long-period oscillation starting at 23:47 GMT; note that it is maximum on the S11°E component

is in excellent agreement with the value predicted by that equation, assuming a rigidity $\mu = 4\times10^{11}$ dyn/cm^2, intermediate between crustal and mantle values.

Equation (3) expresses the response to a tsunami of the ocean-solid Earth system in terms of an apparent horizontal displacement of the ocean floor. It is then possible to combine it with the instrument, in our case the STS-2 operated at NUUG. The latter has a broadband *velocity* response, essentially flat below 100 s, before falling like ω^2 at longer periods. This means that the resulting combination has a *displacement* response peaked around 100 s (10 mHz), and falling like ω and ω^{-1}, respectively on each side; in other words, an STS-2 recording a tsunami acts like a moderate band-pass filter centered around 10 mHz.

In this context, we present on Fig. 11 the result of the deconvolution of the S11°E component of the NUUG record of the Karrat Fjord event. This figure is conceptually similar to Figure 10 of Okal (2007), except for adjusted bandwidth parameters. Frame (a) reproduces the raw seismogram in Fig. 7. Frame (b) shows the result of deconvolving the instrument response in the frequency band 1.7–17 mHz, and thus represents the apparent horizontal motion of the ocean floor, $u_x^{app.}(t)$; note that this particular time series has no direct mechanical interpretation. Finally, Frame (c) is obtained by deconvolving the Gilbert Response Function and is thus representative of the particle motion $\eta(t)$ at the surface of the ocean. We recall that Okal (2007) was able to compare favorably the amplitude of the similarly deconvolved record of the 2004 Sumatra tsunami at Amsterdam Island with that of the direct detection of the tsunami by the JASON altimeter satellite (Scharroo et al. 2005), therefore validating the deconvolution procedure. In the present situation, a major unknown regarding the propagation of the tsunami remains the poorly charted and *a priori* variable depth H of the water column, but as we have seen, the function $GRF(\omega)$ is independent of H, which further justifies our procedure. Finally, we have verified that the spectrogram of the resulting time series $\eta(t)$ does not differ significantly from Fig. 8, with maximum spectral amplitudes in the 6–8 mHz range.

We conclude that the record of the tsunami by seismic station NUUG suggests an offshore zero-to-peak amplitude of $\sim$ 1.9 m. However, we note that this maximum is reached only 15 min after the first arrival (around 00:02 GMT on the 18th), probably under the influence of seiching. During the first 10 min, corresponding to the time window of our simulations, the maximum wave amplitude is only $\sim$1 m.

4. Methods

4.1. Landslide Model

For the purpose of simulating the tsunami generated by the Karrat landslide, we use the parameters determined in Sect. 3.1 as a source condition. Some authors (Løvholt et al. 2008; Abadie et al. 2012) generally use a 3D model for such landslides, with full 3D Navier-Stokes equations applied to

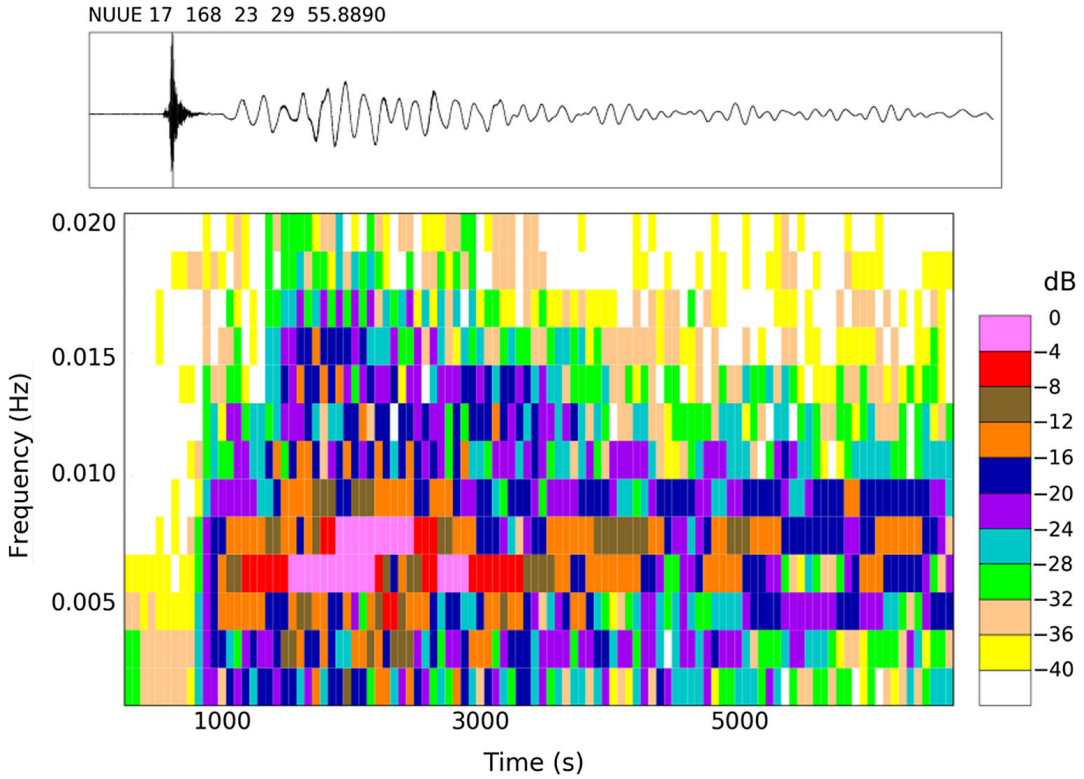

Figure 8
Spectrogram of the raw S11°E seismogram at NUUG. A standard Fourier transform is performed in a 600-s long window moving across the seismogram in increments of 60 s, and the resulting spectral amplitude in each time and frequency pixel is color coded according to the logarithmic scale at right. Note the dominant frequency component between 6 and 8 mHz

multimaterial flow. Here, and following our previous studies, we use a simpler, depth-averaged model to simulate both the landslide and the propagation of water waves (Assier-Rzadkiewicz et al. 2000; Labbé et al. 2012).

Examination of photos of the scar suggests that the landslide can be considered as a homogeneous, incompressible fluid-like flow of granular material following a Coulomb-type friction law. We further assume that the entire mass suddenly fails in one block after losing its equilibrium, and that it has no initial velocity.

For simplicity, basal friction is modeled in this study by a Coulomb-type friction law with a constant friction angle. This hypothesis may show limitations, since the friction angle depends on the velocity, as shown by laboratory experiments on granular flows but it should also be valid in the case of a rough bed with high inclination angles (Pouliquen 1999).

Following the one-phase grain-flow model of Savage and Hutter (1989) and taking into account Coulomb basal friction and gravity, we model the slide by solving the equations of conservation of mass and momentum in a (x', y') coordinate system linked to the topography :

$$\frac{\partial h_s}{\partial t} + \frac{\partial}{\partial x'}(h_s u_s) + \frac{\partial}{\partial x'}(h_s v_s) = 0; \quad (4)$$

$$\frac{\partial}{\partial t}(h_s u_s) + \frac{\partial}{\partial x'}(h_s u_s^2) + \frac{\partial}{\partial y'}(h_s u_s v_s) = -\frac{1}{2}\kappa \frac{\partial}{\partial x'}(g h_s^2 \cos\theta) + \kappa g h_s \sin\theta_{x'} + F_{x'}; \quad (5)$$

$$\frac{\partial}{\partial t}(h_s v_s) + \frac{\partial}{\partial x'}(h_s v_s u_s) + \frac{\partial}{\partial y'}(h_s v_s^2) = -\frac{1}{2}\kappa \frac{\partial}{\partial y'}(g h_s^2 \cos\theta) + \kappa g h_s \sin\theta_{y'} + F_{y'} \quad (6)$$

where h_s is the slide's thickness in a direction perpendicular to the slope, $\mathbf{u} = (u_s, v_s)$ the depth-averaged velocity vector parallel to the bed, $\kappa = 1 - \rho_w/\rho_s$ where ρ_w and ρ_s are the water and rock densities with a ratio $\rho_s/\rho_w = 1.7$ (for the subaerial part of the slide, κ is identically equal to 1), $\theta(x, y)$

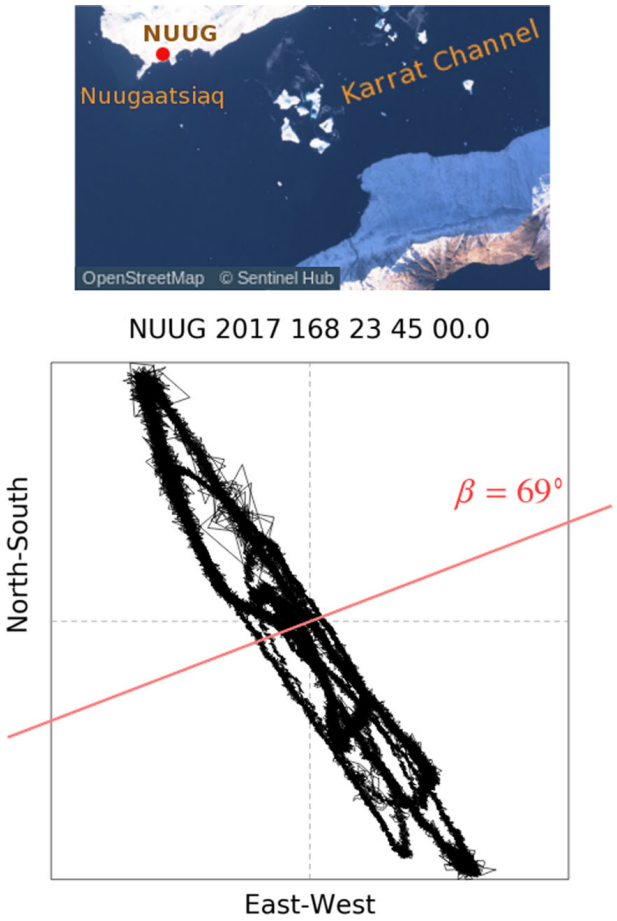

Figure 9
Two-dimensional plot of the horizontal components of the seismogram at NUUG, after counterclockwise rotation of 79° to correct for instrument misorientation (Clinton, pers. comm., 2018). The time window starts at 23:45 GMT and lasts 55 min, thus excluding the seismic waves. Note that the motion is not polarized in the direction of the back-azimuth to the epicenter ($\beta = 69°$), shown as the red line, but rather across the Karrat Channel (Sentinel inset at upper), whose width is $\sim$ 3.5 km in front of Nuugaatsiaq. On the scale of the inset, the red dot corresponds to the location of station NUUG

the local steepest slope angle, $\theta_{x'}$ and $\theta_{y'}$ the slope angles along the x' and y' axes respectively, and $\mathbf{F} = -\kappa g h \cos(\theta) \tan(\phi) \mathbf{u}/\|\mathbf{u}\|$ where ϕ is the friction angle. Curvature terms representing the effects of coordinate transformations (Savage and Hutter 1991) are considered as second-order terms in this paper. A sketch of the situation is visible on Fig. 12.

These equations are solved by the code Avalanche, that simulates both landslides and generated tsunamis. While it has been used mainly with sources fully contained under water, e.g., Papua New Guinea (Heinrich et al. 2001a) and the 1979 landslide at

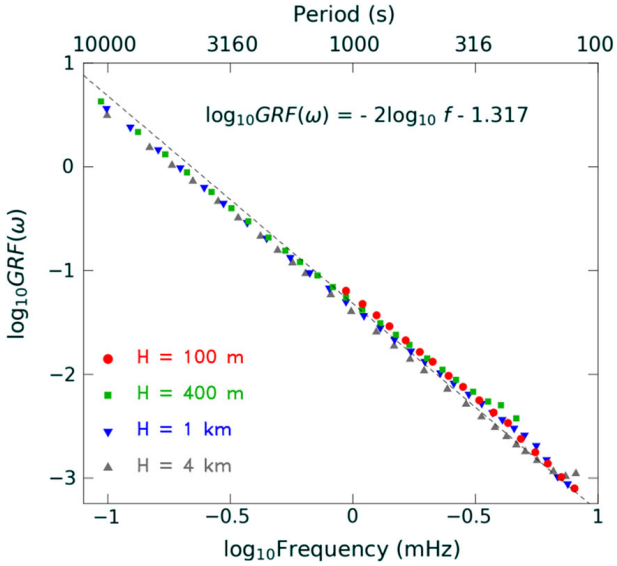

Figure 10
"Gilbert Response Function" $GRF(\omega)$ defined by Okal (2007), computed theoretically as a function of frequency for oceanic models of various depths. This figure is a generalization of Figure 10 of Okal (2007), and uses a logarithmic scale for frequency, to emphasize the power law behavior of $GRF(\omega)$; note that it is essentially independent of the water depth H. The dashed line is the regression (3) used in the deconvolution

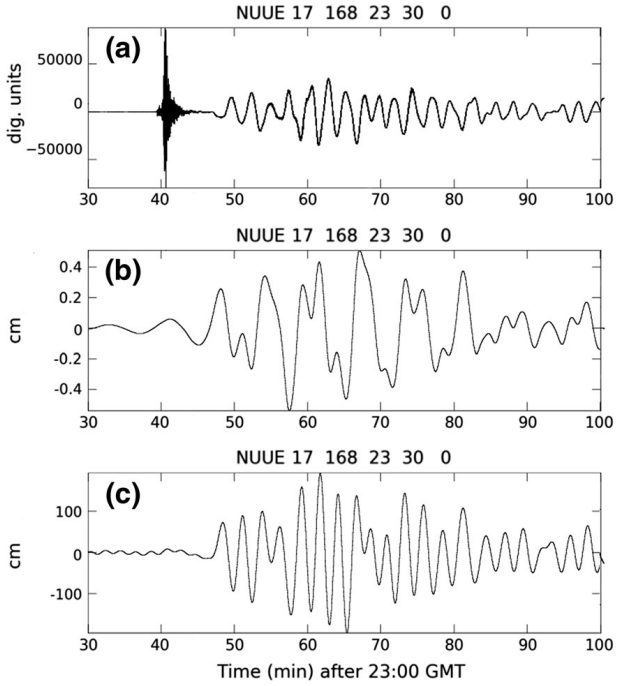

Figure 11
Deconvolution of the sea-surface tsunami amplitude $\eta(t)$ from the seismic record at NUUG. **a** Raw S11°E seismogram (see Fig. 7). **b** Apparent horizontal motion recorded by the instrument, after deconvolution of the instrument response. **c** Reconstructed time series $\eta(t)$ after deconvolution of the Gilbert Response Function

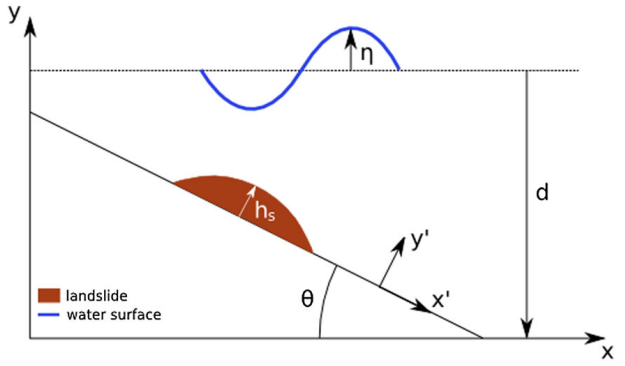

Figure 12
Sketch of our landslide-generated tsunami model. Along the x′ and y′ axes, h_s is the slide's thickness and along the x and y axes, η is the water surface elevation, d the unperturbed depth and θ the steepest slope angle

Mururoa (Poupardin et al. 2017), it was developed with the capacity to handle hybrid sources involving both subaerial debris flow and underwater sliding, as validated by the successful modeling of the 1997 Montserrat tsunami (Heinrich et al. 2001b) and the 2003 Montagne Pelée collapse event (Le Friant et al. 2003), this approach being similar to Weiss et al.'s (2009) simulation of the Lituya Bay event.

The shape of the bathymetry is typical of a fjord, with an abrupt slope (ranging from 40° to 60°) along the coasts. Due to this topography, ϕ is fixed at 50°. While this value may appear high, it results in a physically acceptable speed of the landslide: for a smaller friction angle of 30° we would obtain unrealistic aerial speeds of more than 200 m/s; with $\phi = 50°$, we obtain a maximum aerial speed of 85 m/s, which is still very high: while a maximum speed of 100 m/s has been suggested for aerial landslides (e.g., Satake et al. 2002), this figure was proposed based on the value of 70 m/s, documented by filming the avalanche during the 1980 eruption of Mount Saint Helens (Voight 1981), which involved a powerful atmospheric explosion as the triggering mechanism. In the present case, we obtain a runout length of $\sim$ 5000 m and a vertical fall height of $\sim$ 1900 m.

4.2. Tsunami Model

Our strategy for the tsunami propagation is to start with the Saint–Venant equations during 80 s to simulate the tsunami generation in shallow water, then to continue with the Boussinesq model in order to take into account any possible dispersive effects. We use the code Avalanche to solve the Saint–Venant equations, which are Navier–Stokes equations integrated over depth:

$$\frac{\partial \eta}{\partial t} + \frac{\partial (hu)}{\partial x} + \frac{\partial (hv)}{\partial y} = -\frac{\partial d}{\partial t}; \tag{7}$$

$$\frac{\partial u}{\partial t} + u\frac{\partial u}{\partial x} + v\frac{\partial u}{\partial y} = -g\frac{\partial \eta}{\partial x} + F_x; \tag{8}$$

$$\frac{\partial v}{\partial t} + u\frac{\partial v}{\partial x} + v\frac{\partial v}{\partial y} = -g\frac{\partial \eta}{\partial y} + F_y \tag{9}$$

where η is the surface elevation, $h = \eta + d$ the water column height where d is the unperturbed depth, u and v the depth-averaged velocities along the x and y axes and F_x and F_y the friction and Coriolis forces along the x and y axes, which remain negligible on the scale of the present experiment.

The sea-bottom deformation $\partial d/\partial t$ in Eq. (7) is computed as a forcing term:

$$\frac{\partial d}{\partial t} = \frac{1}{\cos\theta}\frac{\partial h_s}{\partial t} \tag{10}$$

Avalanche can also use a Boussinesq model, following Løvholt et al. (2008):

$$\frac{\partial \eta}{\partial t} + \frac{\partial (hu)}{\partial x} + \frac{\partial (hv)}{\partial y} = -\frac{\partial d}{\partial t}; \tag{11}$$

$$\begin{aligned}\frac{\partial u}{\partial t} + u\frac{\partial u}{\partial x} + v\frac{\partial u}{\partial y} &= -g\frac{\partial \eta}{\partial x} + \frac{d^3}{3}\left[\frac{\partial^2 u_t}{\partial x^2} + \frac{\partial^2 v_t}{\partial x \partial y}\right] \\ &+ \frac{d}{2}\left[u_t\frac{\partial^2 d}{\partial x^2} + u_t\frac{\partial^2 d}{\partial x \partial y}\right] + d\frac{\partial d}{\partial x}\frac{\partial u_t}{\partial x} \\ &+ \frac{d}{2}\left[\frac{\partial d}{\partial x}\frac{\partial v_t}{\partial y} + \frac{\partial d}{\partial y}\frac{\partial v_t}{\partial x}\right] + F_x;\end{aligned} \tag{12}$$

$$\begin{aligned}\frac{\partial v}{\partial t} + u\frac{\partial v}{\partial x} + v\frac{\partial v}{\partial y} &= -g\frac{\partial \eta}{\partial y} + \frac{d^3}{3}\left[\frac{\partial^2 v_t}{\partial y^2} + \frac{\partial^2 u_t}{\partial x \partial y}\right] \\ &+ \frac{d}{2}\left[v_t\frac{\partial^2 d}{\partial y^2} + v_t\frac{\partial^2 d}{\partial x \partial y}\right] + d\frac{\partial d}{\partial y}\frac{\partial v_t}{\partial y} \\ &+ \frac{d}{2}\left[\frac{\partial d}{\partial x}\frac{\partial u_t}{\partial y} + \frac{\partial d}{\partial y}\frac{\partial u_t}{\partial x}\right] + F_y\end{aligned} \tag{13}$$

where u_t and v_t the time-derivatives of u and v.

Both the landslide and Saint–Venant equations, which are very similar, are solved by Godunov's finite-volume scheme, extended to second order by a Van Leer scheme (Heinrich and Piatanesi 2000; Labbé et al. 2012).

The lone bathymetric dataset available in the region, the International Bathymetric Chart of the Artic Ocean (IBCAO) (Jakobsson et al. 2012), only features a 500-m resolution; we had to interpolate it to a sampling of 25 m, in order to project the slide over more than a single pixel. After cropping, we obtain a bathymetric map of a 25 $\times$ 60 km^2 area, covering the slide's location and the village of Nuugaatsiaq located 32 km SSW from the source.

However, we found that the maximum depth proposed in Karrat Fjord (430 m) is clearly too shallow, as it results in propagation times to Nuugaatsiaq of 14 min, incompatible with the difference in time of only 8 min documented on the seismic record at NUUG between the seismic and tsunami waves. For this reason, we later increased all depths in the fjord by an admittedly arbitrary factor of 2.

5. *Results and Discussion*

5.1. *Results for the 2017 Event*

The results are analyzed at a number of virtual gauges (Fig. 13) located in front of the landslide (Gauge 1), then along the path of the tsunami (Gauges 2 and 3), and finally in front of the village of Nuugaatsiaq (Gauge 4).

Our first simulations, using the bathymetry of Model IBCAO (Jakobsson et al. 2012) with a maximum depth of 430 m in Karrat Fjord, predict a travel time of $\sim$ 12 min to Nuugaatsiaq, about 4 min longer than observed on the seismic recording at NUUG (Fig. 14). We first note that the misfit in travel is much longer than the initial duration of the wave at Gauge 1 (Fig. 15); thus it cannot be a source effect, and is clearly due to propagation, from Gauge 1 to Gauge 4. In addition, Chao et al. (2018) have similarly noticed that the tsunami is observed on the NUUG seismometers about 5 min earlier than simulated using GEBCO bathymetry. They explain this discrepancy by interpreting the seismic signal as generated by the impact of the tsunami on a coastline located about 15 km upstream Karrat Fjord. Based on our observation that onland seismic recordings of tsunami falter at distances of a fraction of wavelength (Okal 2007), and on the horizontal polarization of the recordings (Fig. 9), we prefer to invoke an inaccurate bathymetry in Karrat Fjord.

In this context, we decided to increase the water depth by a factor of two across the board, with a new maximum value of 860 m. Under the Saint–Venant approximation, this admittedly arbitrary correction increases the tsunami velocity (and reduces the travel

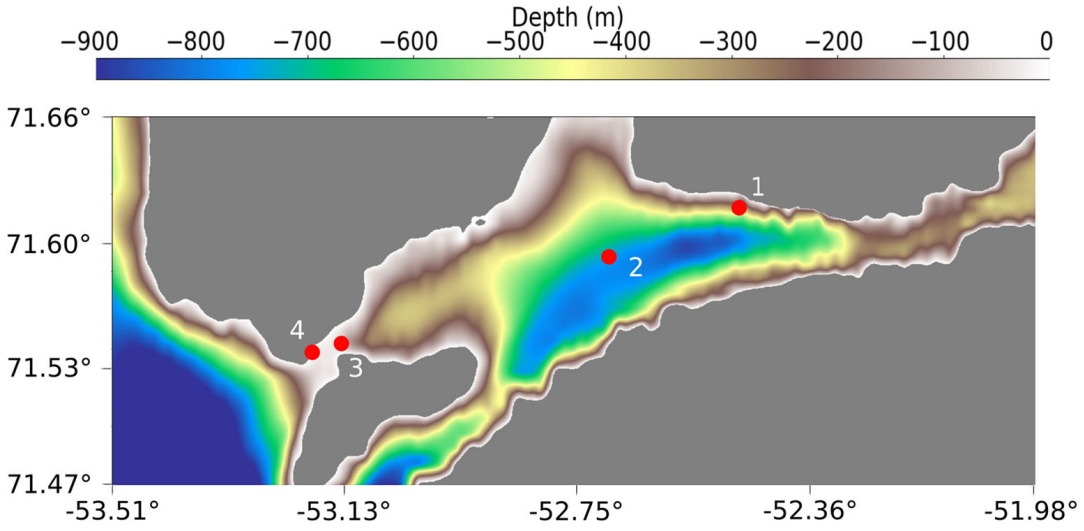

Figure 13
Bathymetric grid in Karrat Fjord and gauge locations (red dots) along the path of the tsunami. The tsunami is initialized at Gauge 1, and progresses to Gauges 2, 3 and finally 4 in front of Nuugaatsiaq

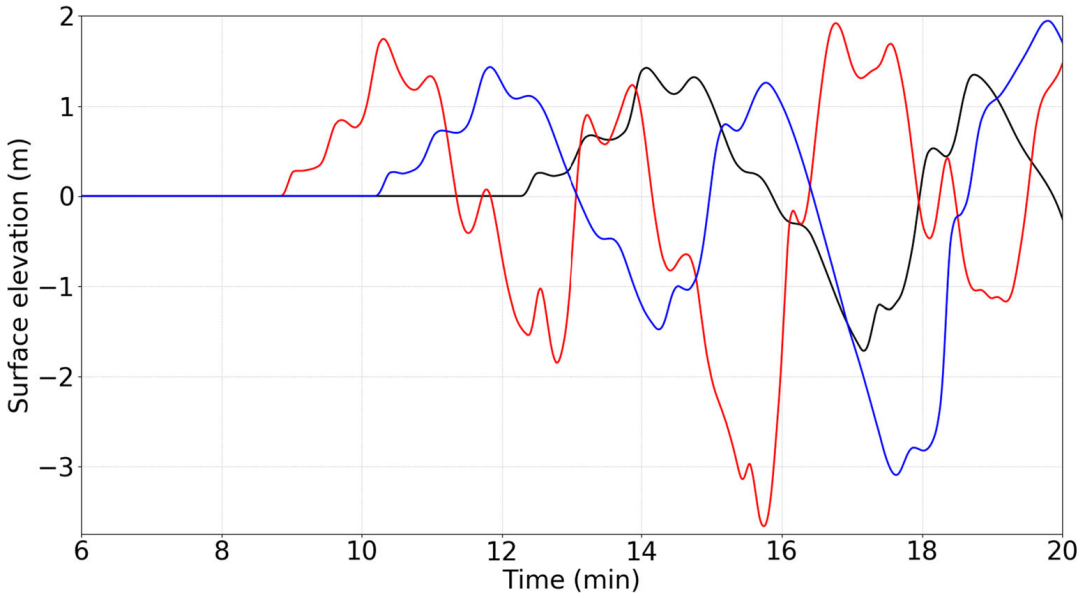

Figure 14
Surface elevation at Gauge 4 (in front of Nuugaatsiaq) for the initial bathymetry (black), increased by a factor 1.5 (blue) and by a factor 2 (red), simulated by the Saint–Venant model

time) by a factor of $\sqrt{2}$ (Fig. 14); in the Boussinesq model used herein, where the relationship between velocity and square root of depth is not linear, the effect is only slightly smaller, and in both models the leading wave now reaches the village in $\sim$ 8 min, in much better agreement with the observed arrival time.

While our correction of the fjord bathymetry may appear drastic, we stress that a similar situation was documented recently in Palu Bay, Sulawesi; following the earthquake and tsunami of 28 September 2018, it became clear that the bathymetry available from global models such as IBCAO or GEBCO grossly underestimated (by a factor as large as 4) the

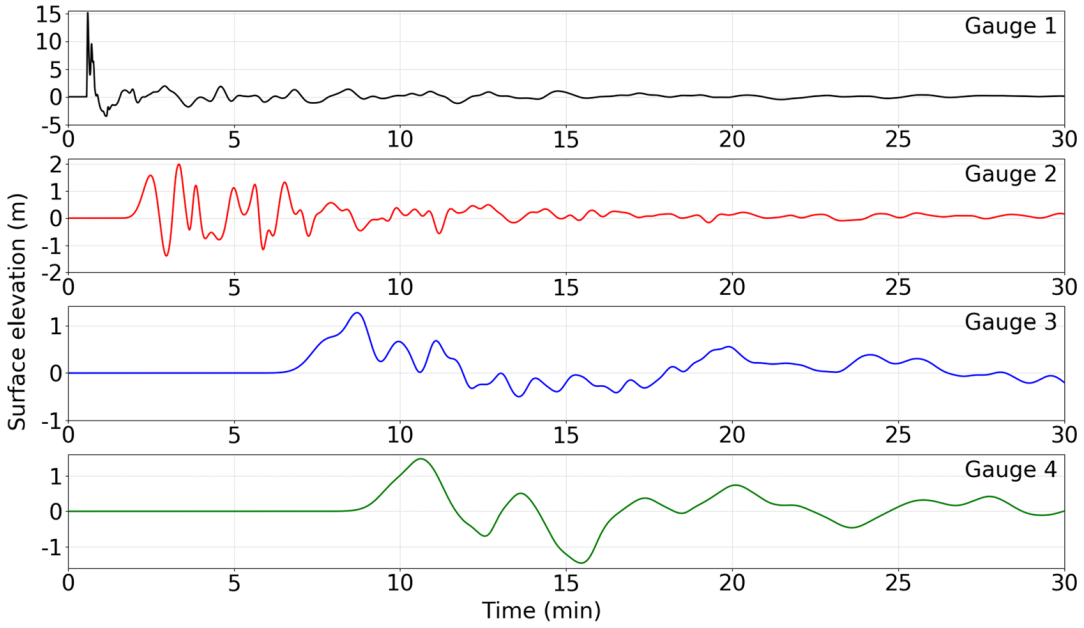

Figure 15
Surface elevations for Gauges 1, 2, 3 and 4, obtained with the Boussinesq model

water depth in the bay (Fritz et al. 2018b). We must conclude that such models cannot pretend to give a reliable small-scale bathymetry, especially in profoundly indented bays such as Karrat Fjord, where the proposed bathymetry is most likely inaccurate.

Under our model of deepened bathymetry, and as shown on Fig. 15, water waves reach 15.5 m at the source (Gauge 1), 2 m at the maximum depth (Gauge 2), 1.3 m before Nuugaatsiaq (Gauge 3) and 1.5 m in front of Nuugaatsiaq (Gauge 4). These figures are not directly comparable to the results of Fritz et al.'s (2018a) field survey, who reported run-up reaching 90 m in the source area, and 50 m on the opposite side of the 6-km wide fjord. We stress that our simulations do not include run-up computations, and that our virtual gauges are located in deep water (340 and 750 m, respectively for Gauges 1 and 2).

We obtain a wave-train at Gauge 4 (in front of Nuugaatsiaq) similar to the signal recorded at the seismic station (Fig. 16), featuring three waves with a period of $\sim$ 3 min (see Gauge 4 on Fig. 15).

Finally, we note on Fig. 16 that while the amplitude of the simulated wave is on the same order (1.5 m) as that deconvolved in a comparable time window from the S11°E component of the NUUG seismometer (1.0 m), the simulated wave features significantly lower frequencies (4.6–5.4 mHz vs. 6.2 mHz), presumably as a result of seiching in the channel, which may also explain the longer duration (and later higher amplitudes) of the deconvolved time series. Nevertheless, the acceptable agreement between them serves as an *a posteriori* validation of the deconvolution procedure in Sect. 3.3.

Although we used the Boussinesq model to simulate the tsunami, results show (Fig. 17) that three water waves are still observed within the first 12 min when using the Saint–Venant equations. This suggests that the generation of these three water waves depends on the bathymetry's shape and is not a result of dispersive effects, but more probably of reflection on the coasts.

This is further confirmed through the use of Glimsdal et al.'s (2013) dimensionless parameter $\tau = 6ht/gT^3$, where h is water depth, t travel time and T dominant period. In the present case, the packet of three waves corresponds to $\tau \approx 0.03$, which is clearly

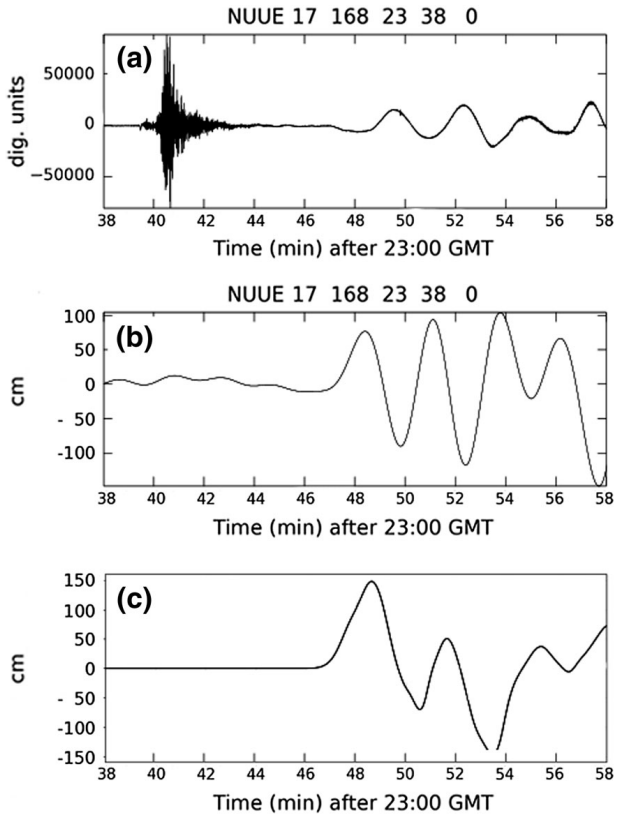

Figure 16
Comparison of recorded and simulated tsunami waveshapes. **a**, **b** Respectively the raw seismogram and the deconvolved tsunami amplitude η for a time window starting at 23:38 GMT (72 s before the initiation of the slide), and lasting 20 min; they are close-ups of Frames (**a**, **c**) of Fig. 11. **c** Simulated tsunami wave at Gauge 4 (in front of Nuugaatsiaq); this is simply a 20-min window of frame **b** of Fig. 15. Note the good agreement of amplitudes between (**b**) and (**c**), but the lower-frequency character of the simulated wave

below the value of 0.5 given by the authors as a threshold for significant dispersion effects (following Shuto 1991).

On Fig. 20, maximum elevations through the entire simulation show that the water level reaches up to 40 m at the source, and we then observe a decrease of the water heights due to propagation in deeper water. Finally the water waves reach between 1 and 1.5 m at Nuugaatsiaq.

While we eventually obtained a good agreement between our simulations and the seismic recording at NUUG, we note that we had to significantly increase (by a factor of 2) the field of depths available from published bathymetric charts, confirming if need be, the critical role of an accurate bathymetry in allowing realistic simulations of the propagation of tsunamis in

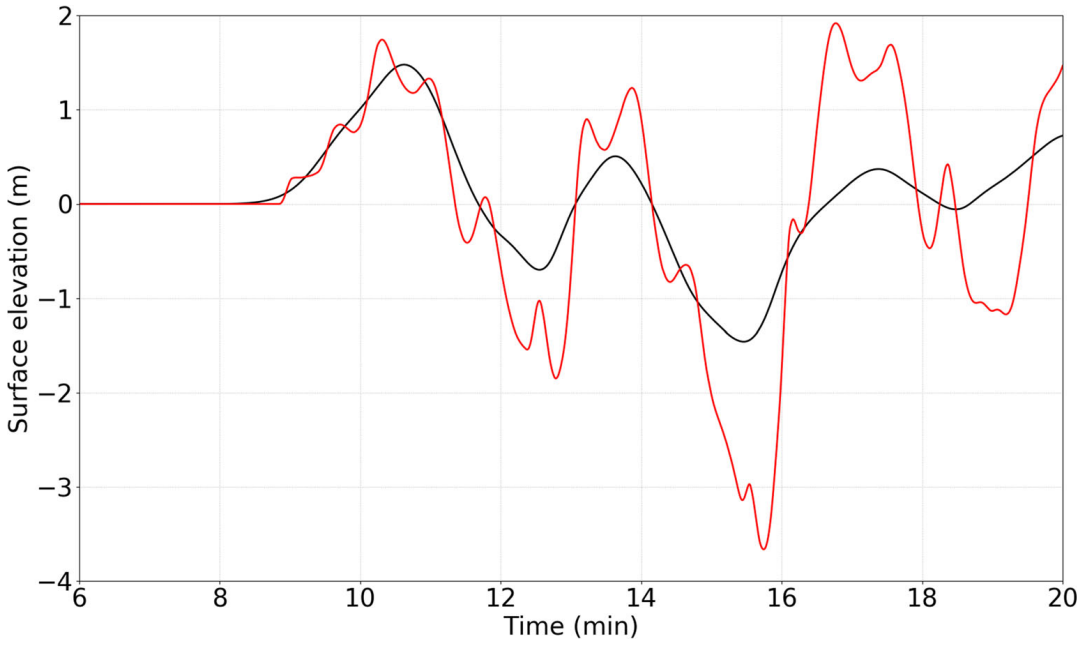

Figure 17
Surface elevation at Gauge 4 simulated by the Boussinesq model (black curve) and the Saint–Venant model (red curve)

complex, poorly chartered marine environments. For the sake of simplicity, we used an across-the-board, constant, and indeed arbitrary, factor of 2 which provided an adequate gain of about 4 min in travel-time. In particular, we did not try more sophisticated, laterally variable, corrections to the available

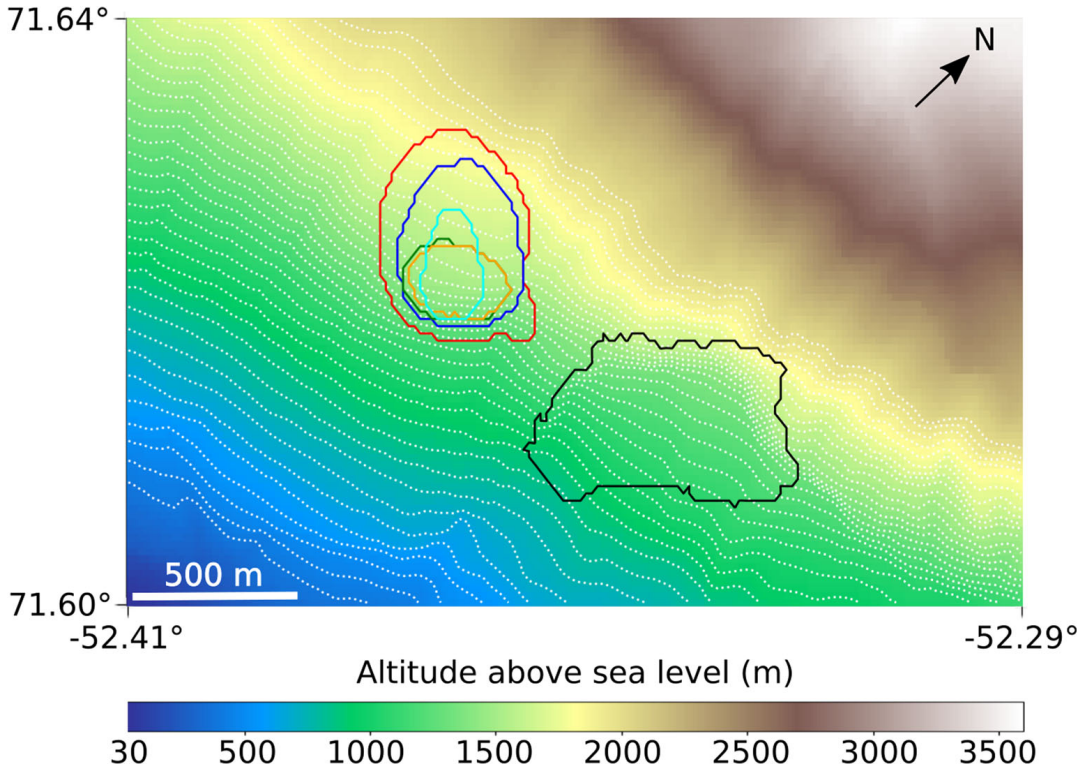

Figure 18
Footprints of the various landslides, the 2017 event (black) and the western hypothetic volumes of 38 million m^3 (red), 14 million m^3 (blue), 7 million m^3 (green), 2 million m^3 "E–W" (orange) and 2 million m^3 "N–S" (cyan)

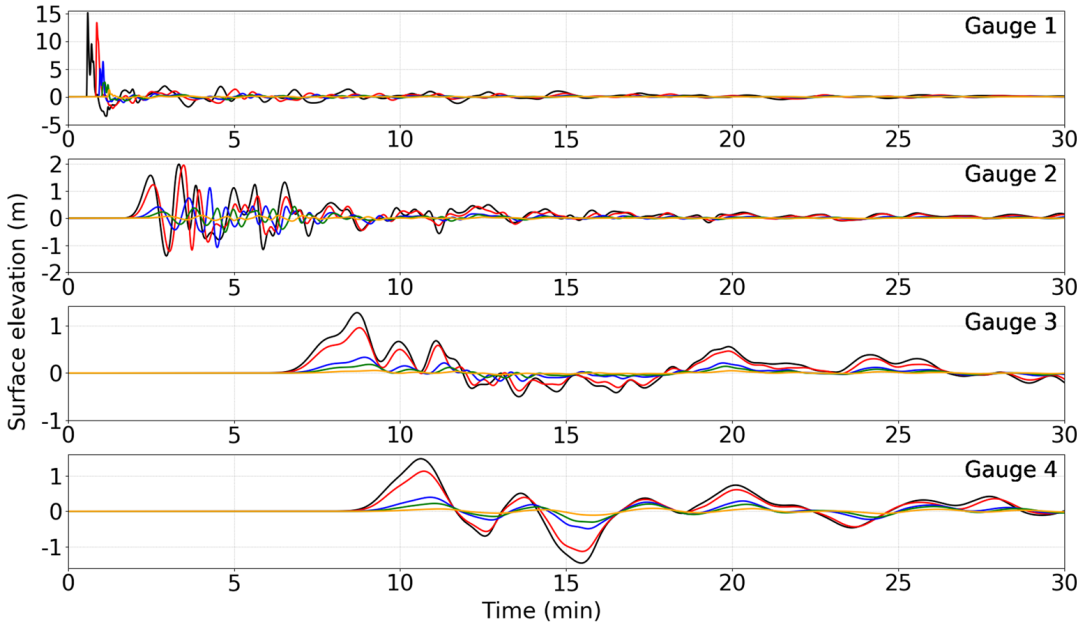

Figure 19
Surface elevations for different volumes of landslide on Gauges 1, 2, 3 and 4, for the 2017 event of 53 million m^3 (black) and for the potential events of 38 million m^3 (red), 14 million m^3 (blue), 7 million m^3 (green) and 2 million m^3 (orange)

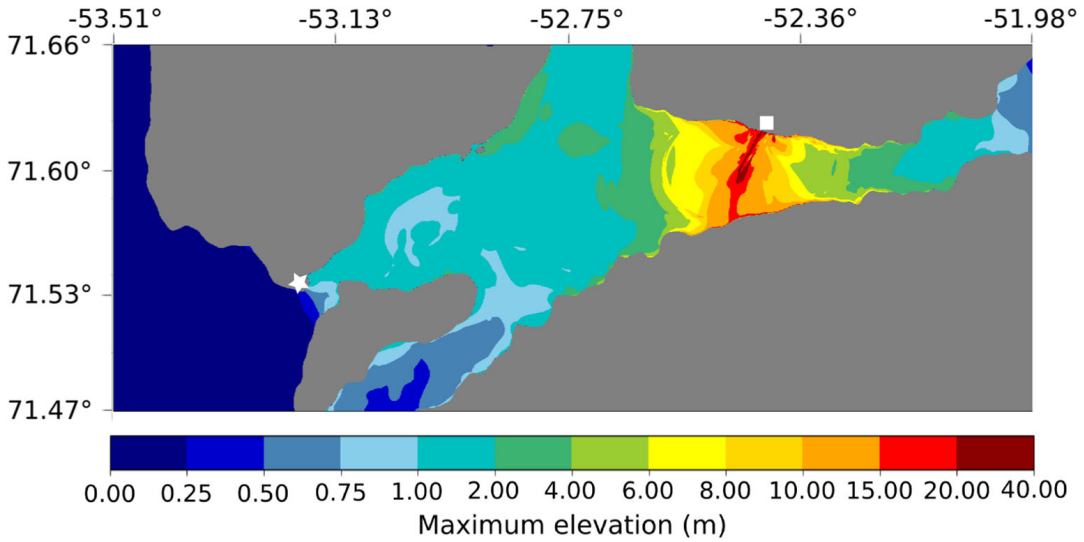

Figure 20
Maximal surface elevations simulated between the source (white square) and the village of Nuugaatsiaq (white star) for the 2017 event of 53 million m^3

bathymetry, which would have been futile, given its present quality, which the original misfit of travel times documents as grossly erroneous. In view of the potential for failure of the Western slide, and in the context of the general regional hazard expressed by the previous tsunamis of 1952, 2000, and to a lesser extent, 1954 and 2012 (see Sect. 2 for details), a high-quality bathymetric survey would be desirable in Karrat Fjord, and in the other fjords with populated settlements on their shores.

5.2. *The Next, Potential, Event: Sensitivity Studies on Its Volume and Shape*

We now address the question of the "next" slide, *i.e.*, the potential failure of the material immediately

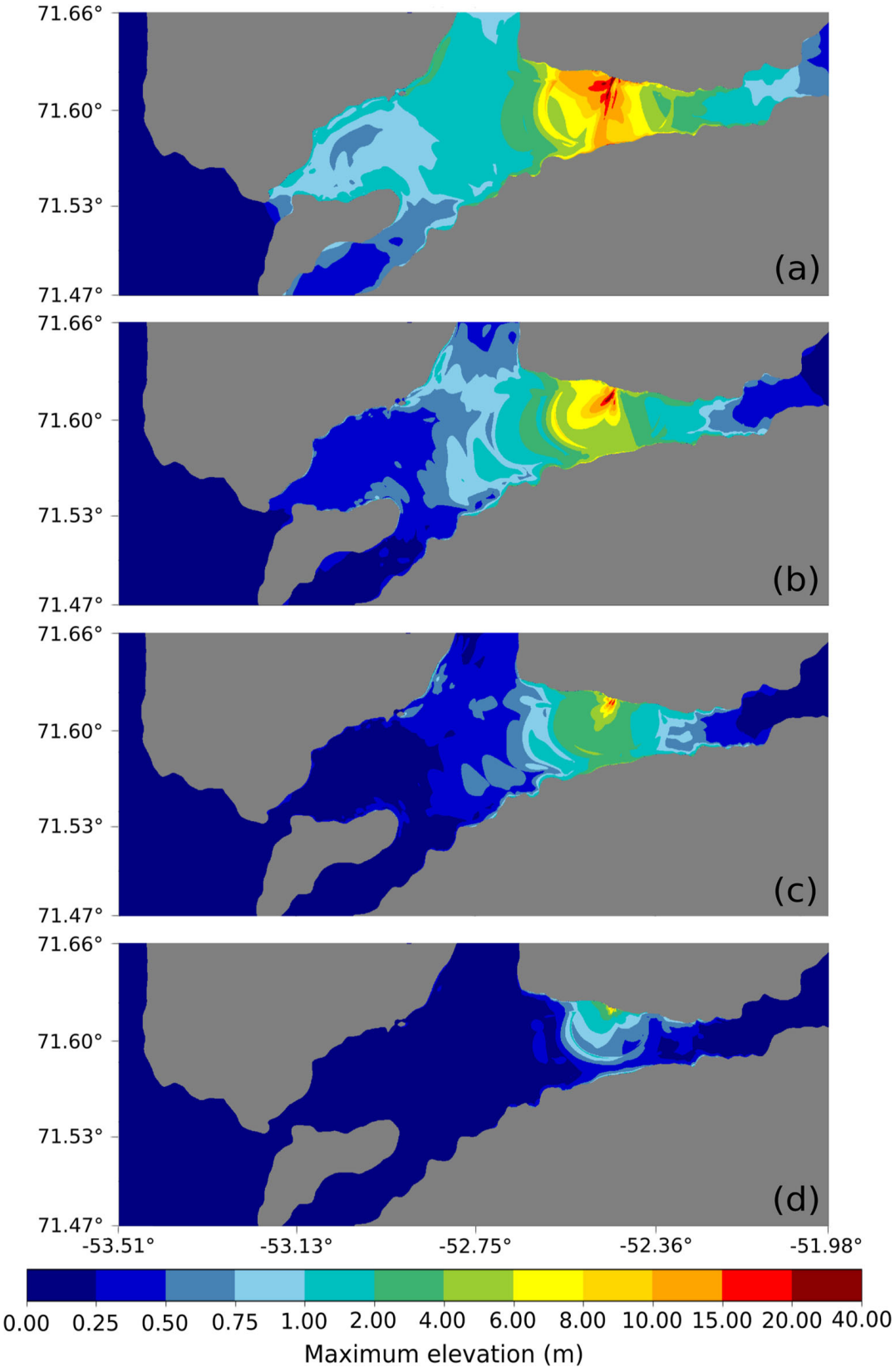

Figure 21
Maximal surface elevations simulated between the source and the village of Nuugaatsiaq for different volumes of the western landslide, **a** 38 million m^3; **b** 14 million m^3; **c** 7 million m^3; **d** 2 million m^3

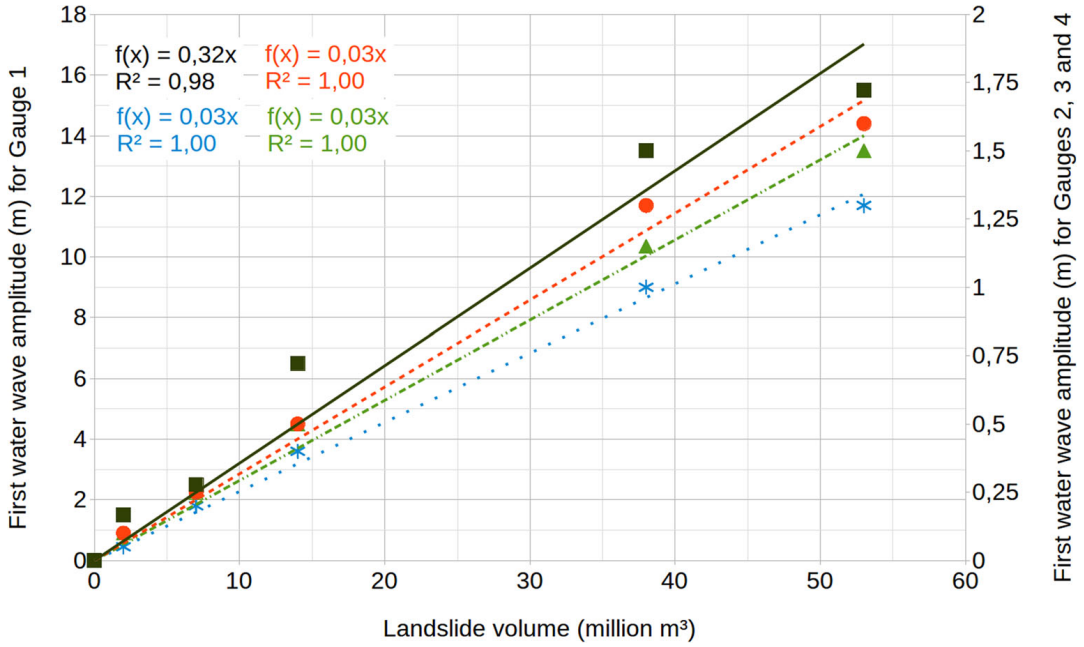

Figure 22

Amplitude (in m) of the first generated water wave *vs.* the landslide volume (in million m^3), for Gauges 1 (black squares, solid line, left vertical scale), 2 (red circles, dashed line, right vertical scale), 3 (blue asterisks, dotted line, right vertical scale) and 4 (green triangles, dash-dotted line, right vertical scale). Gauges 2, 3 and 4 are referred to the right scale while Gauge 1 is referred to the left scale

to the West of the 2017 slide (Fig. 2). Unlike for the latter, we can only speculate as to its volume, shape and of course timing. In order to investigate the impact of that potential event, and in particular, the influence of its volume, we consider four landslide geometries of variable volume, ranging from 2 million m^3 (hereafter Model "E–W") to 7, 14 and 38 million m^3, respectively (Fig. 18; Table 1), and also compare our results with those of the 2017 slide (53 million m^3).

The range of volumes proposed here (2–38 million m^3) remains small, as compared to that studied by Scheidegger (1973), and thus the range of friction angles derived from the application of his power law (with an exponent of $-1/6$) between volume and friction coefficient, is only a few degrees (from 15 to 23). A similar range of friction angles was studied in Mergili et al. (2017), showing some difference in runout between 15° and 23° , for a rock avalanche of 6.4 million m^3. Nevertheless, we have argued in Sect. 4.1 that such angles would lead to unrealistic velocities upon reaching the water. In this context, we keep a friction angle of 50° for the present calculations. The landslide rheology is a major source of uncertainties when considering the landslide dynamics. However, its effect is of the second order when considering the water waves amplitudes.

Simulated time series are compiled on Fig. 19; note that for the various scenarios of the Western slide, Gauge 1 is moved 1 km to the West, without significant difference in water depth (Fig. 20). In addition, Fig. 21 maps maximum wave elevations for the various western slides.

Figure 19 documents a good linearity between the volume of the landslides and the simulated water heights, as evidenced directly in front of the slide (Gauge 1), as well as farther along the path of the tsunami (Gauges 2, 3, and 4). For example, the largest case simulated (38 million m^3) from the

Table 1

Summary of dimensions and volumes of the western landslide

Volume (million m^3)	Width × length × thickness (m, max)	Altitude (m, center)
38	400 × 600 × 200	1500
14	300 × 500 × 146	1550
7	250 × 200 × 171	1500
2 "E–W"	250 × 200 × 110	1500
2 "N–S"	125 × 400 × 103	1500

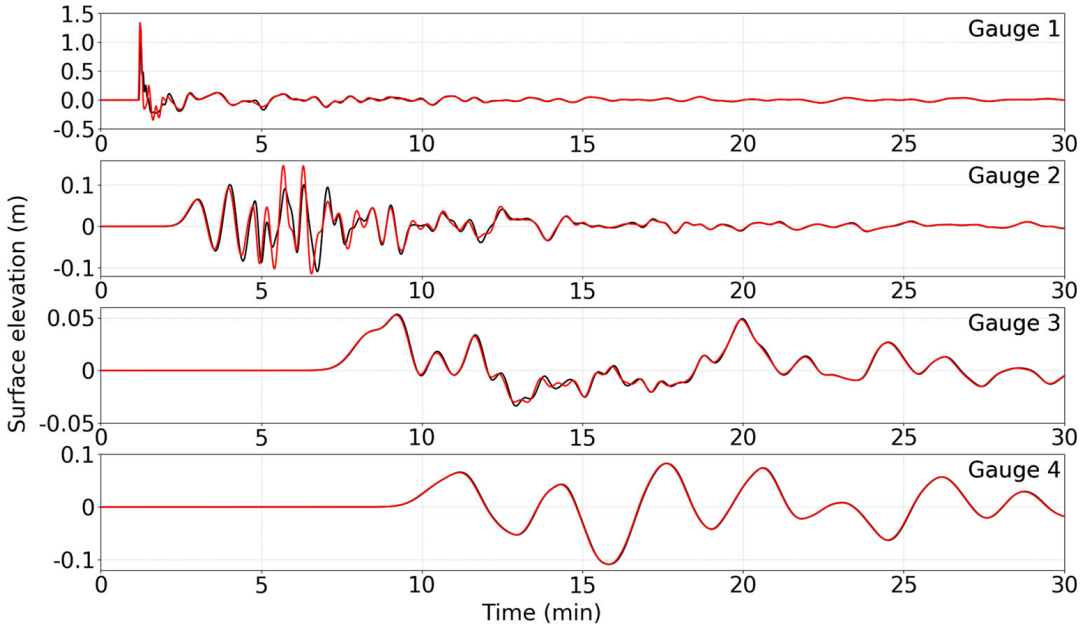

Figure 23
Surface elevations comparison for the 2 million m^3 "E–W" (black) and "N–S" (red), at Gauges 1, 2, 3 and 4

western landslide is smaller than the 2017 slide by a factor of 1.5, and the resulting water waves by a comparable factor (1.3). At the next lower level (14 million m^3), the water height remains 40 cm, which still presents a risk for the population. Dividing this volume by two, we obtain a water height of 20 cm, which is considered the limit of hazard for flooding by a tsunami. This linear relationship between the first generated water wave amplitude and the landslide volume is confirmed on Fig. 22 by excellent regression coefficients [R^2= 0.99 for Gauge 1, black: R^2 = 1.00 with two significant digits for Gauges 2, 3, 4 (red, blue, green)]. We note that the least linear relationship is for Gauge 1, located in the area where we use the Saint–Venant equations, so it appears that the linearity is most valid for the Boussinesq model.

Finally, we explore the possible influence of the shape of the landslide on the characteristics of the tsunami, such as its amplitude and dominant period. For this purpose, we consider a landslide (Model "N–S") with the same volume (2 million m^3) as our smallest "E–W" scenario (*d*), but with a narrower and taller footprint (shown in cyan on Fig. 18, and detailed in Table 1). Figure 23 presents the surface elevation comparison at the different gauges for the "E–W" and "N–S" 2 million m^3 western landslides and shows no significant difference either in amplitude or dominant period between the two cases, allowing us to conclude that the total volume of the slide is the primary factor controlling the characteristics of the wave.

6. Conclusion

Simulation of the tsunami generated by the landslide of June 17, 2017 in Karrat Fjord, Greenland satisfactorily matches both inferred wave activity at Nuugaatsiaq, 32 km WSW of the source, and the early portion of the signal recorded at the seismic station NUUG. Using a slide volume of $\sim$ 50 million m^3, we model three water waves with periods of $\sim$ 3 min, reaching the village of Nuugaatsiaq after 8 min. While these results are satisfying, they require doubling the depths documented by available bathymetry; this effect cannot be simply an artifact of our forced interpolation (from a 500 to a 25-m resolution) of the IBCAO dataset, and thus attests to the poor quality of the latter.

Our sensitivity study on different scenarios for the potential landslide, immediately to the West of the 2017 scar, supports a general linearity between their volumes and the heights of resulting tsunami waves. Using a threshold of 30 cm (at Gauge 4, considered as

a "last", initially wet grid point) for a potentially hazardous tsunami at Nuugaatsiaq, we estimate that it corresponds to a 7 million m^3 slide, considerably smaller than the more realistic volume of 38 million m^3 regarded as precarious to the West of the 2017 event, a scenario which would lead to a level flooding and destruction comparable to the 2017 event.

Acknowledgements

We thank John Clinton, Director of Seismic Networks, ETH, Zürich, for access to the NUUG seismograms, and for critical metadata concerning their misorientation. Some figures were produced using the GMT software (Wessel and Smith 1991). This work was supported by the LRC Yves Rocard (Laboratoire de Recherche Conventionné CEA-ENS). The paper was improved by the constructive comments of David Tappin and a second, anonymous, reviewer.

References

Abadie, S. M., Harris, J. C., Grilli, S. T., & Fabre, R. (2012). Numerical modeling of tsunami waves generated by the flank collapse of the Cumbre Vieja Volcano (La Palma, Canary Islands): Tsunami source and near field effects. *Journal of Geophysical Research Oceans*, *117*(5), 1–26.

Ambraseys, N., & Bilham, R. (2012). The Sarez–Pamir earthquake and landslide of 18 February 1911. *Seismological Research Letters*, *83*(2), 294–314.

Assier-Rzadkiewicz, S., Heinrich, P., Sabatier, P. C., Savoye, B., & Bourillet, J. F. (2000). Numerical modelling of a landslide-generated Tsunami: The 1979 nice event. *Pure and Applied Geophysics*, *157*(10), 1707–1727.

Chao, W.-A., Wu, T.-R., Ma, K.-F., Kuo, Y.-T., Wu, Y.-M., Zhao, L., et al. (2018). The large greenland landslide of 2017: Was a Tsunami warning possible? *Seismological Research Letters*, *89*(4), 1335–1344.

Clinton, J., Larsen, T., Dahl-Jensen, T., Voss, P., & Nettles, M. (2017). Special event: Nuugaatsiaq Greenland landslide and tsunami. *Incorporated Research Institutions for Seismology Washington DC* . https://ds.iris.edu/ds/nodes/dmc/specialevents/2017/06/22/nuugaatsiaq-greenland-landslide-and-tsunami/.

Dahl-Jensen, T., Larsen, L. M., Pedersen, S. A. S., Pedersen, J., Jepsen, H. F., Pedersen, G., et al. (2004). Landslide and Tsunami 21 November 2000 in Paatuut, West Greenland. *Natural Hazards*, *31*(1), 277–287.

Ekström, G., & Stark, C. P. (2013). Simple scaling of catastrophic landslide dynamics. *Science*, *339*(6126), 1416–1419.

Fine, I. V., Rabinovich, A. B., Thomson, R. E., & Kulikov, E. A. (2003). *Numerical modeling of Tsunami generation by submarine and subaerial landslides* (pp. 69–88). Dordrecht: Springer.

Fritz, H. M. (2002). *Initial phase of landslide generated impulse waves.* PhD Thesis, ETH Zurich.

Fritz, H. M., Giachetti, T., Anderson, S., & Gauthier, D. (2018a). Field survey of the 17 June 2017 landslide generated Tsunami in Karrat Fjord, Greenland. In *EGU General Assembly Conference Abstracts*, Vol. 20 of *EGU General Assembly Conference Abstracts*, p. 18345.

Fritz, H. M., Synolakis, C., Kalligeris, N., Skanavis, V., Santoso, F., Rizal, M., et al. (2018b). Field survey of the 28 September 2018 Sulawesi tsunami. *Eos Transactions American Geophysical Union*, *99*, 53. **(NH22B-04, [abstract])**.

Gauthier, D., Anderson, S. A., Fritz, H. M., & Giachetti, T. (2018). Karrat Fjord (Greenland) tsunamigenic landslide of 17 June 2017: Initial 3D observations. *Landslides*, *15*(2), 327–332.

Geist, E. L. (2000). Origin of the 17 July 1998 Papua New Guinea Tsunami: Earthquake or landslide. *Seismological Research Letters*, *71*(3), 344–351.

Gilbert, J. (1980). An introduction to low-frequency seismology. In A. Dziewopnski & E. Boschi (Eds.), *Proceedings of the International School of Physics "Enrico Fermi'* (Vol. 78, pp. 41–81). Amsterdam: North Holland.

Glimsdal, S., Pedersen, G. K., Harbitz, C. B., & Løvholt, F. (2013). Dispersion of tsunamis: Does it really matter? *Natural Hazards and Earth System Sciences*, *13*, 1507–1526.

Guérin, C. (2017). Effect of the DTM quality on the bundle block adjustment and orthorectification process without GCP: Example on a steep area. In *Proceedings of 2017 IEEE international geoscience remote sensing symposium (IGARSS). IEEE*, pp. 1067–1070.

Guérin, C., Binet, R., & Pierrot-Deseilligny, M. (2014). Automatic detection of elevation changes by differential DSM analysis: Application to urban areas. *IEEE Journal of Selected Topics in Applied Earth Observations and Remote Sensing*, *7*(10), 4020–4037.

Haeberli, W., & Gruber, S. (2009). *Global warming and mountain permafrost* (pp. 205–218). Berlin: Springer.

Hanson, J. A., & Bowman, J. R. (2005). Dispersive and reflected tsunami signals from the 2004 Indian Ocean tsunami observed on hydrophones and seismic stations. *Geophysical Research Letters*, *32*, 17.

Hébert, H., Piatanesi, A., Heinrich, P., & Schindelé, F. (2002). Numerical modeling of the September 13, 1999 landslide and tsunami on Fatu Hiva Island (French Polynesia). *Geophysical Research Letters*, *29*(10), 10–13.

Heinrich, P., Boudon, G., Komorowski, J. C., Sparks, R. S. J., Herd, R., & Voight, B. (2001b). Numerical simulation of the December 1997 Debris Avalanche in Montserrat, Lesser Antilles. *Geophysical Research Letters*, *28*(13), 2529–2532.

Heinrich, P., & Piatanesi, A. (2000). Near-field modeling of the July 17, 1998 tsunami in Papua New Guinea. *Geophysical Research Letters*, *27*(19), 3037–3040.

Heinrich, P., Piatanesi, A., & Hébert, H. (2001a). Numerical modelling of tsunami generation and propagation from

submarine slumps: The 1998 Papua New Guinea event. *Geophysical Journal International*, *145*(1), 97–111.

Hermanns, R. L., Blikra, L. H., Naumann, M., Nilsen, B., Panthi, K. K., Stromeyer, D., et al. (2006). Examples of multiple rock-slope collapses from Köfels (Ötz valley, Austria) and western Norway. *Engineering Geology*, *83*(1–3), 94–108.

Higman, B., Shugar, D. H., Stark, C. P., Ekström, G., Koppes, M. N., Lynett, P., et al. (2018). The 2015 landslide and tsunami in Taan Fiord, Alaska. *Scientific Reports*, *8*(1), 12993.

Huggel, C., Clague, J. J., & Korup, O. (2012). Is climate change responsible for changing landslide activity in high mountains? *Earth Surface Processes and Landforms*, *37*(1), 77–91.

ICAO. (1955). International Civil Aviation (ICAO) Meteorological Stations in Greenland. *ICAO Bulletin*, *10*(7), 7–11.

Jakobsson, M., Mayer, L., Coakley, B., Dowdeswell, J. A., Forbes, S., Fridman, B., et al. (2012). The international bathymetric chart of the Arctic Ocean (IBCAO) Version 3.0. *Geophysical Research Letters*, *39*, L12609.

La Rocca, M., Galluzzo, D., Saccorotti, G., Tinti, S., Cimini, G. B., & Del Pezzo, E. (2004). Seismic signals associated with landslides and with a tsunami at Stromboli volcano, Italy. *Bulletin of the Seismological Society of America*, *94*(5), 1850–1867.

Labbé, M., Donnadieu, C., Daubord, C., & Hébert, H. (2012). Refined numerical modeling of the 1979 tsunami in Nice (French Riviera): Comparison with coastal data. *Journal of Geophysical Research Earth Surface*, *117*, F1.

Le Friant, A., Heinrich, P., Deplus, C., & Boudon, G. (2003). Numerical simulation of the last flank-collapse event of Montagne Pelée, Martinique, Lesser Antilles. *Geophysical Research Letters*, *30*, 2.

Løvholt, F., Pedersen, G., & Gisler, G. (2008). Oceanic propagation of a potential tsunami from the La Palma Island. *Journal of Geophysical Research Oceans*, *113*(9), 1–21.

McNamara, D., Ringler, A., Hutt, C., & Gee, L. (2011). Seismically observed seiching in the Panama Canal. *Journal of Geophysical Research Solid Earth*, *116*, B4.

Mergili, M., Fischer, J.-T., Krenn, J., & Pudasaini, S. P. (2017). r.avaflow v1, and advances open-source computational framework for the propagation and interaction of two-phase mass flows. *Geoscientific Model Development*, *10*(2), 553–569.

Miller, D. J. (1960). Giant waves in Lituya Bay, Alaska. *US Geological Survey Professional Paper, 354-C*.

Naranjo, J. A., Arenas, M., Clavero, J., & Muñoz, O. (2009). Mass movement-induced tsunamis: Main effects during the Patagonian Fjordland seismic crisis in Aisén (45° 25'S), Chile. *Andean Geology*, *36*, 1.

NOAA. (2018). *National Geophysical Data Center/ World Data Service: NCEI/WDS Global Historical Tsunami Database. NOAA National Centers for Environmental Information*. https://data.nodc.noaa.gov/cgi-bin/iso?id=gov.noaa.ngdc.mgg.hazards:G02151

Okal, E. A. (2003). *T* waves from the 1998 Papua New Guinea earthquake and its aftershocks: Timing the tsunamigenic slump. *Pure and Applied Geophysics*, *160*, 1843–1863.

Okal, E. A. (2007). Seismic records of the 2004 Sumatra and other tsunamis: A quantitative study. *Pure and Applied Geophysics*, *164*, 325–353.

Okal, E. A., Fryer, G. J., Borrero, J. C., & Ruscher, C. (2002). The landslide and local tsunami of 13 September 1999 on Fatu Hiva (Marquesas islands; French Polynesia). *Bulletin de la Société géologique de France*, *173*(4), 359–367.

Okal, E. A., & Synolakis, C. E. (2001). Comment on "Origin of the 17 July 1998 Papua New Guinea tsunami: Earthquake or landslide?" by EL Geist. *Seismological Research Letters*, *72*(3), 363–366.

Okal, E. A., & Synolakis, C. E. (2003). A theoretical comparison of tsunamis from dislocations and landslides. *Pure and Applied Geophysics*, *160*(10–11), 2177–2188.

Pedersen, S. A. S., Larsen, L. M., Dahl-jensen, T., Jepsen, H. F., Krarup, G., Nielsen, T., et al. (2002). Tsunami-generating rock fall and landslide on the south coast of Nuussuaq, central West Greenland. *Geology of Greenland Survey Bulletin*, *191*, 73–83.

Pierrot-Deseilligny, M., Paparoditis, N. (2006). A multiresolution and optimization-based image matching approach: An application to surface reconstruction from SPOT5-HRS stereo imagery. In *IAPRS vol XXXVI-1/W41 in ISPRS Workshop On Topographic Mapping From Space (With Special Emphasis on Small Satellites, Ankara, Turquie)*.

Pouliquen, O. (1999). Scaling laws in granular flows down rough inclined planes. *Physics of Fluids*, *11*(3), 542–548.

Poupardin, A., Heinrich, P., Frère, A., Imbert, D., Hébert, H., & Flouzat, M. (2017). The 1979 submarine landslide-generated Tsunami in Mururoa, French Polynesia. *Pure and Applied Geophysics*, *174*, 3293–3311.

Rodriguez, M., Chamot-Rooke, N., Hébert, H., Fournier, M., & Huchon, P. (2013). Owen Ridge deep-water submarine landslides: Implications for tsunami hazard along the Oman coast. *Natural Hazards and Earth System Science*, *13*, 417–424.

Saito, M. (1967). Excitation of free oscillations and surface waves by a point source in a vertically heterogeneous earth. *Journal of Geophysical Research*, *72*(14), 3689–3699.

Satake, K., Smith, J., & Shinozaki, K. (2002). *Three-dimensional reconstruction and tsunami model of the Nuuanu and Wailau giant landslides* (pp. 333–346). American Geophysical Union Geophysical Monograph Series: Hawaii.

Savage, S. B., & Hutter, K. (1989). The motion of a finite mass of granular material down a rough incline. *Journal of Fluid Mechanics*, *199*, 177–215.

Savage, S. B., & Hutter, K. (1991). The dynamics of avalanches of granular materials from initiation to runout. Part I: Analysis. *Acta Mechanica*, *86*(1), 201–223.

Scharroo, R., Smith, W., Titov, V., & Arcas, D. (2005). Observing the Indian Ocean tsunami with satellite altimetry. *Geophysical Research Abstracts*, *7*, 230.

Scheidegger, A. E. (1973). On the prediction of the reach and velocity of catastrophic landslides. *Rock Mechanics and Rock Engineering*, *5*(4), 231–236.

Schuster, R. L., & Alford, D. (2004). Usoi landslide dam and lake sarez, Pamir mountains, Tajikistan. *Environmental and Engineering Geoscience*, *10*(2), 151–168.

Sepúlveda, S. A., & Serey, A. (2009). Tsunamigenic, earthquake-triggered rock slope failures during the April 21, 2007 Aisén earthquake, southern Chile (45.5 S). *Andean Geology*, *36*, 1.

Shuto, N. (1991). Numerical simulation of tsunamis—its present and near future. *Natural Hazards*, *4*, 171–191.

Synolakis, C. E., Bardet, J.-P., Borrero, J. C., Davies, H. L., Okal, E. A., Silver, E. A., Sweet, S., & Tappin, D. R. (2002). The slump origin of the 1998 Papua New Guinea tsunami. In *Proceedings of the Royal Society of London, Series A: Mathematical, Physical and Engineering Sciences, Vol. 458, The Royal Society*, pp. 763–789.

Thomson, R. E., Rabinovich, A. B., Kulikov, E. A., Fine, I. V., & Bornhold, B. D. (2001). *On Numerical simulation of the landslide-generated Tsunami of November 3, 1994 in Skagway Harbor* (pp. 243–282). Dordrecht: Springer.

Tinti, S., Pagnoni, G., & Zaniboni, F. (2006). The landslides and tsunamis of the 30th of December 2002 in Stromboli analysed through numerical simulations. *Bulletin of Volcanology*, *68*(5), 462–479.

Viroulet, S., Cébron, D., Kimmoun, O., & Kharif, C. (2013). Shallow water waves generated by subaerial solid landslides. *Geophysical Journal International*, *193*(2), 747–762.

Voight, B. (1981). The 1980 eruptions of Mount St. Helens, Washington. Time scale for the first moments of the May 18 eruption. *US Geological Survey Professional Paper*, *1250*, 69–86.

Wang, J., Ward, S. N., & Xiao, L. (2015). Numerical simulation of the December 4, 2007 landslide-generated tsunami in Chehalis Lake, Canada. *Geophysical Journal International*, *201*(1), 372–376.

Ward, S. N. (1980). Relationships of tsunami generation and an earthquake source. *Journal of Physics of the Earth*, *28*(5), 441–474.

Ward, S. N., & Day, S. (2011). The 1963 landslide and flood at Vajont Reservoir Italy. A tsunami ball simulation. *Italian Journal of Geosciences*, *130*(1), 16–26.

Weiss, R., Fritz, H. M., & Wünnemann, K. (2009). Hybrid modeling of the mega-tsunami runup in Lituya Bay after half a century. *Geophysical Research Letters*, *36*, 9.

Wessel, P., & Smith, W. H. F. (1991). Free software helps map and display data. *Eos Transactions American Geophysical Union*, *72*(41), 441–446.

Yuan, X., Kind, R., & Pedersen, H. A. (2005). Seismic monitoring of the Indian Ocean tsunami. *Geophysical Research Letters*, *32*, 15.

(Received September 13, 2018, revised January 29, 2019, accepted January 31, 2019)

2.2 The 2018 Anak Krakatau, Indonesia, landslide tsunami

Pure Appl. Geophys.

https://doi.org/10.1007/s00024-019-02394-y

Pure and Applied Geophysics

The December 22, 2018 Anak Krakatau, Indonesia, Landslide and Tsunami: Preliminary Modeling Results

Alexandre Paris,[1,3] Philippe Heinrich,[1] Raphaël Paris,[2] and Stéphane Abadie[3]

Abstract—On the evening of December 22, 2018, the coasts of the Sunda Strait, Indonesia, were hit by a tsunami generated by the collapse of a part of the Anak Krakatau volcano. Hundreds of people were killed, thousands were injured and displaced. This paper presents a preliminary modeling of the volcano flank collapse and the tsunami generated based on the results of a 2D depth-averaged coupled model involving a granular rheology and a Coulomb friction for the slide description and dispersive effects for the water flow part. With a reconstructed total volume (subaerial and submarine) of the landslide of 150 million m^3 inferred from pre and post-collapse satellite and aerial images, the comparison of the simulated water waves with the observations (tide gauges located all around the strait, photographs and field surveys) is satisfactory. Due to the lack of information for the submarine part of the landslide, the reconstructed submarine slope is assumed to be approximately constant. A significant time delay on the results and particularly in the Bandar Lampung Bay could be attributed to imprecisions of bathymetric data. The sensitivity to the basal friction and to dispersive effects is analyzed through numerical tests. Results show that the influence of the basal friction angle on the simulated wave heights decreases with distance and that a value of 2° gives consistent results with the observations. The dispersive effects are assessed by comparing water waves simulated by a shallow water model and a Boussinesq model. Simulations with frequency dispersion produce longer wave periods and smaller wave amplitudes in the Sunda Strait and particularly in deep waters.

Keywords: Tsunami, landslide, Anak Krakatau, simulation.

1. Introduction

Landslide tsunamis are not very well known to the general public, although they are quite common and devastating. This phenomenon can happen wherever weakened volumes of rocks or sediments lie, i.e in deltas, coastal cliffs, rivers, fjords and lakes (Masson et al. 2006). As the velocity of the terrain deformation due to a landslide can reach very high values (up to 100 $m.s^{-1}$ according to Satake et al. (2002)), the tsunami energy may be initially of the same order as that generated by a major earthquake (Okal and Synolakis 2003), but the generated amplitudes generally decrease quickly and the tsunami effects are local.

One of the largest landslide tsunamis may probably be the Storegga slide, off Norway, with its volume between 2400 and 3200 km^3, 8200 years ago (Haflidason et al. 2004; Bondevik et al. 2005). Another famous case is the 1958 Lituya Bay landslide-generated mega-tsunami (Miller 1960). After a 8.3-magnitude earthquake, a volume of 30.6 million m^3 collapsed in Gilbert Inlet, generating a tsunami which run-up height reached 524 m on the opposite side (Fritz et al. 2009).

Until now, one of the deadliest recent landslide tsunamis is the Papua New Guinea one, 1998, during which over 2100 people died after a 4 km^3 landslide collapsed at a depth of 550 m, generating a tsunami with run-up heights up to 15 m (Heinrich et al. 2001a; Synolakis et al. 2002). More recently, the 2014 Tangjiaxi, China (0.16 million m^3, 3 deaths, 9 people missing and 11 injured (Huang et al. 2017)), the 2017 Karrat Fjord, Greenland (50 million m^3, 4 people killed (Paris et al. 2019)) events and now the 2018 Anak Krakatau, Indonesia collapse remind us of

[1] CEA, DAM, DIF, 91297 Arpajon Cedex, France. E-mail: alexandre.antoine.paris@gmail.com

[2] Université Clermont Auvergne, CNRS, IRD, OPGC, Laboratoire Magmas et Volcans, 63000 Clermont-Ferrand, France.

[3] Université de Pau et des Pays de l'Adour, E2S UPPA, SIAME, Anglet, France.

Published online: 20 December 2019

the threat landslide tsunamis represent, even if their volume appear relatively small compared to historical events such as Ritter Island in 1888 (5 km^3 (Cooke 1981; Johnson 1987)) and Oshima–Oshima in 1741 (2.4 km^3 (Satake and Kato 2001).

A possible way to better understand a physical phenomenon is to use numerical modeling. A review of landslide-generated tsunami models can be found in Heidarzadeh et al. (2014) and Yavari-Ramshe and Ataie-Ashtiani (2016). Two approaches are used to simulate landslide-generated tsunamis: simulate the tsunami propagation considering the bottom deformation due to the landslide as a boundary condition for the water surface elevation or simulate both the landslide and the tsunami in a single model. In the first category, the landslide movement is reproduced as a bathymetry deformation in time (see Harbitz (1992), Grilli and Watts (2005) or Tappin et al. (2008)). In the second category, the landslide is modeled together with the free surface using a rheology law. Among them we can find Newtonian fluid approaches as in the numerical experiments of Fine et al. (2003), or in the modeling of the 1979 Nice events (Assier-Rzadkiewicz et al. 2000), or in the Franz et al.'s (2015) study of the 2006 Nicolet, Québec, Canada, landslide. Non-Newtonian models such as the Bingham model of Skvortsov and Bornhold (2007) or the BING model (e.g. the modeling of the 1888 Brattora, Norway, landslide tsunami (L'Heureux et al. 2011) or the 2014 submarine landslide at Statland, Norway (Glimsdal et al. 2016)) can also be used. Finally, landslides rheologies can be modeled as granular flows, as in the study of Reunion Island landslide-tsunamis by Kelfoun et al. (2010) or the Güímar debris avalanche simulation of Giachetti et al. (2011).

Landslides are mostly simulated using 2D depth-averaged (2DH) models, although more complex and time-consuming 3D computations may be envisaged (Løvholt et al. 2008; Abadie et al. 2012; Horrillo et al. 2013). Nevertheless, they are generally spatially restricted to the landslide and wave generation area. Tsunami propagation can be realized in 2DH using shallow water equations (Jiang and LeBlond 1992; Harbitz et al. 1993) or Boussinesq equations (Tappin et al. 2014; Harbitz et al. 2014; Grilli et al. 2015). Here, we use the 2D depth-integrated model AVALANCHE (Heinrich and Piatanesi 2000; Hébert et al. 2002; Le Friant et al. 2003) that has been successfully employed to simulate subaerial or submarine landslides (Rodriguez et al. 2013; Poupardin et al. 2017; Paris et al. 2019), considering the landslide as a granular flow following a Coulomb frictional law and using shallow water or Boussinesq equations.

On December 22, 2018 at 13:50 UTC (20:50 local time) the southwestern flank of Anak Krakatau volcano (Sunda Strait, Indonesia) collapsed to the sea and generated a tsunami that devastated the coasts of Java and Sumatra, killing more than 430 people and damaging thousands of houses and boats, as reported by BNPB (Badan Nasional Penanggulangan Bencana[1]). Human casualties and material losses were recorded all around the Sunda Strait, on the islands of Java and Sumatra, with run-up heights reaching up to 14 m (TDMRC 2019). A summary of the available observations data is provided in Sect. 3. This Anak Krakatau event was recently studied by Grilli et al. (2019), using the 3D model NHWAVE (Ma et al. 2012, 2015; Kirby et al. 2016) for the landslide simulation and the tsunami generation, then the 2D model FUNWAVE-TVD (Shi et al. 2012) for the tsunami propagation. It was also simulated by Heidarzadeh et al. (2020) using the COMCOT model (Cornell Multi-grid Coupled Tsunami Model (Liu et al. 1998; Wang and Liu 2006)) and an initial sea surface elevation as the landslide source. We present a comparison between water heights of the two latter mentioned studies and our simulation.

In this paper, the landslide-generated water waves are calculated by AVALANCHE and compared with available tsunami observations around Sunda Strait (tide gauge records, wave heights, and flow depths, inundation heights and run-up heights reported from three field surveys). The influence of the rheology on water wave heights is discussed using different basal friction angle values and finally the dispersive effects are assessed through numerical tests comparing a shallow water to a Boussinesq model.

[1] https://bnpb.go.id/volume-tubuh-gunung-anak-krakatau-berkurang-jumlah-korban-tsunami-bertambah, last accessed 10 september 2019.

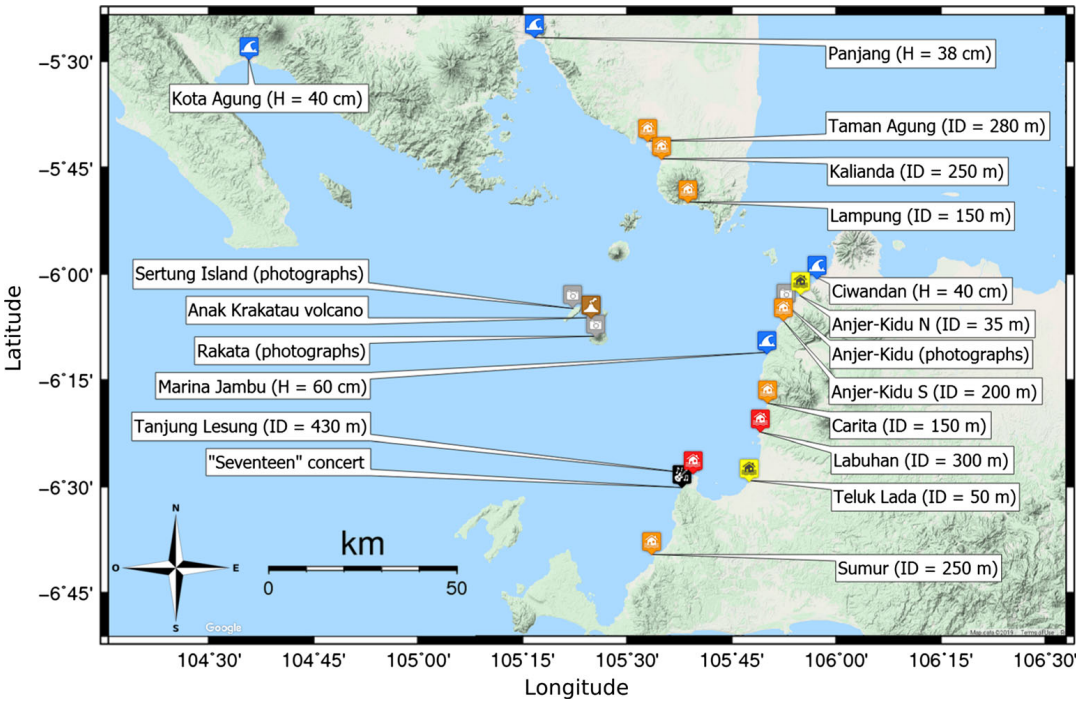

Figure 1
Location map of Anak Krakatau volcano in the Sunda Strait (brown volcano icon) and of the different observations of the event: inundation distance *ID* (less than 100 m in yellow, between 100 and 300 m in orange and more than 300 m in red), recorded height *H* at tide gauges (blue icons) and photographs (grey icons)

2. *Geological Setting*

The Krakatau volcanic complex is a group of islands that lies in the middle of the Sunda Strait, between Java and Sumatra. The tectonic setting of the strait is characterized by an extensional regime that formed different grabens at the southeastern end of the Sumatra fault zone (Harjono et al. 1991; Susilohadi et al. 2009). With a water depth not exceeding 200 m, the eastern part of the strait is relatively shallow, compared with the 1000 m deep Semangko graben to the west (see Figure 2 in Susilohadi et al. (2009)).

Krakatau is the only active volcano of a south-southwest to north-northeast volcanic line that extends across the strait from Ujung Kulon in western Java to Rajabasa in eastern Sumatra (Nishimura et al. 1986). The 1883 caldera-forming eruption completely reshaped the morphology of the Krakatau volcanic complex (e.g. Simkin and Fiske (1983)), and the present-day active edifice Anak Krakatau ('child of Krakatau' in Indonesian) was built on the steep northeast wall of the submarine caldera that was formed during the 1883 eruption (Deplus et al. 1995). The 5×4 km^2 large rectangular caldera is characterized by a flat bottom of 200–240 m deep. The location of Anak Krakatau on the northeast rim of this steep-sided submarine basin led several authors to question its stability (Camus et al. 1987; Deplus et al. 1995; Giachetti et al. 2012). During this 1883 eruption, a tsunami was generated, reaching 15 up to 40 m run-up heights in the Sunda Strait (Nomanbhoy and Satake 1995; Choi et al. 2003) and killing more than 35,000 people (Sigurdsson et al. 1991).

Anak Krakatau first emerged from the sea in January 1928 (Stehn 1929). From 1928 to 1959 phreatomagmatic activity progressively formed a 1.7 km large, 150 m high tuff-ring (Sudradjat 1982). In 1960, eruptive activity shifted to a Strombolian style, thus building a new cone on the SW flank of the initial tuff-ring. During the last 60 years, recurrent lava flows and pyroclastic fall deposits contributed to the growth of Anak Krakatau Island, and the cone was 350 m high before its collapse in December

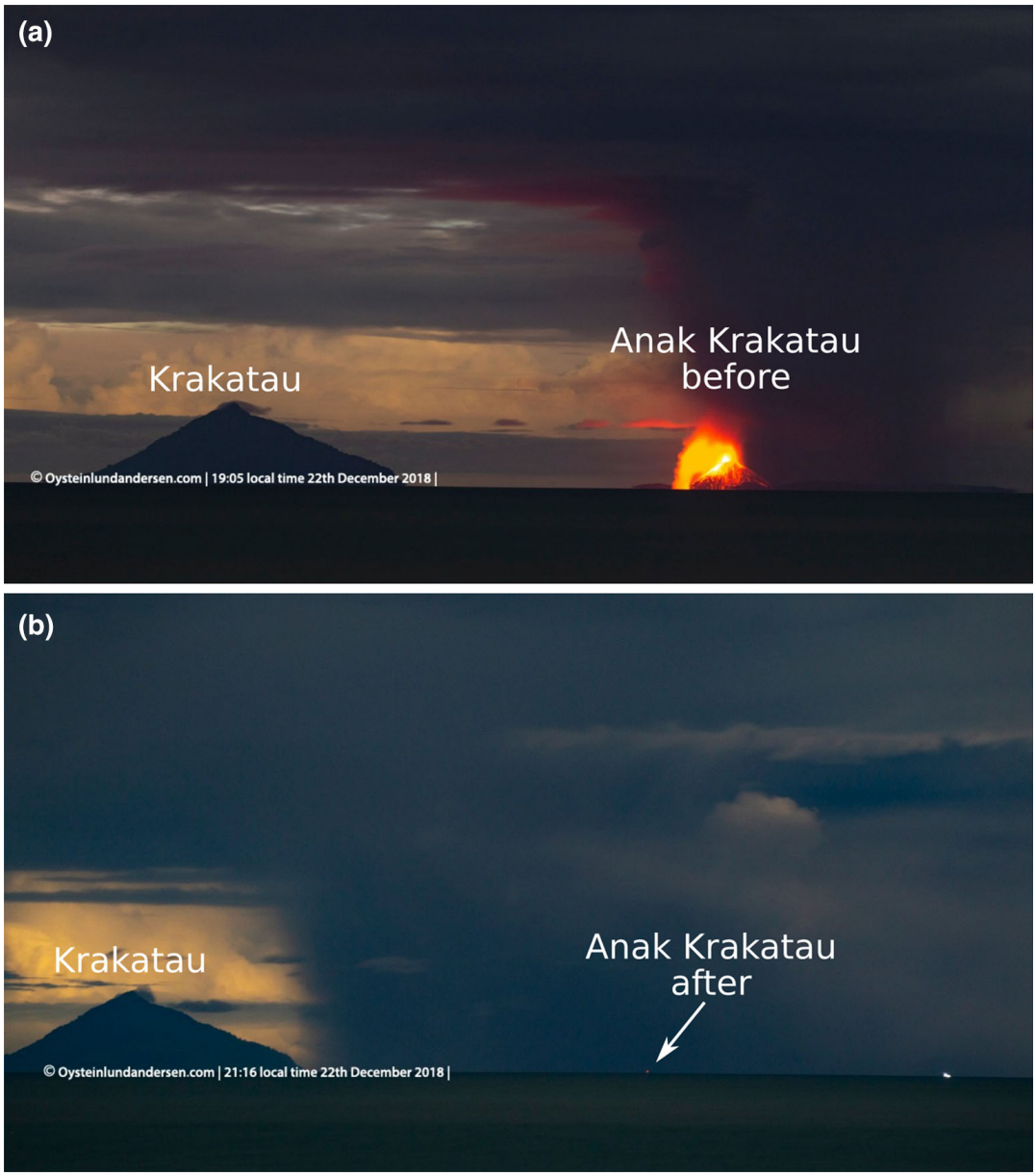

Figure 2
Photographs taken in Anjer-Kidu, 50 km east of the volcano, **a** before the landslide at 19:05 local time and **b** after the landslide at 21:16 local time (https://www.oysteinlundandersen.com/krakatau-volcano-witnessing-the-eruption-tsunami-22december2018/)

2018. Photographs captured from the coast of Java[2] confirmed that the cone had grew by almost 100 m between July 2016 and December 2018. There are many coastal resorts, harbors and cities within a radius of 60 km around the volcano [e.g. Kalianda in Sumatra, Anjer, Labuhan and Sumur in Java (Fig. 1)].

[2] https://www.oysteinlundandersen.com/krakatau-volcano-witnessing-the-eruption-tsunami-22december2018/.

3. Anatomy of the Event

Before any satellite revealed the effects of the ongoing volcanic eruption and collapse, photographs captured by Øystein Lund Andersen in Anjer-Kidu (western coast of Java, 50 km east of Krakatau volcano) show a strong strombolian activity (Fig. 2a), followed by a phase of ash emission that blurred the entire volcano (Fig. 2b). The collapse was recorded on a seismic signal at 20:55 local time, i.e. 13:55

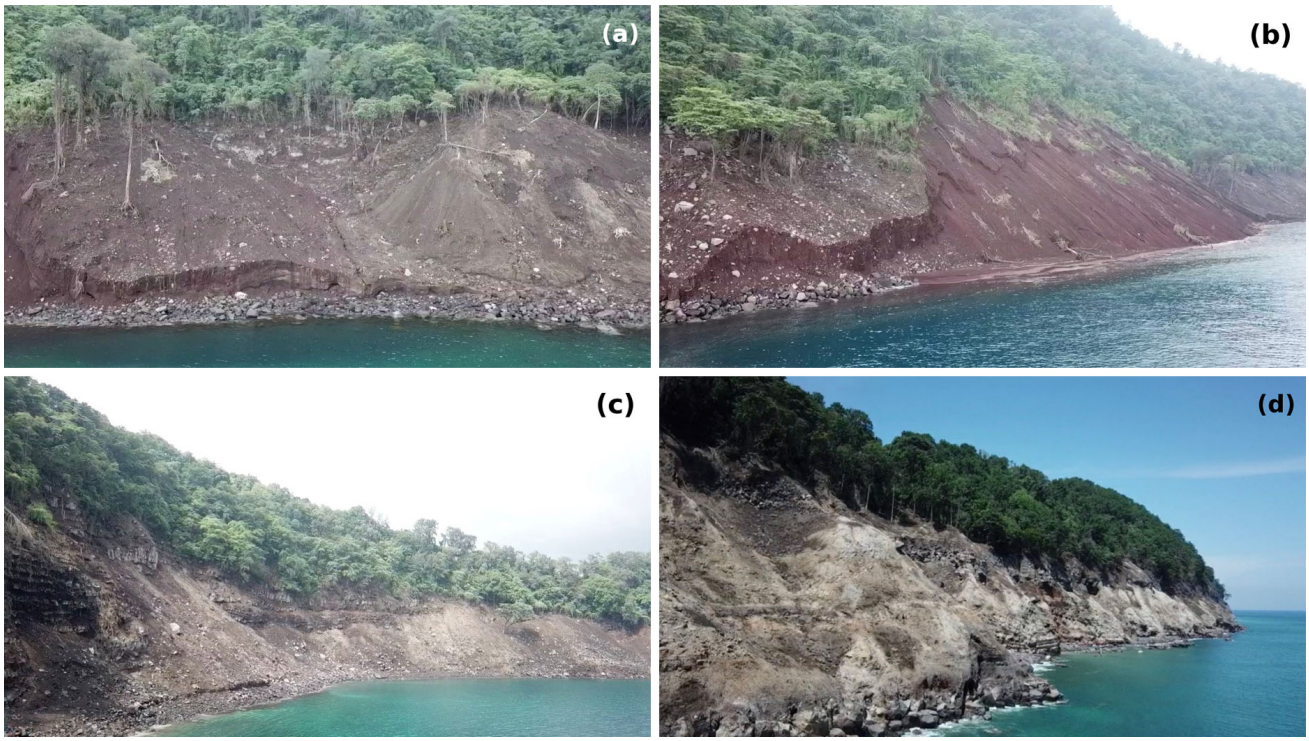

Figure 3
Photographs of inundation effects in the near-field on **a**, **b**, **c** Rakata Island and **d** Sertung Island (Fig. 1), close to the Anak Krakatau volcano (James Reynolds @EarthUncutTV on Twitter: https://twitter.com/earthuncuttc/status/1083305942228160513). The base of trees is estimated to be now 25 to 30 m above sea level

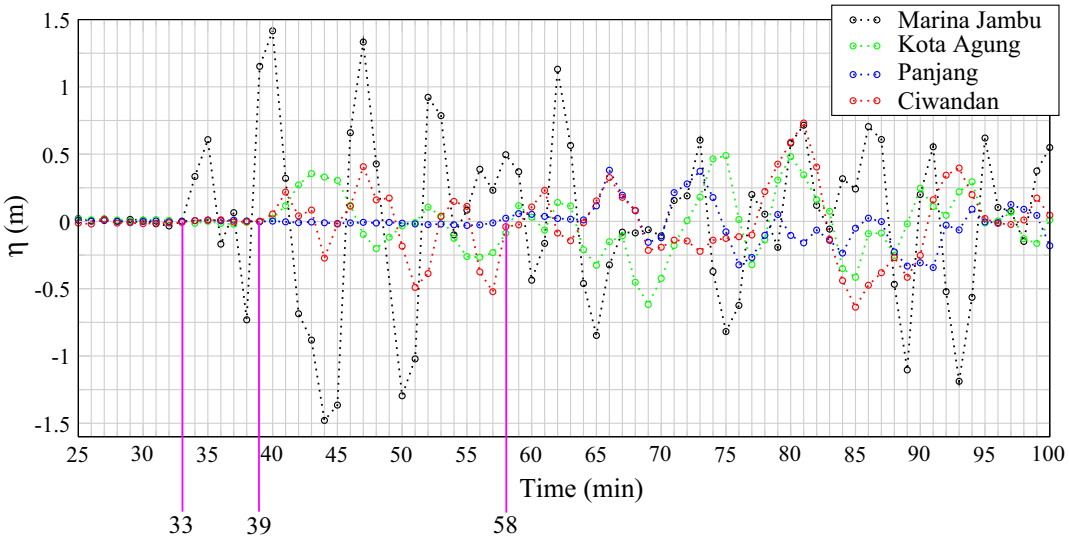

Figure 4
Time series of surface elevation recorded by tide gauges at Marina Jambu (black), Ciwandan (red), Kota Agung (green) and Panjang (blue) tide gauges (see Fig. 9 for locations). Pink lines mark the arrival times at each tide gauges. The arrival times at Kota Agung and Ciwandan are identical

UTC (Walter et al. 2019). The flank collapse which removed 93.8 million m^3 of subaerial volcanic rocks from the western side of the volcano (Gouhier and Paris 2019) followed a period of 6 months of volcanic activity and rapid growth of the volcanic cone (Gouhier and Paris 2019; Walter et al. 2019).

Local effects of the tsunami generated by the flank collapse are visible on Rakata Island (Fig. 3a–c)

Table 1

Summary of results sorted by arrival times

Gauges location	Coordinates (longitude, latitude)	Depth (m)	Travel time (min)			Wave Height (cm)	
			Giachetti et al. (2012)	Comp.	Rec.	Comp.	Rec.
1-Near the volcano	105.31376, − 6.14967	100	ø	5	ø	560	ø
2-Tanjung Lesung	105.64894, − 6.47980	1.5	28	29	ø	170	100–200
3-Marina Jambu	105.84263, − 6.18953	1.8	33	34	33	75	60
4-Ciwandan	105.95513, − 6.01441	1.1	42	42	39	22	20
6-Kota Agung	104.62044, − 5.50120	1.0	ø	45	39	33	35
5-Kalianda	105.55701, − 5.70134	2.9	47	49	ø	120	ø
7-Panjang	105.29036, − 5.44579	1.3	68	66	58	20	37

Computed (*Comp.*) results are compared with recorded (*Rec.*) data and Giachetti et al.'s (2012) results. Gauges number refer to Fig. 9

and Sertung Island (Fig. 3d). Taking into account the trimline, the run-up height is estimated to 25 up to 30 m on Rakata and Sertung islands, located respectively 4 km south and 3 km north-northwest of Anak Krakatau Island.

About 33 min after the collapse, the tsunami was recorded at Marina Jambu, Banten, east of the volcano on Java Island (Fig. 1), with a first water wave height of 60 cm and 6 min later a 20 cm high wave was recorded at Ciwandan, north of Marina Jambu (Fig. 4). At the same time, on Sumatra Island, a tide gauge located at Kota Agung, northwest of the Anak Krakatau, recorded a wave height of 35 cm. Finally, 58 min after the collapse, the tsunami was recorded in the Bandar Lampung Bay at Panjang, north of the volcano, with a wave height of 37 cm. Note that for the two locations of Marina Jambu and Ciwandan, on Java Island, the first wave is not the highest one. In both cases, the second wave height is twice or more the first one and reached 140 cm at Marina Jambu, and 40 cm at Ciwandan.

Thanks to the work of the Copernicus program,[3] preliminary summary maps about the consequences of the tsunami were made available. These maps give an idea about inundation distances and damages on houses. On Java Island, the most affected areas are Labuhan, with up to 300 m of inundation distance and Tanjung Lesung (see Fig. 1 for locations), where the water entered up to 430 m inland. South of Tanjung Lesung, a Youtube video[4] shows a water wave, that can be estimated between 1 and 2 m high, destroying a concert stage. Elsewhere, the inundation distances reached approximately 35 m north of Anjer-Kidu, 50 m at Teluk Lada, 170 m at Carita, 200 m south of Anjer-Kidu, and 250 m in Sumur. On Sumatra Island, the water penetrated the land up to 150 m at Lampung, 250 m at Kalianda and 280 m at Taman Agung. Locations, inundation distances and recorded water heights are summarized in Fig. 1 and Table 1.

Finally, the field surveys conducted by the KKP (Kementerian Kelautan dan Perikanan, Ministry of Marine Affairs and Fisheries) south of Tanjung Lesung and between Labuhan and Anjer-Kidu (Muhari et al. 2019), the BMKG (Badan Meteorologi, Klimatologi, dan Geofisika) at Tanjung Lesung and Carita, and the Tsunami and Disaster Mitigation Research Center of Syiah Kuala University confirmed that the areas of Tanjung Lesung, Labuhan, Carita and Anjer-Kidu on Java Island and Kalianda on Sumatra Island were among the most impacted, with destroyed brick walls and boulder(s) displaced (TDMRC 2019). These different field surveys confirmed that the waves penetrated up to 300 m inland at Tanjung Lesung (run-up height of 5 m asl), 170 m at Carita (run-up height of 6.2 m asl) and 330 m at Sakarame, north Carita (run-up height of 4.6 m asl). A local run-up height of 13.5 m asl for an inundation distance of 125 m was measured in a location between Tanjung Lesung and Sumur. Another remarkable run-up height of 12.5 m was measured at Cipenyu Beach by Takabatake et al. (2019). The locations of the places studied by these field surveys are listed in Tables 2 and 3.

[3] https://emergency.copernicus.eu/mapping/list-of-components/EMSR335.

[4] https://www.youtube.com/watch?v=2ERXCR86GU4.

Table 2

Computed water heights (W.H.) (m) at the shoreline compared with flow depths (F.D.), inundation heights (I.H.) and run-up heights (R.H.) identified by the Takabatake et al. (2019) and BMKG surveys

Places	Coordinates (longitude, latitude)	W.H. (m) computed	Takabatake et al.'s (2019) Survey		
			F.D. (m)	I.H. (m)	R.H. (m)
Sinar Agung	105.10208, − 5.77083	0.4		2.35 (10)	
Sinar Agung	105.10128, − 5.77061	0.4		1.58 (20)	
Bandung Jaya	105.10533, − 5.77611	0.4		0.81 (0)	
Bandung Jaya	105.10936, − 5.77353	0.5		1.74 (36)	
Selesung	105.29231, − 5.80242	0.4		3.38 (15)	
Selesung	105.29231, − 5.80261	0.4		3.38 (31)	
Central Waymuli	105.63419, − 5.83739	0.6			5.04 (75)
East Waymuli	105.64164, − 5.83558	1.2			3.97 (79)
Kunjir	105.65161, − 5.83592	0.9		4.21 (76)	
Kahai Beach	105.66814, − 5.83789	2.3		6.83 (22)	
Tangkolo	105.82944, − 6.26461	1.3		1.01 (198)	
Lantera	105.82314, − 6.37628	1.9		3.36 (39)	
Cipenyu Beach	105.64139, − 6.50536	2.7			12.58 (185)
Cipenyu Beach	105.64083, − 6.50417	2.7		11.28 (85)	
Cipenyu Beach	105.64108, − 6.50419	2.7		10.17 (114)	
Tanjung Jaya	105.62436, − 6.54508	2.5		5.39 (170)	
Babakanciberber	105.61847, − 6.60589	0.9			2.55 (48)

Places	Coordinates (longitude, latitude)	W.H. (m) computed	BMKG Survey		
			F.D. (m)	I.H. (m)	R.H. (m)
Tanjung Lesung	105.65463, − 6.48015	3		5.06 (60) [303.31]	
Tanjung Lesung	105.65453, − 6.48010	3	4.23 (50) [303.31]		
Mutiara Carita	105.83200, − 6.31613	3		3.05 (24) [170.28]	
Mutiara Carita	105.83200, − 6.31644	3	2.9 (55) [170.28]		
Mutiara Carita	105.83018, − 6.31634	2.4		5.08 (14) [170.28]	
Mutiara Carita	105.82907, − 6.31728	3		5.04 (10) [170.28]	
Mutiara Carita	105.82828, − 6.31876	3.4		5.64 (12) [170.28]	
Mutiara Carita	105.82828, − 6.31996	4.3		6.22 (14) [170.28]	
Carita Lagon	105.82678, − 6.28562	2.5	3.05 (18) [95.90]		

Values in parenthesis are the distances from the shoreline. Values in brackets are the maximum inundation distances measured by the different team surveys

4. Methods

4.1. Landslide Model

In the code AVALANCHE (Heinrich et al. 2001b; Paris et al. 2019) the flank collapse is modeled using the one-phase grain-flow model of Savage and Hutter (1989) and a Coulomb basal friction. The equations of conservation of mass and momentum are solved in a (x', y') coordinate system linked to the topography (Fig. 5):

$$\frac{\partial h_s}{\partial t} + \frac{\partial}{\partial x'}(h_s u_s) + \frac{\partial}{\partial y'}(h_s v_s) = 0; \tag{1}$$

$$\begin{aligned} &\frac{\partial}{\partial t}(h_s u_s) + \frac{\partial}{\partial x'}(h_s u_s^2) + \frac{\partial}{\partial y'}(h_s u_s v_s) \\ &= -\frac{1}{2}\kappa\frac{\partial}{\partial x'}(g h_s^2 \cos\theta) + \kappa g h_s \sin\theta_x + F_{x'}; \end{aligned} \tag{2}$$

$$\begin{aligned} &\frac{\partial}{\partial t}(h_s v_s) + \frac{\partial}{\partial x'}(h_s v_s u_s) + \frac{\partial}{\partial y'}(h_s v_s^2) \\ &= -\frac{1}{2}\kappa\frac{\partial}{\partial y'}(g h_s^2 \cos\theta) + \kappa g h_s \sin\theta_y + F_{y'} \end{aligned} \tag{3}$$

where h_s is the slide's thickness in a direction perpendicular to the slope, $\mathbf{u} = (\mathbf{u_s}, \mathbf{v_s})$ the depth-averaged velocity vector parallel to the slope, $\kappa = 1 - \rho_w/\rho_s$ where ρ_w and ρ_s are the water and rock densities with a ratio $\rho_s/\rho_w = 1.5$ (for the subaerial

Table 3

Computed water heights (W.H.) (m) at the shoreline compared with flow depths (F.D.), inundation heights (I.H.) and run-up heights (R.H.) identified by the KKP survey

Places	Coordinates (longitude, latitude)	W.H. (m) computed	KKP survey		
			F.D. (m)	I.H. (m)	R.H. (m)
Karang Suraga	105.85470, − 6.15110	0.8			3.74 (31) [84.47]
Karang Suraga	105.84969, − 6.16902	0.8			3.29 (51) [57.76]
Karang Suraga	105.84697, − 6.17453	0.9	0.81 (26)		
Karang Suraga	105.84747, − 6.17476	0.9			4.54 (85) [94.64]
Bulakan	105.83830, − 6.19698	0.8	0.63 (− 21)		
Bulakan	105.83619, − 6.20232	1.2			5.8 (90) [124.13]
Umbul Tanjung	105.82577, − 6.23888	1.8			5.34 (64) [68.8]
Sukarame	105.82887, − 6.26210	1.2	3.2 (15)		4.57 (15) [330]
Sukarame	105.82698, − 6.27677	1.6			3.45 (105) [158.92]
Sukarame	105.82700, − 6.27700	1.6	1.14 (94)		
Tanjung Jaya	105.65939, − 6.48078	3			7.07 (74) [158.84]
Tanjung Jaya	105.65935, − 6.48047	3	1.65 (64)		
Tanjung Jaya	105.65940, − 6.48005	3	3.1 (18)		
Tanjung Jaya	105.65817, − 6.47995	3	1.23 (37)		
Tanjung Jaya	105.65817, − 6.48033	3	0.77 (77)		
Cipenyu Beach	105.64078, − 6.50363	2.7	1.3 (90)		
Cipenyu Beach	105.64101, − 6.50466	2.7	2.24 (117)		
Cipenyu Beach	105.64165, − 6.50461	2.7	1.51 (186)		
Cipenyu Beach	105.63815, − 6.50781	2.1			8.51 (42) [66.59]
Pantai Legon	105.63335, − 6.51699	2.3			13.49 (42) [124.58]
Tanjung Jaya	105.62888, − 6.52415	2.6			10.94 (97) [159.42]
Tanjung Jaya	105.62673, − 6.5296	2.8			13.2 (154) [121.83]
Pantai Batu	105.62356, − 6.54209	1.2	1.54 (62)		
Banyuasih	105.62223, − 6.55211	2.5	1.82 (63)		
Banyuasih	105.61664, − 6.56774	1.8	5.40 (11)		
Banyuasih	105.61785, − 6.56787	1.8	1.25 (144)		
Banyuasih	105.61800, − 6.56839	1.8	0.43 (176)		

Values in parenthesis are the distances from the shoreline. Values in brackets are the maximum inundation distances measured by the different team surveys

part of the slide, κ is equal to 1), $\theta(x, y)$ the local steepest slope angle, θ_x and θ_y the slope angles along the x and y axes respectively, and $\mathbf{F} = -\kappa \mathbf{g} \mathbf{h}_\mathbf{s} \cos(\theta) \tan(\phi) \mathbf{u} / \|\mathbf{u}\|$ the friction forces, where ϕ is the friction angle of the sliding materials. Curvature terms representing the effects of coordinate transformations (Savage and Hutter 1991) are considered as second-order terms in this paper. In this set of equations, water acts on the slide only through a buoyancy term and any drag contribution is neglected.

The basal friction angle is adjusted through a sensitivity study to fit with the observed water waves at the four tide gauges that recorded the tsunami. Values of 1, 2, 5 and 10° were tested and results were analyzed in the near-field (Gauge 1, Fig. 6a) and in the far-field (Gauge 3, Fig. 6b and Gauge 6, Fig. 6c). Gauges locations are presented in Fig. 9 and listed in Table 1.

4.2. Tsunami Model

As in Paris et al. (2019), tsunami generation is modeled by solving shallow water equations (Eqs. 4, 5, 6) during 80 s after the landslide triggering. Beyond 80 s, Boussinesq equations Eqs. (7, 8, 9) are solved in order to take into account any possible dispersive effects during the propagation. The shallow water equations solved by AVALANCHE are written as:

$$\frac{\partial \eta}{\partial t} + \frac{\partial (hu)}{\partial x} + \frac{\partial (hv)}{\partial y} = -\frac{\partial d}{\partial t}; \qquad (4)$$

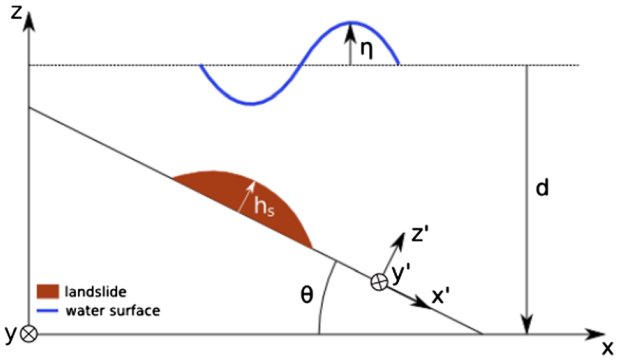

Figure 5
Definition of parameters used in the AVALANCHE model, with h_s the slide's thickness, η the surface elevation, d the depth and θ the local steepest slope angle

$$\frac{\partial u}{\partial t} + u\frac{\partial u}{\partial x} + v\frac{\partial u}{\partial y} = -g\frac{\partial \eta}{\partial x} + F_x; \tag{5}$$

$$\frac{\partial v}{\partial t} + u\frac{\partial v}{\partial x} + v\frac{\partial v}{\partial y} = -g\frac{\partial \eta}{\partial y} + F_y \tag{6}$$

where η is the surface elevation, $h = \eta + d$ the water column height, d is the depth, u and v the depth-averaged velocities along the x and y axes respectively and F_x and F_y the friction and Coriolis forces, which are assumed to be negligible in our modeling.

Following Løvholt et al. (2008), the Boussinesq equations read:

$$\frac{\partial \eta}{\partial t} + \frac{\partial (hu)}{\partial x} + \frac{\partial (hv)}{\partial y} = -\frac{\partial d}{\partial t}; \tag{7}$$

$$\begin{aligned}\frac{\partial u}{\partial t} + u\frac{\partial u}{\partial x} + v\frac{\partial u}{\partial y} = &-g\frac{\partial \eta}{\partial x} + \frac{d^3}{3}\left[\frac{\partial^2 u_t}{\partial x^2} + \frac{\partial^2 v_t}{\partial x \partial y}\right] \\ &+ \frac{d}{2}\left[u_t\frac{\partial^2 d}{\partial x^2} + u_t\frac{\partial^2 d}{\partial x \partial y}\right] + d\frac{\partial d}{\partial x}\frac{\partial u_t}{\partial x} \\ &+ \frac{d}{2}\left[\frac{\partial d}{\partial x}\frac{\partial v_t}{\partial y} + \frac{\partial d}{\partial y}\frac{\partial v_t}{\partial x}\right] + F_x;\end{aligned} \tag{8}$$

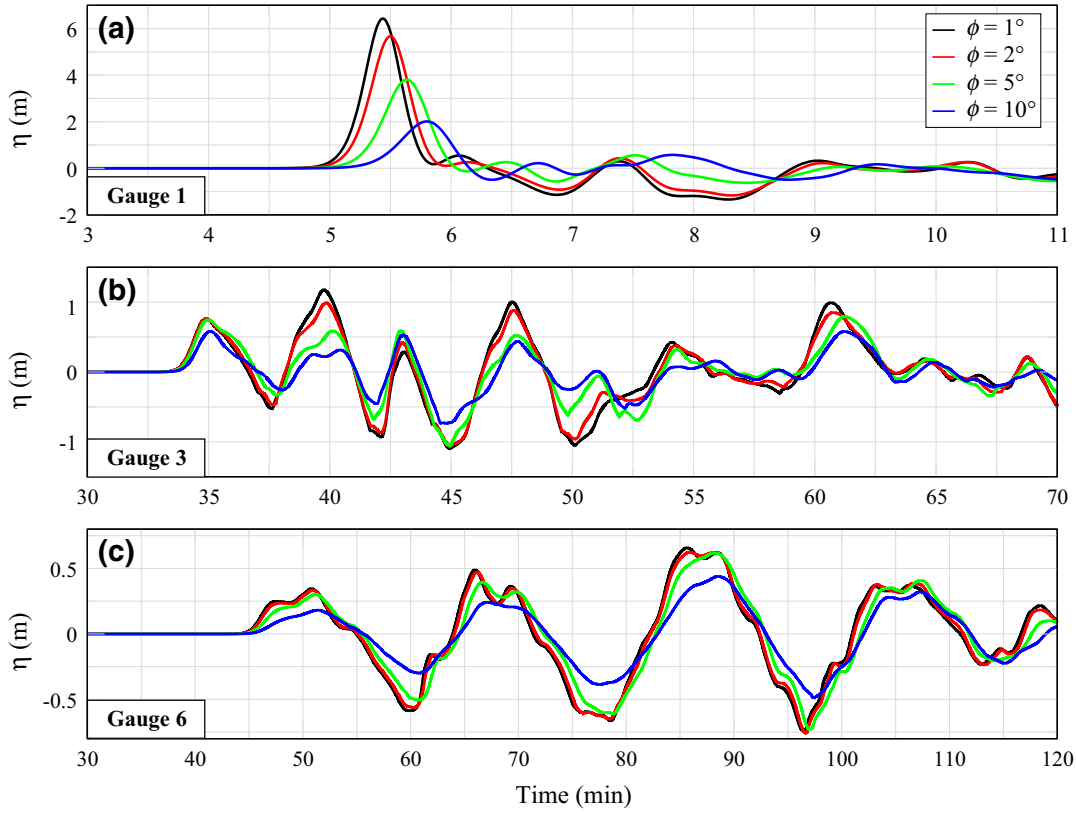

Figure 6
Time series calculated **a** at Gauge 1 near the Anak Krakatau volcano, **b** at Marina Jambu tide gauge (Gauge 3) and **c** at Kota Agung tide gauge (Gauge 6), using friction angles ϕ of 1° (black line), 2° (red line), 5° (green line) and 10° (blue line)

$$\frac{\partial v}{\partial t}+u\frac{\partial v}{\partial x}+v\frac{\partial v}{\partial y}=-g\frac{\partial \eta}{\partial y}+\frac{d^3}{3}\left[\frac{\partial^2 v_t}{\partial y^2}+\frac{\partial^2 u_t}{\partial x\partial y}\right]+\frac{d}{2}\left[v_t\frac{\partial^2 d}{\partial y^2}+v_t\frac{\partial^2 d}{\partial x\partial y}\right]+d\frac{\partial d}{\partial y}\frac{\partial v_t}{\partial y}+\frac{d}{2}\left[\frac{\partial d}{\partial x}\frac{\partial u_t}{\partial y}+\frac{\partial d}{\partial y}\frac{\partial u_t}{\partial x}\right]+F_y \quad (9)$$

where u_t and v_t the time-derivatives of u and v.

Both the landslide and shallow water equations, which are very similar, are solved by Godunov's finite-volume scheme, extended to second order by a Van Leer scheme (Heinrich et al. 2001a; Labbé et al. 2012). This numerical scheme was validated with an analytical solution in Mangeney et al. (2000). Boussinesq equations are solved using a finite-difference scheme for spatial derivatives together with a Crank–Nicolson scheme for the temporal discretization. This latter scheme is based on an iterative procedure that uses centered differences for linear terms and forward differences for advection terms. The implicit momentum equations are solved by alternating implicit sweeps in the x and y components using an ADI method (Alternating Direction Implicit). For a given direction, the dispersion terms in the other direction are discretized explicitly. For each direction (x and y), a tridiagonal matrix is then solved at each iteration, following Pedersen and Løvholt (2008).

The sea-bottom deformation due to the landslide, $\partial d/\partial t$ in Eq. (7), is computed as a forcing term:

$$\frac{\partial d}{\partial t}=\frac{1}{\cos\theta}\frac{\partial h_s}{\partial t} \quad (10)$$

4.3. Models Set-Up

For simulating the landslide and tsunami in the near-field (i.e. Anak Krakatau volcano and the other islands of the Krakatau archipelago), a pre-collapse topography and bathymetry of Gouhier and Paris (2019) was used. The pre-collapse topography of Anak Island was derived from the DEMNAS (national digital elevation model of Indonesia, spatial resolution of 0.27 arc-second using the vertical datum EGM2008, provided by the Indonesian Geospatial Agency, and available at http://tides.big.go.id/DEMNAS/index.html). The original DEMNAS was slightly modified in order to include the latest growth of the edifice, as seen on photographs taken in August and November 2018,[5] and satellite images (e.g. Sentinel-2 image captured on 30 September 2018, and PlanetScope image captured on 17 December 2018). Pre-collapse bathymetry is from Deplus et al. (1995). As explained in Gouhier and Paris (2019), the contour of the collapse scar was inferred from a Sentinel-1A image captured $\sim$ 8:30 hours after the collapse (22/12/2018 at 22:33:44 UTC) and photographs taken by Susi Air flight crew the day after (23/12/2018).

Note that the subaerial volume estimated by Gouhier and Paris (2019) likely corresponds to a minimum value because there is no data available on post-collapse bathymetry and the submarine extent of the collapse scar. Considering a slope between 5 and 8° in the continuity of the subaerial landslide part, the total volume approaches 150 million m^3. This volume is two times smaller than the volume of 270 million m^3 modeled by Grilli et al. (2019). Pre and post-collapse topography and bathymetry around the Anak Krakatau are presented in Fig. 7c, d, respectively.

The bathymetric grids are built from the BATNAS one, with a spatial resolution of 180 m (available at http://tides.big.go.id/DEMNAS/Batnas.php). The model uses a system of multiple grids (coarse grid over deep water regions and fine grids over coastal regions) to model local effects of bathymetry. The parent nested grid covers the Sunda Strait, from eastern of Sumatra to western of Java Island (see Figs. 1 or 9 for the grid footprint). Five child grids are used with a resolution of approximately 25 m: the first domain covers the Kota Agung Bay, the second the Bandar Lampung Bay, the third the Kalianda area from northern of Taman Agung to southern of Lampung, the fourth the Teluk Lada area from western of Tanjung Lesung to southern of Anjer-Kidu, and the fifth the Anjer-Kidu area from Marina Jambu to eastern of Ciwandan (grids A, B, C, D and E, respectively, see Fig. 9).

[5] https://www.oysteinlundandersen.com/krakatau-volcano/krakatau-eruption-seen-from-anyer-west-java-17th-november-2018/.

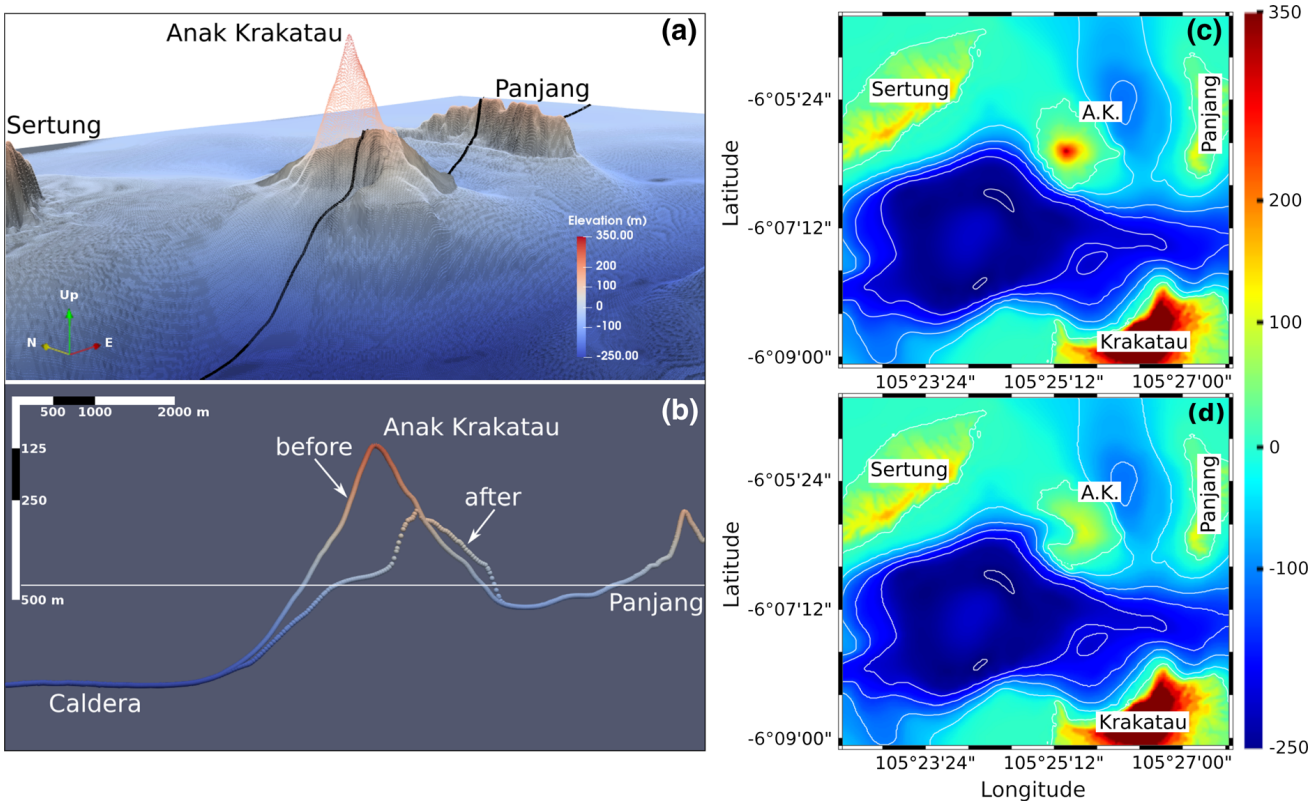

Figure 7
a Pre and post-collapse topo-bathymetry of Anak Krakatau volcano (dotted grid in transparency illustrating the pre-collapse volcanic edifice); **b** cross-section of the pre-collapse (solid line) and post-collapse (dotted line) topo-bathymetry following the black line in **a**. The water surface at rest is represented by the horizontal white line. There is a ×5 vertical exaggeration. The scale in **a**, **b** is the same and only the view angle changes. Right panels show **c** pre and **d** post-collapse topo-bathymetry of Anak Krakatau volcano. Bathymetric contours range from 0 to −250 m every 50 m

5. *Results*

5.1. *Landslide Simulation*

The sensitivity study realized on the basal friction angle shows that its influence on the generated wave heights decreases with distance. The basal friction angle plays a major role in the near-field (Gauge 1, Fig. 6a) but its influence is minor in the far-field (Gauges 3 and 6, Fig. 6b, c). There is no significant difference between 1 and 2°, at least in terms of computed wave height at the coasts. Using a friction angle of 2°, calculated water heights are of 75 cm at Marina Jambu and 33 cm at Kota Agung, whereas observed ones are of 60 and 35 cm, respectively. A friction angle of 10° results in wave heights of 56 and 16 cm respectively. Based on all the tide gauges, the best fit is obtained with a friction angle of 2°. This low value is consistent with the one used in Giachetti et al. (2012) and other studies about landslides on volcanoes slopes [e.g. Le Friant et al. (2003) with 7° for the flank collapse of Montagne Pelée (Martinique, Lesser Antilles), Kelfoun et al. (2010) with values between 3 and 5° for different landslides scenarios envisaged at Reunion Island or Giachetti et al. (2011) with values between 1.3 and 3.9° for reproducing the Güìmar debris avalanche (Tenerife, Canary Islands)].

A large part of the simulated landslide collapses in about 40 s (Fig. 8c), the volcano summit decreasing from about 350 m of altitude to about 120 m (Figs. 7, 8), which is concordant with the topographic reconstruction of Gouhier and Paris (2019). Beyond 40 s, the calculated ground displacement is negligible and no longer has any effect on the water surface deformation. The landslide covers a horizontal distance of about 4000 m from the volcano to the

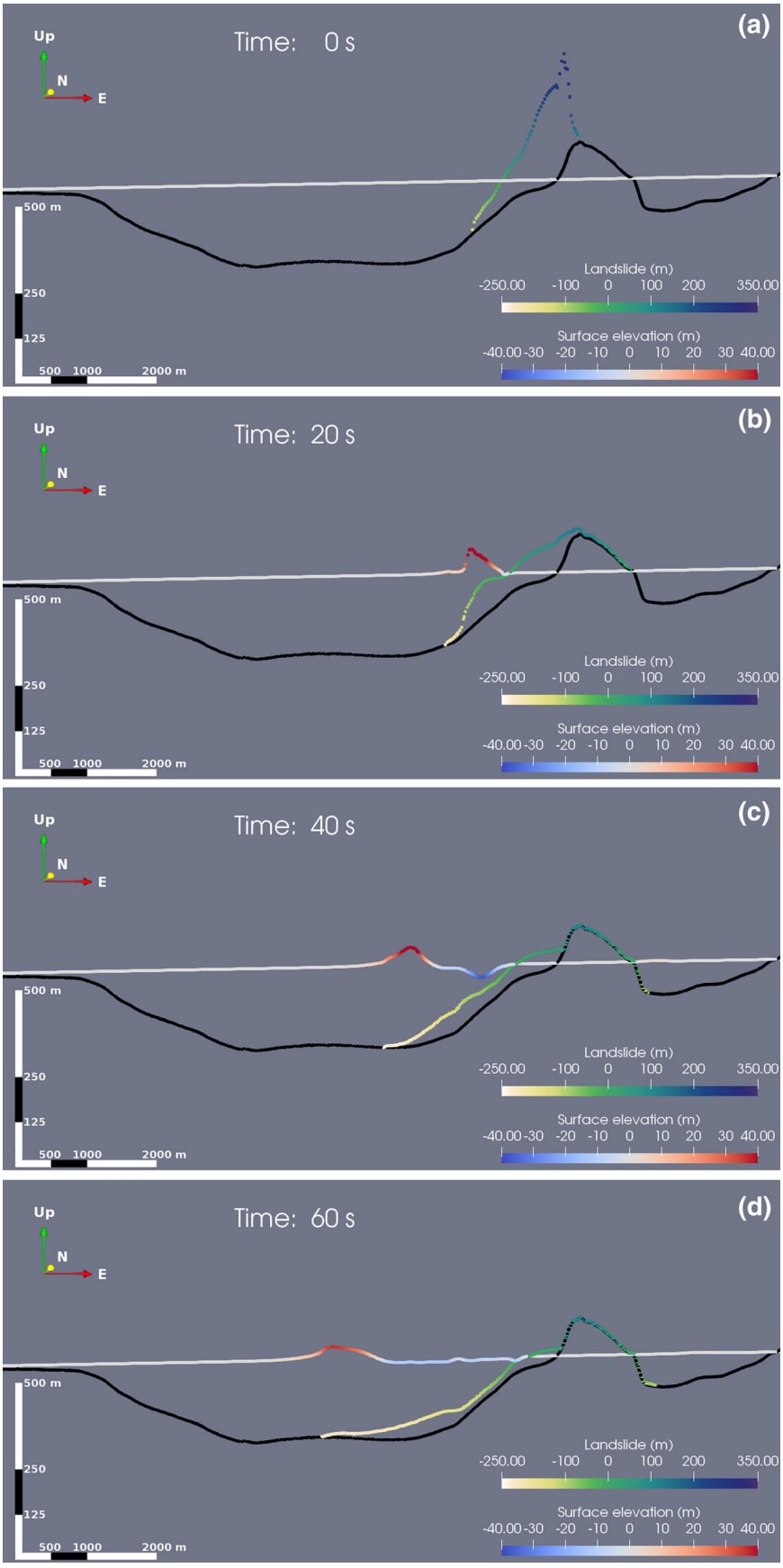
(a)
Time: 0 s
Up
N
E
500 m
250
125
500 1000 2000 m
Landslide (m)
-250.00 -100 0 100 200 350.00
Surface elevation (m)
-40.00 -30 -20 -10 0 10 20 30 40.00
(b)
Time: 20 s
Up
N
E
500 m
250
125
500 1000 2000 m
Landslide (m)
-250.00 -100 0 100 200 350.00
Surface elevation (m)
-40.00 -30 -20 -10 0 10 20 30 40.00
(c)
Time: 40 s
Up
N
E
500 m
250
125
500 1000 2000 m
Landslide (m)
-250.00 -100 0 100 200 350.00
Surface elevation (m)
-40.00 -30 -20 -10 0 10 20 30 40.00
(d)
Time: 60 s
Up
N
E
500 m
250
125
500 1000 2000 m
Landslide (m)
-250.00 -100 0 100 200 350.00
Surface elevation (m)
-40.00 -30 -20 -10 0 10 20 30 40.00

◀Figure 8
Snapshots along a W–E cross-section of the simulated water wave (blue to red scale) and landslide (white to dark blue scale) at **a** t = 0 s, **b** t = 20 s, **c** t = 40 s and **d** t = 60 s. The post-collapse topo-bathymetry is represented in black solid line. There is a ×5 vertical exaggeration

1883 submarine caldera, with an average velocity of 35 m.s^{-1}. Figure 7 shows both the numerical initial and final states of the volcano, with a cross-section illustrating the major topographic change induced by the flank collapse.

As shown by the temporal evolution of the landslide tip and the associated tsunami front (Fig. 8), velocities are quite similar, which can signify efficient transfer process. But further investigation may be needed as the part of the landslide with the largest thickness situated in smaller depth may be more important for energy transfer than the slide tip, and the wave is a bit too fast to stay in contact with this area.

5.2. *Tsunami Simulation*

Computed results are analyzed through a maximum surface elevations map (Fig. 9) covering the entire domain. On the tsunami path, synthetic gauges are located at places where tide gauges recorded the tsunami, i.e. Marina Jambu and Ciwandan for Java, Kota Agung and Panjang for Sumatra (Gauges 3, 4, 6 and 7 respectively, see Fig. 9, Table 1) and results are compared with detided data (the tide filter is based on the MATLAB package T_TIDE (Pawlowicz et al. 2002)) in Fig. 10. Other synthetic gauges are used, near the volcano, at Tanjung Lesung and Kalianda (Gauges 1, 2 and 5 respectively, see Fig. 9, Table 1) in order to compare the results to the field surveys data in these areas.

During the first 20 s of collapse the tsunami wave is being generated until it reaches a maximum positive elevation of 80 m (Fig. 8). Sertung Island is the first place to be hit after 80 s of wave propagation. It is located 3 km from the volcano which results in a wave celerity of about 38 m.s^{-1}. Rakata Island is hit in about the same time, with a

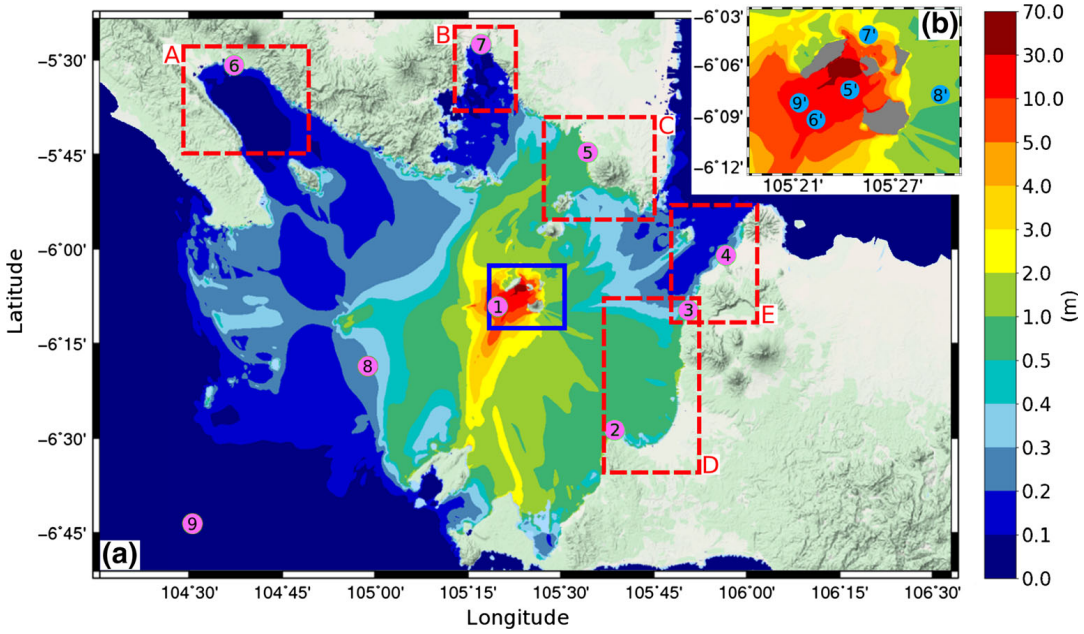

Figure 9
a Maximum surface elevations computed in Sunda Strait after the collapse of Anak Krakatau volcano. Pink discs with numbers represent the synthetic gauges locations: 10 km away from the volcano (1), at Tanjung Lesung (2), Marina Jambu (3), Ciwandan (4), Kalianda (5), Kota Agung (6), Panjang (7) and the two gauges (8 and 9) used for the comparison between the shallow water and the Boussinesq models. Child grids described in Sect. 4.3 are represented by the dashed red rectangles. **b** Close-up of the results around the volcano, corresponding to the blue box in **a**. Blue discs with numbers represent the synthetic gauges locations used by Grilli et al. (2019)

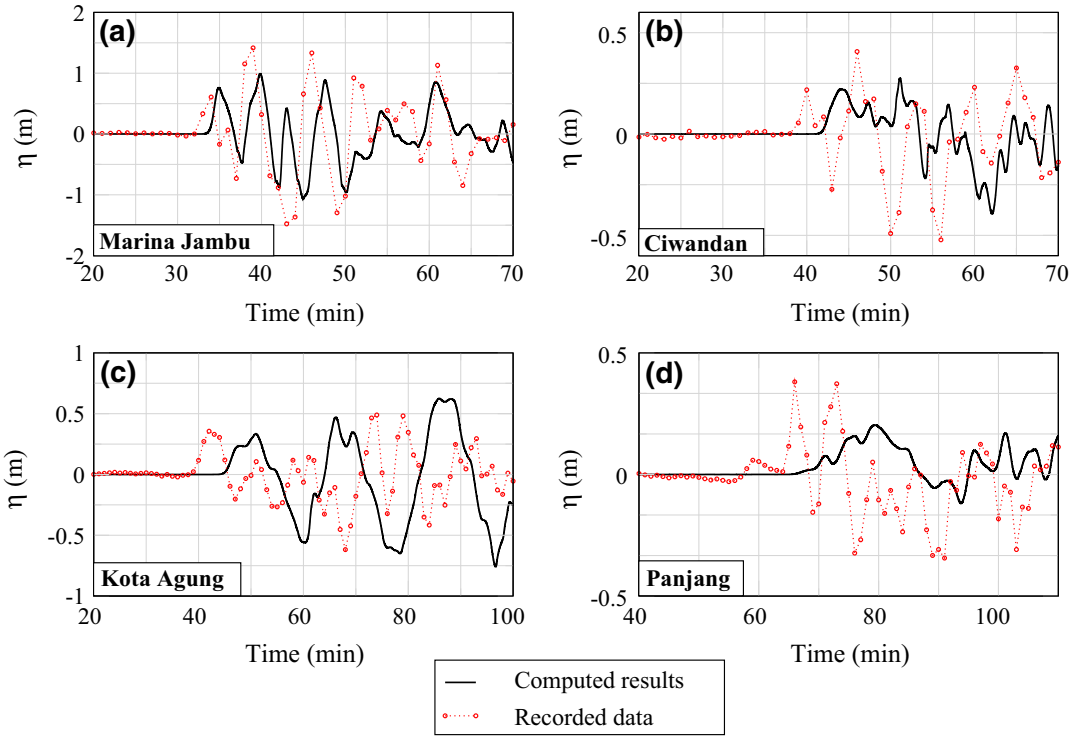

Figure 10
Comparison between recorded data (in red) and simulated water surface elevations (in black) at **a** Marina Jambu, **b** Ciwandan, **c** Kota Agung and **d** Panjang (Gauges 3, 4, 6 and 7, respectively, see Fig. 9)

speed of 50 m.s^{-1}. Then the wave travels around the Sunda Strait and reaches Gauge 1 [5 min after the collapse, with 5.6 m of wave height (Fig. 11a)], Gauge 2 [Tanjung Lesung, 29 min, 1.7 m (Fig. 11b)], Gauge 3 [Marina Jambu, 34 min, 75 cm (Fig. 10a)], Gauge 4 [Ciwandan, 42 min, 22 cm (Fig. 10b)], Gauge 5 [Kalianda, 49 min, 1.2 m (Fig. 11c)], Gauge 6 [Kota Agung, 45 min, 33 cm (Fig. 10c)] and Gauge 7 [Panjang, 1:06 hours, 20 cm (Fig. 10d)].

For the first wave, simulated water heights on the synthetic gauges are quite consistent with the tide gauges records (75 cm computed vs 60 cm recorded at Marina Jambu, 22 cm vs 20 cm at Ciwandan, 33 cm vs 35 cm at Kota Agung), excepted at Panjang (20 cm vs 37 cm). In addition, according to the concert video, the height of the first water wave is estimated to be 1–2 m, which is consistent with the computed water height of 1.7 m at Tanjung Lesung (Fig. 11b, Gauge 2). However, computed arrival times are late compared to the recorded ones (1 min at Marina Jambu, 3 min at Ciwandan, 5 min at Kota Agung and 8 min at Panjang). The general wave pattern is well reproduced at Marina Jambu but poorly at Ciwandan, Kota Agung and Panjang.

5.3. *Dispersion Assessment*

In order to assess and highlight the potential dispersive effects in the Sunda Strait, shallow water simulation was performed with AVALANCHE and compared with the present Boussinesq simulation (Fig. 12). Time series calculated by the two models are compared at three synthetic gauges (Gauges 1, 8 and 9, Fig. 9) located in deep water at depths of 100 (Fig. 12a), 1140 (Fig. 12b) and 1960 m (Fig. 12c). Close to the source, both simulations produce approximately the same first water wave as depicted in Fig. 12a with water wave heights of about 5.5 m. However, dispersion effects are noticed in the far-field and in deep ocean. Compared to shallow water simulations, the period of the first wave increases during the propagation, ranging from about 1 min (Gauge 1, Fig. 12a) to about 1 min 30 s (Gauge 8, Fig. 12b) and about 2 min (Gauge 9, Fig. 12c).

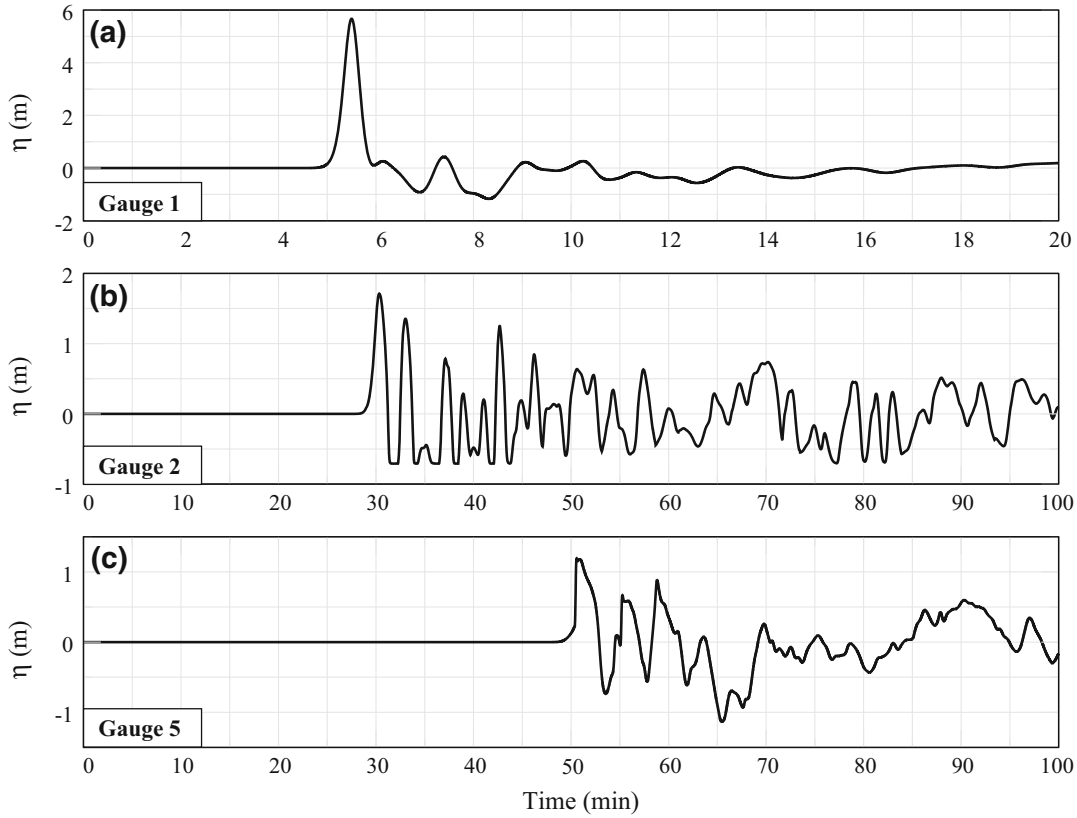

Figure 11
Computed surface elevations (m) **a** near the Anak Krakatau volcano, **b** at Tanjung Lesung and **c** at Kalianda (Gauges 1, 2 and 5, respectively, see Fig. 9)

6. *Discussion*

This study presents preliminary results of the 22 December 2018 Anak Krakatau collapse and tsunami simulations, comparing the computed numerical results with several observed data such as flow depths or recorded surface elevations. The main goal of this study was to better understand the landslide that occurred and assess its volume, despite the lack of submarine information. With the collapse of 150 million m^3 modeled following a Coulomb frictional law, the obtained water heights are quite consistent with the observed ones, all over the Sunda Strait, and the computed amplitudes of the first wave match the tide gauges-extracted amplitudes (with errors ranging from 6% at Kota Agung to 25% at Marina Jambu), excepted at Panjang (error of 46%).

In comparison with the study of Grilli et al. (2019), our results (water heights and time delays of the first wave) are very similar at the four tide gauges, with water heights differences of 50% at Marina Jambu, 12% at Ciwandan, 10% at Kota Agung and 0% at Panjang. In the near-field, our results are also very similar to the time series calculated at five additional gauges used by Grilli et al. (2019) (see Fig. 9b for gauges locations). The amplitudes of the generated water wave calculated by Grilli et al. (2019) are obviously larger in the near-field since the authors consider a landslide volume of 270 million m^3. Nevertheless, we obtain the same arrival times, periods and to a lesser extent the same wave behaviour [see Fig. 13 in our paper and Figure 5 in Grilli et al. (2019)]. Our results are also similar in the near-field to those of Heidarzadeh et al. (2020). Considering a forward modeling trial-error approach, the latter ones obtain a wave height of about 100–150 m with a wavelength of 1.5–2 km. Their results are close to our first simulated wave characterized by a maximum amplitude of 80 m and a wavelength of

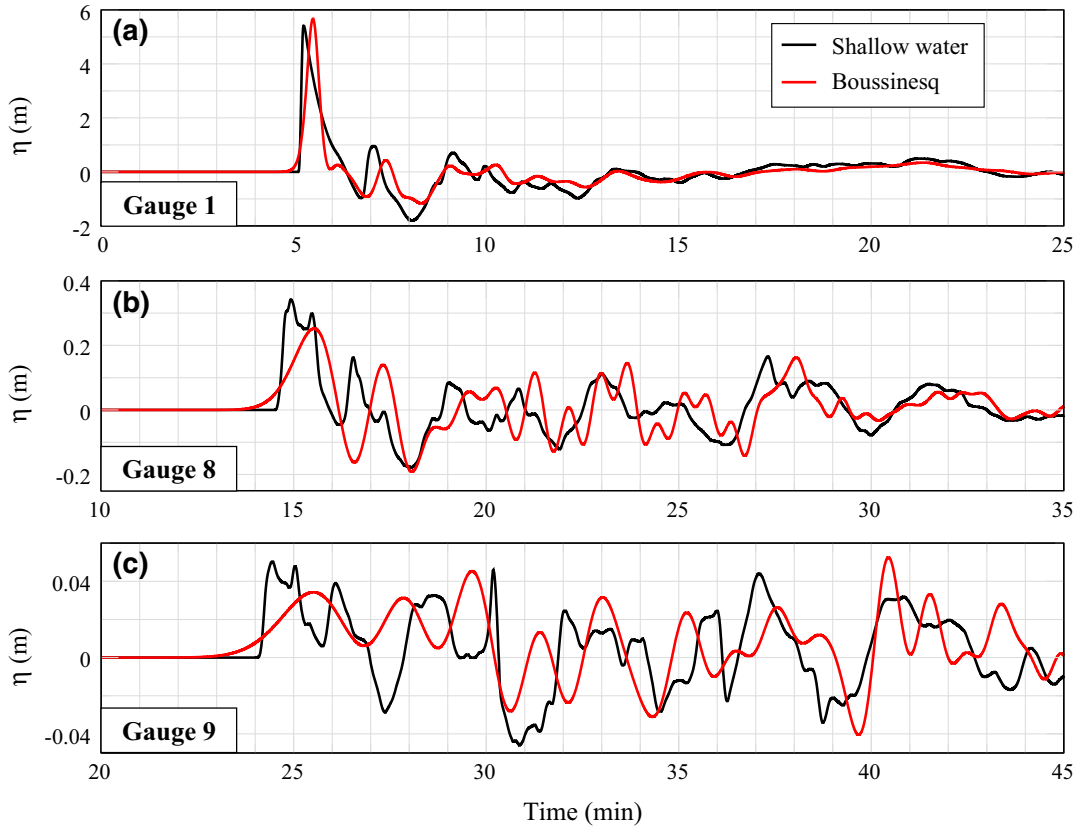

Figure 12
Comparison of time series calculated by the shallow water (in black) and the Boussinesq (in red) models at Gauges **a** 1, **b** 8 and **c** 9 (Fig. 9). The water depths of these gauges are: **a** 100 m, **b** 1140 m and **c** 1960 m

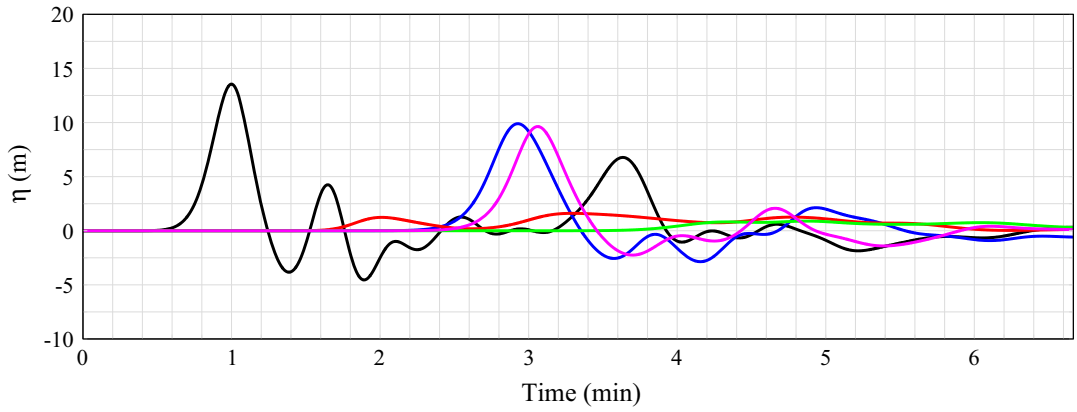

Figure 13
Time series of surface elevation calculated in the near-field by our model (150 million m^3 and the code AVALANCHE) at the Gauges 5′ (black), 6′ (blue), 7′ (red), 8′ (green) and 9′ (magenta) used by Grilli et al. (2019) and presented in Fig. 9b. Results are very similar to those presented in Figure 5e in Grilli et al. (2019)

about 2 km [see Fig. 8 in this study and Figure 12 in Heidarzadeh et al. (2020)].

Tables 2 and 3 show computed water heights at places studied by the field surveys of Takabatake et al. (2019) and the BMKG, and the KKP, respectively. Although the comparison between inundation or run-up heights with water wave heights may be hard to realise, we see for instance that at Cipenyu

Beach, where highest run-up values were measured, we obtain the highest water heights. The computed wave heights are a little bit shorter than the observed ones by the BMKG survey, with 3–4 m vs 5–6 m. At the 5 locations close to the shoreline, i.e. distance lower than 30 m [Carita Lagon for BMKG survey (Table 2); Karang Suraga, Bulakan, Tanjung Jaya and Banyuasih for the KKP survey (Table 3)], the measured flow depths are on the same order that the computed tsunami height at the coast. Note that the bathymetric resolution (180 m interpolated to 25 m for the child grids) used in this study does not allow to compare precise inundation or run-up heights.

Although the results are encouraging, some limitations can be pointed out. First of all, the landslide reconstruction may be subject to discussion. It has been realized based on satellite images of the 23rd of December for the subaerial part and a quasi constant slope hypothesis for the submarine part. Unfortunately, the intense volcanic activity of the days following the tsunami has completely changed the shape of the volcano and it has made precise reconstruction impossible. Nevertheless, tsunami simulation associated to this landslide is rather consistent with observed water heights. A sensitivity study on the basal friction coefficient ϕ (Fig. 6) suggests that these water heights may vary quasi linearly with ϕ in the near-field, the smaller the friction angle, the higher the water wave heights. In the far-field along the coasts of Java or Sumatra, differences of water heights between $\phi = 1^\circ$ or $\phi = 2^\circ$ are not significant.

Second, the time delays of wave arrivals at the four tide gauges (Gauges 3, 4, 6 and 7, Fig. 9) could indicate that the landslide volume and its dynamics are unknown. However, sensitivity tests (not shown in this study) on the landslide volume produce similar results in terms of wave arrivals. In addition, our travel times are similar to those calculated by Giachetti et al. (2012) and Grilli et al. (2019) for landslide volumes of 280 million m^3 and 270 million m^3, respectively. A possible explanation would be inaccuracies of the bathymetric data in this area. Travel times should thus be interpreted carefully. More information on the landslide will be available thanks to forthcoming surveys in the caldera.

Third, this study is a first attempt of simulating the collapse of Anak Krakatau volcano using 2D depth-averaged models both for the landslide and the tsunami. Several complex phenomena are not taken into account such as mixing of the slide with the surrounding water, soil erosion or dissipation of water waves due to wave breaking or friction.

Finally, according to Glimsdal et al. (2013), the dispersive effects can be estimated using the dispersion parameter:

$$\tau = \frac{4{h_0}^2 L}{\lambda^3} \tag{11}$$

where h_0 is the depth at the source, L the distance to the coast of interest and λ the source width or in other terms the wavelength.

The dispersion parameter is ~ 1.4 at Kalianda up to ~ 3.4 at Kota Agung, with $h_0 = 250$ m, L between 45 and 110 km (see Table 1) and $\lambda = 2000$ m (see Fig. 8b), and suggests that the propagation is highly dispersive. Results of the comparison between the shallow water and Boussinesq simulations (Fig. 12) confirm that the first wave is subjected to dispersion, losing high-frequency components and being stretched by dispersive effects. After 25 min of propagation in deep ocean (Fig. 12c), the period is approximately two times longer and the amplitude decreases by about 50% compared to the one calculated by the shallow water model. The use of the Boussinesq model in this study is therefore relevant.

7. Conclusion

The 22 December, 2018 Anak Krakatau southwestern flank collapse is modeled by a 2D depth-integrated code with a Coulomb frictional law and a basal friction angle of 2°. The generated tsunami is propagated using a Boussinesq model. This study highlighted some points and revealed some issues:

- The computed water heights from the present modeling fit well with those recorded at tide gauges of Marina Jambu, Ciwandan and Kota Agung (errors of 25%, 10% and 6%, respectively), with the video recorded at Tanjung Lesung and

with the different observed data from the KKP, BMKG and Takabatake et al. (2019) field surveys.

- Results presented in this study are very similar to those obtained by Grilli et al. (2019) both in the near-field and in the far-field. However, their model is 3D, suggesting proper representation of the governing processes in both studies. Heights and wavelengths of the first wave are also very close to those obtained by Heidarzadeh et al. (2020) in the near-field.
- Delays between simulated and observed travel times may be attributed to inaccuracies in the bathymetric data, particularly in the Bandar Lampung Bay.
- Despite the lack of submarine information at the bottom of the volcano, the collapse of the reconstructed volume of 150 million m^3 produces water waves that fit well with the observed results.
- The sensitivity study on the basal friction angle shows that its influence on the generated wave heights decreases with distance and that there are no significant differences of water heights between basal friction coefficients of 1° or 2°.
- Finally, a comparison between a Boussinesq model and a shallow water propagation highlights dispersive effects in the Sunda Strait that appear to be significant for the first waves. In deep waters, their periods progressively increase whereas their amplitudes progressively decrease.

Acknowledgements

We thank Abdul Muhari, from the Directorate of Sustainable Utilization of Coastal Zone and Small Islands, Ministry of Marine Affairs and Fisheries, Indonesia, for providing us with the tide gauges data and the KKP field survey data, and Gegar Prasetya, for providing us the BMKG field survey data.

References

Abadie, S., Harris, J., Grilli, S., & Fabre, R. (2012). Numerical modeling of tsunami waves generated by the flank collapse of the Cumbre Vieja Volcano (La Palma, Canary Islands): Tsunami source and near fiedl effects. *Journal of Geophysical Research*, *117*, 5.

Assier-Rzadkiewicz, S., Heinrich, P., Sabatier, P., Savoye, B., & Bourillet, J. (2000). Numerical modelling of a landslide-generated tsunami: The 1979 Nice event. *Pure and Applied Geophysics*, *157*(10), 1707–1727.

Bondevik, S., Løvholt, F., Harbitz, C., Mangerud, J., Dawson, A., & Svendsen, J. (2005). The Storegga slide tsunami—comparing field observations with numerical simulations. *Marine and Petroleum Geology*, *22*, 195–208.

Camus, G., Gourgaurd, A., & Vincent, P. (1987). Petrologic evolution of Krakatau (Indonesia): Implications for a future activity. *Journal of Volcanology and Geothermal Research*, *33*, 299–316.

Choi, B., Pelinovsky, E., Kim, K., & Lee, J. (2003). Simulation of the trans-oceanic tsunami propagation due to the 1883 Krakatau volcanic eruption, Copernicus Publications on behalf of the European Geosciences Union. *Natural Hazards and Earth System Science*, *3*(5), 321–332.

Cooke, R. (1981). Eruptive history of the volcano at Ritter Island. *Geological Survey of Papua New Guinea Memoir*, *10*, 115–123.

Deplus, C., Bonvalot, S., Dahrin, D., Diament, M., Harjono, H., & Dubois, J. (1995). Inner structure of the Krakatoa volcanic complex (Indonesia) from gravity and bathymetry data. *Journal of Volcanology and Geothermal Research*, *64*, 23–51.

Fine, I. V., Rabinovich, A. B., Thomson, R. E., & Kulikov, E. A. (2003). *Numerical modeling of tsunami generation by submarine and subaerial landslides* (pp. 69–88). Dordrecht: Springer.

Franz, M., Jaboyedoff, M., Locat, J., & Podladchikov, Y. (2015). Testing a landslide-generated tsunami model. The case of the Nicolet landslide (Québec, Canada), In *Conference GEOQuébec 2015*, Québec City, QC, Canada.

Fritz, H., Mohammed, F., & Yoo, J. (2009). Lituya Bay landslide impact generated mega-tsunami 50th anniversary. *Pure and Applied Geophysics*, *166*, 153–175.

Giachetti, T., Paris, R., Kelfoun, K., & Ontowirjo, B. (2012). Tsunami hazard related to a flank collapse of Anak Krakatau volcano, Sunda Strait, Indonesia. *Geological Society London Special Publication*, *361*, 79–89.

Giachetti, T., Paris, R., Kelfoun, K., & Pérez-Torrado, F. (2011). Numerical modelling of the tsunami triggered by the Güìmar debris avalanche, Tenerife (Canary Islands): Comparison with field-based data. *Marine Geology*, *284*, 189–202.

Glimsdal, S., L'Heureux, J.-S., Harbitz, C., & Løvholt, F. (2016). The 29th January 2014 submarine landslide at Statland, Norway-landslide dynamics, tsunami generation, and run-up. *Landslides*, *13*(6), 1435–1444.

Glimsdal, S., Pedersen, G., Harbitz, C., & Løvholt, F. (2013). Dispersion of tsunamis: Doest it really matter? *Natural Hazards and Earth System Sciences*, *13*, 1507–1526.

Gouhier, M., & Paris, R. (2019). SO2 and tephra emissions during the December 22, 2018 Anak Krakatau flank-collapse eruption. *Volcanica*, *2*(2), 91–103.

Grilli, S., O'Reilley, C., Harris, J., Tajalli Bakhsh, T., Tehranirad, B., Banihashemi, S., et al. (2015). Modeling of SMF tsunami

hazard along the upper US East Coast: Detailed impact around Ocean City, MD. *Natural Hazards*, *76*, 705–746.

Grilli, S., Tappin, D., Carey, S., Watt, S., Ward, S., Grilli, A., et al. (2019). Modelling of the tsunami from the December 22, 2018 lateral collapse of Anak Krakatau volcano in the Sunda Straits, Indonesia. *Scientific Reports*, *9*, 11946.

Grilli, S., & Watts, P. (2005). Tsunami generation by submarine mass failure. I: Modeling, experimental validation, and sensitivity analyses. *Journal of Waterway, Port, Coastal and Ocean Engineering*, *131*(6), 283–297.

Haflidason, H., Sejrup, H., Nygard, A., Meinert, J., Bryn, P., Lien, R., et al. (2004). The Storegga slide: Architecture, geometry and slide development. *Marine Geology*, *213*(1–4), 201–234.

Harbitz, C. (1992). Model simulations of tsunamis generated by the Storegga slides. *Marine Geology*, *105*(1–4), 1–21.

Harbitz, C., Glimsdal, S., Løvholt, F., Kveldsvik, V., Pedersen, G., & Jensen, A. (2014). Rockslide tsunamis in complex fjords: From an unstable rock slope at Åkerneset to tsunami risk in western Norway. *Coastal Engineering*, *88*, 101–122.

Harbitz, C., Pedersen, G., & Gjevik, B. (1993). Numerical simulations of large water waves due to landslides. *Journal of Hydraulic Engineering*, *119*(12), 1325–1342.

Harjono, H., Diament, M., Dubois, J., & Larue, M. (1991). Seismicity of the Sunda strait: Evidence for crustal extension and volcanological implications. *Tectonics*, *10*, 17–30.

Heidarzadeh, M., Ishibe, T., Sandanbata, O., Muhari, A., & Wijanarto, A. (2020). Numerical modeling of the subaerial landslide source of the 22 December 2018 Anak Krakatoa volcanic tsunami Indonesia. *Ocean Engineering*, *20*, 195.

Heidarzadeh, M., Krastel, S., & Yalçiner, A. (2014). The state-of-the-art numerical tools for modeling landslide tsunamis: A short review. In S. Krastel, J.-H. Behrmann, D. Völker, M. Stipp, C. Berndt, R. Urgeles, J. Chaytor, K. Huhn, M. Strasser, & C. Harbitz (Eds.), *Submarine mass movements and their consequences: 6th international symposium* (pp. 483–495). Cham: Springer.

Heinrich, P., Boudon, G., Komorowski, J. C., Sparks, R. S. J., Herd, R., & Voight, B. (2001b). Numerical simulation of the December 1997 Debris Avalanche in Montserrat, Lesser Antilles. *Geophysical Research Letters*, *28*(13), 2529–2532.

Heinrich, P., & Piatanesi, A. (2000). Near-field modeling of the July 17, 1998 tsunami in Papua New Guinea. *Geophysical Research Letters*, *27*(19), 3037–3040.

Heinrich, P., Piatanesi, A., & Hébert, H. (2001a). Numerical modelling of tsunami generation and propagation from submarine slumps: The 1998 Papua New Guinea event. *Geophysical Journal International*, *145*(1), 97–111.

Horrillo, J., Wood, A., Kim, G.-B., & Parambath, A. (2013). A simplified 3-D Navier–Stokes numerical model for landslide-tsunami: Application to the Gulf of Mexico. *Journal of Geophysical Research: Oceans*, *118*(12), 6934–6950.

Huang, B., Yin, Y., Wang, S., Tan, J., & Liu, G. (2017). Analysis of the Tangjiaxi landslide-generated waves in the Zhexi Reservoir, china, by a granular flow coupling model. *Natural Hazards and Earth System Sciences*, *17*, 657–670.

Hébert, H., Piatanesi, A., Heinrich, P., & Schindelé, F. (2002). Numerical modeling of the September 13, 1999 landslide and tsunami on Fatu Hiva Island (French Polynesia). *Geophysical Research Letters*, *29*(10), 10–13.

Jiang, L., & LeBlond, P. (1992). The coupling of a submarine slide and the surface waves which it generates. *Journal of Geophysical Research: Oceans*, *97*(C8), 12731–12744.

Johnson, R. (1987). Large-scale volcanic cone collapse; the 1888 slope failure of Ritter volcano. *Bulletin of Volcanology*, *49*, 669–679.

Kelfoun, K., Giachetti, T., & Labazuy, P. (2010). Landslide-generated tsunamis at Réunion Island. *Journal of Geophysical Research: Earth Surface*, *115*, F4.

Kirby, J., Shi, F., Nicolsky, D., & Misra, S. (2016). The 27 April 1975 Kitimat, British Columbia, submarine landslide tsunami: A comparison of modeling approaches. *Landslides*, *13*, 1421–1434.

Labbé, M., Donnadieu, C., Daubord, C., & Hébert, H. (2012). Refined numerical modeling of the 1979 tsunami in Nice (French Riviera): Comparison with coastal data. *Journal of Geophysical Research: Earth Surface*, *117*, F1.

Le Friant, A., Heinrich, P., Deplus, C., & Boudon, G. (2003). Numerical simulation of the last flank-collapse event of Montagne Pelée, Martinique, Lesser Antilles. *Geophysical Research Letters*, *30*, 2.

L'Heureux, J.-S., Glimsdal, S., Longva, O., Hansen, L., & Harbitz, C. (2011). The 1888 shoreline landslide and tsunami in Trondheimsfjorden, central Norway. *Marine Geophysical Research*, *32*(1), 313–329.

Liu, P.-F., Woo, S.-B., & Cho, Y.-S. (1998). *Computer programs for tsunami propagation and inundation* (p. 25). Cornell: Cornell University.

Løvholt, F., Pedersen, G., & Gisler, G. (2008). Oceanic propagation of a potential tsunami from the La Palma Island. *Journal of Geophysical Research: Oceans*, *113*(9), 1–21.

Ma, G., Kirby, J., Hsu, T.-J., & Shi, F. (2015). A two-layer granular landslide model for tsunami wave generation: Theory and computation. *Ocean Modelling*, *93*, 40–55.

Ma, G., Shi, F., & Kirby, J. (2012). Shock-capturing non-hydrostatic model for fully dispersive surface wave processes. *Ocean Modelling*, *43–44*, 22–35.

Mangeney, A., Heinrich, P., & Roche, R. (2000). Analytical solution for testing debris avalanche numerical models. *Pure and Applied Geophysics*, *157*, 1081–1096.

Masson, D., Harbitz, C., Wynn, R., Pedersen, G., & Løvholt, F. (2006). Submarine landslides: Processes, triggers and hazard prediction. *Philosophical Transactions of the Royal Society A: Mathematical, Physical and Engineering Sciences*, *364*(1845), 2009–2039.

Miller, D. J. (1960). Giant waves in Lituya Bay, Alaska. *US Geological Survey Professional Paper*, 354-C.

Muhari, A., Heidarzadeh, M., Susmoro, H., Nugroho, H., Kriswati, E., Supartoyo, W. A., et al. (2019). The December 2018 Anak Krakatau Volcano tsunami as inferred from post-tsunami field surveys and spectral analysis. *Pure and Applied Geophysics*, *21*, 1–5.

Nishimura, S., Nishida, J., Yokoyama, T., & Hehuwat, F. (1986). Neotectonics of the Straits of Sunda, Indonesia. *Journal of Southeast Asian Earth Science*, *1*, 81–91.

Nomanbhoy, N., & Satake, K. (1995). Generation mechanism of tsunamis from the 1883 Krakatau eruption. *Geophysical Reasearch Letters*, *22*(4), 509–512.

Okal, E. A., & Synolakis, C. E. (2003). A theoretical comparison of tsunamis from dislocations and landslides. *Pure and Applied Geophysics*, *160*(10–11), 2177–2188.

Paris, A., Okal, E., Guérin, C., Heinrich, P., Schindelé, F., & Hébert, H. (2019). Numerical modeling of the June 17, 2017 landslide and tsunami events in Karrat Fjord, west Greenland. *Pure and Applied Geophysics*, *176*(7), 3035–3057.

Pawlowicz, R., Beardsley, B., & Lentz, S. (2002). Classical tidal harmonic analysis including error estimates in MATLAB using T_TIDE. *Computers and Geosciences*, *28*, 929–937.

Pedersen, G. & Løvholt, F. (2008). Documentation of a global Boussinesq solver. *Preprint series in Applied Mathematics 1*. http://urn.nb.no/URN:NBN:no-27775.

Poupardin, A., Heinrich, P., Frère, A., Imbert, D., Hébert, H., & Flouzat, M. (2017). The 1979 submarine landslide-generated tsunami in Mururoa, French Polynesia. *Pure and Applied Geophysics*, *174*, 3293–3311.

Rodriguez, M., Chamot-Rooke, N., Hébert, H., Fournier, M., & Huchon, P. (2013). Owen Ridge deep-water submarine landslides: Implications for tsunami hazard along the Oman coast. *Natural Hazards and Earth System Science*, *13*, 417–424.

Satake, K., & Kato, Y. (2001). The 1741 Oshima–Oshima eruption: Extent and volume of submarine debris avalanche. *Geophysical Research Letters*, *28*, 427–430.

Satake, K., Smith, J., & Shinozaki, K. (2002). *'Three-dimensional reconstruction and tsunami model of the Nuuanu and Wailau giant landslides* (pp. 333–346). Hawaii: American Geophysical Union Geophysical Monograph Series.

Savage, S. B., & Hutter, K. (1989). The motion of a finite mass of granular material down a rough incline. *Journal of Fluid Mechanics*, *199*, 177–215.

Savage, S. B., & Hutter, K. (1991). The dynamics of avalanches of granular materials from initiation to runout. Part I: Analysis. *Acta Mechanica*, *86*(1), 201–223.

Shi, F., Kirby, J., Harris, J., Geiman, J., & Grilli, S. (2012). A high-order adaptive time-stepping TVD solver for Boussinesq modeling of breaking waves and coastal inundation. *Ocean Modelling*, *43–44*, 36–51.

Sigurdsson, H., Carey, S., Mandeville, C., & Bronto, S. (1991). Pyroclastic flows of the 1883 Krakatau eruption. *Eos Transactions of the American Geophysical Union*, *72*(36), 377–392.

Simkin, T., & Fiske, R. (1983). *Krakatau 1883: The volcanic eruption and its effects*. Washington, D.C.: Smithsonian Institution Press.

Skvortsov, A., & Bornhold, B. (2007). Numerical simulation of the landslide-generated tsunami in Kitimat Arm, British Columbia, Canada, 27 April 1975. *Journal of Geophysical Research: Earth Surface*, *112*, 2.

Stehn, C. (1929). The geology and volcanism of the Krakatau Group. In *Proceedings of the Fourth Pacific science congress*, pp. 1–55.

Sudradjat, A. (1982). The morphological development of Anak Krakatau Volcano, Sunda Strait. *Geologi Indonesia*, *9*, 1–11.

Susilohadi, S., Gaedicke, C., & Djajadihardja, D. (2009). Structures and sedimentary deposition in the Sunda Strait, Indonesia. *Tectonophysics*, *467*, 55–71.

Synolakis, C. E., Bardet, J.-P., Borrero, J. C., Davies, H. L., Okal, E. A., Silver, E. A., Sweet, S., & Tappin, D. R. (2002). The slump origin of the 1998 Papua New Guinea tsunami. In *Proceedings of the Royal Society of London, series A: Mathematical, physical and engineering sciences*, Vol. 458, The Royal Society, pp. 763–789.

Takabatake, T., Shibayama, T., Esteban, M., Achiari, H., Nurisman, N., Gelfi, M., et al. (2019). Field survey and evacuation behaviour during the 2018 Sunda Strait tsunami. *Coastal Engineering Journal*, *20*, 1–21.

Tappin, D., Grilli, S., Harris, J., Geller, R., Masterlark, T., Kirby, J., et al. (2014). Did a submarine landslide contribute to the 2011 Tohoku tsunami? *Marine Geology*, *357*, 344–361.

Tappin, D., Watts, P., & Grilli, S. (2008). The Papua New Guinea tsunami of 17 July 1998: Anatomy of a catastrophic event. *Natural Hazards and Earth System Sciences*, *8*, 243–266.

TDMRC (2019) The latest update from post-Sunda Strait tsunami survey. http://tdmrc.unsyiah.ac.id/the-latest-update-from-post-sunda-strait-tsunami-survey/.

Walter, T., Haghighi, M., Schneider, F., Coppola, D., Motagh, M., Saul, J., Babeyko, A., Dahm, T., Troll, V., Tilmann, F., Heimann, S., Valade, S., Triyono, R., Khomarudin, R., Kartadinata, N., Laiolo, M., Massimetti, F., & Gaebler, P. (2019). Precursors and processes culminating in the Anak Krakatau December 2018 sector collapse and tsunami. *Nature Communications***(in revision)**.

Wang, X., & Liu, P.-F. (2006). An analysis of 2004 Sumatra earthquake fault plane mechanisms and Indian Ocean tsunami. *Journal of Hydraulic Research*, *44*, 147–154.

Yavari-Ramshe, S., & Ataie-Ashtiani, B. (2016). Numerical modeling of subaerial and submarine landslide-generated tsunami waves-recent advances and future challenges. *Landslides*, *13*, 1325–1368.

(Received September 13, 2019, revised December 8, 2019, accepted December 11, 2019)

Chapter 3

Modeling of a 3D complex case with OpenFOAM

3.1 General setup

Besides the interesting exercise of comparing a depth-averaged and a Navier-Stokes models, one of the practical aims of this thesis was to improve the laboratory's knowledge of OpenFOAM and develop a procedure to simulate complex landslide tsunamis. The latter is detailed in Appendix A and the outlines are presented hereafter.

Two files are required to simulate a landslide tsunami with OpenFOAM, in xyz format:

- a file for the bathymetry: named *bathymetry_after.xyz* in the following, it corresponds to the topo-bathymetry with the scar of the landslide, 'after' the event.

- a file for the slide: named *slide.xyz* in the following, it corresponds to the volume that fills the scar.

These .xyz files have to be converted into .stl geometry files to be read by OpenFOAM (with Matlab for example). Then, with the blockMesh utility that decomposes a domain in hexahedral blocks, a first box is generated, with a rectangular mesh. Thanks to snappyHexMesh, a mesh generator that refines an existing mesh, the previous mesh is refined around the *bathymetry_after.stl* file. Cells generated by blockMesh that are outside the domain defined by the bathymetry are removed.

SnappyHexMesh can be run in parallel to spare CPU time. In this case, the domain has to be decomposed, using decomposePar. The number of subdomains is given by the number of processors. After snappyHexMesh run in parallel, a reconstruction is required before starting the proper simulation, using reconstructParMesh.

Finally, after a new decomposition and in parallel, the three phases, air, water and sediment, are defined through the setFields utility and the computation can start with the solver multiphaseInterFoam.

3.2 The problem of the initial free surface

Whereas the free surface in the first instants should be at rest, surface elevations present numerical perturbations at several gauges (Figure 39). The generation of a water surface at rest is challenging and is strongly dependent on the mesh resolution. Initiating the simulation with a lower time-step than the one calculated by OpenFOAM helps to keep the water surface still in the early moments but perturbations still remain.

Two procedures can help getting a still water surface at the beginning of the simulation. The first one consists in refining the mesh around the surface, but then the cell sizes in horizontal and vertical directions could be very different. Due to lack of time, this strategy was not pursued. The second method, actually applied in this thesis, is to generate the finer mesh as possible for the entire domain, with homogeneous hexahedral cells. In our simulations, due to the RAM limitations of the cluster during blockMesh computation and the impossibility to run blockMesh in parallel, the maximal number of cells was limited to around 80 million. Therefore, no convergence studies could be conducted for the two complex cases modeled hereafter.

After the mesh generation, the mesh refinement in the vicinity of the bottom with snappyHexMesh is critical and many parameters are used for this step. Figure 39 shows the effect of a snappyHexMesh parameter ("tolerance") on synthetic gauges close to the Anak Krakatau (see Part III, Chapter 2, Section 2.2). This parameter is a scalar that "tells" snappyHexMesh how far to go to find a point to snap to the .stl file. Here, by dividing the tolerance by 20, the synthetic gauges record almost flat signals (a value close to zero) before the wave arrival (Figure 39).

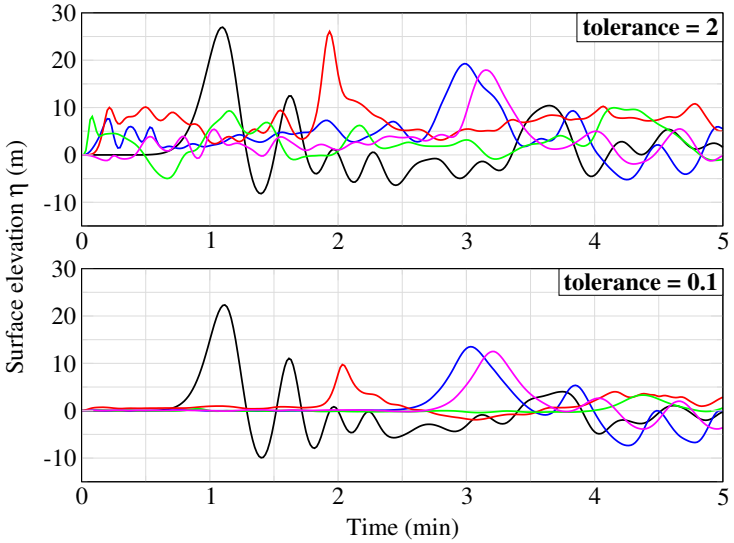

Figure 39: Influence of the tolerance parameter in snappyHexMesh for the mesh refinement of the Anak Krakatau case at five gauges.

3.3 Application to the 2017 Karrat Fjord events

3.3.1 Initial parameters and configuration

In this section, the simulations performed in Part III, Chapter 2, Section 2.1 using a Coulomb law in AVALANCHE are repeated using viscous fluids in both AVALANCHE and OpenFOAM. The landslide volume is the same as in Paris et al. (2019), *i.e.* around 50 million m^3. Three values of viscosity μ are tested: 1, 1000 and 100000 Pa.s, which leads to slide Reynolds number of 30.10^6, 30000 and 300, respectively.

The domain is 9880×9880 m, with a 25 m resolution in AVALANCHE and a 494×494×138 division in OpenFOAM, which represents about 34 million cells (for a 15 m resolution in the three directions). Four synthetic gauges are placed in the fjord in front of the landslide. Initial configuration in OpenFOAM and gauges locations are presented in Figure 40.

Due to complications during the simulations, only the shallow water model was applied in AVALANCHE. As in Part II, Chapter 4, a 0.4 partialSlip bottom boundary condition was used in OpenFOAM. Note that around 8 h of simulation is required to simulate 180 s with 96 processors in OpenFOAM, using an adaptative time step set to 0.05 s initially.

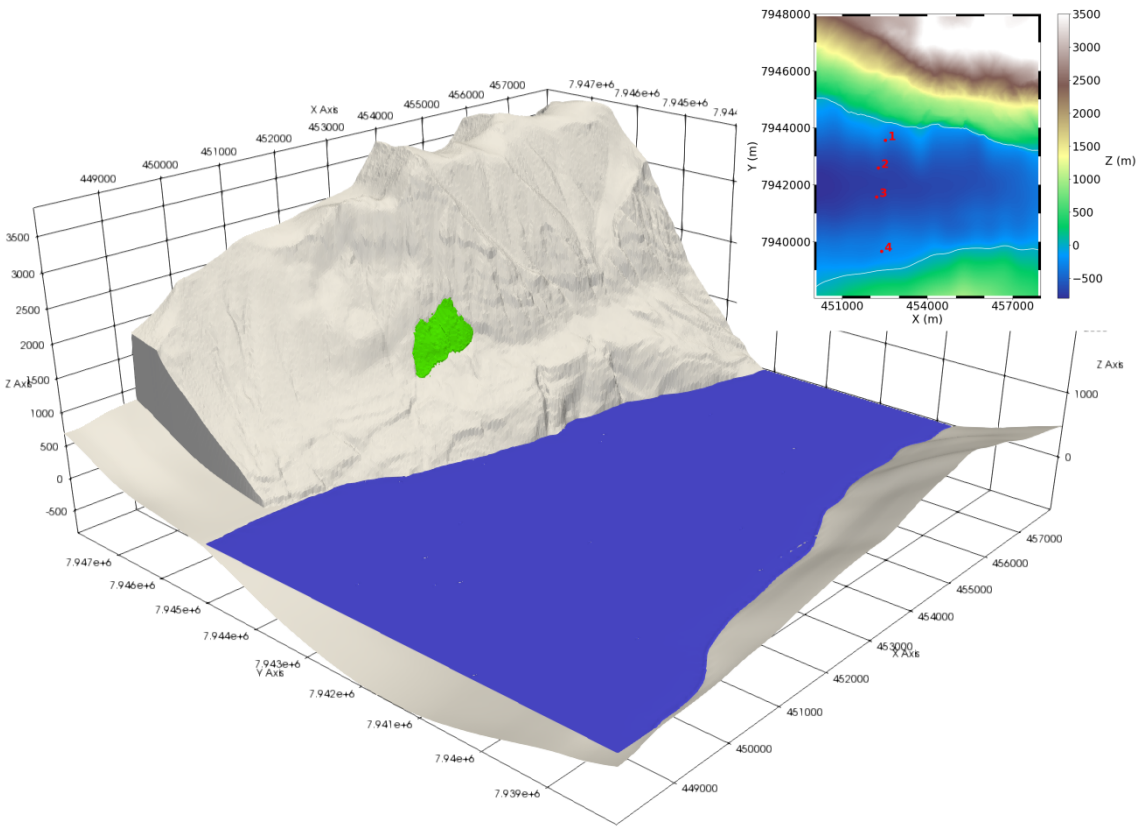

Figure 40: 3D initial configuration of the Karrat Fjord landslide in OpenFOAM. The landslide is in green, the terrain in off-white and the still water surface in blue. The insert on top right represents a 2D view of the fjord topo-bathymetry and the location of Gauges 1, 2, 3 and 4.

3.3.2 Results

The waves generated by OpenFOAM are about 2 times (for μ=1 Pa.s), 10 times (for μ=1000 Pa.s) and 5 times (for μ=100000 Pa.s) higher than the ones generated by AVALANCHE (Figures 41 and 42). Note that these results are in agreement with Figure 34 in Part II, Chapter 4, Section 4.2: considering the high slide Reynolds values, the slope angles of the Karrat Fjord between 50 and 60° and the high initial landslide position, the generated waves are larger in the Navier-Stokes model. This underestimation of water heights in AVALANCHE may be explained by the spread of the landslide along the slope during the slide which is not observed in OpenFOAM results. As a result, the landslide front is much thinner in AVALANCHE and generates smaller waves.

Regarding AVALANCHE, the influence of the viscosity cannot be fully demonstrated because only half the volume collapsed for μ=100000 Pa.s. The viscosity in OpenFOAM seems to have no effect until values reach around 100000 Pa.s (Figure 42). This may be due to the scale of the problem.

With μ=100000 Pa.s, the first wave is about 12 m high for AVALANCHE and 20 m high for OpenFOAM (Figures 41 and 42). These values are close to the 15 m wave height obtained in Paris et al. (2019). Moreover, the maximum landslide velocities are likely closer to the reality, e.g. about 100 m.s^{-1} with μ=100000 Pa.s whereas the maximum velocity is about 300 m.s^{-1} for a viscosity μ=1000 Pa.s in AVALANCHE.

Figure 43 illustrates that with μ=100000 Pa.s and OpenFOAM, the wave is already formed at t=50 s, reaching a height of 40 m, before decreasing to 20 m at t=100 s. This decrease is also observed at Gauge 1 using the same viscosity (from 22 m at t=48 s to 7 m at t=68 s, see Figure 42), indicating that the waves disperse.

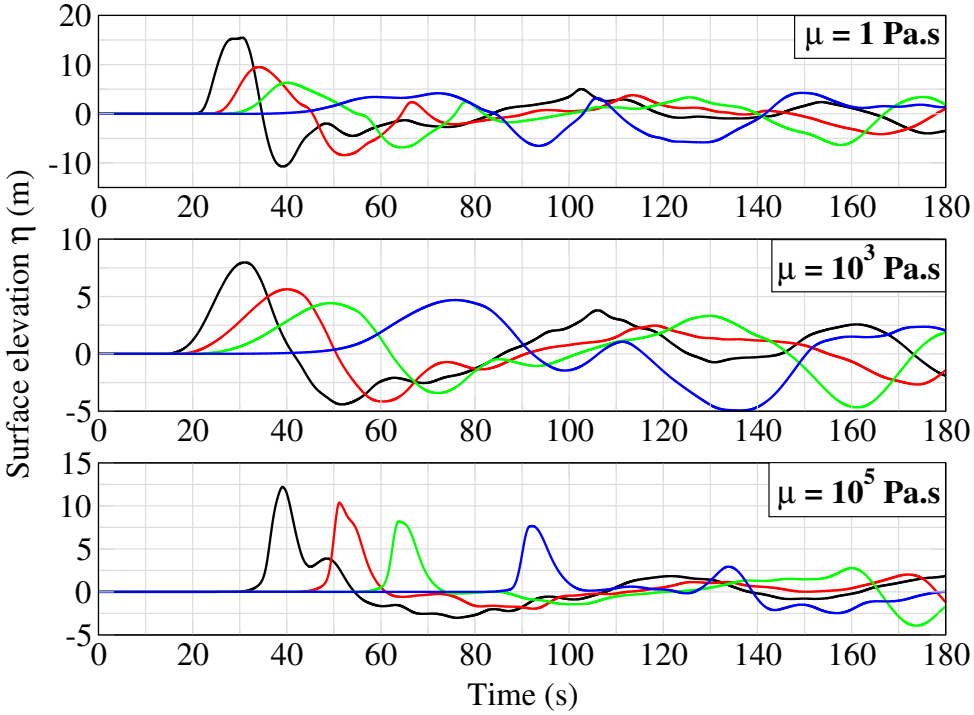

Figure 41: Surface elevation time series (m) of the AVALANCHE simulations with μ=1 Pa.s, μ=1000 Pa.s and μ=100000 Pa.s at the four gauges.

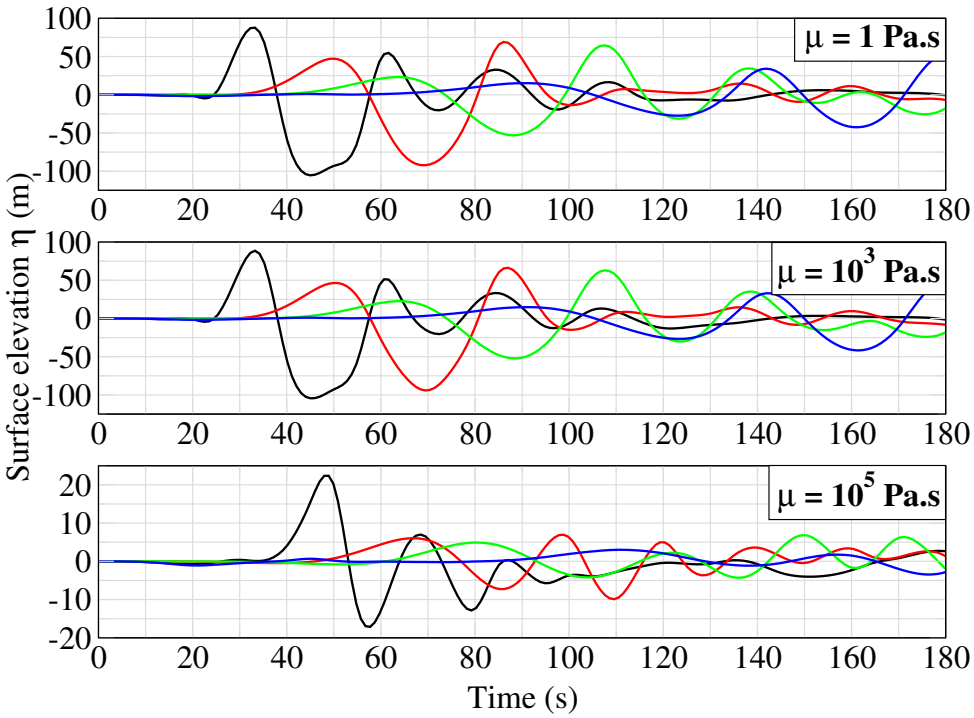

Figure 42: Surface elevation time series (m) of the OpenFOAM simulations with μ=1 Pa.s, μ=1000 Pa.s and μ=100000 Pa.s at the four gauges.

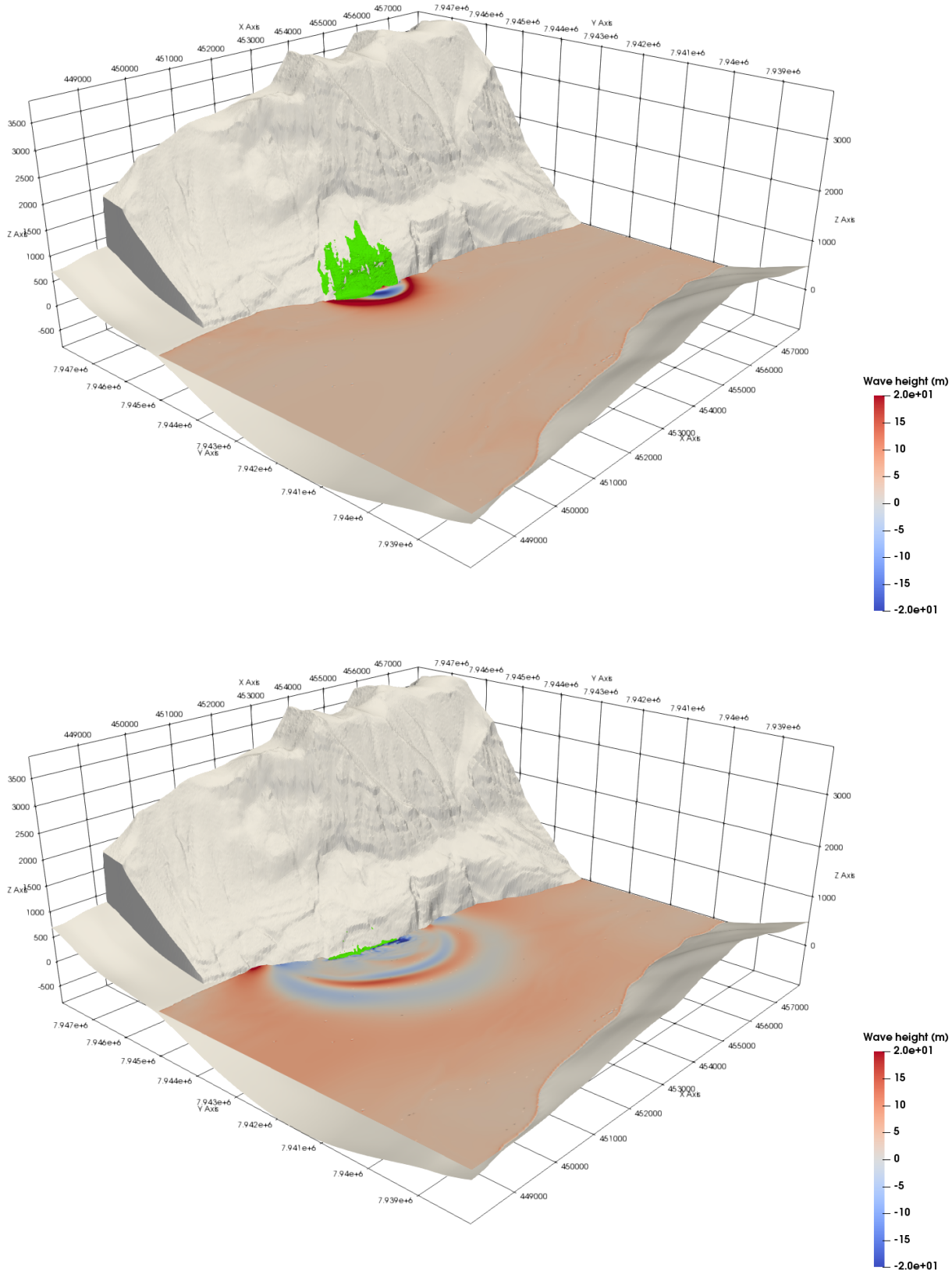

Figure 43: OpenFOAM results at t=50 s (top) and t=100 s (bottom) for μ=100000 Pa.s and a 0.4 partialSlip condition. The landslide is in green and the terrain in off-white.

3.4 Application to the 2018 Anak Krakatau events

3.4.1 Initial parameters and configuration

A few months after the event, a bathymetric survey highlighted deposits from the collapse (Hunt et al., 2021). They evaluated the volume of these deposits to 214±36 million m^3, which is greater than the volume used in the preliminary study available in Chapter 2, Section 2.2. However, according to Hunt et al. (2021), a volume of 175±15 million m^3 is more likely, which is close to the volume used in Paris et al. (2020), around 150 million m^3. In any case, the results of this bathymetric survey were published too late for this thesis work, so it was decided to keep the same volume as the one initially published in Paris et al. (2020).

The landslide is considered as a viscous fluid in both models and results are compared to AVALANCHE simulations of Paris et al. (2020) that used a Coulomb law with a basal friction angle $\phi = 2°$. Two viscosity values are tested, μ=750 Pa.s (Grilli et al., 2019) and μ=5 Pa.s, and a 0.4 partialSlip bottom boundary condition is applied in OpenFOAM. Only the near-field is computed, considering a 18491×13000 m domain, using a 25 m resolution grid in AVALANCHE and a 1233×867×44 division in OpenFOAM (about 47 million cells for a 15 m resolution in the three directions). Results are analyzed through the five gauges defined in Grilli et al. (2019). Figure 44 presents the initial domain configuration and gauges locations. Using an adaptive time step initially set to 0.003 s, more than one day of execution time was required to run the simulation over a period of 5 min. The total computational time taking into account the writing time, every second, is about two days.

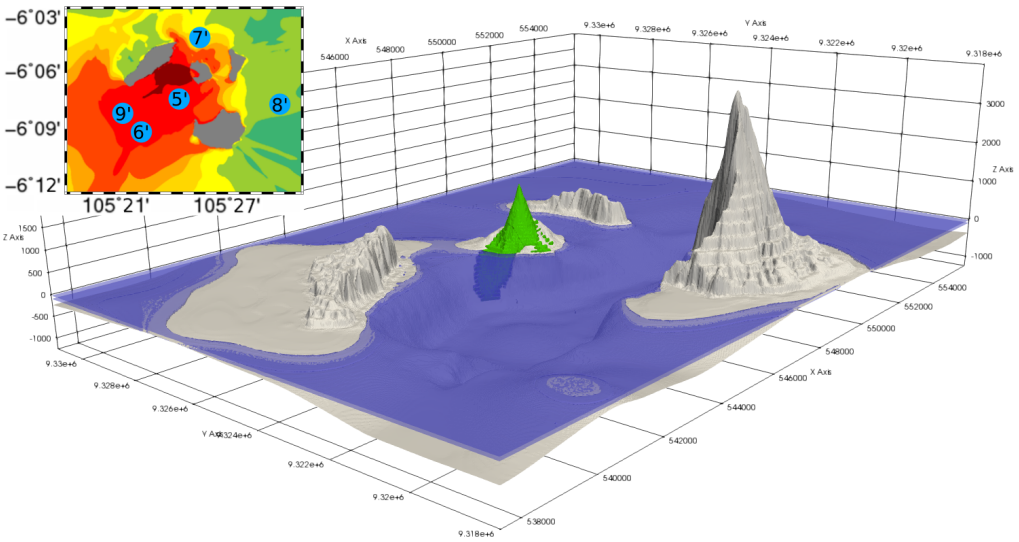

Figure 44: 3D initial configuration of the Anak Krakatau landslide in OpenFOAM. The landslide is in green, the terrain in off-white and the still water surface in blue. The insert on top left represents a 2D view of the domain and the location of Gauges 5', 6', 7', 8' and 9' used in Grilli et al. (2019). Vertical exaggeration is 5.

3.4.2 Results

Figure 45 shows the surface elevation time series computed by AVALANCHE, considering the landslide as a granular mass with a Coulomb basal friction coefficient $\phi = 2°$ or as a viscous fluid with a viscosity value μ of 5 and 750 Pa.s. In the three cases, both the free surface elevations and the waves amplitude are similar, which suggests a low influence of the viscosity in the range of values in AVALANCHE. However, as shown by the previous study of the Karrat Fjord event (Section 3.3), these viscosity values are probably too small.

Figure 46 also shows extremely similar, if not identical, surface elevation time series computed by OpenFOAM, with μ=5 and 750 Pa.s. The first waves in the near-field (Gauge 5') are about 10 m higher than the ones calculated with AVALANCHE, whereas the wave heights in the far-field (Gauges 6' and 9') are more similar. Moreover we note that the waves generated by the depth-averaged model are generally longer, due to the spread out of the landslide on small slopes (around 8°).

Concerning the first wave, this difference of amplitudes between models may be explained by the configuration of the landslide. Indeed, Figure 34A in Chapter 4, Section 4.2, showed that for small slopes, high slide Reynolds number (here Re_s between 60000 and 8 million) and partially submerged initial landslide position, the depth-averaged model produced smaller wave heights than the Navier-Stokes model.

Figure 47 shows intermediate states of this preliminary OpenFOAM modeling of the Anak Krakatau landslide tsunami. The generated wave reached up to 50 m at t=50 s and the three islands around the volcano were reached at t=100 s.

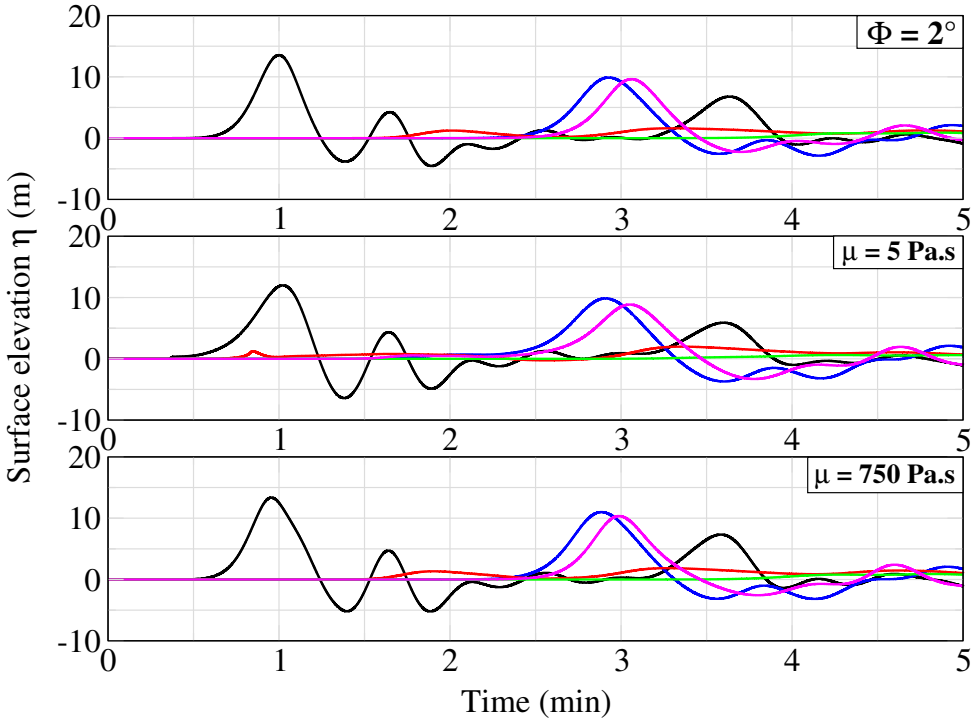

Figure 45: Surface elevation time series (m) of the AVALANCHE simulations with ϕ=2° (Paris et al., 2020), μ=5 Pa.s and μ=750 Pa.s at the five gauges from Grilli et al. (2019).

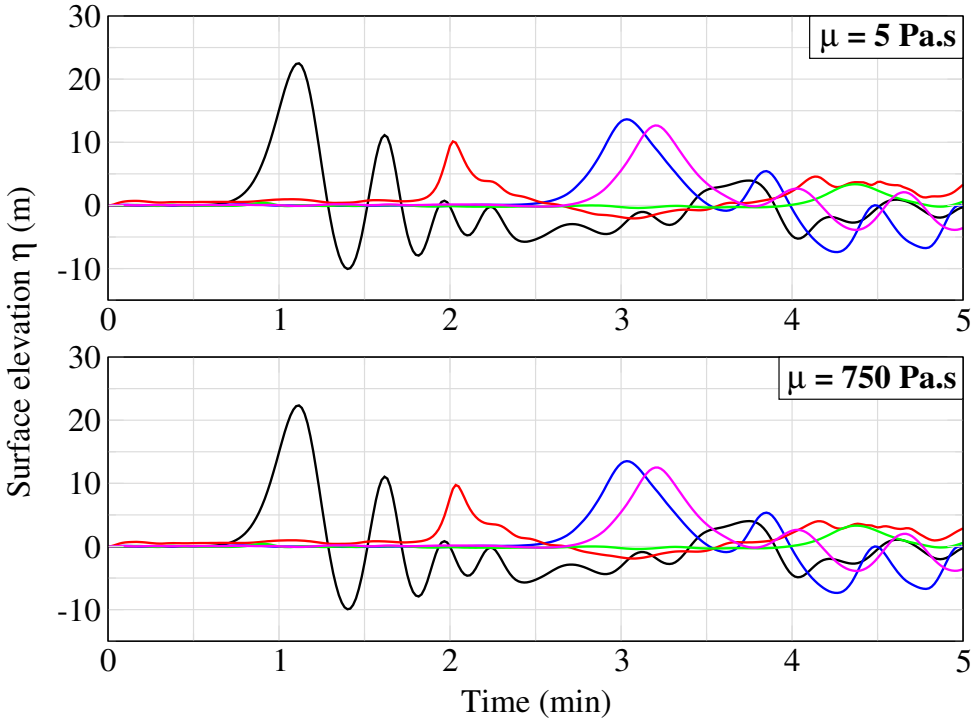

Figure 46: Surface elevation time series (m) of the OpenFOAM simulations with μ=5 Pa.s and μ=750 Pa.s at the five gauges from Grilli et al. (2019).

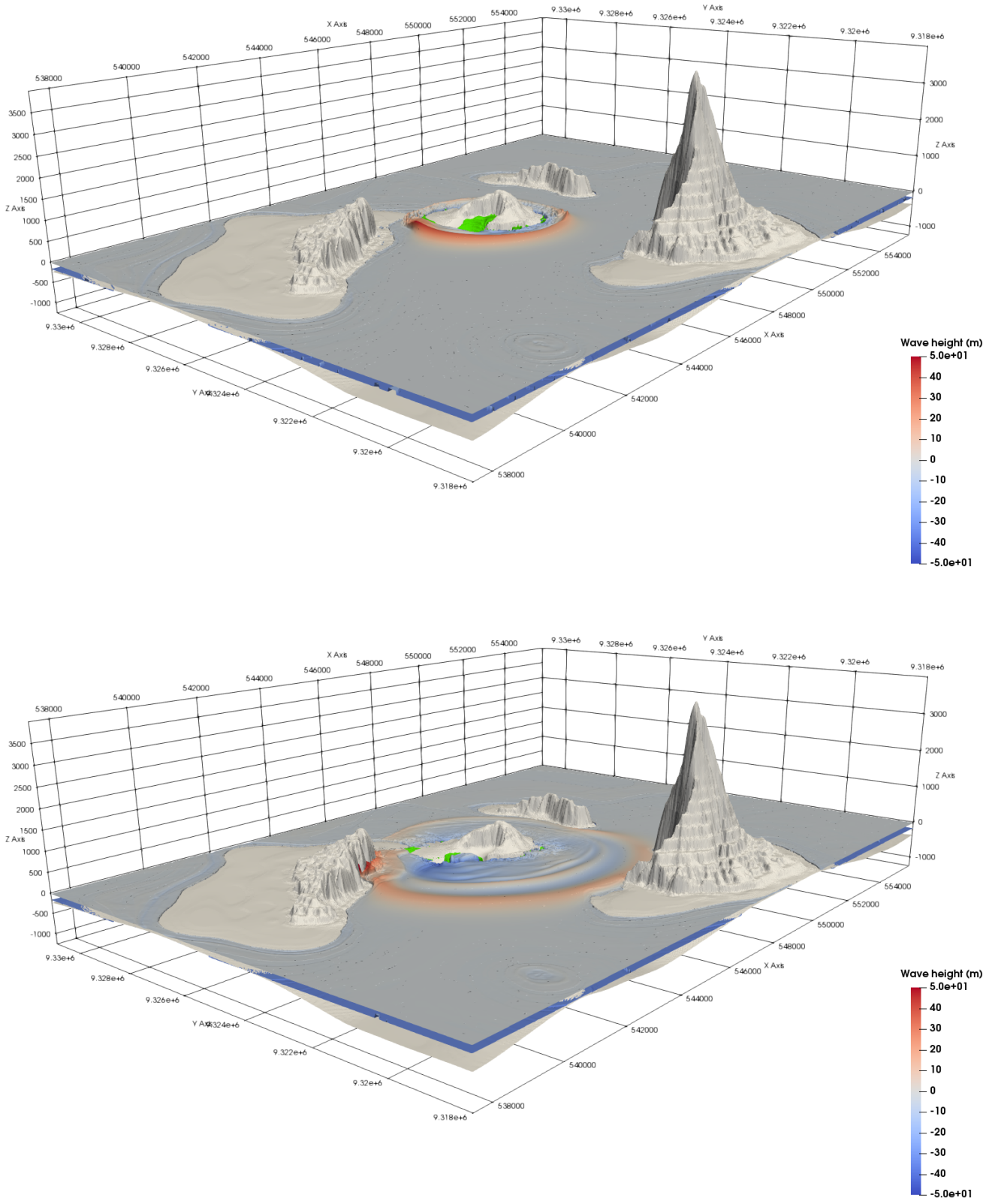

Figure 47: OpenFOAM results at t=50 s (top) and t=100 s (bottom) for μ=750 Pa.s and a 0.4 partialSlip condition. Vertical exaggeration is 5. The landslide is in green and the terrain in off-white.

Chapter 4

Conclusion on the comparison in real cases

In this part, two real events were simulated with OpenFOAM: the 2017 Karrat Fjord event which is a subaerial landslide with high positive submergence value, collapsing on steep slopes between 50 and 60°, and the 2018 Anak Krakatau event which is a partially submerged landslide, sliding on gentle slopes around 10°. In both configurations, considering the high slide Reynolds numbers, the landslide front in the depth-averaged model was thinner than the one in the Navier-Stokes model, resulting in smaller generated waves. However, similar wave heights can be obtained in both models by adjusting the viscosity. Further analysis should be focused on the landslide itself, its behavior in both models and the way it enters into water.

Compared to AVALANCHE, the computational time with OpenFOAM is considerably longer and the generated outputs of a parallel simulation take much more memory space. Nevertheless, these first real events studies with OpenFOAM are promising.

For now, both events were modeled in OpenFOAM using a homogeneous mesh, leading to a maximal resolution of 15 m in the horizontal and vertical directions. Considering the wave heights generated in such events, the mesh should be refined around the water free surface. Moreover, the resolution of the .stl bathymetry file, on which the refinement using snappyHexMesh is based, should also be investigated. These improvements of the mesh would likely permit a better definition of the coastlines and a initial still free surface in the entire domain.

Conclusion

Preliminary comparisons between depth-averaged and Navier-Stokes models have been carried out in this thesis. In Part II, Chapter 3, a subaerial and a submerged experimental landslide case were simulated to validate the models. In Part II, Chapter 4, Section 4.1, two depth-averaged models were compared to a Navier-Stokes model, based on the analysis of waves generated by various landslide cases. In Part II, Chapter 4, Section 4.2, sensitivity studies on the slope angle and the initial position of the slide were carried out. In Part III, both models were applied to real events, the 2017 Karrat Fjord, Greenland, and the 2018 Anak Krakatau, Indonesia, landslide tsunamis. In the light of the results obtained in this thesis, some questions raised in the introduction can now be at least partially answered:

Frequency dispersion versus shallow water models

In Part II, Chapter 4, considering the Navier-Stokes model as a reference solution, two sets of equations for the depth-averaged model have been tested: the shallow water equations and the Boussinesq equations. The landslide was simulated by the Navier-Stokes model and the landslide contour was introduced in the depth-averaged models as a varying bathymetry. Results showed that the Navier-Stokes solution was better approached by the shallow water model in the generation zone and the Boussinesq model in the propagation zone. Therefore, a mixed depth-averaged model with a combination of shallow water equations during the generation and Boussinesq equations once the wave is formed is used and produces better results. In summary, frequency dispersion must be considered for landslide tsunamis, especially in the propagation zone.

Which model is more adapted for subaerial or submerged landslides? What is the influence of the slope angle?

In Part II, Chapter 4, sensitivity studies on the landslide initial position have been carried out considering a triangular slide. For both models, the relationship between the slope angle and the generated wave is generally linear, the higher the slope angle, the greater the generated wave. For the Navier-Stokes model and submerged landslides, the relationships are more complex.

Results of both models are strongly dependent on the initial landslide position and the slope angle. For landslide behaviors close to each other (e.g. for medium slopes and landslides close to the free surface), the generated waves are similar. So far, taking into account results of Part II, Chapter 4, we cannot conclude on the appropriateness of a

model in a given configuration.

Is a Navier-Stokes model always more accurate than a depth-integrated model?

In Part II, Chapter 3, a depth-averaged and a Navier-Stokes model were validated against two benchmarks consisting in a subaerial and a submerged triangular granular material that collapses into water. In both models simulations, the landslide was considered as a Newtonian fluid and sensitivity studies on the viscosity showed that both models can lead to similar landslide behaviors and generated waves. Additionally, several combinations of viscosity values and boundary conditions give results close to the experiments. However, it is hard to correctly reproduce both the entire landslide behavior and the generated waves in the same simulation.

The comparison between both models carried out in Part III for real events showed that the Navier-Stokes model tends to overestimate the generated waves heights compared to the depth-averaged model, in the near-field. Moreover, results in the Navier-Stokes model are strongly dependent on the bottom boundary condition and the viscosity.

In summary, the depth-averaged model being less complex than the Navier-Stokes model and involving far fewer parameters, the possibility of matching data (experiments or real events) is facilitated. For now and using a Newtonian rheology, results of this thesis show that a Navier-Stokes model is not always more accurate than a depth-averaged model. Further studies are required, considering more complex landslide rheologies and higher mesh resolutions.

Perspectives

All the previous results are valid for particular shapes of landslide: a parallelogram shape for the comparison of depth-averaged equations and a triangular shape for the comparison of depth-averaged and Navier-Stokes models. It is likely that the generation of a tsunami strongly depends on the initial landslide shape, because the way the water is impacted will not be the same. Further studies should then use other landslide shapes, such as rectangular or gaussian shapes.

The computations carried out with OpenFOAM in this thesis have to be considered as an early work for the landslide tsunami modeling with this tool. They gave insight into the many possibilities of OpenFOAM but also its high complexity. There are a lot of available parameters that can be modified and further studies could evaluate the influence of several of them, for instance those involved in the mesh refinement with snappyHexMesh.

In this thesis, the landslide was considered as a Newtonian fluid in OpenFOAM, but other rheologies could be applied, such as the μ(I)-rheology (Rauter, 2021). Moreover, porosity could be added to take into account the water infiltrating the granular

material, as seen in Viroulet et al. (2016) and Grilli et al. (2017) experiments. This is now possible with the complete two-phase flow approach of Si et al. (2018) and Lee and Huang (2021). However, the aim of this thesis was to develop a method to model real events with OpenFOAM and we were not interested in an accurate modeling of the landslide. As explained above, a Navier-Stokes model involves many more parameters than a depth-averaged model (for instance the mesh generation or bottom boundary conditions). As a result, the Newtonian rheology, being based only on the viscosity, is likely the easiest way and a first step to model real events.

Des comparaisons préliminaires entre les modèles intégrés sur la profondeur et les modèles Navier-Stokes ont été effectuées dans cette thèse. Dans le Chapitre 3 de la Partie II, des expériences de glissement de terrain subaérien et submergé ont été simulées pour valider les modèles. Dans la Section 4.1 du Chapitre 4 de la Partie II, deux modèles intégrés sur la profondeur ont été comparés à un modèle Navier-Stokes, en se basant sur l'analyse des vagues générées par plusieurs cas de glissements de terrain. Dans la Section 4.2 du Chapitre 4 de la Partie II, des études de sensibilité sur l'angle de la pente et la position initiale du glissement ont été réalisées. Dans la Partie III, les deux modèles ont été appliqués à des événements réels, le tsunami et le glissement de terrain de 2017 dans le Karrat Fjord, au Groenland, et de 2018 autour du volcan Anak Krakatau, en Indonésie. À la lumière des résultats obtenus dans cette thèse, certaines questions soulevées dans l'introduction peuvent désormais trouver une réponse au moins partielle :

Importance de la dispersion fréquentielle

Dans le Chapitre 4 de la Partie II, en considérant le modèle Navier-Stokes comme solution de référence, deux types d'équations pour le modèle intégré sur la profondeur ont été testés : les équations shallow water et les équations de Boussinesq. Le glissement de terrain a été simulé par le modèle Navier-Stokes et le contour du glissement a été introduit dans les modèles intégrés sur la profondeur en tant que bathymétrie variable. Les résultats ont montré que la solution de Navier-Stokes était mieux approchée par le modèle shallow water dans la zone de génération et le modèle de Boussinesq dans la zone de propagation. Par conséquent, un modèle mixte intégré sur la profondeur utilisant une combinaison des équations shallow water pendant la génération et des équations de Boussinesq une fois la vague formée est proposé et donne de meilleurs résultats. En résumé, la dispersion fréquentielle doit être prise en compte pour les tsunamis générés par des glissements de terrain, en particulier dans la zone de propagation.

Quel modèle est plus adapté aux glissements de terrain subaériens ou submergés ? Quelle est l'influence de l'angle de la pente ?

Dans le Chapitre 4 de la Partie II, des études de sensibilité sur la position initiale du glissement ont été réalisées en considérant une masse triangulaire. Pour les deux modèles, la relation entre l'angle de la pente et la vague générée est généralement linéaire, plus la pente est forte, plus la vague générée est haute. Pour le modèle Navier-Stokes et les glissements de terrain submergés, les relations sont plus complexes.

Les résultats des deux modèles dépendent fortement de la position initiale du glissement de terrain et de l'angle de la pente. Pour des comportements de glissement proches les uns des autres (par exemple pour des pentes moyennes et un glissement

proche de la surface libre), les vagues générées sont similaires. Jusqu'à présent, en tenant compte des résultats du Chapitre 4 de la Partie II, nous ne pouvons pas conclure sur la pertinence d'un modèle dans une configuration donnée.

Un modèle Navier-Stokes est-il toujours plus précis qu'un modèle intégré sur la profondeur ?

Dans le Chapitre 3 de la Partie II, un modèle intégré sur la profondeur et un modèle Navier-Stokes ont été validés par rapport à deux benchmarks qui consistent en une masse granulaire de forme triangulaire, subaérienne et submergée, qui s'effondre dans l'eau. Dans les simulations des deux modèles, le glissement de terrain a été considéré comme un fluide newtonien et des études de sensibilité sur la viscosité ont montré que les deux modèles pouvaient conduire à des comportements de glissement et des vagues générées similaires. De plus, plusieurs combinaisons de valeurs de viscosité et de conditions aux limites donnent des résultats proches des expériences. Cependant, il est difficile de reproduire correctement à la fois le comportement complet du glissement et les vagues générées dans la même simulation.

La comparaison entre les deux modèles effectuée dans la Partie III pour des événements réels a montré que le modèle Navier-Stokes avait tendance à surestimer les hauteurs des vagues générées par rapport au modèle intégré sur la profondeur, en champ proche. De plus, les résultats du modèle Navier-Stokes dépendent fortement de la condition limite sur le fond et de la viscosité.

En résumé, le modèle intégré sur la profondeur étant moins complexe que le modèle Navier-Stokes et impliquant beaucoup moins de paramètres, la possibilité de faire correspondre les données (expériences ou événements réels) aux simulations est facilitée. Pour l'instant, et en utilisant une rhéologie newtonienne, les résultats de cette thèse montrent qu'un modèle Navier-Stokes n'est pas toujours plus précis qu'un modèle intégré sur la profondeur. D'autres études sont nécessaires, en considérant des lois de comportement plus complexes pour le glissement de terrain et des résolutions de maillage plus élevées.

Perspectives

Tous les résultats précédents sont valables pour des formes particulières de glissement de terrain : une forme de parallélogramme pour la comparaison des équations intégrées sur la profondeur et une forme triangulaire pour la comparaison des modèles intégrés et Navier-Stokes. Il est probable que la génération d'un tsunami dépende fortement de la forme initiale du glissement de terrain, car la manière dont l'eau est impactée ne sera pas la même. Les études ultérieures devraient donc utiliser d'autres formes de glissements de terrain, comme des formes rectangulaires ou gaussiennes.

Les calculs effectués avec OpenFOAM dans cette thèse doivent être considérés comme un travail préliminaire pour la modélisation des glissements de terrain et des tsunamis avec cet outil. Ils ont donné un aperçu des nombreuses possibilités qu'offre OpenFOAM mais aussi de sa grande complexité. Il y a beaucoup de paramètres disponibles qui peuvent être modifiés et des études ultérieures pourraient évaluer l'influence de plusieurs d'entre eux, par exemple ceux impliqués dans le raffinement du maillage avec snappyHexMesh.

Dans cette thèse, le glissement de terrain a été considéré comme un fluide newtonien dans OpenFOAM, mais d'autres lois de comportement pourraient être appliquées, comme la rhéologie μ-(I) (Rauter, 2021). De plus, la porosité pourrait être ajoutée pour prendre en compte l'eau qui s'infiltre dans le matériau granulaire, comme cela a été vu dans les expériences Viroulet et al. (2016) et Grilli et al. (2017). Ceci est maintenant possible avec l'approche complète par écoulement diphasique de Si et al. (2018) et Lee and Huang (2021). Cependant, l'objectif de cette thèse était de développer une méthode pour modéliser des événements réels avec OpenFOAM mais pas de modéliser avec précision un glissement de terrain. Comme expliqué plus haut, un modèle Navier-Stokes implique beaucoup plus de paramètres qu'un modèle intégré sur la profondeur (par exemple la génération de maillage ou les conditions aux limites du fond). Par conséquent, une rhéologie newtonienne, basée uniquement sur la viscosité, est probablement le moyen le plus simple et une première étape pour modéliser des événements réels.

Résumé des travaux

L'objectif de cette thèse est de comparer deux types de modèles de tsunamis générés par glissements de terrain : un modèle intégré sur la profondeur et un modèle Navier-Stokes.

La Partie I est consacrée à un état de l'art reprenant les grands événements historiques, les expériences en laboratoire récentes et les différents modèles que l'on trouve aujourd'hui.

La Partie II présente une comparaison des deux modèles à travers plusieurs études de sensibilité, après les avoir validés grâce à deux expériences (subaérienne et submergée).

Enfin la Partie III est dédiée à l'utilisation des deux modèles pour la modélisation numérique de deux événéments récents, les tsunamis de Karrat Fjord au Groenland, en 2017 et du volcan Anak Krakatoa en Indonésie en 2018. Une méthode est proposée pour la reproduction d'événements complexes avec le modèle Navier-Stokes.

Les recherches historiques effectuées dans le Chapitre 1 de la Partie I montrent que la plupart des tsunamis d'origine gravitaire sont générés par des effondrements subaériens. Elles ont aussi illustré la diversité de ces tsunamis, de leur localisation et de leurs caractéristiques (largeur, épaisseur, altitude).

Depuis 150 ans, environ 40 tsunamis générés par glissements de terrain ont été observés et sont listés dans le Tableau 1. Certains événements n'ont pas été retenus dans cette liste à cause de leur ancienneté mais sont néanmoins importants. Parmi eux, le glissement de Storegga, en Norvège (Bondevik, 2019) est le plus gros glissement sous-marin connu et aurait eu lieu aux alentours de -8150 ans. Avec un volume compris entre 2400 et 3200 km^3, le tsunami généré a atteint des valeurs de runup de 3 à 20 m sur les côtes d'Écosse, de Norvège ainsi que les îles Féroé et Shetland.

Le tsunami généré par l'éruption du volcan Krakatoa en 1883 est un autre exemple d'événement important et non listé ici. L'effondrement de sa caldera a produit des vagues de 40 à 50 m de haut et a tué plus de 30000 personnes dans le détroit de la Sonde. D'autres tsunamis générés par de très importants glissements ont eu lieu dans le passé. Par exemple, des traces géologiques de quatorze paléo glissements sous-marins ont été identifiées autour des îles Canaries (Masson et al., 2002).

Sur les 40 événements identifiés et listés ici, les volumes des glissements subaériens sont en moyenne plus petits que ceux submergés. Dans le Tableau 1, le volume moyen des premiers est d'environ 35 million de m^3 alors que pour les glissements submergés il atteint 18500 million de m^3 si les événements de Grand Banks et de Papouasie-Nouvelle-Guinée sont pris en compte, seulement 400 million de m^3 sans Grand Banks et seulement 6.5 million m^3 sans ces deux cas extrêmes.

Bien que les données soient manquantes pour beaucoup de cas, les vagues générées

sont en moyenne de 18 m pour les glissements subaériens, contre environ 7.5 m pour les glissements submergés (en comptant Grand Banks), ce qui confirme que les glissements subaériens sont potentiellement les plus dangereux, comme le montre le bilan humain (2200 morts) du tsunami de Papouasie-Nouvelle-Guinée.

L'altitude moyenne du glissement relevée dans le Tableau 1 est d'environ 560 m. En ce qui concerne la taille, les glissements subaériens font en moyenne 575 m de large, 845 m de long et 90 m d'épaisseur. Avec ces valeurs de largeur, longueur et épaisseur, on obtient un volume moyen d'environ 45 million m^3. Enfin, peu d'informations sont disponibles à propos des pentes, et on trouve une valeur moyenne de 25°. Toutes les valeurs moyennes précédentes ne sont pas statistiquement significatives à cause de la petite taille de l'échantillon et d'événements qui ne seraient pas listés.

Dans le Chapitre 2 de la Partie I, plusieurs expériences en laboratoire récentes sont listées. Dans un canal en 2D ou un bassin en 3D, le glissement peut être considéré comme rigide ou déformable. Un glissement rigide peut représenter le comportement d'écoulements cohésifs tandis qu'un glissement déformable peut représenter un écoulement granulaire. Des expériences en laboratoires sont réalisées depuis les années 1970 (Noda, 1970; Kamphuis and Bowering, 1970) mais l'état de l'art présenté ici ne s'intéresse qu'aux expériences réalisées depuis le début des années 2000.

Les expériences en laboratoire sont très utiles pour étudier chaque étape d'un tsunami généré par glissement de terrain : la génération, la propagation et l'impact sur les côtes. Elles peuvent être utilisées pour reproduire des événements réels à échelle réduite ou bien comprendre des événements passés. Elles peuvent aussi constituer des benchmarks pour la validation des modèles numériques ou bien être utilisées pour le développement de formules empiriques liant différents paramètres du problème.

Ces paramètres sont nombreux, ce qui mène à un vaste choix d'expériences dans lesquelles sont testées les variations de pente (de 10 à 90°), de position initiale du glissement (subaérien ou submergé), de nature du glissement (rigide ou déformable), du matériau utilisé (eau, sable, billes de verre, ...), de profondeur d'eau ou de forme du glissement.

Le Chapitre 3 de la Partie I est dédié aux modèles numériques de tsunamis générés par glissements de terrain. Ces modèles peuvent être calibrés et validés en utilisant des solutions analytiques ou en reproduisant des expériences en laboratoire ou des événement passés. Plus simples à mettre en place que des expériences en laboratoire, les modèles numériques permettent de simuler un tsunami en quelques minutes. La reproductibilité des simulations permet par exemple d'étudier facilement l'influence d'un paramètre. Les modèles numériques sont aussi utilisés pour évaluer la menace que constituent des glissements potentiels et établir des cartes de risque ou de danger. Cependant, à cause de la taille relativement petite des glissements de terrain, il est absolument nécessaire de disposer de données à haute résolution, au moins autour du

glissement. De plus, certains paramètres rhéologiques peuvent être difficiles à obtenir.

La modélisation de tsunamis générés par glissements de terrain implique deux phénomènes distincts et peut être divisée en deux catégories : un couplage unilatéral ou bilatéral. Dans un couplage bilatéral, le glissement et le tsunami généré interagissent l'un avec l'autre et le mouvement du glissement est impacté par l'eau (Jiang and LeBlond, 1992). Dans un couplage unilatéral, le glissement est calculé sans prendre en compte les gradients de pression de surface et la déformation du fond générée est reportée sur à la surface de l'eau. Ce report peut être direct ou indirect en utilisant des formules de transfert (Kelfoun et al., 2010; Glimsdal et al., 2013).

Que ce soit pour le glissement ou le tsunami, les simulations peuvent être réalisées en résolvant les équations complètes de Navier-Stokes ou bien des approximations intégrées sur la profondeur. Pour la partie tsunami, on utilise ces dernières en considèrant que la longueur d'onde du tsunami est beaucoup plus grande que la profondeur d'eau. Ces approximations sont les plus utilisées (Wei et al., 1995; Pedersen and Løvholt, 2008; Løvholt et al., 2008, 2010; Harbitz et al., 2014; Grilli et al., 2013; Abadie et al., 2020) et on trouve parmi elles les équations shallow water, ou celles de Boussinesq qui prennent en compte la dispersion fréquentielle. Pour la partie glissement, les équations intégrées sur la profondeur sont basés sur les modèles de Savage and Hutter (1989) et Jiang and LeBlond (1992).

Les modèles Navier-Stokes sont de plus en plus utilisés pour le glissement et le tsunami (Abadie et al., 2008; Biscarini, 2010; Davies et al., 2011; Ma et al., 2013; Horrillo et al., 2013; Wu et al., 2020), grâce à la réduction constante des temps de calcul CPU. Parmi eux, le modèle OpenFOAM s'est développé ces dernières années (Lee et al., 2016; Si et al., 2018; Yu and Lee, 2019; Romano et al., 2020; Rauter et al., 2021; Lee and Huang, 2021).

En utilisant un modèle Navier-Stokes ou un modèle intégré sur la prodonfeur, il faut choisir une loi rhéologique pour la glissement. Le plus simple est de considérer le glissement comme un bloc rigide mais les lois granulaires de type Coulomb ou Voellmy sont les plus utilisées. Le glissement peut également être considéré comme un fluide, newtonien, non newtonien (de Bingham par exemple), ou suivant une autre loi rhéologique.

Il existe donc de nombreux modèles pour simuler les tsunamis générés par glissements de terrain, avec chacun leurs forces et leurs faiblesses, mais un modèle est-il plus précis qu'un autre ? Quelle est la contribution de la troisième dimension ? Est-ce qu'un modèle est plus pertinent pour la génération ou pour une géométrie de glissement particulière ? La Partie II tente de répondre à quelques unes de ces questions, en comparant un modèle intégré sur la profondeur (AVALANCHE) et un modèle Navier-Stokes (OpenFOAM), grâce à des benchmarks et des études de sensibilité.

Dans le Chapitre 3 de la Partie II, deux expériences, l'une considérant un glissement subaérien, l'autre un glissement submergé, sont utilisées pour valider les modèles en considérant le glissement comme un fluide visqueux. Les deux modèles peuvent

reproduire les vagues générées par les écoulements granulaires des expériences, en calibrant la viscosité. Cependant, la dynamique générale du glissement n'est généralement pas parfaite, surtout pour le modèle Navier-Stokes. Loin de la zone de génération, le champ de vague est moins sensible à la variation de viscosité. Le rang optimal de cette viscosité est plus faible dans le modèle intégré sur la profondeur mais on constate que les deux modèles partagent des valeurs de viscosité qui mènent à des résultats similaires.

Dans la Section 4.1 du Chapitre 4 de la Partie II, un modèle shallow water et un modèle de Boussinesq sont comparés l'un à l'autre en considérant la solution d'un modèle Navier-Stokes comme référence. Le glissement utilisé a une forme de parallélogramme et de nombreuses simulations sont lancées en faisant varier sa hauteur et sa largeur. Les résultats ont montré que le modèle Boussinesq n'était pas capable de représenter correctement les vagues dans la zone de génération. Pour des grands volumes de glissement, le modèle shallow water est efficace à la fois pour la génération et la propagation des vagues. Une stratégie basée sur un changement de modèle une fois la vagué générée, passant des équations shallow water à Boussinesq, est proposée et semble améliorer la précision des simulations.

Dans la Section 4.2 du Chapitre 4 de la Partie II, un modèle intégré sur la profondeur et un modèle Navier-Stokes sont comparés en utilisant les simulations numériques d'un effondrement dans l'eau d'un glissement de type granulaire et de forme triangulaire. Avec cette forme initiale, les vagues les plus hautes sont généralement générées quand le glissement est proche de la surface de l'eau. Pour des glissements placés plus hauts ou plus bas, les vagues sont plus petites. Avec le modèle intégré sur la profondeur, la hauteur des vagues augmente avec la pente et le nombre de Reynolds du glissement. Avec le modèle Navier-Stokes ces relations sont plus complexes. La concordance des deux modèles dépend fortement du glissement, de sa position initiale et de son nombre de Reynolds. Quand ce dernier est autour de 20, les deux modèles donnent des vagues similaires pour des glissements initialement proches de la surface de l'eau. Quand le Reynolds augmente, la différence entre les deux modèles est plus prononcée.

Dans la Partie III, le Chapitre 2 est consacré à la présentation de deux études d'événements récents. La première (Section 2.1) concerne le glissement et le tsunami qui ont eu lieu le 17 juin 2017 dans le fjord Karrat au Groenland (Paris et al., 2019), tuant 4 personnes et détruisant de nombreuses habitations. Les simulations de ces événements ont été réalisées avec AVALANCHE en utilisant une loi de glissement de type Coulomb avec un coefficient de friction basale de 50°. La cicatrice de glissement a été parfaitement identifiée grâce à des images satellites. Une reconstruction du glissement a montré un volume d'environ 50 million de m^3. Les dommages à Nuugaatsiaq 30 km à l'ouest du glissement sont considérables et bien documentés, mais aucun marégraphe n'a enregistré

le tsunami, ce qui complique la validation du modèle. La transformation d'un signal sismique en une élévation de surface de l'eau équivalente donne une idée de la hauteur de la vague qui a frappé Nuugaatsiaq, environ 1 m. De plus, des études de terrain ont relevé une valeur de runup de 90 m autour du glissement.

La deuxième étude (Section 2.2) est dédiée à l'effondrement de l'Anak Krakatoa le 22 décembre 2018 et le tsunami généré qui a dévasté le détroit de la Sonde, entre les îles de Java et Sumatra en Indonésie et tué plus de 430 personnes (Paris et al., 2020). L'effondrement était à la fois subaérien et sous-marin. S'il a été possible d'établir une reconstruction de la partie aérienne, des incertitudes demeurent concernant la partie sous-marine. En supposant une pente constante de 8°, un volume d'environ 150 million de m^3 a été défini. En utilisant un coefficient de friction basale de 2°, les résultats des simulations effectuées avec AVALANCHE étaient globalement en accord avec les données des nombreuses études de terrain, sauf dans la baie de Panjang au nord du volcan.

Le Chapitre 3 de la Partie III présente une méthode de modélisation de cas complexes avec OpenFOAM. Elle est basée sur une approche multiphasique (en utilisant le solver multiphaseInterFoam) et un glissement considéré comme un fluide visqueux. Le maillage est généré par blockMesh puis un raffinement sur la bathymétrie est appliqué par snappyHexMesh. Cette méthode est appliquée aux deux événements du chapitre précédent et comparée à de nouvelles simulations réalisées avec AVALANCHE.

Dans les deux cas, comme montré dans la Partie II pour des hautes valeurs de Reynolds, le glissement a tendance à plus s'étaler dans AVALANCHE que dans OpenFOAM, ce qui mène à des vagues plus petites. Cependant des vagues similaires peuvent être obtenues dans les deux modèles en ajustant la viscosité.

Par rapport à AVALANCHE, le temps de calcul est considérablement plus long avec OpenFOAM et le stockage des résultats demande énormément de mémoire. Néanmoins, ces premières études d'événements réels avec OpenFOAM sont prometteuses. Pour le moment, avec un maillage homogène et en utilisant le maximum de RAM disponible sur le cluster, la résolution la plus fine obtenue a été de 15 m. Étant donné la hauteur des vagues dans ce genre d'événements, il est probablement nécessaires d'affiner cette résolution, au moins autour de la surface de l'eau. De plus, la résolution du fichier de bathymétrie utilisé dans snappyHexMesh a probablement une forte influence qui devrait être étudiée afin de réduire les aberrations lors du maillage proche des côtes.

En conclusion, plusieurs enseignements peuvent être tirés de cette thèse. Tout d'abord, lorsque l'on utilise un modèle intégré sur la profondeur, il est préférable de prendre en compte la dispersion fréquentielle en résolvant les équations de Boussinesq pour la propagation des vagues, après avoir résolu les équations shallow water lors de la génération. Ensuite, si les deux types de modèles (Navier-Stokes et intégrés sur la profondeur) conduisent à des résultats similaires dans certains cas (par exemple un

glissement proche de la surface de l'eau et des pentes moyennes), il est difficile de dire avec certitude pour quelle configuration un des deux modèles sera plus approprié que l'autre. Enfin, les simulations des tsunamis de Karrat Fjord 2017 et Anak Krakatau 2018 réalisées avec OpenFOAM sont prometteuses et montrent que considérer le glissement comme un fluide newtonien est une première approche acceptable. Ces deux études préliminaires ouvrent la porte à de futures modélisations prenant en compte un maillage plus fin et d'autres lois de comportement pour le glissement.

Bibliography

Abadie, S., Harris, J., Grilli, S. and Fabre, R. (2012), 'Numerical modeling of tsunami waves generated by the flank collapse of the Cumbre Vieja Volcano (La Palma, Canary Islands): Tsunami source and near fiedl effects', *Journal of Geophysical Research* **117**(5).

Abadie, S., Morichon, D., Grilli, S. and Glockner, S. (2008), 'VOF/Navier-Stokes numerical modeling of surface waves generated by subaerial landslides', *La Houille Blanche* **1**, 21–26.

Abadie, S., Morichon, D., Grilli, S. and Glockner, S. (2010), 'Numerical simulation of waves generated by landslides using a multiple-fluid Navier-Stokes model', *Coastal Engineering* **57**, 779–794.

Abadie, S., Paris, A., Ata, R., Le Roy, S., Arnaud, G., Poupardin, A., Clous, L., Heinrich, P., Harris, J., Pedreros, R. and Krien, Y. (2020), 'La Palma landslide tsunami: calibrated wave source and assessment of impact on French territories', *Natural Hazards and Earth System Sciences* **20**, 3019–3038.

Assier-Rzadkiewicz, S., Heinrich, P., Sabatier, P., Savoye, B. and Bourillet, J. (2000), 'Numerical modelling of a landslide-generated tsunami: The 1979 Nice event', *Pure and Applied Geophysics* **157**(10), 1707–1727.

Ataie-Ashitiani, B. and Najafi-Jilani, A. (2008), 'Laboratory investigations on impulsive waves caused by underwater landslide', *Coastal Engineering* **55**(12), 989–1004.

Ataie-Ashtiani, B. and Yavari-Ramshe, S. (2011), 'Numerical simulation of wave generated by landslide incidents in dam reservoirs', *Landslides* **8**, 417–432.

Audusse, E., Bouchut, F., Bristeau, M.-O., Klein, R. and Perthame, B. (2004), 'A fast and stable well-balanced scheme with hydrostatic reconstruction for shallow water flows', *SIAM J. Sci. Comput.* **25**(6), 2050–2065.

Audusse, E., Caldas Steinstraesser, J., Emerald, L., Heinrich, P., Paris, A. and Parisot, M. (2021), 'Comparison of models for the simulation of landslide generated tsunamis', *ESAIM: Proceedings and Surveys* **70**, 14–30.

Biscarini, C. (2010), 'Computational fluid dynamics modelling of landslide generated water waves', *Landslides* **7**, 117–124.

Bolin, H., Yueping, Y., Xiaoting, C., Guangning, L., Sichang, W. and Zhibing, J. (2014), 'Experimental modeling of tsunamis generated by subaerial landslides: two case studies of the Three Gorges Reservoir, China', *Environmental Earth Sciences* **71**, 3813–3825.

Bondevik, S. (2019), Tsunami from the storegga landslide, *in* R. A. Meyers, ed., 'Encyclopedia of Complexity and Systems Science', Springer Berlin Heidelberg, Berlin, Heidelberg, pp. 1–33.

Bornhold, B. (2011), Submarine Failures and Associated Tsunamis, Norway - Literature Review, Technical report, Coastal and Ocean Resources Inc.

Borrero, J., Solihuddin, T., Fritz, H., Lynett, P., Prasetya, G., Skanavis, V., Husrin, S., Kushendratno, Kongko, W., Istiyanto, D., Daulat, A., Purbani, D., Salim, H., Hidayat, R., Asvaliantina, V., Usman, M., Kodijat, A., Son, S. and Synolakis, C. (2020), 'Field Survey and Numerical Modelling of the December 22, 2018 Anak Krakatau Tsunami', *Pure and Applied Geophysics* **177**, 2457–2475.

Bosa, S. and Petti, M. (2011), 'Shallow water numerical model of the wave generated by the Vajont landslide', *Environmental Modelling & Software* **26**, 406–418.

Bouchut, F. (2004), *Nonlinear stability of finite volume methods for hyperbolic conservation laws, and well-balanced schemes for sources*, Springer Science & Business Media.

Bregoli, F., Pinzón, A., Medina Iglesias, V. and Gómez Cortés, D. (2013), 'Experimental studies on 3D impulse waves generated by rapid landslides and debris flows', *Italian Journal of Engineering Geology and Environment* **2013**(TOPIC1), 115–122.

Bullard, G., Mulligan, R. and Take, W. (2019), 'An Enhanced Framework to Quantify the Shape of Impulse Waves Using Asymmetry', *Journal of Geophysical Research: Oceans* **124**, 652–666.

Chen, F., Heller, V. and Briganti, R. (2020), 'Numerical modelling of tsunamis generated by iceberg calving validated with large-scale laboratory experiments', *Advances in Water Resources* **142**(103647).

Clous, L. (2018), Modelling of waves generated by landslides. Discontinuous and continuous approaches and focus on energy transfers, PhD thesis, Université de Pau et des Pays de l'Adour.

Clous, L. and Abadie, S. (2019), 'Simulation of energy transfers in waves generated by granular slides', *Landslides* **16**(9), 1663–1679.

Davies, D., Wilson, C. and Kramer, S. (2011), 'Fluidity: A fully unstructured anisotropic adaptive mesh computational modeling framework for geodynamics', *Geochemistry Geophysics Geosystems* **12**(Q06001).

De Blasio, F., Engvik, L., Harbitz, C. and Elverhøi, A. (2004), 'Hydroplaning and submarine debris flows', *Journal of Geophysical Research* **109**(C01002).

Dutykh, D. and Kalisch, H. (2013), 'Boussinesq modeling of surface waves due to underwater landslides', *Nonlinear Processes in Geophysics* **20**, 267–285.

Enet, F. and Grilli, S. (2007), 'Experimental Study of Tsunami Generation by Three-Dimensional Rigid Underwater Landslides', *Journal of Waterway, Port, Coastal, and Ocean Engineering* **133**(6), 442–454.

Evans, S. (1989), 'The 1946 Mount Colonel Foster rock avalanche and associated displacement wave, Vancouver Island, British Columbia', *Canadian Geotechnical Journal* **26**(3), 447–452.

Evers, F., Hager, W. and Boes, R. (2019), 'Spatial Impulse Wave Generation and Propagation', *Journal of Waterway, Port, Coastal, and Ocean Engineering* **145**(3), 04019011.

Fernández-Nieto, E., Morales de Luna, T., Narbona-Reina, G. and Zabsonré, J. (2017), 'Formal deduction of the saint-venant-exner model including arbitrarily sloping sediment beds and associated energy', *ESAIM: M2AN* **51**(1), 115–145.

Fine, I., Rabinovich, A., Bornhold, B., Thomson, R. and Kulikov, E. (2005), 'The Grand Banks landslide-generated tsunami of November 18, 1929: preliminary analysis and numerical modeling', *Marine Geology* **215**(1–2), 45–57.

Franz, M., Jaboyedoff, M., Locat, J. and Podladchikov, Y. (2015), Testing a landslide-generated tsunami model. The case of the Nicolet landslide (Québec, Canada), *in* 'Conference GEOQuébec 2015', Québec City, QC, Canada.

Fritz, H. (2002), Initial phase of landslide generated impulse waves, PhD thesis, ETH Zurich.

Fuhrman, D. and Madsen, P. (2009), 'Tsunami generation, propagation and run-up with a high-order Boussinesq model', *Coastal Engineering* **56**, 747–758.

Giachetti, T., Paris, R., Kelfoun, K. and Ontowirjo, B. (2012), 'Tsunami hazard related to a flank collapse of Anak Krakatau volcano, Sunda Strait, Indonesia', *Geological Society Londo, Special Publication* **361**, 79–89.

Glimsdal, S., L'Heureux, J.-S., Harbitz, C. and Løvholt, F. (2016), 'The 29th January 2014 submarine landslide at Statland, Norway–landslide dynamics, tsunami generation, and run-up', *Landslides* **13**(6), 1435–1444.

Glimsdal, S., Pedersen, G., Harbitz, C. and Løvholt, F. (2013), 'Dispersion of tsunamis: doest it really matter?', *Natural Hazards and Earth System Sciences* **13**, 1507–1526.

Grilli, S., Harris, J., Bakhsh, T., Masterlark, T., Kyriakopoulos, C., Kirby, J. and Shi, F. (2013), 'Numerical simulation of the 2011 Tohoku tsunami based on a new transient FEM coseismic source: Comparison to far and near-field observations', *Pure and Applied Geophysics* **170**, 1333–1359.

Grilli, S., Shelby, M. and Kimmoun, O. (2017), 'Modeling coastal tsunami hazard from submarine mass failures: effect of slide rheology, experimental validation, and case studies off the US East Coast', *Natural Hazards* **86**, 353–391.

Grilli, S., Tappin, D., Carey, S., Watt, S., Ward, S., Grilli, A., Engwell, S., Zhang, C., Kirby, J., Schambach, L. and Muin, M. (2019), 'Modelling of the tsunami from the December 22, 2018 lateral collapse of Anak Krakatau volcano in the Sunda Straits, Indonesia', *Scientific Reports* **9**(11946).

Grilli, S., Zhang, C., Kirby, J., Grilli, A., Tappin, D., Watt, S., Hunt, J., Novellino, A., Engwell, S., Nurshal, M., Abdurrachman, M., Cassidy, M., Madden-Nadeau, A. and Day, S. (2021), 'Modeling of the Dec. 22nd 2018 Anak Krakatau volcano lateral collapse and tsunami based on recent field surveys: Comparison with observed tsunami impact', *Marine Geology* **440**(106566).

Gylfadóttir, S., Kim, J., Helgason, J., Brynjólfsson, S., Höskuldsson, Á., Jóhannesson, T., Harbitz, C. and Løvholt, F. (2017), 'The 2014 Lake Askja rockslide-induced tsunami: Optimization of numerical tsunami model using observed data', *Journal of Geophysical Research: Oceans* **122**, 4110–4122.

Haeussler, P., Gulick, S., McCall, N., Walton, M., Reece, R., Larsen, C., Shugar, D., Geertsema, M., Venditti, J. and Labay, K. (2018), 'Submarine deposition of a subaerial landslide in Taan Fiord, Alaska', *Journal of Geophysical Research: Earth Surface* **123**(10), 2443–2463.

Hansen, L., Waldmann, N., Storms, J., Eilertsen, R., Ariztegui, D., Chapron, E. and Nesje, A. (2016), 'Morphological signatures of mass wasting and delta processes in a fjord-lake system: insights from Lovatnet, western Norway', *Norvegian Journal of Geology* **96**(3), 179–199.

Harbitz, C. and Glimsdal, S. (2011), Numerical simulations of tsunamis from potential and historical rock slides in Storfjorden; Hazard zoning and comparison with 3D laboratory experiments, Technical report, Norwegian Geotechnical Institute Report.

Harbitz, C., Glimsdal, S., Løvholt, F., Kveldsvik, V., Pedersen, G. and Jensen, A. (2014), 'Rockslide tsunamis in complex fjords: From an unstable rock slope at Åkerneset to tsunami risk in western Norway', *Coastal Engineering* **88**, 101–122.

Heidarzadeh, M., Ishibe, T., Sandanbata, O., Muhari, A. and Wijanarto, A. (2020), 'Numerical modeling of the subaerial landslide source of the 22 December 2018 Anak Krakatoa volcanic tsunami, Indonesia', *Ocean Engineering* **195**.

Heinrich, P. and Piatanesi, A. (2000), 'Near-field modeling of the July 17, 1998 tsunami in Papua New Guinea', *Geophysical Research Letters* **27**(19), 3037–3040.

Heinrich, P., Piatanesi, A. and Hébert, H. (2001), 'Numerical modelling of tsunami generation and propagation from submarine slumps: The 1998 Papua New Guinea event', *Geophysical Journal International* **145**(1), 97–111.

Heller, V. and Hager, W. (2010), 'Impulse Product Parameter in Landslide Generated Impulse Waves', *Journal of Waterway, Port, Coastal, and Ocean Engineering* **136**(3), 145–155.

Heller, V., Hager, W. and Minor, H.-E. (2008), 'Scale effects in subaerial landslide generated impulse waves', *Experiments in Fluids* **44**, 691—703.

Heller, V. and Spinneken, J. (2013), 'Improved landslide-tsunami prediction: Effects of block model parameters and slide model', *Journal of Geophysical Research: Oceans* **118**, 1489–1507.

Heller, V. and Spinneken, J. (2015), 'On the effect of the water body geometry on landslide-tsunamis: Physical insight from laboratory tests and 2D to 3D wave parameter transformation', *Coastal Engineering* **104**, 113–134.

Higman, B., Shugar, D., Stark, C., Ekström, G., Koppes, M., Lynett, P., Dufresne, A., Haeussler, P., Geertsema, M., Gulick, S., Mattox, A., Venditti, J., Walton, M., McCall, N., Mckittrick, E., MacInnes, B., Bilderback, E., Tang, H., Willis, M., Richmond, B., Reece, R., Larsen, C., Olson, B., Capra, J., Ayca, A., Bloom, C., Williams, H., Bonno, D., Weiss, R., Keen, A., Skanavis, V. and Loso, M. (2018), 'The 2015 landslide and tsunami in Taan Fjord, Alaska', *Scientific Reports* **8**(12993).

Hirt, C. W. and Nichols, B. D. (1981), 'Volume of fluid (VOF) method for the dynamics of free boundaries', *Journal of Computational Physics* **39**(1), 201–225.

Honarmand, M., Shanehsazzadeh, A. and Zandi, S. (2020), '3D numerical simulation of tsunami generation and propagation, case study: Makran tsunami generation and penetrating in Chabahar Bay', *Coastal Engineering* **218**, 108109.

Horrillo, J., Grilli, S., Nicolsky, D., Roeber, V. and Zhang, J. (2015), 'Performance Benchmarking Tsunami Models for NTHMP's Inundation Mapping Activities', *Pure and Applied Geophysics* **172**, 869–884.

Horrillo, J., Wood, A., Kim, G.-B. and Parambath, A. (2013), 'A simplified 3-D Navier-Stokes numerical model for landslide-tsunami: Application to the Gulf of Mexico', *Journal of Geophysical Research: Oceans* **118**, 6934–6950.

Huang, B., Yin, Y., Wang, S., Tan, J. and Liu, G. (2017), 'Analysis of the Tangjiaxi landslide-generated waves in the Zhexi Reservoir, china, by a granular flow coupling model', *Natural Hazards and Earth System Sciences* **17**, 657–670.

Hunt, J., Tappin, D., Watt, S., Susilohadi, S., Novellino, A., Ebmeier, S., Cassidy, M., Engwell, S., Grilli, S., Hanif, M., Priyanto, W., Clare, M., Abdurrachman, M. and Udrekh, U. (2021), 'Submarine landslide megablocks show half of Anak Krakatau island failed on December 22nd, 2018', *Nature Communications* **12**(2827).

Hébert, H., Occhipinti, G., Schindelé, F., Gailler, A., Pinel-Puysségur, B., Gupta, H., Rolland, L., Lognonné, P., Lavigne, F., Meilianda, E., Chapkanski, S., Crespon, F., Paris, A., Heinrich, P., Monnier, A., Jamelot, A. and Reymond, D. (2020), 'Contributions of Space Missions to Better Tsunami Science: Observations, Models and Warnings', *Surveys in Geophysics* **45**, 1535–1581.

Hébert, H., Piatanesi, A., Heinrich, P. and Schindelé, F. (2002), 'Numerical modeling of the September 13, 1999 landslide and tsunami on Fatu Hiva Island (French Polynesia)', *Geophysical Research Letters* **29**(10), 10–13.

Ionescu, I., Mangeney, A., Bouchut, F. and Roche, O. (2015), 'Viscoplastic modeling of granular column collapse with pressure-dependent rheology', *Journal of Non-Newtonian Fluid Mechanics* **219**, 1–18.

Jiang, L. and LeBlond, P. (1992), 'The coupling of a submarine slide and the surface waves which it generates', *Journal of Geophysical Research: Oceans* **97**(C8), 12731–12744.

Jiang, L. and LeBlond, P. (1994), 'Three-Dimensional Modeling of Tsunami Generation Due to a Submarine Mudslide', *Journal of Physical Oceanography* **24**(3), 559–572.

Kamphuis, J. and Bowering, R. (1970), 'Impulse Waves Generated by Landslides', *Coastal Engineering Proceedings* **1**(12), 35.

Kelfoun, K., Giachetti, T. and Labazuy, P. (2010), 'Landslide-generated tsunamis at Réunion Island', *Journal of Geophysical Research: Earth Surface* **115**(F4).

Kim, G.-B., Cheng, W., Sunny, R., Horrillo, J., McFall, B., Mohammed, F., Fritz, H., Beget, J. and Kowalik, Z. (2020), 'Three Dimensional Landslide Generated Tsunamis: Numerical and Physical Model Comparisons', *Landslides* **17**, 1145–1161.

Kim, J., Løvholt, F., Issler, D. and Forsberg, C. (2019), 'Landslide material control on tsunami genesis–The Storegga Slide and tsunami (8100 y BP)', *Journal of Geophysical Research: Oceans* **124**, 3607–3627.

Kulikov, E., Rabinovich, A., Thomson, R. and Bornhold, B. (1996), 'The landslide tsunami of November 3, 1994, Skagway Harbor, Alaska', *Journal of Geophysical Research: Oceans* **101**(C3), 6609–6615.

Lannes, D. (2013), *The water waves problem : mathematical analysis and asymptotics*, Vol. 188, Mathematical Surveys and Monographs.

Lassa, J. (2009), 'The forgotten disaster? Remembering the Larantuka and Lembata disaster 1979–2009', *Journal of NTT Studies* **1**(2), 159–184.

Le Friant, A., Heinrich, P., Deplus, C. and Boudon, G. (2003), 'Numerical simulation of the last flank-collapse event of Montagne Pelée, Martinique, Lesser Antilles', *Geophysical Research Letters* **30**(2).

Leblanc, J., Turmel, D., Therrien, J. and Locat, J. (2016), Observations of coastal landslide-generated tsunami under an ice cover: The case of Lac-des-Seize-Îles, Québec, Canada, *in* G. Lamarche, J. Mountjoy, S. Bull, T. Hubble, S. Krastel, E. Lane, A. Micallef, L. Moscardelli, C. Mueller, I. Pecher and S. Woelz, eds, 'Submarine Mass Movements and their Consequences', Vol. 41, Springer International Publishing, Cham, pp. 607–614.

Lee, C.-H. and Huang, Z. (2021), 'Multi-phase flow simulation of impulsive waves generated by a sub-aerial granular landslide on an erodible slope', *Landslides* **18**, 881–895.

Lee, C.-H., Low, Y. and Chiew, Y.-M. (2016), 'Multi-dimensional rheology-based two-phase model for sediment transport and applications to sheet flow and pipeline scour', *Physics of Fluids* **28**(053305).

Lefebvre, G., Rosenberg, P., Paquette, J. and Lavallée, J. (1991), 'The September 5, 1987, landslide on the La Grande River, James Bay, Quebec, Canada', *Canadian Geotechnical Journal* **28**(2), 263–275.

L'Heureux, J.-S., Glimsdal, S., Longva, O., Hansen, L. and Harbitz, C. (2011), 'The 1888 shoreline landslide and tsunami in Trondheimsfjorden, central Norway', *Marine Geophysical Research* **32**(1), 313–329.

L'Heureux, J.-S., Hansen, L., Longva, O., Emdal, A. and Grande, L. (2010), 'A multidisciplinary study of submarine landslides at the Nidelva fjord delta, Central Norway - Implications for geohazard assessment', *Norwegian Journal of Geology* **90**, 1–20.

L'Heureux, J.-S., Longva, O., Hansen, L. and Vanneste, M. (2014), The 1930 Landslide in Orkdalsfjorden: Morphology and Failure Mechanism, *in* S. Krastel, J.-H. Behrmann, D. Völker, M. Stipp, C. Berndt, R. Urgeles, J. Chaytor, K. Huhn, M. Strasser and C. Harbitz, eds, 'Submarine Mass Movements and Their Consequences. Advances in Natural and Technological Hazards Research', Vol. 37, Springer International Publishing, Cham.

Liu, P., Wu, T., Raichlen, F., Synolakis, C. and Borrero, J. (2005), 'Runup and rundown generated by three-dimensional sliding masses', *Journal of Fluid Mechanics* **536**, 107–144.

Locat, J., Turmel, D. and Leblanc, J. (2016), Tsunamigenic landslides in Québec, *in* 'Landslides and Engineered Slopes. Experience, Theory and Practice', Vol. 2, 12th International Symposium on Landslides, 2016; Napoli, Italy, pp. 1305–1312.

Løvholt, F., Pedersen, G. and Gisler, G. (2008), 'Oceanic propagation of a potential tsunami from the La Palma Island', *Journal of Geophysical Research: Oceans* **113**(9), 1–21.

Løvholt, F., Pedersen, G. and Glimsdal, S. (2010), 'Coupling of dispersive tsunami propagation and shallow water coastal response', *The Open Oceanography Journal* **4**, 71–82.

Lynett, P., Gately, K., Wilson, R., Montoya, L., Arcas, D., Aytore, B., Bai, Y., Bricker, J., Castro, M., Cheung, K., David, C., Dogan, G., Escalante, C., González-Vida, J., Grilli, S., Heitmann, T., Horrillo, J., Kânoğlu, U., Kian, R., Kirby, J., Li, W., Macías, J., Nicolsky, D., Ortega, S., Pampell-Manis, A., Park, Y., Roeber, V., Sharghivand, N., Shelby, M., Shi, F., Tehranirad, B., Tolkova, E., Thio, H., Velioğlu, D., Yalçiner, A., Yamazaki, Y., Zaytsev, A. and Zhang, Y. (2017), 'Inter-model analysis of tsunami-induced coastal currents', *Ocean Modelling* **114**, 14–32.

Ma, G., Kirby, J. and Shi, F. (2013), 'Numerical simulation of tsunami waves generated by deformable submarine landslides', *Ocean Modelling* **69**, 146–165.

Macías, J., Vázquez, J., Fernández-Salas, L., González-Vida, J., Bárcenas, P., Castro, M., Díaz-del Río, V. and Alonso, B. (2015), 'The Al-Borani submarine landslide and associated tsunami. A modelling approach', *Marine Geology* **361**, 79–95.

Mader, C. and Gittings, M. (2002), 'Modeling the 1958 Lituya Bay mega-tsunami, II', *Science of Tsunami Hazards* **20**(5), 241.

Mangeney, A., Heinrich, P., Roche, R., Boudon, G. and Cheminée, J. (2000), 'Modeling of Debris Avalanche and Generated Water Waves: Application to Real and Potential Events in Montserrat', *Physics and Chemistry of the Earth, Part A: Solid Earth and Geodesy* **25**(9–11), 741–745.

Maramai, A., Graziani, L. and Tinti, S. (2003), Updating and revision of the European Tsunami Catalogue, *in* A. Yalçiner, E. Pelinovsky, E. Okal and C. Synolakis, eds, 'Submarine Landslides and Tsunamis', Springer Netherlands, Dordrecht, pp. 25–32.

Masson, D., Watts, A., Gee, M., Urgeles, R., Mitchell, N., Le Bas, T. and Canals, M. (2002), 'Slope failures on the flanks of the western Canary Islands', *Earth-Science Reviews* **57**, 1–35.

Mazzanti, P. and Vittorio de Blasio, F. (2011), 'The dynamics of coastal landslides: insights from laboratory experiments and theoretical analyses', *Bulletin of Engineering Geology and the Environment* **70**, 411–422.

McFall, B. and Fritz, H. (2016), 'Physical modelling of tsunamis generated by three-dimensional deformable granular landslides on planar and conical island slopes', *Proceedings of the Royal Society A* **472**(20160052).

Miller, D. J. (1960), 'Giant waves in Lituya Bay, Alaska', *US Geological Survey Professional Paper* **354-C**.

Mohammed, F. and Fritz, H. (2012), 'Physical modeling of tsunamis generated by three-dimensional deformable granular landslides', *Journal of Geophysical Research* **117**(C11015).

Mulligan, R. and Take, W. (2017), 'On the transfer of momentum from a granular landslide to a water wave', *Coastal Engineering* pp. 16–22.

Naranjo, J., Arenas, M., Clavero, J. and noz, M. (2009), 'Mass movement-induced tsunamis: main effects during the Patagonian Fjordland seismic crisis in Aisén (45°25'S), Chile', *Andrean Geology* **36**(1), 137–145.

Noda, E. (1970), 'Water Waves Generated by Landslides', *Journal of the Waterways, Harbors and Coastal Engineering Division* **96**(4), 835–855.

Omira, R., Ramalho, I., Terrinha, P., Baptista, M., Batista, L. and Zitellini, N. (2016), 'Deep-water seamounts, a potential source of tsunami generated by landslides? The Hirondelle Seamount, NE Atlantic', *Marine Geology* **379**, 267–280.

Panizzo, A. (2004), Physical and numerical modelling of subaerial landslide generated waves, PhD thesis, L'Aquila University.

Panizzo, A., De Girolamo, P., Di Risio, M., Maistri, A. and Petaccia, A. (2005), 'Great landslide events in Italian artificial reservoirs', *Natural Hazards and Earth System Sciences* **5**, 733–740.

Papadopoulos, G., Lobkovsky, L., Mazova, R., Garagash, I., Karastathis, V., Kataeva, L. Y. and Kaz'min, V. (2007), 'Numerical Modeling of Sediment Mass Sliding and Tsunami Generation: The Case of February 7, 1963, in Corinth Gulf, Greece', *Marine Geodesy* **30**(4), 315–331.

Paris, A., Heinrich, P. and Abadie, S. (2021), 'Landslide tsunamis: Comparison between depth-averaged and Navier–Stokes models', *Coastal Engineering* **170**(104022).

Paris, A., Heinrich, P., Paris, R. and Abadie, S. (2020), 'The December 22, 2018 Anak Krakatau, Indonesia, landslide and tsunami: preliminary modeling results', *Pure and Applied Geophysics* **177**, 571–590.

Paris, A., Okal, E., Guérin, C., Heinrich, P., Schindelé, F. and Hébert, H. (2019), 'Numerical modeling of the June 17, 2017 landslide and tsunami events in Karrat Fjord, west Greenland', *Pure and Applied Geophysics* **176**(7), 3035–3057.

Parisot, M. (2019), 'Entropy-satisfying scheme for a hierarchy of dispersive reduced models of free surface flow', *International Journal for Numerical Methods in Fluids* **91**(10), 509–531.

Pedersen, G. and Løvholt, F. (2008), 'Documentation of a global Boussinesq solver', *Preprint series in Applied Mathematics 1* .

Pedersen, S., Larsen, L., Dahl-Jensen, T., Jepsen, H., Krarup, Pedersen, G., Nielsen, T., Pedersen, A., von Platen-Hallermund, F. and Weng, W. (2002), 'Tsunami-generating rock fall and landslide on the south coast of Nuussuaq, central West Greenland', *Geology of Greenland Survey Bulletin* **191**, 73–83.

Perlin, M. and Bustamante, M. (2016), 'A robust quantitative comparison criterion of two signals based on the Sobolev norm of their difference', *Journal of Engineering Mathematics* **101**, 115–124.

Poupardin, A., Heinrich, P., Frère, A., Imbert, D., Hébert, H. and Flouzat, M. (2017), 'The 1979 Submarine Landslide-Generated Tsunami in Mururoa, French Polynesia', *Pure and Applied Geophysics* **174**, 3293–3311.

Pudasaini, S. and Miller, S. (2012), 'Buoyancy induced mobility in two-phase debris flow', *AIP Conference Proceedings* **1479**, 149–152.

Qin, X., Motley, M., LeVeque, R., Gonzalez, F. and Mueller, K. (2018), 'A comparison of a two-dimensional depth-averaged flow model and a three-dimensional RANS model for predicting tsunami inundation and fluid forces', *Natural Hazards and Earth System Sciences* **18**, 2489–2506.

Qin, X., Motley, M. and Marafi, N. (2018b), 'Three-dimensional modeling of tsunami forces on coastal communities', *Coastal Engineering* **140**, 43–59.

Quarteroni, A., Sacco, R. and Saleri, F. (2006), *Numerical Mathematics*, Springer.

Rabinovich, A., Thomson, R., Kulikov, E., Bornhold, B. and Fine, I. (1999), 'The landslide-generated tsunami of November 3, 1994 in Skagway Harbor, Alaska: A case study', *Geophysical Research Letters* **26**(19), 3009–3012.

Rauter, M. (2021), 'The compressible granular collapse in a fluid as a continuum: validity of a Navier-Stokes model with $\mu(J)$, $\phi(J)$-rheology', *Journal of Fluid Mechanics* **915**(A87).

Rauter, M., Hoße, L., Mulligan, R., Take, W. and Løvholt, F. (2021), 'Numerical simulation of impulse wave generation by idealized landslides with OpenFOAM', *Coastal Engineering* **165**(103815).

Redfield, T., Hermanns, R., Oppikofer, T., Duhart, P., Mella, M., Derch, P., Bascuñán, I., Fernandez, J., Arenas, M., Sepúlveda, S., Rebolledo, S., Loew, S., Yugsi Molina, F., Abächerli, A., Henderson, I., Jaboyedoff, M. and Kveldsvik, V. (2011), Analysis of the 2007 earthquake-induced Punta Cola rockslide and tsunami, Aysén Fjord, Patagonia, Chile (45.3° S, 73.0° W), *in* '5th International Conference on Earthquake Geotechnical Engineering', Vol. 12, Santiago, Chile.

Robbe-Saule, M. (2019), Modélisation expérimentale de génération de tsunami par effondrement granulaire, PhD thesis, Université Paris-Saclay (ComUE).

Robertson, D. and Gisler, G. (2019), 'Near and far-field hazards of asteroid impacts in oceans', *Acta Astronautica* **156**, 262–277.

Rodriguez, M., Chamot-Rooke, N., Hébert, H., Fournier, M. and Huchon, P. (2013), 'Owen Ridge deep-water submarine landslides: Implications for tsunami hazard along the Oman coast', *Natural Hazards and Earth System Science* **13**, 417–424.

Romano, A., Lara, J., Barajas, G., Di Paolo, B., Bellotti, G., Di Risio, M., Losada, I. and De Girolamo, P. (2020), 'Tsunamis Generated by Submerged Landslides: Numerical Analysis of the Near-Field Wave Characteristics', *Journal of Geophysical Research: Oceans* **125**(7).

Salmanidou, D., Georgiopoulou, A., Guillas, S. and Dias, F. (2018), 'Rheological considerations for the modelling of submarine sliding at Rockfall Bank, NE, Atlantic Ocean', *Physics of Fluids* **30**(030705).

Savage, S. B. and Hutter, K. (1989), 'The motion of a finite mass of granular material down a rough incline', *Journal of Fluid Mechanics* **199**, 177–215.

Schambach, L., Grilli, S. and Tappin, D. (2021), 'New High-Resolution Modeling of the 2018 Palu Tsunami, Based on Supershear Earthquake Mechanisms and Mapped Coastal Landslides, Supports a Dual Source', *Frontiers in Earth Science* **8**, 627.

Schambach, L., Grilli, S., Tappin, D., Gangemi, M. and Barbaro, G. (2020), 'New simulations and understanding of the 1908 Messina tsunami for a dual seismic and deep submarine mass failure source', *Marine Geology* **421**(106093).

Serrano-Pacheco, A., Murillo, J. and García-Navarro, P. (2009), 'A finite volume method for the simulation of the waves generated by landslides', *Journal of Hydrology* **273**, 273–289.

Si, P., Shi, H. and Yu, X. (2018), 'A general numerical model for surface waves generated by granular material intruding into a water body', *Coastal Engineering* **142**, 42–51.

Skvortsov, A. and Bornhold, B. (2007), 'Numerical simulation of the landslide-generated tsunami in Kitimat Arm, British Columbia, Canada, 27 April 1975', *Journal of Geophysical Research: Earth Surface* **112**(2).

Sogut, D. and Yalçiner, A. (2019), 'Performance Comparison of NAMI DANCE and FLOW-3D® Models in Tsunami Propagation, Inundation and Currents using NTHMP Benchmark Problems', *Pure and Applied Geophysics* **176**(7), 3115–3153.

Sosio, R., Crosta, G. and Hungr, O. (2012), 'Numerical modeling of debris avalanche propagation from collapse of volcanic edifices', *Landslides* **9**, 315–334.

Sue, L., Nokes, R. and Davidson, M. (2011), 'Tsunami generation by submarine landslides: comparison of physical and numerical models', *Environmental Fluid Mechanics* **11**, 133–165.

Sugawara, D. (2021), 'Numerical modeling of tsunami: advances and future challenges after the 2011 Tohoku earthquake and tsunami', *Earth-Science Reviews* **214**(103498).

Synolakis, C. E., Bardet, J.-P., Borrero, J. C., Davies, H. L., Okal, E. A., Silver, E. A., Sweet, S. and Tappin, D. R. (2002), The slump origin of the 1998 Papua New Guinea tsunami, *in* 'Proceedings of the Royal Society of London, Series A: Mathematical, Physical and Engineering Sciences', Vol. 458, The Royal Society, pp. 763–789.

Tappin, D. (2021), 'Submarine Landslides and Their Tsunami Hazard', *Annual Review of Earth and Planetary Sciences* **49**, 551–578.

Tappin, D., Watts, P. and Grilli, S. (2008), 'The Papua New Guinea tsunami of 17 July 1998: anatomy of a catastrophic event', *Natural Hazards and Earth System Sciences* **8**, 243–266.

Thuro, K. and Hatem, M. (2010), The 1806 Goldau landslide event–analysis of a large rock slide, *in* A. Williams, G. Pinches, C. Chin, T. McMorran and C. Massey, eds, 'Geologically Active', Taylor & Francis Group, London.

Tinti, S., Bortolucci, E. and Armigliato, A. (1999), 'Numerical simulation of the landslide-induced tsunami of 1988 on Vulcano Island, Italy', *Bulletin of Volcanology* **61**, 121–137.

Tinti, S., Pagnoni, G. and Zaniboni, F. (2006), 'The landslides and tsunamis of the 30th of December 2002 in Stromboli analysed through numerical simulations', *Bulletin of Volcanology* **68**, 462–479.

Toro, E. (2009), *Riemann solvers and numerical methods for fluid dynamics: A practical introduction*, Springer Berling Heidelberg.

Vilibić, I., Denamiel, C., Zemunik, P. and Monserrat, S. (2021), 'The Mediterranean and Black Sea meteotsunamis: an overview', *Natural Hazards* **106**, 1223–1267.

Vilibić, I. and Šepić, J. (2009), 'Destructive meteotsunamis along the eastern Adriatic coast: Overview', *Physics and Chemistry of the Earth* **34**(17–18), 904–917.

Vilibić, I., Šepić, J., Rabinovich, A. and Monserrat, S. (2016), 'Modern approaches in meteotsunami research and early warning', *Frontiers in Marine Science* **3**(MAY), 57.

Violeau, D. (2021), 'Cosmogenic tsunamic risk assessment: a first application to the European Atlantic coasts', *Natural Hazards* **105**, 735–753.

Viroulet, S., Sauret, A. and Kimmoun, O. (2014), 'Tsunami generated by a granular collapse down a rough inclined plane', *EPL (Europhysics Letters)* **105**(3), 34004.

Viroulet, S., Sauret, A., Kimmoun, O. and Kharif, C. (2016), Tsunami waves generated by cliff collapse: comparison between experiments and triphasic simulations, *in* E. Pelinovsky and C. Kharif, eds, 'Extreme Ocean Waves', Springer International Publishing, Cham, pp. 173–190.

Walder, J., Watts, P., Sorensen, O. and Janssen, K. (2003), 'Tsunamis generated by subaerial mass flows', *Journal of Geophysical Research* **108**(B5), 2236.

Waldmann, N., Vasskog, K., Simpson, G., Chapron, E., Støren, E., Hansen, L., Loizeau, J.-L., Nesje, A. and Ariztegui, D. (2021), 'Anatomy of a Catastrophe: Reconstructing the 1936 Rock Fall and Tsunami Event in Lake Lovatnet, Western Norway', *Frontiers in Earth Science* **9**, 364.

Wang, F.-W., Zhang, Y.-M., Huo, Z.-T., Matsumoto, T. and Huang, B.-L. (2004), 'The July 14, 2003 Qianjiangping landslide, Three Gorges Reservoir, China', *Landslides* **1**, 157–162.

Wang, J., Ward, S. and Xiao, L. (2015), 'Numerical simulation of the December 4, 2007 landslide-generated tsunami in Chehalis Lake, Canada', *Geophysical Journal International* **201**, 372–376.

Ward, S. and Asphaug, E. (2000), 'Asteroid Impact Tsunami: A Probabilistic Hazard Assessment', *Icarus* **154**(1), 64–78.

Ward, S. and Day, S. (2011), 'The 1963 landslide and flood at Vaiont reservoir Italy. A tsunami ball simulation', *Italian Journal of Geosciences* **130**(1), 16–26.

Watt, S., Pyle, D., Naranjo, J. and Mather, T. (2009), 'Landslide and tsunami hazard at Yate volcano, Chile as an example of edifice destruction on strike-slip fault zones', *Bulletin of Volcanology* **71**, 559–574.

Wei, G., Kirby, J., Grilli, S. and Subramanya, R. (1995), 'A fully non-linear Boussinesq model for surface waves. Part 1. Highly non-linear unsteady waves', *Journal of Fluid Mechanics* pp. 71–92.

Wu, T.-R., Vuong, T.-H.-N., Lin, C.-W., Wang, C.-Y. and Chu, C.-R. (2020), 'Modeling the Slump-Type Landslide Tsunamis Part I: Developing a Three-Dimensional Bingham-Type Landslide Model', *Applied Sciences* **10**(6501).

Xiao, L., Ward, S. and Wang, J. (2015), 'Tsunami Squares Approach to Landslide-Generated Waves: Application to Gongjiafang Landslide, Three Gorges Reservoir, China', *Pure and Applied Geophysics* **172**(12), 3639–3654.

Yavari-Ramshe, S. and Ataie-Ashtiani, B. (2016), 'Numerical modeling of subaerial and submarine landslide-generated tsunami waves–recent advances and future challenges', *Landslides* **13**, 1325–1368.

Yu, M.-L. and Lee, C.-H. (2019), 'Multi-phase-flow modeling of underwater landslides on an inclined plane and consequently generated waves', *Advances in Water Resources* **133**(103421).

Yudhicara, Bani, P. and Darmawan, A. (2015), 'Geothermal system as the cause of the 1979 landslide tsunami in Lembata Island, Indonesia', *Indonesian Journal on Geoscience* **2**(2), 91–99.

Zech, Y., Soares-Frazão, S., Spinewine, B., Savary, C. and Goutière, L. (2009), 'Inertia effects in bed-load transport models', *Canadian Journal of Civil Engineering* **36**(10), 1587–1597.

Zhang, C., Kirby, J., Shi, F., Ma, G. and Grilli, S. (2021a), 'A two-layer non-hydrostatic landslide model for tsunami generation on irregular bathymetry. 1. Theoretical basis', *Ocean Modelling* **159**(101749).

Zhang, C., Kirby, J., Shi, F., Ma, G. and Grilli, S. (2021b), 'A two-layer non-hydrostatic landslide model for tsunami generation on irregular bathymetry. 2. Numerical discretization and model validation', *Ocean Modelling* **160**.

A - OpenFOAM procedure to model 3D complex cases

The following lines detail the procedure to build and run a complex 3D case with OpenFOAM. The file are in italic and the directory in bold.

- *surf2stl.m* in Matlab

  This script convert the bathymetry after the collapse and the bathymetry before the event (the area around the landslide is enough) in geometric .stl file. Both bathymetry files need to be in xyz format. The .stl files produced are necessary to define the mesh and fluids regions in OpenFOAM. Here is an example of Matlab script to launch before using surf2stl.m:

```
A=load('bathymetry_after.xyz');
x=A(:,1); y=A(:,2); z=A(:,3);
x0=unique(x); y0=unique(y);
[X,Y]=meshgrid(x0,y0);
Z=zeros(size(X));
for i=1:length(A)
      ind=find(X==x(k) & Y==y(k));
      Z(ind)=z(k);
end
surf2stl('bathymetry_after.stl',X,Y,Z,'ascii');
```

  From this moment, all the steps take place in your sourced OpenFOAM work directory, containing the directories **constant**, **system** and **0.orig**, along with the *Allclean* and *Allrun* files. The *slide.stl* file has to be placed in this directory and the *bathymetry_after.stl* file in **constant/triSurface**. Warning, the .stl geometry file must be larger than the box generated by blockMesh, in every direction.

  Before to launch the *Allrun* script, a few steps are necessary to build the case.

- in **system**
  - *controlDict* → define the start and end times, timestep, precision and type of outputs, etc...
  - *surfaceFeatureExtractDict* → change the name of the *bathymetry_after.stl* file. This will generate a *bathymetry_after.eMesh* file

  - *blockMeshDict* → change vertices coordinates and blocks resolution
  - *snappyHexMeshDict*

    → change the name of the *bathymetry_after.stl* in 'geometry'

    → change the name of the *bathymetry_after.eMesh* file in 'features'
  - *setFieldsDict*

    → change the coordinates of the box in 'boxToCell' for the definition of alpha.water

    → change the name of the *slide.stl* file and the 'outsidePoints' coordinates in 'surfaceToCell'
  - *decomposeParDict* → change the number of processors and the n(x y z) decomposition
  - *fvSchemes*, *fvSolution* and *meshQualityDict* → nothing to change here

- in **constant**

  - *transportProperties* → change viscosity and density values
  - *g*, *turbulenceProperties*, **extendedFeatureEdgeMesh** and **triSurface** → nothing to change here

- in **0.orig** → change the boundary conditions

Run the command *surfaceFeatureExtract*. It will be necessary just one time. Now use the following *Allrun* script:

```
#!/bin/sh
cd ${0%/*} || exit 1
. $WM_PROJECT_DIR/bin/tools/RunFunctions
#application=$(getApplication)
runApplication blockMesh
runApplication $decompDict decomposePar -cellDist
srun -w proc1,proc2 -n nb_procs snappyHexMesh -parallel -overwrite
runApplication $decompDict reconstructParMesh -constant
mv log.decomposePar log.decomposePar1
mv log.reconstructParMesh log.reconstructParMesh1
rm -rf 0
mkdir 0
cp 0.orig/* 0/
rm -rf processor*
runApplication $decompDict decomposePar -cellDist
srun -w proc1,proc2 -n nb_procs setFields -parallel
```

```
srun -w proc1,proc2 -n nb_procs $(getApplication) -parallel
runApplication postProcess -func writeCellCentres -time 0
runApplication $decompDict reconstructParMesh -latestTime
runApplication $decompDict reconstructPar -withZero -latestTime
runApplication paraFoam -touch-all
```

Let us see in details the meaning of each line.

- **#!/bin/sh**
  cd ${0%/*} || exit 1
  . $WM_PROJECT_DIR/bin/tools/RunFunctions
  #application=$(getApplication)
  → these four lines define the environment and read the name of the application in **system/***controlDict* (e.g. multiphaseInterFoam)

- **runApplication blockMesh** → build the initial rectangular mesh

- **runApplication $decompDict decomposePar -cellDist** → decompose the mesh in the number of processors specified and write this decomposition in **constant**

- **srun -w proc1,proc2 -n nb_procs snappyHexMesh -parallel -overwrite** → run snappyHexMesh in parallel to refine the mesh around the bathymetry_after.stl file. Here srun is used but it works also with mpirun. The name of the processors is specifies in the -w option and their number in the -n option

- **runApplication $decompDict reconstructParMesh -constant** → concatenate the meshes generated by snappyHexMesh in each processor into an unique mesh

- **mv log.decomposePar log.decomposePar1**
  mv log.reconstructParMesh log.reconstructParMesh1
  → change the name of outputs to avoid their replacement in the following

- **rm -rf 0**
  mkdir 0
  cp 0.orig/* 0/
  → make sure that there is no **0** directory, create a **0** directory and copy the files contained in **0.orig** into **0**

- **rm -rf processor*** → delete the generated **processor** directories before creating new ones

- **runApplication $decompDict decomposePar -cellDist** → same as previously
- **srun -w proc1,proc2 -n nb_procs setFields -parallel** → run setFields in parallel
- **srun -w proc1,proc2 -n nb_procs $(getApplication) -parallel** → run the chosen application in parallel (here multiphaseInterFoam)
- **runApplication postProcess -func writeCellCentres -time 0** → write cell centers coordinates in **constant**
- **runApplication $decompDict reconstructParMesh -latestTime** → same as previously for the latest time calculated
- **runApplication $decompDict reconstructPar -withZero -latestTime** → concatenate the results of each processor into one directory for the latest time calculated, or for all times without the -latestTime option (in this case it may be long to process)
- **runApplication paraFoam -touch-all** → make the results readable by Paraview